UNIVERSITA' DEGLI STUDI DI PADOVA

Sede Amministrativa: Università degli Studi di Padova

Dipartimento di Scienze Chimiche

SCUOLA DI DOTTORATO IN SCIENZA ED INGEGNERIA DEI MATERIALI

CICLO XXI

Tesi di Dottorato

SMALL CRYSTAL MODELS FOR THE ELECTRONIC PROPERTIES OF CARBON NANOTUBES

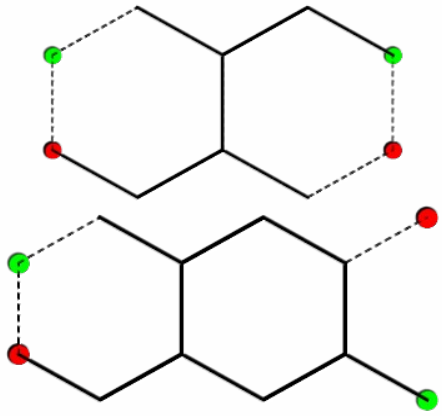

Direttore della Scuola : Prof. GAETANO GRANOZZI

Supervisore : Prof. MORENO MENEGHETTI

Dottoranda : JESSICA ALFONSI

Matricola: 964499-DR

31 Dicembre 2008

Meglio soli che male accompagnati, ma …
… l'unione fa la forza !

Riassunto

Questa tesi sviluppa gli aspetti teorici basilari delle proprietà elettroniche dei nanotubi di carbonio che sono necessari per una comprensione dettagliata delle misure di caratterizzazione ottica tramite fotoluminescenza e spettroscopia Raman. Nella prima parte di questo lavoro vengono introdotte le nozioni generali sui nanotubi di carbonio, la loro struttura geometrica e i fondamenti delle proprietà elettroniche ed ottiche. Queste proprietà sono state descritte sulla base di un calcolo tight-binding svolto in spazio reciproco, noto anche come schema *zone-folding*, che è stato ampiamente utilizzato negli studi teorici sulla struttura elettronica dei nanotubi. In particolare, si è posta grande attenzione ai punti speciali della zona di Brillouin che giocano un ruolo critico nella densità degli stati e negli elementi di matrice elettrone-fotone dei nanotubi a parete singola, dando così il contributo essenziale dominante agli spettri di assorbimento ottico di questi sistemi. La conoscenza dei vettori d'onda critici nella zona di Brillouin è di fondamentale importanza per un'applicazione saggia dell'approccio del cristallo piccolo (*small crystal approach*), che costituisce il contributo originale di questa tesi e che viene introdotto nel Cap. 4. Partendo da una porzione finita del reticolo reale opportunamente scelta con condizioni periodiche al contorno appropriate, l'approccio *small crystal* consente di trovare l'insieme più piccolo di punti della zona di Brillouin che sono sufficienti per calcolare il profilo essenziale degli spettri ottici di sistemi periodici, come i nanotubi a parete singola. Il Cap. 4 stabilisce l'equivalenza completa tra i metodi di tipo *small crystal* e *zone folding*, applicati ai calcoli tight-binding della struttura elettronica per semplici sistemi modello e nanotubi a parete singola. La visione in spazio reale presente nell'approccio del cristallo piccolo consente di superare le limitazioni inerenti ai metodi in spazio reciproco, quando si debbano considerare effetti di rottura locale di simmetria nella struttura elettronica dei nanotubi di carbonio, come interazioni elettrone-elettrone, difetti puntuali e interazioni intertubo dipendenti dall'orientazione dei tubi costituenti, quest'ultimo nel caso particolare dei nanotubi a parete doppia. I Capp. 5 e 6 mostrano l'applicazione dell'approccio small crystal a questi problemi e i risultati ottenuti vengono discussi in relazione alle attuali conoscenze sperimentali e teoriche. In particolare, i nanotubi a parete doppia sono ampiamente studiati per le promettenti applicazioni biologiche e nanoelettromeccaniche. Un'adeguata modellizzazione dell'accoppiamento intertubo dipendente dall'orientazione delle pareti costituenti questi sistemi è necessaria per interpretare le caratterizzazioni sperimentali Raman di questi sistemi. Data la sua formulazione in spazio reale, l'approccio small crystal offre la flessibilità di variare l'orientazione mutua delle pareti costituenti e i parametri che descrivono l'intensità dell'interazione intertubo. I nostri calcoli mostrano variazioni importanti negli spettri di assorbimento ottici dei nanotubi a parete doppia, che rendono conto delle difficoltà solitamente riscontrate nell'assegnazione dei picchi Raman ai diametri e chiralità dei tubi costituenti. Infine, le proprietà eccitoniche dei nanotubi costituiscono forse la questione più discussa nella scienza dei nanotubi, sia teorica che sperimentale. Il Cap. 6 prende in rassegna re-

centi calcoli presenti in letteratura su questo problema e mostra l'applicazione ultima dell'approccio small crystal per introdurre gli effetti di correlazione coulombiana nella descrizione di particella singola, secondo il modello di Hubbard. Selezionando una porzione sufficientemente piccola del reticolo reale con opportune condizioni periodiche al contorno, si può impostare un calcolo many-body completo che consente di ottenere una descrizione qualitativa delle proprietà elettroniche dei nanotubi a parete singola che risulta essere consistente con l'attuale descrizione dei livelli eccitonici di questi sistemi fornita dalle tecniche *ab initio*. Anche se limitata da stringenti requisiti computazionali sulla dimensione dei sistemi trattati, che potranno essere superati con tutta probabilità usando algoritmi più raffinati, la semplice implementazione fornita in questa tesi conferma che per questo metodo si possono certamente prospettare interessanti sviluppi per lo studio delle proprietà di stato eccitato di tubi a diametro grande e per la trattazione dell'inclusione di difetti puntuali in questi sistemi.

Abstract

This thesis develops the basic theoretical aspects of the electronic properties of carbon nanotubes which are necessary for a detailed understanding of optical characterization measurements by photoluminescence and Raman spectroscopy. In the first part of this work I introduced the general facts about carbon nanotubes, their geometrical structure and the fundamentals of their electronic and optical properties. These properties have been described on the basis of a tight-binding calculation scheme carried in reciprocal space, also called *zone-folding* scheme, which has been widely adopted in theoretical investigations on nanotube electronic structure. In particular, great attention has been paid to the special Brillouin zone points which play a critical role in the density of states and electron-photon matrix elements of single-walled nanotubes, thus giving the essential dominant contribution to the optical absorption spectra of these systems. The knowledge of the critical wavevectors in the Brillouin zone is of fundamental importance for a wise application of the *small crystal approach*, which constitutes the original contribution of this thesis and is introduced in Chapt. 4. Starting from a wisely chosen finite portion of the real lattice with proper boundary conditions, the small crystal approach allows to find the minimal set of Brillouin zone points, which are sufficient for computing the essential features of the optical spectra of periodic systems, such as single-walled nanotubes. Chapt. 4 establishes the full equivalence between small crystal and zone folding methods applied to tight-binding electronic structure calculations for simple model systems and single-walled nanotubes. The real space vision embedded in small crystal approach allows to overcome some limitations inherent to reciprocal space based methods, when dealing with local symmetry breaking effects in the electronic structure of carbon nanotubes, such as electron-electron interactions, point-defects and orientation-dependent intertube interactions, the last one in the particular case of double-walled nanotubes. Chapters 5 and 6 show the application of small crystal approach to these issues and discuss the obtained results with respect to the currently available experimental and theoretical findings. In particular, double-walled nanotubes are widely investigated due to promising biological and nanoelectromechanical applications. An adequate modeling of the orientation dependent interwall coupling effects on the optical spectra is necessary for interpreting experimental Raman characterizations of these systems. Given its real space formulation, the small crystal approach offers the flexibility of changing the mutual orientation of the constituent walls and the parameters describing the strength of the interwall interaction. Our calculations show that important changes occur in the optical absorption spectra of double-walled nanotubes which can account for the usual difficulty in assigning experimental Raman features to the diameters and chiralities of the constituent tubes. Finally, excitonic properties of single-walled nanotubes are perhaps the most debated issues both in experimental and theoretical nanotube science. Chapt. 6 reviews recent literature many-body calculations on this subject and shows the ultimate application of small crystal approach for introducing Coulomb correlation effects in the

single-particle picture, according to the Hubbard model. By selecting a sufficiently small portion of the real lattice with suitable boundary conditions, a full many-body calculation can be set up which allow to obtain a qualitative description of the electronic properties of single-walled nanotubes, which is found to be consistent with the current picture of excitonic levels for these systems provided by *ab initio* techniques. Although limited by strict computational requirements on the system size, which are likely to be overcome by using more refined algorithms, the simple implementation provided in this thesis confirms that interesting developments can be certainly prospected for this method, in order to investigate excited state properties of larger diameter tubes and treating the inclusion of point defects in these systems.

Publications

Related papers and conference participations during my PhD are listed in the following.

Papers J. Alfonsi and M. Meneghetti, *Small crystal approach for the electronic properties of double-wall carbon nanotubes* (under review, submitted to *New Journal of Physics*)

J. Alfonsi and M. Meneghetti, *Small crystal Hubbard model for the excitonic properties of zigzag single wall carbon nanotubes* (in preparation)

Posters J. Alfonsi and M. Meneghetti, *Small crystal approach for studying the electronic spectra of carbon nanotubes*, 213th Meeting of the ElectroChemical Society, 18-22 May 2008 , Phoenix (Arizona), U.S.

J. Alfonsi and M. Meneghetti, *Small crystal approach for the optical properties of carbon nanotubes*, TransAlpNano 2008, 27-29 Octorber 2008, Lyon (France)

Other papers F. G. Brunetti, M. A. Herrero, J. de M. Muñoz, A. Dáz-Ortiz, J. Alfonsi, M. Meneghetti, M. Prato and E. Vaázquez, *Microwave-Induced Multiple Functionalization of Carbon Nanotubes*, *J. Am. Chem. Soc.* **30**, *n. 20, 40*

S. Giordani, J-F. Colomer, F. Cattaruzza, J. Alfonsi, M. Meneghetti, M. Prato, D. Bonifazi, *Multifunctional hybrid materials composed of [60]fullerene- based functionalized-single-walled carbon nanotubes*, Carbon, (in press)

Foreword

The present thesis is submitted in candidacy for the Ph.D. degree within the *PhD School in Materials Science and Engineering* at the University of Padua. The thesis describes parts of the work that I have carried out under supervision of Prof. Moreno Meneghetti from Nanophotonics Laboratory in the Department of Chemical Sciences, University of Padua. I thank him for kindly introducing me to small crystal modeling of Hubbard chains and for supporting me in the preparation of article manuscripts and poster presentations. Technical support for Linux and LICC cluster by Ing. G. Sella and M. Furlan is also gratefully acknowledged. I also would like to thank Google, Wolfram Research, Ubuntu and, in general, the whole Open Source Community for providing me a wonderful mine of information and formidable pieces of software.
During my research I have benefitted from correspondance with physicists from widely recognized international research groups. In particular, I'd like to mention A. Grüneis, G. Ge. Samsonidze and N. Nemec for their extremely helpful correspondence. Also, I'd like to thank Dr. A. Thumiger from Prof. Zanotti's group for helping me with practical issues in working with Discrete Fourier Transform.
Last but not least important, this thesis is dedicated to my parents, family and all those people who have always been extremely supporting and who can recognize themselves in this acknowledgment words.

Padua, 31 December, 2008

Jessica Alfonsi

Document typeset in LaTeX 2_ε

Contents

Chapter 1

Introduction

In this chapter we give a general overview about sp^2-hybridized carbon materials. In particular, we focus on nanotube structural properties, preparation and characterization techniques. In the final section, we provide a general classification of the main computational methods, which are heavily adopted in computational materials science for the investigation the electronic properties of these systems.

1.1 Carbon and its allotropic forms

Carbon is one of the most abundant chemical species in the universe and the fundamental building block of all organic structures and living organisms, together with hydrogen, oxygen and nitrogen. This is mainly due to the special position occupied by this element in the periodic table, which allows a single C atom to form up to four covalent bonds to its neighboring atoms. Until the Eighties, it was believed that the only crystalline allotropic forms were diamond and graphite. This picture started to change in 1985 with the discovery of fullerenes [1], when it became clear that carbon can form other stable crystalline forms. After the identification of carbon nanotubes in 1991 by Iijima [11], the list of observed and hypothetically proposed carbon nanostructures started to grow soon, including double- and multi-shell fullerenes and nanotubes and many other structures, some of which will be presented in the final part of this section.

1.1.1 Hybridization of carbon orbitals

The electronic configuration of a free carbon atom is $1s^2 2s^2 2p^2$. The electrons in the 1*s* orbitals are the core electrons, while the remaining four electrons in the 2*s* and 2*p* orbitals are the valence electrons and are available to form chemical bonds. We recall that the electronic wavefunction of an atom can be obtained as an eigenstate of the angular momentum operator. The 2*p* degenerate orbitals have identical geometrical shape for the three different orientations, as shown in Fig. 1.1. Although the 2*s* are filled in the

ground state by two electrons, the energy difference between 2*s* and the three degenerate 2*p* orbitals is small enough, that hybridization of these orbitals occurs in several ways. Depending on the hybridization, different structures can be obtained, since a different number of nearest neighbour atoms are required.

- Hybridization of the $2s$ with one $2p$ orbital gives a set of two *sp* orbitals in diametrically opposed directions.

$$|2sp_a\rangle = \frac{1}{\sqrt{2}}\left(|2s\rangle + |2p_y\rangle\right) \tag{1.1}$$
$$|2sp_b\rangle = \frac{1}{\sqrt{2}}\left(|2s\rangle - |2p_y\rangle\right)$$

  This is the so called *sp*-hybridization $(n = 1)$, which is relevant for organic molecules (acetylene), but not for crystalline carbon structures.

- Hybridization of the $2s$ with two $2p$ orbital results in three equivalent sp^2 orbitals arranged in plane and pointing each at an angle of 120^{o} from one another:

$$|2sp_a^2\rangle = \frac{1}{\sqrt{3}}\left(|2s\rangle + \sqrt{2}|2p_x\rangle\right) \tag{1.2}$$
$$|2sp_b^2\rangle = \frac{1}{\sqrt{3}}\left(|2s\rangle - \frac{|2p_x\rangle}{\sqrt{2}} + \frac{\sqrt{3}|2p_y\rangle}{\sqrt{2}}\right)$$
$$|2sp_c^2\rangle = \frac{1}{\sqrt{3}}\left(|2s\rangle - \frac{|2p_x\rangle}{\sqrt{2}} - \frac{\sqrt{3}|2p_y\rangle}{\sqrt{2}}\right)$$

  These orbitals can form strong covalent σ bonds with neighboring carbon atoms giving rise to planar crystalline structures. The remaining unhybridized p_z orbital is perpendicular to the plane and forms the so called valence π orbitals with other parallel p_z orbitals of neighboring atoms. Valence π orbitals are strongly delocalized, therefore they are responsible for the electronic and optical properties of the sp^2 structures in the visible range (1-3 eV), as it happens with graphite.

- Hybridization of the $2s$ with all three $2p$ orbital results in four equivalent sp^3 orbitals in a tetrahedral arrangement at an angle of 109.5^{o} (tetrahedral angle):

$$|2sp_a^3\rangle = \frac{1}{2}\left(|2s\rangle + |2p_x\rangle + |2p_y\rangle + |2p_z\rangle\right) \tag{1.3}$$
$$|2sp_b^3\rangle = \frac{1}{2}\left(|2s\rangle + |2p_x\rangle - |2p_y\rangle - |2p_z\rangle\right)$$
$$|2sp_c^3\rangle = \frac{1}{2}\left(|2s\rangle - |2p_x\rangle + |2p_y\rangle - |2p_z\rangle\right)$$
$$|2sp_d^3\rangle = \frac{1}{2}\left(|2s\rangle - |2p_x\rangle - |2p_y\rangle + |2p_z\rangle\right)$$

These orbitals form four strong covalent σ bonds with the neighboring carbon atoms but are electronically inactive because of their low energy. Hence the resulting material will have very stiff geometry and insulating properties, as for instance diamond.

According to the type of hybridization, carbon materials can be classified into diamond-like and graphite-like materials, if the hybrid orbitals are sp^3 or sp^2, respectively. This give rise to two different kind of crystalline structures, a tetrahedral structure for diamond and a layered structure for graphite (Fig. 1.1). The graphitic layers are held together by weak *van der Waals* forces, which allow them to slide against each other with minimal friction.

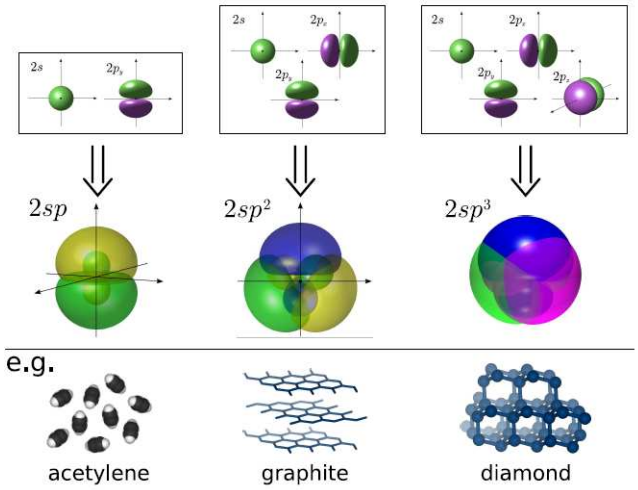

Fig. 1.1: The three hybridized form of carbon: *sp* hybridization occurs only in some organic compunds (i. e. alkynes). sp^2 hybridization gives planar structures such as graphitic layers, sp^3 hybridization forms diamond-like structures. Image taken from Ref. [123].

A single graphitic layer is called graphene. From this two-dimensional structure a whole pletora of structures can be derived, as shown in Fig. 1.2. The in-plane σ-bonds of sp^2 hybridized carbon are stiff with respect to longitudinal forces, but allow for angular deformation. In a graphene layer this is the cause for the observed ripples [4]. More generally, this flexibility opens the way for a large family of stable graphitic nanostructures, with a mixed sp^2-sp^3 hybridization. The mixing degree is expressed by the pyramidalization angle, which is highest for systems with lowest dimensionality, such as fullerenes, which are zero-dimensional. As previously noticed, the π orbitals are close to the Fermi energy, leading to either conducting or semiconducting properties, according also to the

degree of curvature of these systems. This opens up the path to a great deal of potential applications in future nanoelectronics [44]. In the following section we will give a more detailed overview of the structural properties of graphitic materials, with some hints about their preparation techniques.

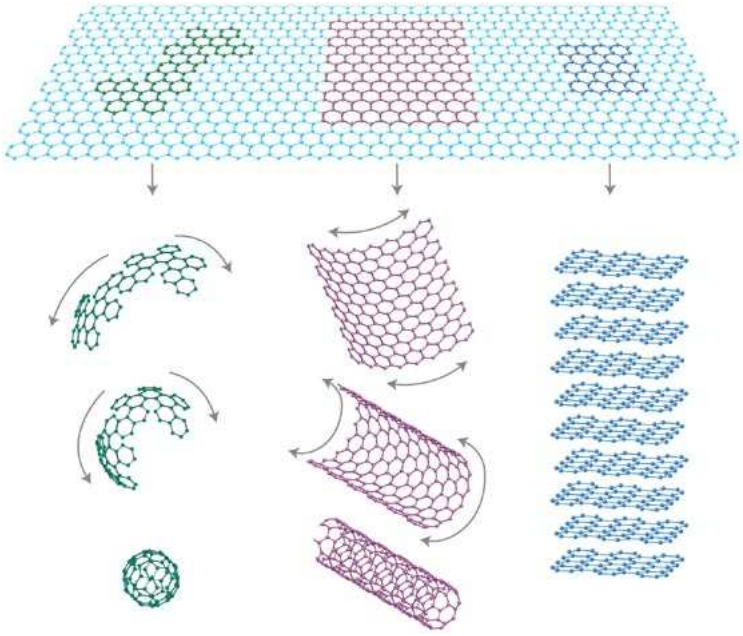

Fig. 1.2: Hypothetical construction of various graphitic structures. Starting from fragments of two-dimensional planar graphene (top), quasi-0 D fullerenes (bottom left) and quasi-1 D nanotubes (bottom center) are obtained. Stacks of graphene sheets give 3D graphite (bottom right). Image taken from Ref. [5].

1.1.2 Graphite

Graphite is the most stable carbon allotrope. Usually it is found in nature in polycrystalline form with small grains of size up to a few micrometers. It is mechanically soft, since individual layers can slide easily against each other, making graphene an important lubricant in tribological applications. It is electrically conducting, with a highly anisotropic conductivity due to its layered structure: the in-plane conductivity is much larger than the conductivity perpendicular to the layers. Usually it is not used as thermal energy source, because it is hard to ignite. The first recognition based on x-ray diffraction of the hexagonal layered structure of graphite was given by A. W. Hull in 1917 [45]. Then, in 1924 J. D. Bernal completed the picture by identifying the individual planar layers [46]. Graphite consists of parallel graphene sheets with interlayer

spacing $d_{\text{interlayer}} = 3.34\,\text{Å}$. There are two possible stackings of the layered structure: the *Bernal stacking* with alternation ABAB and the *rhombohedral stacking* with alternation ABCABC. Although the latter form has never been isolated, it has been shown that natural graphite often contains a certain amount of rhombohedral stacking, which has been explained as an intermediate state in the transition from graphite to diamond. A further modification is *turbostratic graphite*, which has the individual layers rotated by random angles againts each other. In this case the system can be considered a sort of quasi-crystalline structure.

1.1.3 Graphene

Single layer graphene was discovered experimentally only in 2004 and is actually the basic building block for the theoretical understanding of all other sp^2-hybridized carbon structures, such as graphite, fullerenes and nanotubes. According to the theoretical prediction by Mermin and Peierls [47, 48], two-dimensional systems with long-range order cannot exist in nature, because of the logarithmic divergence associated with the quantum-mechanical fluctuations of the atomic displacements. Only in three dimensions the displacements would converge with the distance, allowing the formation of a stable crystal. However, this theoretical argument does not prevent freely suspended graphene sheets to exist, since the structure can be stabilized in the third dimension by ripples, which were actually observed by electron diffraction [4] (see Fig. 1.3). Thus graphene can be considered effectively as a truly two-dimensional crystal. It is characterized by a honeycomb structure, with the distance between neighboring atoms being $d_{CC} = 1.42\,\text{Å}$ and the lattice constant $a = \sqrt{3}d_{CC} \approx 2.46\,\text{Å}$. For further details about the graphene structure both in real and reciprocal space, the reader is advised to consult Sect. 2.1 in the following chapter. Graphene crystals can break at crystal edges in two ways, by forming either a zigzag edge, which runs parallel to a graphene lattice vector, or an armchair edge, which runs parallel to the carbon bonds (see Fig. 1.4). The edge states are especially relevant for finite width graphene nanoribbons, as we will see in the dedicated subsection.

Synthesis Historically, it took a long time before the first successful isolation of single graphene layers [2]. However, this fact is even more surprising if we consider the simple approach that led to success: the exfoliation method. In this method, a scotch tape is used repeatedly to peel off flakes from pyrolytic graphite that become thinner with each step until finally, there is a single layer left that can be placed on a clean surface for further handling [3, 4]. The main difficulty with this technique is that such thin structures are generally invisible by optical means and, consequently, there is no electronic signature that would simplify the search. Thus samples have to be screened tediously via atomic force microscopy (AFM). An alternative way to exfoliate graphene can be achieved by wet chemistry [6], which has started to show promising results. Besides exfoliation,

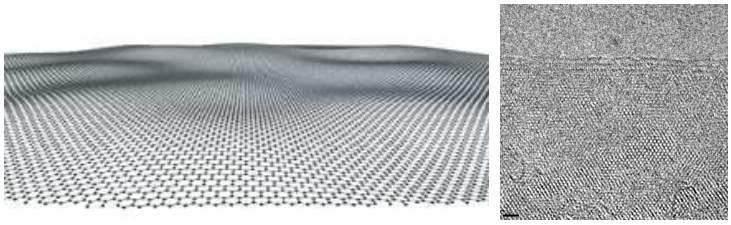

Fig. 1.3: Illustration of the rippled structure of a suspended graphene sheet (left) and TEM-image of a few-layer graphene membrane near its edge (right). The out-of-plane fluctuations are supposed to be necessary for the stabilization of the 2D structure. Image taken from Ref. [4].

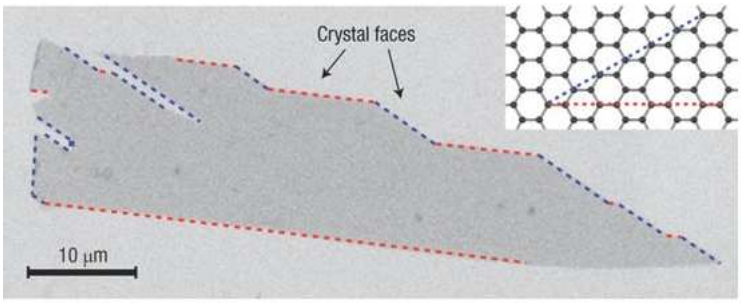

Fig. 1.4: STM image of an exfoliated graphene monolayer. The crystal edges have either zigzag (blue) or armchair (red) edges. Image taken from Ref. [5].

which is a top-down process, one can prepare graphene by bottom-up techniques, such as epitaxial growth. Actually, this procedure has been applied to graphite already 40 years ago, by using pyrolisis of methane on Ni crystals [7]. The technique has been refined to produce graphene sheets on various crystal surfaces and ribbons of well defined width (1.3 nm) [8]. Alternatively, epitaxial growth of graphene can also been achieved by segregation of C atoms from inside a substrate (Pd, Ni, Pt, SiC) to its surface [9, 10]. In general, with these epitaxial growth methods, very high crystal qualities can be obtained, sometimes pseudomorphically with respect to the substrate lattice constant. Successful attempts to lift off epitaxially grown graphene from the surface are not known at the moment, but there isn't any fundamental obstacle preventing to reach this in the future.

1.1.4 Fullerene

Fullerenes were discovered in 1985 by the team of H. W. Kroto, J. R. Heath, S. C. OBrien, R. F. Curl, and R. E. Smalley [1] and named after the geodesic domes by architect R. Buckminster Fuller. Fullerenes are zero-dimensional nanostructures. They consist

of a varying number of carbon atoms, forming 12 pentagons, and a varying number of hexagons in a sphere. Perhaps the most studied fullerene specie is the highly symmetric C_{60} molecule, also named bucky ball, forming a truncated icosahedron, which is the structure of a soccer ball. Fullerenes form crystals called fullerites that occur naturally within shungite (Fig. 1.5). Fullerenes were later found to occur naturally, as for example in regular candle soot. The arc-discharge method allows the easy production of grams of fullerenes, although they have to be purified.

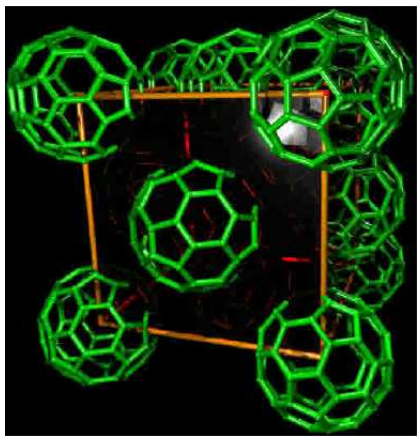

Fig. 1.5: Face centered cubic crystal of C_{60} (fullerite). Image taken from Ref. [43].

1.1.5 Single-wall and multi-wall nanotubes

Nanotubes were discovered officially in 1991 by Iijima and coworkers [11]. However, the credit for the discovery of these nanostructures has been an issue of recent hot discussion in literature [13]. The first images of multiwall carbon nanotubes were actually published in 1952 by the Soviet team of L. V. Radushkevich and V. M. Lukyanovich [14]. Later, they were rediscovered in 1976 by A. Oberlin, M. Endo and T. Koyama [15]. In both cases, the discovery was largely unrecognized for its significance until the real boom of nanotube research initiated by the work of S. Iijima in the Nineties. The first observation of a single-wall CNT was reported soon afterwards in 1993 by two groups independently: S. Iijima and T. Ichihashi [12] as well as D. S. Bethune [16].
A single-walled carbon nanotube can be described as a graphene ribbon rolled up in cylindrical fashion, such that both edges are joined to form a tube with a well-defined chirality. Each of the various ways of forming a tube can be uniquely specified by the chiral vector (n, m). This vector is a lattice vector of the graphene sheet which corresponds exactly to the circumference of the rolled-up tube. A more detailed description of the geometrical structure of a single-wall nanotube (SWNT) according to the way the

graphene sheet is wrapped up is given in Chapt. 2. If more cylindrical shells are nested into one another, then the structure is a multiwall nanotube (MWNT), where the interwall distance is similar to the interlayer distance of graphite $d_{\mathrm{interwall}} \approx 3.34\,\text{Å}$. The simplest carbon MWNT is a double-walled carbon nanotube (DWCNT), which will be considered in detail in Chapt. 5. This kind of structure is the reason behind the extreme mechanical strength in longitudinal direction, which even exceeds that of diamond: for instance, the predicted value of the Young's modulus (1 TPa) is the highest known among all materials [89, 44]. This theoretical property alone has inspired a multitude of potential applications ranging from ultra-strong textiles and compound materials to the famous idea of the space-elevator. Besides, the main reason for this tremendous interest in carbon nanotube reserach is related to their unique electronic properties. They can be semiconducting or metallic according to their geometrical structure, which is basically specified by diameter and chirality. The understanding of these aspects will be a fundamental step towards the advent of an all-carbon-based nanoelectronics. Recent reviews about CNTs electronic and transport properties and their applications can be found in Refs. [44, 49].
The smallest freestanding SWCNTs typically observed in experiment have a diameter of 0.7 nm, corresponding to a C_{60} molecule [17]. However, smaller tubes down to 0.4 nm have been observed either as innermost shell of MWCNTs [18, 19] or embedded in porous crystals such as zeolite [20]. The largest observed SWCNT have a diameter of up to 7 nm [21], even though their section is no longer circular but elliptical, as they have the tendency to collapse.
As stated above, MWCNTs were experimentally discovered earlier than SWNTs. Due to their greater abundance, larger diameter and the consequently easier handling, far more experimental results are available for MWNTs than SWNTs. Yet on the theoretical side, much effort has been devoted to the investigation of SWNTs, whereas due to the greater complexity of MWNTs, the theoretical understanding of the effects of the combination of several walls still remains an open issue [176].

Synthesis It is generally believed that CNTs exist only as a synthetic material. However, there are also indications that natural carbon soot contains certain amounts of these structures mixed in with all other forms of amorphous carbon. Recently, it has been found that nanotube synthesis may actually have been accessible in medieval times already, even though the producers of the legendary Damascus sabers [22] were certainly not aware of the nanosized structures embedded in their manufacts. In the following, we will briefly describe the three major methods adopted for nanotube production: *arc discharge, laser ablation, chemical vapour deposition*. The *arc discharge method* consists in driving a 100 A DC current through graphite electrodes immersed in He atmosphere at 400 mbar. Anyway, the production can be done in open air, as well. It's the method originally used in 1991 by S. Iijima [11], who discovered carbon nanotubes in the soot. Later, the efficiency of the method was improved to yield macroscopic quantities of nanotubes [23]. Although the method is easy to set up, it provides very limited control over the production

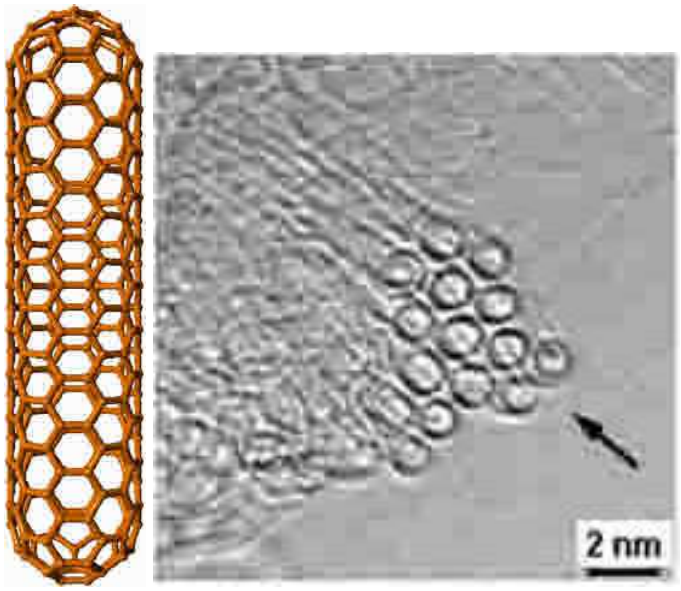

Fig. 1.6: Schematic structure of a capped single-wall nanotube (left) and TEM image of a SWNT bundle (right).

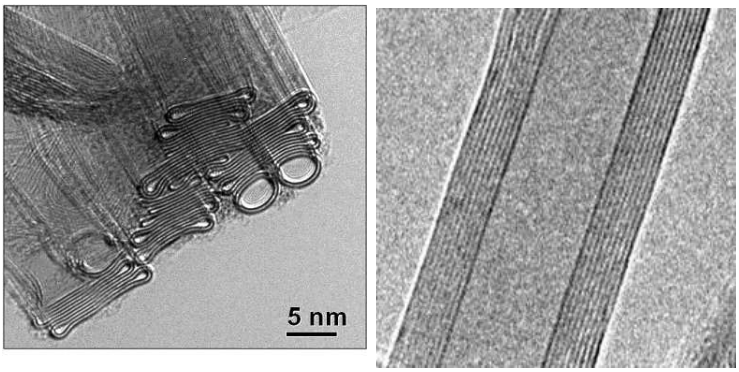

Fig. 1.7: TEM pictures of bundled double-wall nanotubes (left) and of a multiwall nanotube (right).

parameters: the nanotubes are generally very short, have a wide distribution of diameters and mixed with amorphous carbon. Arc discharge nanotubes typically have few defects. The *laser ablation method* was pioneered by R. E. Smalley in 1995 [24]. Pure graphite is thermally evaporized by high-powered laser pulses. By finetuning the parameters, yields of high purity nanotubes can be achieved and the nanotube diameter distribution can be controlled. The main drawback of this method is the need for expensive equipment and

high power laser sources. The *chemical vapor deposition method* (CVD) is the most commonly used low-cost method for the growth of carbon nanotubes. Indeed, this is the method that was used by A. Oberlin and M. Endo for their first observation of carbon nanotubes in 1976 [15]. Generally, this method is based on the thermal decomposition of hydrocarbons species such as CH_4 (methane), C_2H_5OH ethanol, CH_3OH methanol, into atomic carbon from a chemical compound and depositing it on a catalytic surface where nanotube can then grow in very controlled ways. The type and quality of the grown nanotubes depends delicately on the growth parameters. It is possible to selectively grow a narrow diameter range of single-wall tubes [25] or double-wall tubes [26], control the direction of growth [27] or grow highly aligned arrays of tubes [28]. A common drawback of CVD methods is the contamination by catalyst particles and the relatively high defect rate.

1.1.6 Other graphitic nanostructures

In the final part of this section we will provide a brief overview of the three most studied new graphitic nanostructures which are closely related to carbon nanotubes. Other new interesting carbon nanostructures can be found in general reviews, such as Refs. [35, 42, 43].

Graphene nanoribbons (GNRs) were initially considered as a theoretical toy model for studying the electronic and phononic edge states in graphene, without much concerning about how such structures could realistically be produced [30]. In 2002, however, before the first successfull graphene isolation by exfoliation, T. Tanaka *et al.* indeed managed to grow well-defined, narrow GNRs on a TiC surface and measured its phononic edge modes [29]. Soon after the graphene boom, both theoretical and experimental interest in GNRs began to rise, since ribbons are nowadays considered as a serious alternative to carbon nanotubes (CNTs) as quantum wires and devices [31].

Peapods are hybrid hierarchical structures, which consist in fullerenes encased in single-walled nanotubes. They were discovered in 1998 by Luzzi *et al.* in a sample of acid-purified nanotubes [32]. The material is called *peapod*, because its structure resembles miniature peas in a pod. A total energy electronic structure calculation [33, 34] showed that the encased fullerene molecules are energetically very stable, since an energy gain of $\approx 0.5\,\mathrm{eV}$ is involved during peapod formation, while when the C_{60} molecule physisorbs on the outer surface of the tube, the energy gain is only $\approx 0.09\,\mathrm{eV}$. As for the formation mechanism, the general consensus, also supported by molecular dynamic simulations, is that fullerenes enter the nanotubes through the open ends. Potential use of nano-peapods range from nanometer-sized containers for chemical reactions to nanoscale autoclaves, data storage and possibly high-temperature superconductors (see Ref. [42] and references therein). As an interesting application, peapods can be turned into high-purity

double-walled nanotubes by coalescence of the encapsulated fullerenes achieved by electron irradiation at $320\,\mathrm{kV}$ [36, 37].

Scrolls are rolled up graphene sheets with an exposed edge. Formation of a scroll requires both the energy to form the two edges along the entire axis and the strain energy to roll up the graphene sheets. A scroll will be stable as long as the energy gain due to the interwall interaction upon the rolling up of the sheet outweighs the energy cost due to the exposed edges [35]. The existence of such structures was argued in high-resolution transmission electron microscopy (HRTEM) investigations on defective MWNTs [38], where scrolled structures could not be discriminated from MWNTs with line defects analogous to edge dislocation in 3D crystals. It is commonly accepted that less stable scroll structures may exists as a precursor state to multi-wall nanotubes and that the scroll-to-nanotube conversion occurs through a zipper-like transformation at the atomic scale, involving opening and reconnection of the carbon bonds at the interface between the exposed edge and the curved tube wall [35, 39]. A new synthesis route was also devised for the production of scrolls from polymeric suspensions of graphite intercalated alkali compounds (GICs) [40] and graphite ball-milling [41], in order to obtain nanotubes by exploiting the scroll/nanotube conversion mechanism.

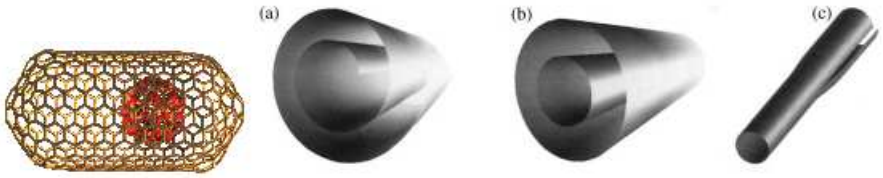

Fig. 1.8: Schematic structure of a carbon peapod (left) and view of a) a scroll, b) a multiwall nanotube, and c) a defect separating the two morphologies within one tube (right). Images taken from Ref. [35, 42]

1.2 Nanotube characterization techniques

1.2.1 Characterization techniques

In general, carbon nanotubes and related graphitic materials have been investigated by a variety of characterization techniques, which allow to probe, even simultaneously in a single experiment, their structural and electronic properties. High resolution X-ray diffraction (HRXRD) and electron diffraction from transmission electron microscopy (HRTEM) have been widely used for the pure structural characterization of carbon nanotubes [51]. A complete identification of the nanotube chiralities from the indexing of the

diffraction patterns could be achieved on the basis of simulations of the x-ray intensity diffraction patterns for systems with helical symmetry [50, 52]. While diffraction-based techniques provide a reciprocal space picture of carbon nanotube structure, scanning tunneling microscopy (STM) provides direct access to the local atomic structure of the sidewall, thanks to the reconstruction of maps of the electronic charge density of the tube surface in real space [53, 54]. Moreover, if scanning tunneling spectroscopy (STS) is performed by measurement of current-voltage characteristics, one can also probe the local electronic density of states at a given location, thus allowing to obtain a direct correlation between electronic and structural information. Scanning tunneling spectroscopy measurements were performed in 1998 by Odom and Lieber on single-walled nanotubes, which proved the electronic one-dimensionality of these systems [55]. Despite the high-resolution structural information provided by these characterization techniques, however their use for routine characterization work is quite impracticable for several reasons, mainly the need of ultra-high vacuum operation conditions and experimental apparatus costs. Moreover, in the case of STM, in order to obtain electronic structure information, STS can be performed exclusively on an isolated tube. Therefore, less expensive and non-destructive analysis techniques, such as optical spectroscopical techniques, become preferable when probing electronic and structural properties on statistical nanotube samples in an unique experiment. In the following we will review the basics of the two main optical characterization techniques used in nanotube research, namely photoluminescence (PL) and resonance Raman spectroscopy.

1.2.2 Photoluminescence and optical absorption measurements

As stated previously, SWNTs can be either metallic or semiconducting, depending on their geometrical structure. In the case of semiconducting tubes, the energy gap is approximately proportional to the inverse of the tube diameter and photoluminescence (PL) from the recombination of electron-hole pairs at the band-gap can be expected, according to the usual band picture for semiconducting materials (Fig. 1.9). The discovery of band-gap fluorescence by M. O'Connell *et al*. occurred on acqueous micelle-like suspension of SWNTs [56]. Thus, spectrofluorimetric measurements are a valid and not so expensive experimental tool for extracting nanotube specific electronic properties from bulk measurements and correlate them to their chirality [57]. However, nanotubes are generally bundled because of the van der Waals interactions and normally contain both metallic and semiconducting species. Metallic SWNTs act as non-radiative channels for the luminescence of semiconducting tubes. Therefore, it may often occur that no PL signal is observed for SWNT bundles. In order to observe PL, the bundles must be separated into individual tubes. In order to achieve this separation, several techniques have been developed: ultrasonication treatment of the nanotubes with surfactants (e.g. sodium dodecyl sulfate or SDS) in acqueous suspensions, growth of individual tubes in channels of zeolite, alternating current dielectrophoresis of the sonicated suspensions and other

techniques based on chemical functionalization for separating metallic and semiconducting tubes [59]. Spectroscopic measurements are performed with spectrofluoremeter equipped with InGaAs near-infrared detector cooled by liquid nitrogen. Emission intensity is measured as a function of both excitation wavelength (from 300 to 900 nm) and emission wavelength (from 810 to 1550 nm), to give the results shown in the contour plot of Fig. 1.9. The different intensities in Fig. 1.9 come from the chiral and diameter dependent distribution of SWNTs in the sample and/or related electron-photon and electron-phonon interaction strengths. On the other hand, measurements of the optical

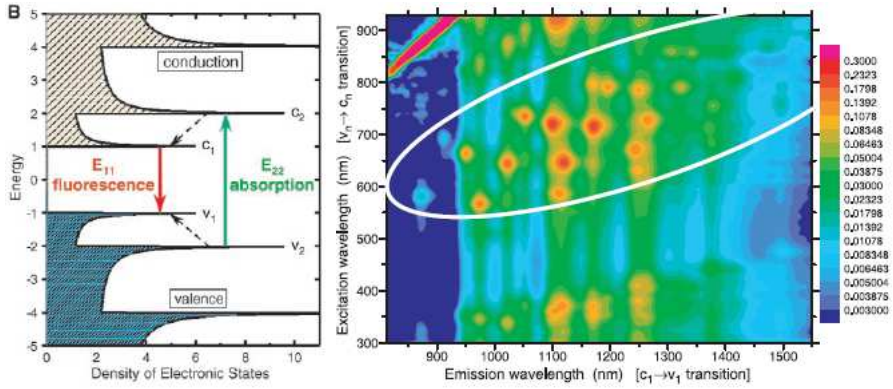

Fig. 1.9: Photoluminescence mechanism in a SWNT according to the band picture (left) and contour plot (right) of the fluorescence emission energy vs the excitation energy for acqueous suspended SWNTs. Pictures taken from Bachilo *et al.* [57]

absorption of bundled SWNTs in trasmission or reflection geometry show the presence of the spectral features of both metallic and semiconducting tubes. In Fig. 1.10 a typical absorption spectrum of SWNT bundles is shown, taken from Ref. [58]. Three peaks can be seen, which are attributed to the van Hove singularities in the joint density of states (see Chapt. 3). Tight-binding calculations suggest that the two lower peaks can be attributed to SWNTs with transition energies E_{11}^S and E_{22}^S, while the third peak originates from metallic nanotubes with transition energy E_{11}^M.

1.2.3 Resonant Raman spectroscopy

This is one of the most powerful tools for characterizing nanotubes and other graphitic materials, since it doesn't require sample preparation and a fast non-destructive analysis is possible. Unlikely PL, metallic nanotubes can also be observed. For general reviews about this technique applied to carbon nanotubes in the last ten years see Refs. [119, 120]. Raman spectroscopy allows to probe the vibrational properties of a material by measuring the energy shift of the inelastically scattered radiation from the energy of the incident light

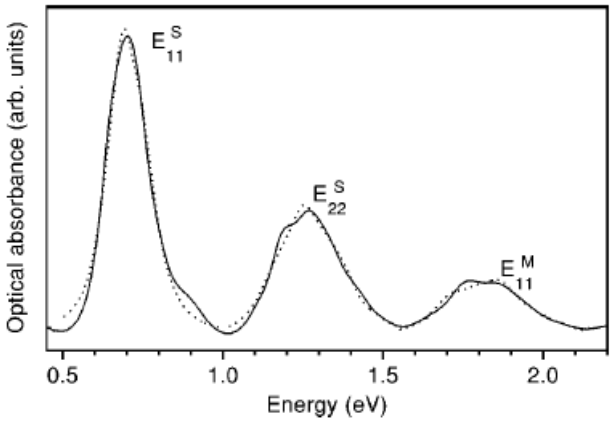

Fig. 1.10: Experimental optical absorption spectrum (solid line) of a sample of SWNTs of all chiralities. The dotted line represents the result of the simulation based on tight-binding calculations. Taken from Ref. [58]

(the so called *Raman effect*). The energy shift can be positive (absorption of a phonon) or negative (emission of a phonon), also referred to as anti-Stokes and Stokes processes, respectively. If the energy of either the incoming or the scattered photon matches the energy of a real electronic state, the process is called *Resonant* Raman scattering (RRS) [98]. First and second order Raman scattering are defined by one and two scattering events, respectively. In particular, in 2nd order Raman scattering we can have either two phonon scattering processes or one phonon and one (defect-mediated) elastic scattering processes. In first order Raman scattering only phonon modes with $q \approx 0$ are probed and the phonon dispersion cannot be provided, because the wavevector of the incoming photon is too small to create phonons with large momentum, that is distant from the center of the Brillouin zone. In 2nd order Raman scattering this condition can be removed because two phonons (or one phonon and one defect) are involved in the process with the sum of the respective wavevectors giving total zero wavevector. Also, in all Raman scattering processes, we have the absorption of the incoming photon and the emission of a photon after electron-hole pair recombination. Thus in the general expression for the resonant Raman scattering event, the electron-photon interaction element appears two times, while the electron-phonon coupling element can appear either one or two times, according to the order of RRS. The general formula used to evaluate the Raman intensity for a 1st order resonance Raman scattering is:

$$I\left(E_{laser}\right)=\int\left|\frac{M_{optA}^{cv}\left(\mathbf{k}\right)M_{vib\rho}^{cc}\left(\mathbf{k}\right)M_{optE}^{vc}\left(\mathbf{k}\right)}{\left(E_{laser}-E\left(\mathbf{k}\right)-i\Gamma_{r}\right)\left(E_{laser}\pm E_{vib}-E\left(\mathbf{k}\right)-i\Gamma_{r}\right)}\right|^{2}d\mathbf{k}. \qquad (1.4)$$

The electron-photon matrix elements are $M_{optA}^{cv}\left(\mathbf{k}\right)$ and $M_{optA}^{vc}\left(\mathbf{k}\right)$ for photon absorption and emission, respectively. $M_{vib\rho}^{cc}\left(\mathbf{k}\right)$ denotes the electron-phonon matrix element for

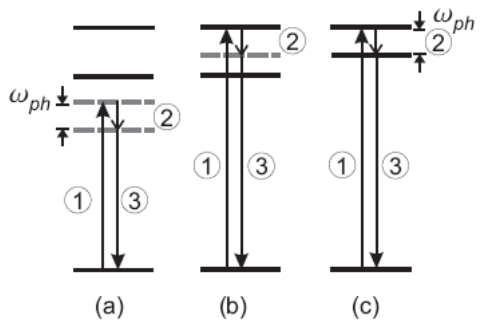

Fig. 1.11: a) Non-resonant, b) single- and c) double-resonant Raman scattering. Solid lines are real electronic states, dashed lines represent virtual electronic states (i. e. they are not eigenstates of the system). In the non-resonant process (a), both intermediate electronic states are virtual. If the laser energy matches a real electronic transition [first step in (b)], the Raman process is single resonant. If the special condition (c) is met, i.e., in addition to (b) another electronic transition matches the phonon energy, a double- or triple-resonance occurs. Taken from Ref. [90].

a photoexcited electron in the conduction band. For phonon absorption (anti-Stokes) we have $\rho = A$, for phonon emission (Stokes) we have $\rho = E$. The factors in the denominator describe the resonance energy difference between incident and scattered light, where the $+(-)$ sign applies to the anti-Stokes (Stokes) process for a phonon of energy E_{vib}. Γ_r gives the inverse lifetime for the scattering process. In Fig. 1.12 a Raman spectrum obtained from a SWNT sample is reported. The first order spectral features of a SWNT consist of only two strong bands, the radial breathing mode (RBM) at about $200\,\mathrm{cm}^{-1}$ and the graphite derived tangential mode or G band at about $1580\,\mathrm{cm}^{-1}$. A typical second order spectral feature is the D band at about $1350\,\mathrm{cm}^{-1}$ for 2.41 eV laser energy and the G′ band at $2700\,\mathrm{cm}^{-1}$. Two relevant characteristics of the D band are that (1) the intensity of the D band depends on the defect concentration in SWNTs and (2) its frequency increases with increasing laser energy [90]. On the other hand, the G′ band intensity is independent on defect concentration and is comparable to the G band intensity. The radial breathing mode is perhaps the most interesting phonon mode used for nanotube characterization [126], since it depends on the nanotube diameter through the relation

$$\omega_{RBM} = \frac{A}{d_t} + B \tag{1.5}$$

where *A* and *B* parameters are determined experimentally. Note that this relation is not valid for nanotube diameters below $1\,\mathrm{nm}$, for which a chirality dependence of ω_{RBM} appears due to the distorsion of the nanotube lattice. For example, for an isolated SWNT on Si/SiO_2 substrate the experimental value of A is found to be $248\,\mathrm{cm}^{-1}$ and $\mathrm{B} = 0\,\mathrm{cm}^{-1}$

[128]. Furthermore environmental effects due to temperature, surfactant, bundling and/or intertube interactions in DWNTs and MWNTs causes a frequency modification of the RBM mode [131]. By plotting the measured transition energy obtained from PL or RRS at different laser excitation energies versus the SWNT diameter the so-called Kataura plots are obtained [127], which are widely adopted for the experimental investigation of the properties of these systems [129, 153]. These plots can also be obtained from theoretical calculations, so that chirality assignment of diameters and transition energies can be performed through the comparison with experimental results [132, 133] (Fig. 1.13).

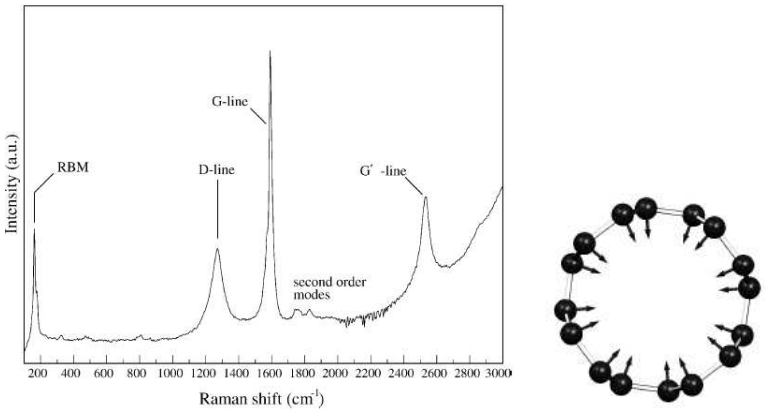

Fig. 1.12: Raman spectrum of single-walled nanotubes (left) and radial breathing mode (RBM) (right). Taken from Ref. [59].

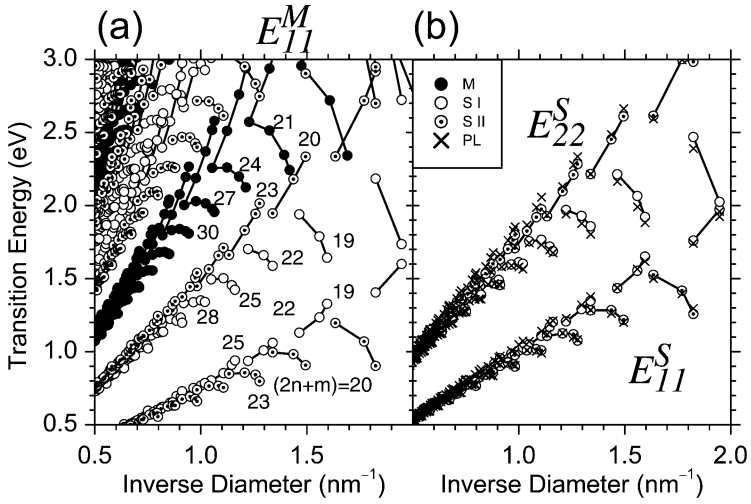

Fig. 1.13: Kataura plot for metallic and semiconducting SWNTs (taken from Ref. [132]).

1.3 Electronic structure computational methods

The role of computational materials science has become of fundamental importance not only for the advancement of basic research but also in the applied field of nanotechnology. Theoretical modeling and computer simulations can directly access with high accuracy the shortest length and time scales of nanoscopic systems and phenomenons. Boosted by the rapidly increasing computing power, nanoscale simulations have thus become a predictive tool for the design of novel devices and now modelling is an integral part of interdisciplinary materials research. In order to study the electronic behaviour of carbon materials, one has to solve the basic equation of quantum mechanics, the many-electron Schrödinger equation. However, in spite of the impressive computer power at our disposal, solving this equation remains a difficult task and requires a deep physical and chemical understanding of many-electrons systems. Combining these notions with modern mathematical concepts leads to algorithms that exploit the characteristics of the electronic systems under investigation to provide powerful new electronic structure methods. Adapting these methods for modern computer architectures will result in powerful programs which aid the research of many systems. A wide range of computational methods is available for the theoretical modeling and simulation of carbon materials properties. These methods are actually based on approximations at various level of detail of the complicate many-body problem, thus they can be considered a compromise between efficiency and accuracy. In general, they can be classified into three groups: *ab initio*, semi-empirical, tight-binding and effective methods. In the following, we will briefly outline a general overview of the methods used in electronic structure calculations together with the respective advantages/disadvantages, without going into technical details for which the reader can consult more specific references, such as Ref. [93].

***Ab initio* methods** allow the computation of materials properties from first principles, without the need of parameters to be adjusted or fitted to experimental input data, apart from the fundamental physical constants and atomic masses. The general advantage of *ab initio* methods is the high accuracy of the quantitative results. The main disadvantages are represented by the high computational cost and the difficulty of getting a deeper understanding of the calculated phenomena. They can be further classified into *wavefunction methods* and *density functional methods* (see for example Ref. [60]).
Wavefunction methods solve self-consistently, in a mean-field approximation, the many-electron Schrödinger equation by expanding the many-electron antisymmetrized wavefunction in Slater determinants, formed by a set of orthonormal one-electrons orbitals $\phi_i(\mathbf{r})$. This constitutes the basics of Hartree-Fock (HF) method. Configuration interaction (CI) and coupled-cluster methods (CC) go beyond this level of approximation and have been widely used in quantum chemistry for treating electronic correlations, but also implementations for periodic systems (oxides and crystals of small organic molecules) have been set up. HF theory is less appropriate for systems with high electron density

such as transition metal systems or with highly delocalized states and fails completely to account for the collective Coulomb screening in a perfect metal. Inclusion of correlation effects reduces the system size accessible to calculation to few hundred atoms, depending on the level of theory. The most accurate correlated methods are restricted to molecules with just a few atoms and are also too slow for performing dynamical simulations even for small molecules and time-scales in the pico-second range.

Density functional theory (DFT) is another independent-particle method, whose basics were formulated in two fundamental papers, the first published in 1964 by P. Hohenberg and W. Kohn [61], and the second in 1965 by W. Kohn and J. L. Sham [62]. The basic idea behind these works is that the ground-state electronic energy (and therefore all other related ground-state properties) is a functional of the electronic density. Then a set of single-particle equations, the so called Kohn-Sham equations, are derived by applying a variational principle to the electronic energy. Electron-electron interactions are again treated in an average way according to several available approximations to the functional dependence of the exchange-correlation energy on density, which actually constitutes the main source of variations in DFT calculations. Actually, the Hohenberg-Kohn theorem doesn't specify the form of the functional to be used, but just confirms that it exists. Starting from a trial density given by the square modulus of guessed wavefunctions, the energy functional of the Kohn-Sham hamiltonian is obtained and then minimized until self-consistency is reached for the input and output ground state charge densities. DFT calculations can be considered the workhorse of all *ab initio* methods, as they can provide accurate predictions of structural, electronic, vibrational and magnetic properties for a wide range of systems, from molecules and clusters to periodic and amorphous solids, either metals, semiconductors or insulators. Density functional calculations are possible for systems of the order of 100 atoms, but by exploiting symmetry also calculations for clusters of over 1000 atoms can be performed [63]. Although DFT is computationally less demanding than HF methods, it has to be pointed out that in DFT calculations the number of variational parameters needed for the expansion of the wavefunction adopted for constructing the trial ground-state density is quite large, thus other methods are required for achieving more efficient calculations and treating systems with larger size.
Soon after the discovery of carbon nanotubes in 1991, the electronic properties of single-walled nanotubes were investigated by density functional methods [64, 65], before the electronic density of states could be actually measured by STS in 1998 by Odom. These calculations also showed that important hybridization effects of the σ^* and π^* orbitals could occurr in small radius carbon nanotubes, which could be relevant for the prediction of metallicity in these systems [66]. Subsequently, calculations were performed also for more complex systems such as double- and multi-wall nanotubes, bundles of single-wall nanotubes and carbon peapods [67, 68, 69].

Semiempirical methods comprise a wide class of self-consistent field HF methods which take into account again Coulomb repulsion, exchange interaction and the full atomic structure of the system, but make use of fewer variational parameters if compared to HF and DFT and not all the integrals needed to set up the Hamiltonian matrix are calculated. Instead they are parametrized according to experimental data. According to the exact number of neglected integrals and the kind of parametrization used, different scheme of semi-emprical calculations have been developed, most based on the modified neglect of diatomic overlap (MNDO) (for an extensive treatment of the derived methods see Ref. [93] or other quantum chemistry books). Clearly, the reasons behind the development of these methods is the need of finding a compromise between computational efficiency and the physical correctness of the adopted approximations. A quantum-chemical semi-empirical electronic structure calculation on nanotube fragments can be found for instance in Ref. [134].

Tight-binding methods make use of a parametric Hamiltonian with a minimum set of parameters, which is parametrized with respect to the atomic positions and solve the Schrödinger equation in an atomic-like basis set. In this sense, they're similar to semi-empirical methods, yet they are not self-consistent. Usually the values for the chosen parameters are obtained from fitting calculations to experimental or *ab initio* density functional results (DFTB) [71]. A small number of basis functions are used, which roughly correspond to the atomic orbitals in the energy range of interest. Therefore, compared with the *ab initio* techniques, these atomistic models can be generally handled with far less computational effort and the general understanding of the underlying physics and symmetry properties is facilitated. However, the quantitative results always depend on the parameters needed as input and obviously, due to the reduced number of variational parameters and exact integral evaluations, the accuracy is reduced if compared with *ab initio* calculations. Parametrized models like TB methods can be adopted both for the treatment of electronic and vibrational properties of solids. For the description of mechanical and vibrational properties, the most common TB-like methods are *force-constant models*, describing the mechanical forces between neighboring atoms in a harmonic approximation [72]. Several works concerning the vibrational properties of graphene and nanotubes calculated with this approach have been published (for a recent comprehensive list of references see Ref. [73]). For the atomistic description of the electronic structure, the concept of the *linear combination of atomic orbitals* (LCAO) is adopted within the TB scheme. This independent-particle method was introduced by Slater and Koster [74], and is today used for efficient, flexible and fairly accurate computations of both model and real systems (for a general review see for instance [75]). Another important parametrized model used for treating strongly correlated electrons in condensed matter is the Hubbard model, which is indeed a many-body model developed in order to account for Coulomb repulsion between electrons. The Hubbard model is presented more in detail in Chapt. 6 of

this thesis. TB calculations with different level of approximations have been widely used for exploring the electronic properties of graphite and its crystalline modifications: with Bernal stacking (Weiss and Slonczewski, 1958 [77]), rhombohedral stacking (McClure, 1957 [78]), simple hexagonal and turbostratic graphite (Charlier, 1991 [79, 80]). Soon after the nanotube discovery by Iijima, the first tight-binding calculations on single-walled nanotubes focused on the folding of the electronic dispersion bands of graphene over the nanotube reciprocal space [81]. Later more refined and general analytical expressions for electronic dispersion for graphene and SWNTs of any given chirality were obtained by Saito and Dresselhaus [89, 90], as shown more in detail in Chapt 3. Symmetry-adapted TB schemes have also been successfully applied by Popov [84] and Damnjanović *et al.* [85] for addressing curvature and hybridization effects in small diameter single-wall nanotubes of any chirality. Tight-binding methods were also applied to the investigation of the electron-photon and electron-phonon coupling strength for understanding resonance Raman spectral features in SWNTs [141, 146]. There have been also early studies concerning the electronic structure of double-walled nanotubes [155, 169], although these attempts were strongly limited by the selected geometries and hamiltonian parametrizations (see the related Chapter in this thesis). After the excitonic nature of optical transitions in SWNTs was experimentally established in 2003 by Wang and Dukovic [197], the band picture provided by TB calculations turned out to be essentially incorrect. Nonetheless still many experimental results, such as Kataura plots, can be interpreted through TB calculations, with adequate modifications of the calculation parameters [204, 205].

Effective models represent another class of methods which do not take into account the detailed atomic structure, but give a simple, although approximate, description of the electronic structure and optical properties. This often allows the advantage of an analytical treatment of the physical problems, which can imply a deeper understanding of the results than provided by purely numerical methods. Effective models have been recently used for the investigation of the electronic structure of graphene [5], where electrons can be described as massless relativistic particles, and also in several works by T. Ando within the $k \cdot p$ scheme about carbon nanotubes electronic properties with and without correlations and disorder effects (for a comprehensive review see Ref. [86]).

1.4 Summary

In this chapter, starting from the hybridization of carbon orbitals, we gave a general summary of the most studied graphitic materials, which will be the potential building-blocks of an all-carbon based nanoelectronics in forthcoming years. In particular, we focused on single and multiwall carbon nanotubes, for which a more detailed description of synthesis and characterization techniques was provided. Optical spectroscopic techniques, such as Photoluminescence and Resonant Raman Spectroscopy have shown to be capa-

ble of providing chirality and diameter specific information about the electronic structure of individual single-walled nanotubes in bundled bulk samples, without the need of a particularly expensive laboratory or separation treatments. In the final part, a general classification scheme for computational electronic structure methods was presented, together with the historically most relevant bibliographic references about the calculation of electronic properties of nanotubes and related structures.

Chapter 2

Geometry of single-wall carbon nanotubes

A single-wall carbon nanotube (SWNT) can be considered as a graphene sheet (a single layer of graphite, with a 2D hexagonal lattice) which can be rolled up with any given orientation into a seamless cylinder with a diameter of a few nanometers and a macroscopic length of several micrometers. The electronic properties of SWNTs, as well as any other physical property, are deeply related to their geometrical structure, which can be defined in terms of diameter, wrapping angle of the graphene sheet and number of atoms contained in the unit cell.
In this chapter, starting from the graphene sheet, we show the basic definitions for characterizing the geometry of a SWNT, in real and reciprocal space. A review of the different algorithms presented in literature for determining the coordinates of the atoms in the unit cell, both in 2D and 3D, is also given together with a general overview of the symmetry classifications based on group theory for these systems. For most conventions we follow those used in Saito's and Dresselhaus' works (see for instance Ref. [89]), except where explicitly stated for different choices.

2.1 Graphene lattice in real and reciprocal space

The honeycomb geometry of a graphene sheet can be described by considering an ideal infinite 2D hexagonal Bravais lattice. The lattice unit vectors are defined by

$$\begin{aligned} \mathbf{a_1} &= \frac{\sqrt{3}a}{2}\hat{\mathbf{x}} + \frac{a}{2}\hat{\mathbf{y}}, \\ \mathbf{a_2} &= \frac{\sqrt{3}a}{2}\hat{\mathbf{x}} - \frac{a}{2}\hat{\mathbf{y}}. \end{aligned} \tag{2.1}$$

where $a = \sqrt{3}a_{CC} = 0.246\,\mathrm{nm} = |\mathbf{a_1}| = |\mathbf{a_2}|$ is the lattice constant of the graphene sheet, $a_{CC} = 0.142\,\mathrm{nm}$ is the carbon-carbon bond length and $(\hat{\mathbf{x}}, \hat{\mathbf{y}})$ are the unitary ba-

sis vectors of the Cartesian coordinate system. Using the lattice vectors $\mathbf{a_1}$ and $\mathbf{a_2}$, the graphene unit cell can be obtained. The unit vectors defined as above make an angle of 60^{o}. The unit cell can be chosen in several ways, a possible choice is a rhombus that contains two *inequivalent* atoms from the sublattices of A- and B-type as shown in gray in Fig. 2.1(left). By using the term *inequivalent* one means that the A and B sites in the unit cell cannot be connected by unit vectors $\mathbf{a_1}$ and $\mathbf{a_2}$. In the graphene lattice each atom of type A is surrounded by three nearest neighbor atoms of type B and viceversa. The reciprocal lattice of the graphene sheet is defined by the unit vectors $\mathbf{b_1}$ and $\mathbf{b_2}$, which are related to the real lattice unit vectors $\mathbf{a_1}$ and $\mathbf{a_2}$ by the standard definition:

$$\mathbf{a_i} \cdot \mathbf{b_j} = 2\pi\delta_{i,j}, \tag{2.2}$$

where $\delta_{i,j}$ is the Kronecker delta function. By substituting Eq. (2.1) into Eq. (2.2), the reciprocal lattice unit vectors $\mathbf{b_1}$ and $\mathbf{b_2}$ are otained:

$$\begin{aligned} \mathbf{b_1} &= \frac{2\pi}{\sqrt{3}a}\hat{\mathbf{x}} + \frac{2\pi}{a}\hat{\mathbf{y}}, \\ \mathbf{b_2} &= \frac{2\pi}{\sqrt{3}a}\hat{\mathbf{x}} - \frac{2\pi}{a}\hat{\mathbf{y}}. \end{aligned} \tag{2.3}$$

The unit vectors $\mathbf{b_1}$ and $\mathbf{b_2}$ make an angle of 120^{o} and define the graphene first Brillouin zone (BZ). The BZ has the same hexagonal shape as the hexagons which tile the real space, but is rotated of $\pi/6$. Consequently, the armchair direction in real space, which runs parallel to the carbon bond, corresponds to the zigzag direction in reciprocal space. Vice versa, the zigzag direction in real space, which points at $\pi/6$ from the armchair one, corresponds to the armchair direction in reciprocal space (see Fig. 2.2). The high-symmetry points in the graphene BZ are the center of the hexagon $\mathbf{\Gamma} = (0, 0)$, the corners $\mathbf{K} = \left(2\pi/\sqrt{3}a, 2\pi/a\right)$ and the midpoint of the hexagonal edge $\mathbf{M} = \left(2\pi/\sqrt{3}a, 0\right)$. Notice that there are two *inequivalent* K points in the BZ which are denoted by $\mathbf{K}$ and $\mathbf{K}'$. As always, equivalent points are obtained by translations of integer multiples of the unit vectors $\mathbf{b_1}$ and $\mathbf{b_2}$. In the next chapter about the electronic structure of graphene, we will show that these points correspond to the Fermi surface points, which are responsible for the metallic character of the system.

2.2 Nanotube unit cell in real space

There are many possible ways of rolling up a graphene sheet into a cylinder, so that nanotubes with quite different structures can be obtained. The geometry of a SWNT can be uniquely specified by introducing the chiral indices (n, m), which are integer multiples of the real space unit vectors $\mathbf{a_1}$ and $\mathbf{a_2}$. In this way the circumferential or chiral vector $\mathbf{C}_h$ is defined as:

$$\mathbf{C}_h = n\mathbf{a_1} + m\mathbf{a_2} = (n, m)\,. \tag{2.4}$$

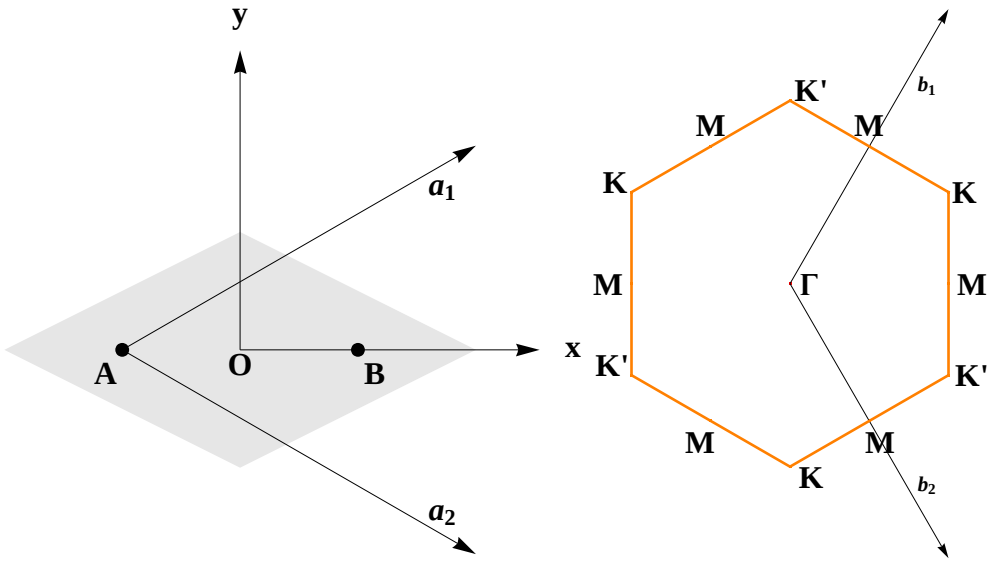

Fig. 2.1: Graphene unit cell (left) and first Brillouin zone (right). The shaded rhombus with the two sites A and B is the unit cell of graphene, the hexagonal lattice is defined by the unit vectors $\mathbf{a_1}$ and $\mathbf{a_2}$. The reciprocal space is defined by the unit vectors $\mathbf{b_1}$ and $\mathbf{b_2}$. The center of the BZ is the Γ point and the corners are the $\mathbf{K}$ and $\mathbf{K}'$ points. The midpoints are the $\mathbf{M}$ points. Equivalent k-points are connected to each other by reciprocal lattice vectors.

The chiral vector defines the translational azimuthal periodicity along the circumference of the graphene cylinder. Moreover, every other nanotube geometric quantities can be specified starting from these indices, as it will be shown in the following. The circumference length is given by $L = \sqrt{\mathbf{C}_h \cdot \mathbf{C}_h}$ and the nanotube diameter is $d_t = L/\pi = \frac{a}{\pi}\sqrt{n^2 + nm + m^2}$. The chiral angle θ is defined as the angle between the chiral vector $\mathbf{C}_h$ and the unit vector $\mathbf{a_1}$ and can be obtained with the aid of Eq. (2.4), that is

$$\theta = \arccos \frac{\mathbf{C}_h \cdot \mathbf{a_1}}{|\mathbf{C}_h||\mathbf{a_1}|} = \arccos \frac{2n + m}{2\sqrt{n^2 + m^2 + nm}}. \tag{2.5}$$

For the special cases $\theta = 0$ and $\theta = \pi/6$ the tubes are referred to as *zigzag* and *armchair*, respectively. Zigzag tubes have $m = 0$, whereas armchair tubes have $m = n$. Because of their mirror symmetry along the tube axis, they are also called *achiral* tubes. In order to avoid confusion related to the handedness of the rolling up of the graphene sheet in two opposite directions (for a detailed discussion see Ref. [141]), the structural indices can be defined in the range $0 \leq m \leq n$ and the chiral angle in the range $0 \leq \theta \leq 30^{\text{o}}$. Obviously achiral SWNTs have no handedness, implying that in a sample the amount of chiral SWNTs for each (n, m) pair is twice the amount of achiral ones. An alternative

way to Eq. (2.5) for defining the chiral angle θ, one can consider the angle $\theta' = \pi/6 - \theta$ between the chiral vector $\mathbf{C}_h$ and the closest of the three armchair chains in the graphene sheet of Fig. 2.2. The translational periodicity along the axis of an ideal infinitely long SWNT is given by the translational vector $\mathbf{T}$, which is orthogonal to $\mathbf{C}_h$ and is defined as

$$\mathbf{T} = t_1\mathbf{a_1} + t_2\mathbf{a_2} = \frac{2m+n}{d_R}\mathbf{a_1} - \frac{2n+m}{d_R}\mathbf{a_2} \tag{2.6}$$

where $d_R = \gcd(2n+m, 2m+n)$, the function $\gcd(i,j)$ denotes the greatest common divisor of the two integers i and j and the integer coefficients t_1 and t_2 for the components of $\mathbf{T}$ have been found using the orthogonality relation $\mathbf{C}_h \cdot \mathbf{T} = 0$. The division by the integer d_R ensures that the shortest lattice vector along the SWNT axial direction is chosen. Additionally, if we define the integer $d = \gcd(n,m)$ and apply Euclid's law[1] to d_R, the following relations are obtained

$$\begin{aligned} d_R &= d \text{ if } \bmod(n-m, 3d) \neq 0 \\ d_R &= 3d \text{ if } \bmod(n-m, 3d) = 0. \end{aligned} \tag{2.7}$$

In the above equation the modulo function gives the remainder of an integer division. The SWNT unit cell is spanned by the real space vectors $\mathbf{C}_h$ and $\mathbf{T}$ and can be obtained by the cross product $|\mathbf{T} \times \mathbf{C}_h| = |(t_1 m - t_2 n)(\mathbf{a_1} \times \mathbf{a_2})|$. Dividing the area of the SWNT cell by the area of the biatomic graphene unit cell $|\mathbf{a_1} \times \mathbf{a_2}|$, one gets the number N of graphene unit cells inside the SWNT unit cell

$$N = t_1 m - t_2 n = \frac{2(n^2 + nm + m^2)}{d_R} \tag{2.8}$$

Note that N is an even number and that zigzag and armchair SWNTs have small unit cells if compared to chiral SWNTs with approximately the same diameter. In fact, for pairs of type $(n,0)$ and (n,n) there are $2n$ graphene cells in the nanotube unit cell, therefore $4n$ carbon atoms.
Finally, substituting the above expression for N the relations for the circumference length L and the length of the unit cell along the tube axis $T = \sqrt{\mathbf{T} \cdot \mathbf{T}}$ can be rewritten as

$$L = a\sqrt{\frac{d_R N}{2}} \quad \text{and} \quad T = a\sqrt{\frac{3N}{2d_R}} = \frac{\sqrt{3}L}{d_R}. \tag{2.9}$$

2.3 Nanotube reciprocal space: the cutting lines

As shown in Section 2.1, again with the aid of Eq. (2.2), one can still construct reciprocal lattice vectors which can be conveniently used in a cylindrical reference frame, i.e.

[1] Euclid's law state that $\gcd(i,j) = \gcd(i-j, j)$

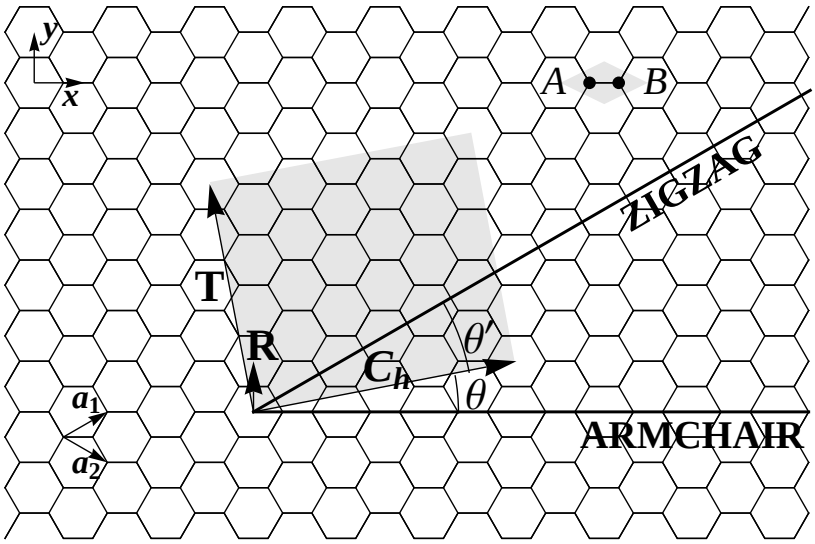

Fig. 2.2: Graphene lattice with armchair and zigzag directions highlighted and geometry of a $(4, 2)$ single-walled nanotube. The large shaded cell is the SWNT unit cell, defined by the chiral vector $\mathbf{C}_h$ and the axial vector $\mathbf{T}$, with *N* atoms of type A (B). The symmetry vector $\mathbf{R}$ is also shown (see Sect. 2.4.1). The chiral angle θ is the angle between the armchair direction and the chiral vector $\mathbf{C}_h$. All vectors are expressed in multiples of $\mathbf{a_1}$ and $\mathbf{a_2}$.

along the circumferential and axial direction of the nanotube, respectively. Therefore, in SWNTs the chiral vector $\mathbf{C}_h$ and the axial vector $\mathbf{T}$ play the role of graphene real space unit vectors $\mathbf{a_1}$ and $\mathbf{a_2}$, whereas the nanotube reciprocal space vectors $\mathbf{K_1}$ and $\mathbf{K_2}$ play the role of graphene reciprocal space unit vectors $\mathbf{b_1}$ and $\mathbf{b_2}$. The new reciprocal vectors $\mathbf{K_1}$ and $\mathbf{K_2}$ are defined as follows:

$$\mathbf{K_1} \cdot \mathbf{T} = 0,\ \mathbf{K_1} \cdot \mathbf{C}_h = 2\pi,\ \mathbf{K_2} \cdot \mathbf{T} = 2\pi,\ \mathbf{K_2} \cdot \mathbf{C}_h = 0. \tag{2.10}$$

Using the definitions given in Eq. 2.4 and Eq. 2.6, one obtains

$$\begin{aligned} \mathbf{K_1} &= \frac{t_1\mathbf{b_2} - t_2\mathbf{b_1}}{N} \\ \mathbf{K_2} &= \frac{m\mathbf{b_1} - n\mathbf{b_2}}{N} \end{aligned} \tag{2.11}$$

from which it can be verified that $\mathbf{K_1}$ is perpendicular to $\mathbf{T}$ and parallel to $\mathbf{C_h}$, whereas $\mathbf{K_2}$ is parallel to $\mathbf{T}$ and perpendicular to $\mathbf{C_h}$. The lengths of $\mathbf{K_1}$ and $\mathbf{K_2}$ are given by

$$|\mathbf{K_1}| = \frac{2\pi}{L} = \frac{2}{d_t} \quad \text{and} \quad |\mathbf{K_2}| = \frac{2\pi}{T}. \tag{2.12}$$

According to the first equation of (2.11), two vectors which differ by $N\mathbf{K_1}$ are equivalent, as this corresponds to a reciprocal lattice vector of graphene. Therefore N wavevectors of type $\mu\mathbf{K_1}$ with $\mu = 0, 1, \ldots, N-1$ will give rise to N discrete lines of length $|\mathbf{K_2}|$ and spacing $|\mathbf{K_1}|$, in the graphene BZ. Therefore, one can think of the nanotube reciprocal space as the result of sectioning the graphene BZ into a set of N 1D BZs or *cutting lines* (see Ref. [116] for a general review), such that the possible **k** values in the SWNT BZ are given by

$$\mathbf{k} = \mu\mathbf{K_1} + k_z\frac{\mathbf{K_2}}{|\mathbf{K_2}|} \text{ with } \mu = 0, \ldots, N-1 \text{ and } -\frac{\pi}{T} \leq k_z < \frac{\pi}{T}. \tag{2.13}$$

For any given **k** the following relation also holds

$$\mathbf{k} \cdot \mathbf{C}_h = 2\pi\mu \tag{2.14}$$

which represents the periodic boundary condition of quantum confinement around the tube circumference. This means that only stationary states having an integer number μ of wavelengths with period $k = 2\pi/\lambda$ are allowed around the circumferential direction. Moreover, from the definition of Eq. (2.13), the possible values for the azimuthal quantum number μ are discrete, whereas the linear momentum k_z changes continuously along the cutting lines as a consequence of the translational periodic boundary conditions along the tube axis.

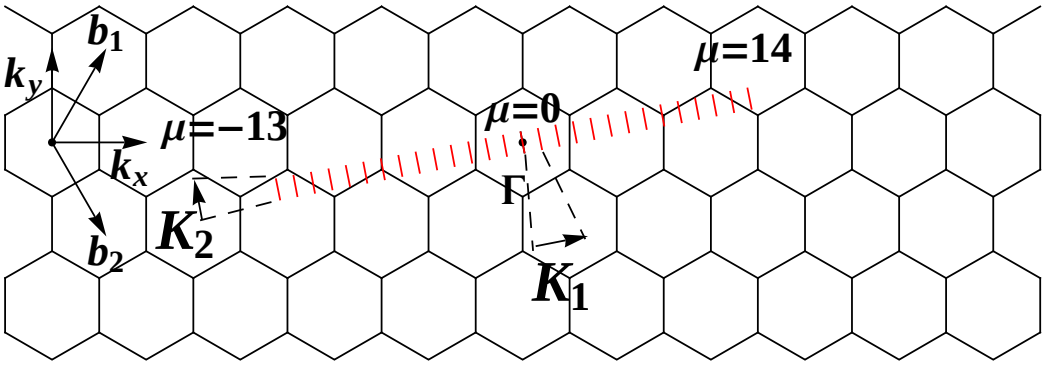

Fig. 2.3: The first Brillouin zone of (4, 2) SWNT is given by a set of $N = 28$ cutting lines of nanotube superimposed on the extended graphene BZ. The origin at the Γ point is marked by a dot. Nanotube reciprocal lattice vectors $\mathbf{K}_1$ and $\mathbf{K}_2$, whose norm give the spacing between cutting line and the length of each cutting line, respectively, are also shown. The borders of the SWNT BZ are the cutting lines with indices $\mu = -13$ and $\mu = 14$.

2.4 Generating coordinates of SWNTs

The task of generating the coordinates of any (n, m) SWNT unit cell is a complex one, because of the high degree of symmetry of the nanotube system (i. e. large number of symmetry elements), as it will be shown in the last section of this chapter. In literature several different algorithms for calculating the atomic coordinates both in the 2D unrolled and 3D unit cell can be found, which rely on different choices for the symmetry vectors generating the whole cell. The purpose of this section is not only intended as a *vade-mecum* for practical use in the computations, but aims also at giving an insight into the three most cited (and documented) geometrical conventions in nanotube science. More specifically, we will overview first the convention used in the works by the Saito and Dresselhaus' group [89, 141], then the convention used by Nemec and Cuniberti's group [123] and finally the one by Damnjanović's group [90], which will be helpful for introducing symmetry elements in nanotubes in the next section. As nanotube literature is now quite vast, also different recipes by other authors can be easily found out, however most of the times they're limited to achiral SWNTs or not explicitly set up into integer-based formulas to be tried straightforwardly. Thus it has been decided not to take into account these cases.

2.4.1 Saito and Dresselhaus' convention

In order to generate coordinates of SWNTs, Saito introduces the symmetry vector $\mathbf{R}$ with indices (p, q), which satisfies the three following conditions:

$$\text{(a)} \quad \mathbf{R} = p\mathbf{a_1} + q\mathbf{a_2}, \quad \text{(b)} \quad \frac{\mathbf{R}\cdot\mathbf{C}_h}{L} = \frac{L}{N}, \quad \text{(c)} \quad \frac{1}{N} \leq \frac{\mathbf{R}\cdot\mathbf{T}}{\mathbf{T}\cdot\mathbf{T}} \leq 1. \tag{2.15}$$

Condition (a) means that $\mathbf{R}$ is a real-space lattice vector, whose component along $\mathbf{C}_h$ is equal to L/N according to condition (b), and it's inside the unit cell according to condition (c) . Making the appropriate substitutions into conditions (b) and (c) of Eq. (2.15), the (p, q) indices of vector $\mathbf{R}$ can be completely determined by solving the following system:

$$qt_1 - pt_2 = 1 \quad \text{and} \quad 1 \leq mp - nq \leq N. \tag{2.16}$$

By translating a graphene unit cell by $i\mathbf{R}$ with $i = 0, \ldots, N-1$ we go over all graphene unit cells inside the 2D unrolled nanotube unit cell, that is two atoms in a graphene sheet are equivalent if they're connected by a translation of $N\mathbf{R}$. In a 3D rolled up SWNT, applying the symmetry vector $\mathbf{R}$ means moving around the tube axis in spiral-like fashion. The pitch τ and the angle ψ of the spiral are given by the following cross products:

$$\begin{aligned} \tau &= \frac{|\mathbf{R}\times\mathbf{C}_h|}{L} = \frac{(mp-nq)\,T}{N} \\ \psi &= \frac{|\mathbf{T}\times\mathbf{R}|}{T}\frac{2\pi}{L} = \frac{2\pi}{N} \end{aligned} \tag{2.17}$$

Additionally, the symmetry vector $\mathbf{R}$ applied N times can be related to translations by integer multiples of the axial vector $\mathbf{T}$, according to the following relation:

$$N\mathbf{R} = \mathbf{C}_h + M\mathbf{T} \quad \text{with} \quad M \equiv mp - nq. \tag{2.18}$$

Now we have all the necessary elements for generating any (n, m) SWNT unit cell, both in 2D and 3D. In a rigth-handed Cartesian $xyz-$coordinate system, we choose the graphene layer to lie in the xy plane. The coordinates of the atomic sites of the 2D unrolled nanotube unit cell are then obtained as follows:

$$\mathbf{R}^u_{h,s} = u\mathbf{T} + h\mathbf{R} - [hM/N]\,\mathbf{T} - \mathbf{r^1}_s/2 \tag{2.19}$$

where the *u*-th unit cell, the *h*-th graphene biatomic cell and the *s*-th atomic site (A or B) inside each graphene cell are labelled by the corresponding subscripts. By the notation $[\xi]$ we mean the integer part of the argument ξ and $\mathbf{r^1}_s$ is a vector pointing from a given *s*-site (e. g. A) to its first nearest-neighbor s' (e. g. B). In order to obtain the coordinates of the SWNT in 3D, the above 2D unit cell needs to be rolled up by aligning the tube along the *z* axis. This is done through the rotation operators Ω_α $(\alpha = x, y, z)$ about the Cartesian principal axes:

$$\Omega = \Omega_z\left(\Theta\varphi_{h,s}\right)\Omega_y\left(\frac{\pi}{6} - \theta\right)\Omega_x\left(\frac{\pi}{2}\right) \tag{2.20}$$

The rotation operator $\Omega_x\left(\frac{\pi}{2}\right)$ is applied to align the cylinder along the *z* axis, then the graphene layer in the *xz* plane is rotated by $\Omega_y\left(\frac{\pi}{6} - \theta\right)$ to account for the SWNT chirality. Finally the rolling up of the graphene layer is obtained by placing the atomic sites around the *z* axis of the cylinder by the operator $\Omega_z\left(\Theta\varphi_{h,s}\right)$, where $\varphi_{h,s}$ is the angular coordinate of the atomic site $\mathbf{R}^u_{h,s}$ on the cylindrical surface of the nanotube and Θ is related to the handedness of the rolling up done to the graphene layer, from the front to the back $(\Theta = +1)$ or from the back to the front $(\Theta = -1)$. The angular coordinates of the atomic sites $\varphi_{h,s}$ are given by:

$$\varphi_{h,s} = \frac{2}{d_t}\left[\Omega_y\left(\frac{\pi}{6} - \theta\right)\Omega_x\left(\frac{\pi}{2}\right)\mathbf{R}^u_{h,s}\right]\cdot\hat{\mathbf{x}} = 2\pi h/N - \varphi^1_s/2 \tag{2.21}$$
$$\text{with} \qquad \varphi^1_A = -\varphi^1_B = \left(2a/\sqrt{3}d_t\right)\cos\left(\pi/6 - \theta\right).$$

where the angular shifts φ^l_s on the cylindrical surface between nearest-neighbor carbon atoms have been introduced. The general expression for these is given by

$$\varphi^l_s = \frac{2}{d_t}\left[\Omega_y\left(\frac{\pi}{6} - \theta\right)\Omega_x\left(\frac{\pi}{2}\right)\mathbf{r}^l_s\right]\cdot\hat{\mathbf{x}} \tag{2.22}$$

These formulas can be straightforwardly implemented in computer programs for calculating any set of atomic coordinates of a given (n, m) SWNT. The above described procedure is found in Ref. [141] and is far more elegant than the one proposed in the sample

code shown in the appendix of Saito's book [89], which is completely based on floating-point arithmetic, therefore bearing the risk of rounding errors. However, apart from the procedure, the main point to remember is that in both references the symmetry vector **R** is used for generating atomic coordinates of a SWNT.

2.4.2 Nemec and Cuniberti's convention

Nemec and Cuniberti's pure integer-based procedure [123], clearly steers away from introducing any additional symmetry vector, and focuses on labelling the graphene unit cells inside the unrolled nanotube unit cell. By indexing a graphene cell or plaquette by a pair of indices (l_1, l_2), each cell around the tube is uniquely identified by the condition $0 \leq l_1 + l_2 < n + m$. New indices for the coordinates are introduced as

$$[i, j] = [l_1 + l_2, l_1] \quad \text{with} \quad 0 \leq i < n + m \tag{2.23}$$

Now the only fundamental step to generate the coordinates is that each plaquette is part of the unit cell if the following condition holds:

$$0 \leq l_1 m - l_2 n < t_1 m - t_2 n \tag{2.24}$$

$$\begin{aligned} 0 \leq jm - (i - j)\, n &< t_1 m - t_2 n \\ in \leq j\,(n + m) &< in + (t_1 m - t_2 n) \end{aligned} \tag{2.25}$$

For every *i* we have the following condition for *j*:

$$\frac{in}{n + m} \leq j < \frac{in + t_1 m - t_2 n}{n + m} \tag{2.26}$$

Finally the plane coordinates of all atoms can be computed exactly with pure integer operations counting over the indices $[i, j]$ as follows:

$$\mathbf{r}^{\pm}_{[i,j]} = j\mathbf{e_1} + (i - j)\,\mathbf{e_2} \pm (\mathbf{e_1} + \mathbf{e_2})\,/6 \tag{2.27}$$

In the above equation the lattice vectors $\mathbf{e}_1$ and $\mathbf{e}_2$ are expressed in cylindrical coordinates as:

$$\begin{aligned} \mathbf{e_1} &= (2\pi t_2, -mT)\,/\,(t_2 n - t_1 m) \\ \mathbf{e_2} &= (2\pi t_1, -nT)\,/\,(t_1 m - n t_2)\,. \end{aligned} \tag{2.28}$$

where the following identities are verified

$$\begin{aligned} n\mathbf{e_1} + m\mathbf{e_2} &= (2\pi, 0) \\ t_1\mathbf{e_1} + t_2\mathbf{e_2} &= (0, T)\,. \end{aligned} \tag{2.29}$$

Thus expressions for the cylindrical coordinates $(\varphi, z)_{[i,j]}$ are obtained, which can be used together with the tube radius $\rho = L/2\pi$ to derive the 3D Cartesian atomic coordinates.

2.4.3 Damnjanović's convention

In the previous sections, we saw that the minimum number of starting atoms needed to generate the SWNT can be at most 2, the number of atoms in the graphene unit cell. However, Damnjanovć *et al.* [90, 124] pointed out that these two atoms are actually mapped onto each other by a rotation by 180^{o} around an axis *U* perpendicular to the tube axis. Therefore, only one atom is needed to generate the whole tube, which is referred to as *orbit*, and carbon nanotubes are defined as *single orbit systems*. Thus, unlikely the previous methods, Damnjanović *et al.* obtain the full set of coordinates starting from a single atom and applying to it the symmetry operators of the line group of the SWNT, which will be described in detail in the next section. For the moment, it's sufficient to say that these operators are the screw roto-translation generator $\left(C_N^w|\frac{Td}{N}\right)$, the pure-rotations operator C_d and the above mentioned rotation of 180^{o} around the horizontal axis *U*. By covention, the *U* axis is chosen to coincide with the *x* axis. We recall that, within the notation of this thesis, *d* is the greatest common divisor of the SWNT chiral indices (n, m), *N* is the number of graphene cells inside the unit cell and *T* is the norm of the tube axial vector **T**, which is quite different from the notation used in Damnjanović's work (*n, q, a*, respectively, for a given SWNT pair indices n_1, n_2). The parameter w which appears in the screw operator is given by:

$$w = N/d\ \mathrm{Fr}\left[\frac{d}{Nd_R/d}\left(3 - 2\frac{n-m}{n}\right) + \frac{d}{m}\left(\frac{n-m}{d}\right)^{\varphi(n/d)-1}\right] \tag{2.30}$$

where Fr is the fractional part of a rational number and $\varphi\,(m)$ is the Euler function[2]. In cylindrical coordinates the position of the starting atom is given by

$$\mathbf{r}_{000} = (\rho, \Phi_0, Z_0) = \left(\rho, 2\pi\left(\frac{n+m}{2\,(n^2+nm+m^2)}\right), \frac{n-m}{2\sqrt{3\,(n^2+nm+m^2)}}\,a\right). \tag{2.31}$$

and by acting on it with the compound operator $\left(C_N^{wt}C_d^sU^u|t\frac{dT}{N}\right)$ the new atomic position is obtained at:

$$\mathbf{r}_{tsu} = \left[\rho, (-1)^u\,\Phi_0 + 2\pi\left(\frac{wt}{N} + \frac{s}{d}\right), (-1)^u\,Z_0 + \frac{td}{N}T\right] \tag{2.32}$$

where the indices tsu are defined as $u = 0, 1$, $s = 0, 1, \ldots, d-1$, and $t = 0, \pm1, \pm2, \ldots$. Thus counting over the indices *t, s* and *u*, with the help of Eq. (2.32), any single-walled nanotube can be constructed.

[2]Euler $\varphi\,(m)$ gives the number of positive integers less than or equal to *m* which are relatively prime to *m*.

2.5 Symmetry of SWNTs

The symmetry of systems which exhibit translational periodicity in one dimension, such as carbon nanotubes and stereoregular polymers have been described by the so called *line groups*, which were introduced by Damnjanović *et al.* [124] and later adopted by Thomsen and Reich [90] for the investigation of second-order resonance Raman scattering on SWNTs. Line groups are the full space group of one-dimensional systems. In addition to point-group symmetries like rotations and reflections, they include pure translations and screw operations. In Sect. 2.4.3 it was shown that, starting from a single atom, the whole tube could be obtained by repeatedly applying the symmetry operations of the line group. In this section we will briefly review the basics of the symmetry of a SWNT from a crystallographic point of view. For further details about group symmetry applied to SWNTs the reader is referred to the above mentioned references by Damnjanović and Reich and to the comprehensive review of Ref. [118]. In order to find the symmetry groups of carbon nanotubes, one has to look for the symmetry operations of the graphene sheet which are preserved when the layer is rolled up into a cylinder. Namely, translations by multiples of the axial translational period *T* of the graphene sheet parallel to $\mathbf{T}$ remain translations of the nanotube parallel to the tube axis. They form a subgroup $\mathfrak{T}$ containing the pure translations of the system. Translation parallel to the chiral vector $\mathbf{C}_h$ become pure rotations of the nanotube about its axis. If we consider *d* lattice points belonging to $\mathbf{C}_h$, the nanotube can be rotated by multiples of $2\pi/d$. Thus the SWNT has *d* pure rotations in its symmetry group which are denoted by C_n^s with $s = 0, 1, \ldots, d-1$. The pure rotations form again a subgroup $\mathfrak{C}_n$ of the full line group. Translations of the graphene sheet along any other direction are combinations of translations along $\mathbf{T}$ and $\mathbf{C}_h$. Therefore, when the graphene sheet is rolled up, they result in translations combined with rotations about the nanotube axis, hence the helical symmetry of carbon nanotubes, due to the presence of screw operators. On the unrolled graphene sheet this corresponds to primitive translations of type $w/N\mathbf{C}_h + d/N\mathbf{T}$. The order of these screw axis operators is equal to the number of graphene cells *N* inside the nanotube unit cell. Therefore, as shown in the previous section, we denote the screw operators by $(C_N^w|dT/N)^t$ with the parameter w defined as in Eq. (2.30). Moreover, by considering the form of Eq. (2.8) and the ratio N/d which is always ≥ 2, it can be shown that the nanotube line group always contain the screw axis. In achiral tubes $N/d = 2$ and $w = 1$, so the screw axis operation consists of a rotation by π/d followed by a translation by *T*. Also, one can observe that from the six-fold rotation of the hexagon about its center point only the two-fold rotation is preserved as a symmetry operation in carbon nanotubes. This is actually the two fold rotational axis, previously denoted as *U*, which is perpendicular to the tube axis and is present both in chiral and achiral nanotubes. The *U*-axis points through the midpoint of a hexagon, perpendicularly to the cylinder surface, the other equivalent two-fold axis U' is found at the midpoint of a bond between two carbon atoms. Mirror planes perpendicular to the graphene sheets must either contain the tube axis or be perpendicular to it. Thus

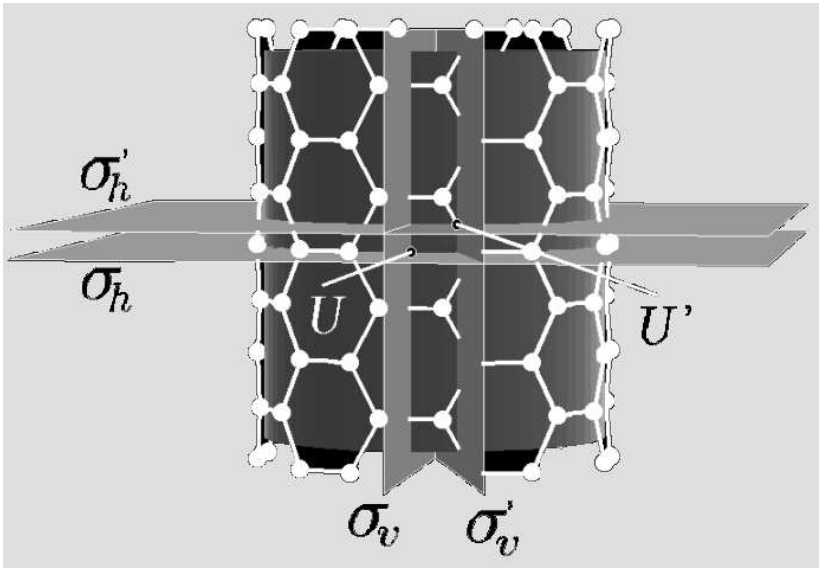

Fig. 2.4: Symmetry elements in a SWNT according to Damnjanović *et al*. Taken from Ref. [124].

we have vertical mirror planes denoted by σ_v[3] and horizontal mirror planes σ_h. However, both kinds of planes are present only in achiral tubes. Note that $\sigma_h = U\sigma_v$. They contain the center points of the graphene hexagons. Additionally, vertical and horizontal mirror planes through the midpoints of the covalent bonds form vertical glide planes $(\sigma_{v'})$ and horizontal rotoreflection planes $(\sigma_{h'})$ (Fig. 2.4). The general element for any carbon nanotube line group can be written as

$$l\,(t,u,s,\nu) = \left(C_N^w|\frac{Td}{N}\right)^t C_d^s U^u, \sigma_v^\nu \tag{2.33}$$

with the values for w, d, N given in the previous equations and the indices t, u, s, ν defined as

$$\begin{aligned} t &= 0, \pm 1, \ldots, \\ u &= 0, 1; \\ s &= 0, 1, \ldots, d-1; \\ \nu &= \begin{cases} 0,1 & \text{achiral} \\ 0 & \text{chiral} \end{cases} \end{aligned} \tag{2.34}$$

The elements in Eq. (2.33) form the line groups $\mathfrak{L}$, which are generally given by the product of a point group and an axial group. More specifically, for achiral and chiral

[3]Sometimes in the papers by Damnjanović *et al.* this can be found denoted as σ_x.

tubes we have the following line groups:

$$\begin{aligned} \mathfrak{L}_{\mathcal{A},\mathcal{Z}} &= \mathfrak{T}^1_{2d}\mathfrak{D}_{dh} \qquad \text{achiral tubes} \\ \mathfrak{L}_{\mathcal{C}} &= \mathfrak{T}^w_N\mathfrak{D}_d \qquad \text{chiral tubes.} \end{aligned} \tag{2.35}$$

Note that, since carbon nanotubes line groups always contain the screw axis, they are *non-symmorphic* groups and the isogonal point group (i. e. a point group with the same order of the principal rotational axis, where the rotations include the screw-axis operations) is not a subgroup of the full symmetry group. The point groups isogonal to the respective nanotube line groups are given by

$$\begin{aligned} \mathfrak{D}_N &\quad \text{for chiral tubes} \\ \mathfrak{D}_{2dh} &\quad \text{for achiral tubes} \end{aligned} \tag{2.36}$$

We conclude this section by reminding that for most applications of symmetry in nanotube science, such as optical spectroscopy or first-order Raman scattering, where only the center of the Brillouin zone is probed, it's sufficient to work with the (isogonal) point group. This can be done safely because electronic and vibrational eigenfunctions at the Γ point always transform as irreducible representations of the isogonal point group.

2.6 Summary

In this chapter the geometry of a single-walled carbon nanotube was completely defined both in real and reciprocal space, starting from the rolling up of a graphene sheet. The Brillouin zone was indexed in terms of a set of discrete azimuthal quantum numbers μ and continuous wavevectors k_z, which give rise to a set of so called *cutting lines* in k-space. It was also shown how the atomic structure could be completely derived from a given chiral vector (n, m) according to three different symmetry choices. Finally, for completeness, a list of the symmetry elements which are present in carbon nanotube was given and related to the full symmetry line group classification for these systems.

Chapter 3

The zone folding method

This chapter introduces the simplest models for describing the electronic and optical properties of single-walled carbon nanotubes within reasonable approximations. It's essential to understand the development of this thesis and the reasons behind the choices we will perform in the following chapters. First we review the derivation of a simple analytical expression for the electronic structure of graphene, based on the tight-binding approximation for crystalline solids and π-electrons. On the basis of the nanotube Brillouin zone construction of the previous chapter, the zone-folding method is applied to the graphene band structure, in order to obtain a general expression for calculating the electronic structure of SWNTs of any chirality. We also show how optical matrix elements for interband transitions and dipole selection rules can be obtained from graphene eigenvectors in order to compute the tight-binding optical absorption spectra of SWNTs. This chapter covers mainly literature materials from Refs. [89, 141, 142, 144, 145].

3.1 Electronic structure of a graphene sheet

As stated in the first chapter, the tight-binding approximation (TBA) gives a simplified but rather good and efficient description of the electronic band structure of covalent solids, such as for instance 3D inorganic semiconductors (C, Si, SiC, GaAs), organic molecules (butadiene, polyacetylene, etc.) and transition 3*d*-band metals. In the TB method a set of localized atomic orbitals is adopted as basis for expanding the crystal wavefunctions and the exact many-body hamiltonian operator is replaced with a parametrized hamiltonian matrix. Actually, the use of the term *tight-binding* is related to the atomic-like wavefunctions, which are *tightly bound* to the atoms. In general, only a small number of basis functions are used, which approximately correspond to the atomic orbitals in the energy range of interest. For instance, when modelling covalently bond carbon based materials, such as diamond and graphitic derivatives, the 1*s* atomic orbitals related to the core electrons can be reasonably neglected and only 2*s* and the three $2p_x, 2p_y, 2p_z$ orbitals for each of the four valence electrons can be safely taken into account.

3.1.1 Schrödinger equation within the tight-binding framework

We consider now the biatomic graphene cell with the basis atoms *s* denoted by A and B and the above mentioned four atomic orbitals *o* for the valence electrons for each atom. In total we have eight atomic orbitals labelled by the atom index and the atomic-like wavefunctions, namely $2s^A, 2p_x^A, 2p_y^A, 2p_z^A$ and $2s^B, 2p_x^B, 2p_y^B, 2p_z^B$, from which eight bands are obtained from solving the single-particle Schrödinger equation for the extended periodic system (Fig. 3.1 a)). In order to obtain the electronic dispersion relation of a periodic system such as the graphene sheet, one has to solve the (time-independent) single-particle Schrödinger equation in presence of an effective periodic potential:

$$H\Psi^b(\mathbf{k},\mathbf{r}) = E^b(\mathbf{k})\,\Psi^b(\mathbf{k},\mathbf{r}), \tag{3.1}$$

where $H = T + V(\mathbf{r})$ is the single-particle Hamiltonian, given by the kinetic energy operator $\mathbf{T}$ and the effective periodic potential $V(\mathbf{r})$. In the spirit of LCAO, the electronic wavefunction for each of the eight bands can be written as:

$$\psi^b(\mathbf{k},\mathbf{r}) = \sum_{so} c_{so}^b(\mathbf{k})\,\Phi_{so}(\mathbf{k},\mathbf{r}) \tag{3.2}$$

where *b* is the band index and the sum is taken over the eight orbitals listed above. The c_{so}^b are wavefunction coefficients for the functions $\Phi_{so}(\mathbf{k},\mathbf{r})$, which can be put in Bloch form as follows:

$$\Phi_{so}(\mathbf{k},\mathbf{r}) = \frac{1}{\sqrt{U}}\sum_{u=0}^{U-1}\exp(i\mathbf{k}\cdot\mathbf{R}_{us})\phi_o(r-\mathbf{R}_{us}) \tag{3.3}$$

where *U* is the number of graphene cells inside the crystal and $\phi_o(r-\mathbf{R}_{us})$ is the atomic orbitals centered at the atomic coordinate $\mathbf{R}_{us}$. According to the Rayleigh-Ritz variational principle, the ground state energy is found by minimization of the energy functional with respect to the wavefunction coefficients $c_{so}^b(\mathbf{k})$:

$$\frac{\partial E^b}{\partial c_{s'o'}^{b*}} = 0 \quad \text{where} \quad E^b = \frac{\langle\Psi^b|H|\Psi^b\rangle}{\langle\Psi^b|\Psi^b\rangle} \tag{3.4}$$

After the functional minimization, the stationary Schrödinger equation for the Bloch amplitude coefficients is obtained, which can be put in matrix form as follows:

$$\sum_{so} H_{s'o'so}(\mathbf{k})\,c_{so}^b(\mathbf{k}) = \sum_{so} E^b(\mathbf{k})\,S_{s'o'so}(\mathbf{k})\,c_{so}^b(\mathbf{k}) \tag{3.5}$$

Here the Hamiltonian $H_{s'o'so}(\mathbf{k})$ and the overlap $S_{s'o'so}(\mathbf{k})$ matrices are given by

$$H_{s'o'so}(\mathbf{k}) = \sum_{u}^{U}\exp(i\mathbf{k}\cdot(\mathbf{R}_{us}-\mathbf{R}_{u's'}))\int\phi_{o'}^*(r-\mathbf{R}_{u's'})\,H\phi_o(r-\mathbf{R}_{us})\,dr \tag{3.6}$$

$$S_{s'o'so}(\mathbf{k}) = \sum_{u}^{U}\exp(i\mathbf{k}\cdot(\mathbf{R}_{us}-\mathbf{R}_{u's'}))\int\phi_{o'}^*(r-\mathbf{R}_{u's'})\,H\phi_o(r-\mathbf{R}_{us})\,dr$$

The orthonormality condition for the electron wavefunction of Eq. (3.2) becomes

$$\int \Psi^{b'*}(\mathbf{k},\mathbf{r})\,\Psi^{b}(\mathbf{k},\mathbf{r})\,dr = \sum_{s'o'}\sum_{so} c^{b'*}_{s'o'}(\mathbf{k})\,S_{s'o'so}(\mathbf{k})\,c^{b}_{so}(\mathbf{k}) = \delta_{b'b} \tag{3.7}$$

where $\delta_{b,b'}$ is the Kronecker delta function. Before solving the matrix problem of Eq. (3.5), the integrals of Eq. (3.6) need to be parametrized as functions of the interatomic vector $\mathbf{R} = \mathbf{R}_{u's'} - \mathbf{R}_{us}$ and the symmetry and relative orientation of the involved orbitals $\phi^{*}_{o'}(r)$ and $\phi_{o}(r)$:

$$\begin{aligned} \varepsilon_o &= \int \phi^{*}_{o}(r)\,H\phi_{o}(r)\,dr \\ t_{oo'}(\mathbf{R}) &= \int \phi^{*}_{o}(r)\,H\phi_{o'}(r-\mathbf{R})\,dr \\ s_{oo'}(\mathbf{R}) &= \int \phi^{*}_{o}(r)\,\phi_{o}(r-\mathbf{R})\,dr \end{aligned} \tag{3.8}$$

Now we can find the eigenvalues of $H(\mathbf{k})$ by solving the secular equation for the 8×8 hamiltonian matrix $H_{s'o'so}(\mathbf{k})$ and the overlap matrix $S_{s'o'so}(\mathbf{k})$

$$\det\left[H_{s'o'so}(\mathbf{k}) - E^{b}(\mathbf{k})\,S_{s'o'so}(\mathbf{k})\right] = 0. \tag{3.9}$$

Before proceeding with the solution of the secular equation in the next subsection, we have to consider in detail the dependence on the symmetry and orientation of the atomic orbitals of the transfer $t_{oo'}(\mathbf{R})$ and the overlap $s_{oo'}(\mathbf{R})$ integrals. We recall that in graphene the 2*s* atomic orbitals mix with the $2p_x$ and $2p_y$ orbitals to form the hybridized σ molecular orbitals, which in turn give the covalent bonds of the hexagonal lattice. The $2p_z$ atomic orbitals form the π-molecular orbitals which point normal to the graphene plane and are uncoupled from the σ molecular orbitals. Unlikely the $2s$ atomic orbital, which is spherically symmetric, the $2p$ atomic orbital has the symmetry of the spherical harmonic $Y_{21}(\theta,\phi)$, so it can be decomposed along two mutually orthogonal directions, namely perpendicular and parallel to the interatomic vector $\mathbf{R}$. These directions are again referred to as π and σ, respectively. From this point on, the $2s$ orbital will be simply denoted for brevity as *s*. To determine the hopping $t_{oo'}(R)$ and the overlap $s_{oo'}(R)$ integrals, one has to consider first all the possible pairs between the $o' = s,\sigma,\pi$ and the $o = s,\sigma,\pi$ orbitals, which amount to nine possible pairs, as we can see in Fig. 3.1 c). Among these, four $(o'o = s\pi,\pi s,\sigma\pi,\pi\sigma)$ give transfer and overlap integral identically zero by simmetry requirements. For the remaning five pairs $(oo' = ss,s\sigma,\sigma s,\sigma\sigma,\pi\pi)$, the two pairs $oo' = s\sigma$ and σs give transfer and overlap integrals of opposite signs and same magnitude. Therefore there are only four independent pairs $(oo' = ss,s\sigma,\sigma\sigma,\pi\pi)$ and the total number of tight-binding parameters is ten: the two atomic orbital energies $(\varepsilon_{2s},\varepsilon_{2p})$, the four hopping integrals $t_{ss}(R), t_{s\sigma}(R), t_{\sigma\sigma}(R), t_{\pi\pi}(R)$ and the four

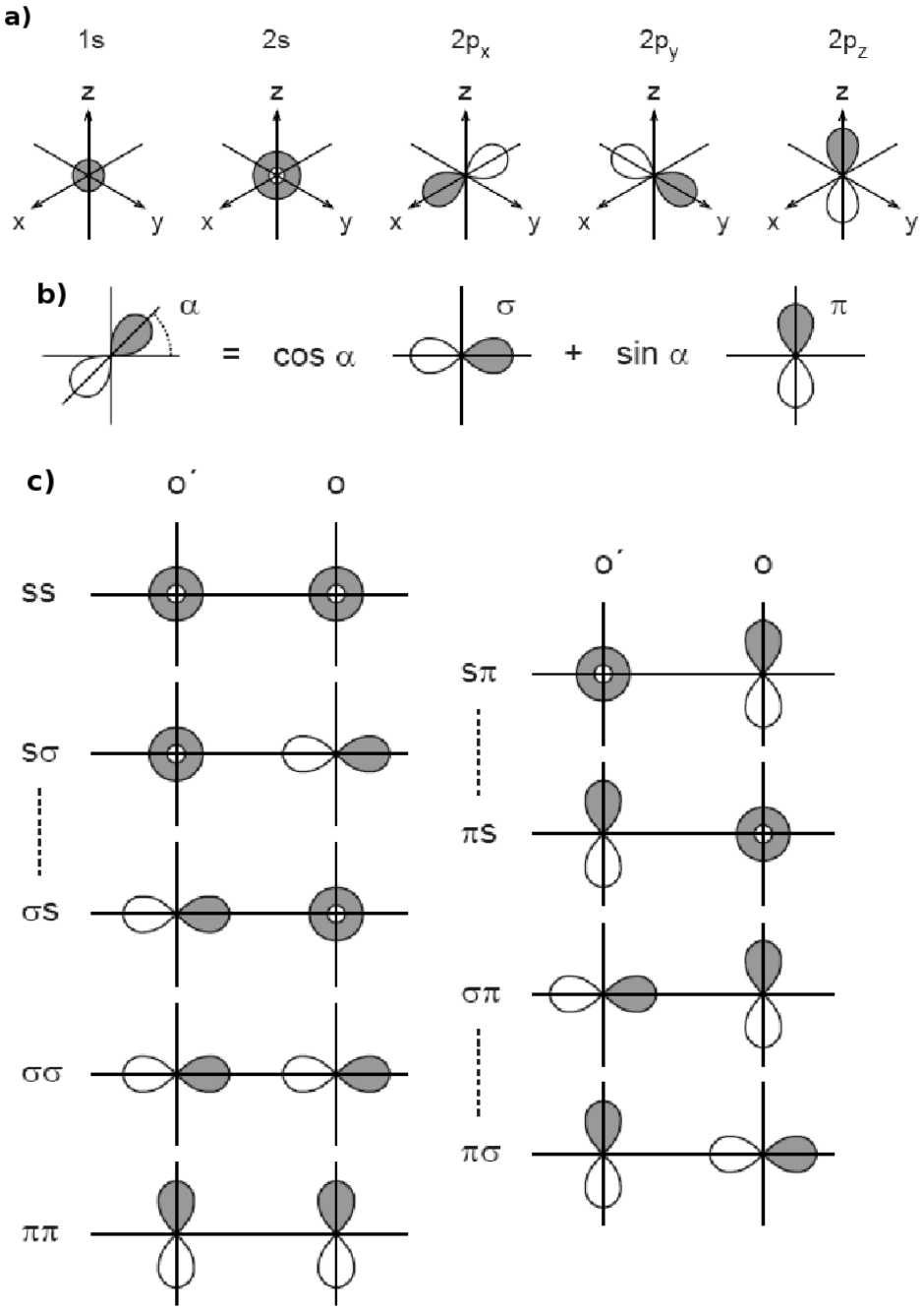

Fig. 3.1: a) Schematic of the $1s$, $2s$, $2p_x$, $2p_y$, and $2p_z$ atomic orbitals of the carbon atom. b) The σ and π projections of the $2p$ atomic orbital. c) (left) The five molecular orbital configurations $o'o = ss, s\sigma, \sigma s, \sigma\sigma, \pi\pi$ that give nonvanishing transfer $t_{o'o}\,(R)$ and overlap integrals $s_{o'o}\,(R)$. The two configurations $o'o = s\sigma, \sigma s$ connected by a dashed line yield the transfer and overlap integrals of equivalent magnitudes and opposite signs. c) (right) The remaining four configurations $o'o = s\pi, \pi s, \sigma\pi, \pi\sigma$ for which the transfer and overlap integrals are identically zero by symmetry requirements. The dashed lines connect the equivalent configurations. Taken from Ref. [122]

overlap integrals $s_{ss}(R), s_{s\sigma}(R), s_{\sigma\sigma}(R), s_{\pi\pi}(R)$. Additionally, we note that within the orthogonal tight-binding model the parameters $s_{oo'}(R)$ are set to zero. Usually the numerical values for the tight-binding parameters are obtained from a fit to an *ab initio* calculation or experimental measurements. Because the σ and π molecular orbitals are decoupled, as noted previously, the 8×8 Hamiltonian $H_{s'o'so}(\mathbf{k})$ and overlap matrices $S_{s'o'so}(\mathbf{k})$ are decomposed into a 6×6 and a 2×2 for the σ and π molecular orbitals, respectively. For graphitic materials, the electronic and optical properties are determined by the π energy bands, which lie near the Fermi level on the energy scale (see Fig. 3.3), thus it's sufficient to take into account only the 2×2 subblock for the solution of the secular determinant.

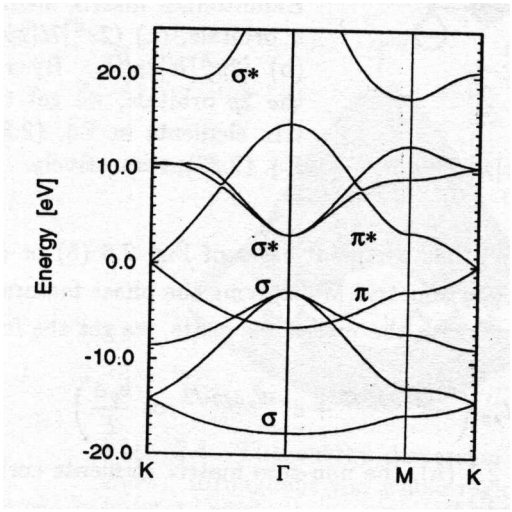

Fig. 3.2: Electronic dispersion relation for graphene along the $K - \Gamma - M - K$ lines of the 2D BZ. Taken from Ref. [89]

3.1.2 Graphene electronic hamiltonian for π-electrons

Now we can solve the secular equation within the framework of the tight-binding model for π electrons in the biatomic graphene cell, in order to obtain a simple analytical expression for the electronic dispersion of graphene over the 2D BZ. Additionally, only nearest-neighbor interactions $(R = a_{CC})$ are taken into account in the Bloch phase factors of Eq. (3.6), so any atom of a given type (A or B) has three nearest neighbors of the opposite type. Obviously, within the same A (or B) sublattice the nearest neighbor interactions are absent and the diagonal hamiltonian and overlap matrix element are simply:

$$\begin{aligned} H_{A\pi A\pi} &= H_{B\pi B\pi} = \varepsilon \\ S_{A\pi A\pi} &= S_{B\pi B\pi} = 1 \end{aligned} \tag{3.10}$$

For the $H_{A\pi B\pi}$ and $S_{A\pi B\pi}$ matrix elements, first the interatomic vectors $\mathbf{r}_s^l = \mathbf{r}_A^l = -\mathbf{r}_B^l$ from one atom A to its three nearest neighbors (or viceversa) must be explicitly written down and substituted into the above cited Bloch exponential phase factors, as follows:

$$\mathbf{r_A^1} = (\mathbf{a_1} + \mathbf{a_2})/3 \qquad \mathbf{r_A^2} = (\mathbf{a_1} - 2\mathbf{a_2})/3 \qquad \mathbf{r_A^3} = (-\mathbf{2a_1} + \mathbf{a_2})/3. \tag{3.11}$$

Thus we obtain for the off-diagonal hamiltonian and overlap matrix elements:

$$\begin{array}{lll} H_{A\pi B\pi} = tf(\mathbf{k}) & \text{and} & H_{B\pi A\pi} = tf^*(\mathbf{k}) \\ S_{A\pi B\pi} = sf(\mathbf{k}) & \text{and} & S_{B\pi A\pi} = sf^*(\mathbf{k}), \end{array} \tag{3.12}$$

where $f(\mathbf{k})$ is the sum of the phase factors over the three nearest neighbors given by:

$$f(\mathbf{k}) = \exp\left(i\frac{k_x a}{\sqrt{3}}\right) + \exp\left(-i\frac{k_x a}{2\sqrt{3}} + i\frac{k_y a}{2}\right) + \exp\left(-i\frac{k_x a}{2\sqrt{3}} - i\frac{k_y a}{2}\right). \tag{3.13}$$

We note that the hamiltonian and overlap matrices are hermitian. The Schrödinger equation in matrix form becomes:

$$\begin{pmatrix} \varepsilon & tf(\mathbf{k}) \\ tf^*(\mathbf{k}) & \varepsilon \end{pmatrix} \begin{pmatrix} C_{A\pi}^b(\mathbf{k}) \\ C_{B\pi}^b(\mathbf{k}) \end{pmatrix} = E^b(\mathbf{k}) \begin{pmatrix} 1 & sf(\mathbf{k}) \\ sf^*(\mathbf{k}) & 1 \end{pmatrix} \begin{pmatrix} C_{A\pi}^b(\mathbf{k}) \\ C_{B\pi}^b(\mathbf{k}) \end{pmatrix} \tag{3.14}$$

Solving the secular equatio yields the energy dispersion relation for graphene valence and conduction bands :

$$E^{v,c}(\mathbf{k}) = \frac{\varepsilon \pm tw(\mathbf{k})}{1 \pm sw(\mathbf{k})} \qquad \text{with} \quad (+) \Rightarrow v, (-) \Rightarrow c \tag{3.15}$$

where *v* and *c* indicate the valence and conduction bands for $t < 0$, respectively. $w(\mathbf{k})$ is the absolute value of the phase factor $f(\mathbf{k})$, that is:

$$w(\mathbf{k}) = \sqrt{f^*(\mathbf{k}) f(\mathbf{k})} = \sqrt{1 + 4\cos\frac{\sqrt{3}k_x a}{2}\cos\frac{k_y a}{2} + 4\cos^2\frac{k_y a}{2}}. \tag{3.16}$$

We must point out that the on-site energy parameter ε is an arbitrary reference energy point for the Fermi level, in the orthogonal tight-binding model it is set equal to $0\,\mathrm{eV}$ together with the parameter *s*, which is set to zero and quantifies the degree of asimmetry of the valence and conduction bands with respect to the Fermi level. Therefore, in the π orthogonal tight-binding model, the analytic expression for the graphene electronic dispersion reduces to a simpler form

$$E^{v,c}(\mathbf{k}) = \pm tw(\mathbf{k}) = \pm t\sqrt{f^*(\mathbf{k}) f(\mathbf{k})} = \sqrt{1 + 4\cos\frac{\sqrt{3}k_x a}{2}\cos\frac{k_y a}{2} + 4\cos^2\frac{k_y a}{2}}. \tag{3.17}$$

Substituting the energy eigenvalues $E^b(\mathbf{k})$ of Eq. (3.15) into Eq. (3.14) yields Bloch amplitudes $C^b_{A\pi}(\mathbf{k})$ and $C^b_{A\pi}(\mathbf{k})$ for each atomic site in the graphene unit cell. For the wavefunction of the valence and conduction bands of each site we get the following relations:

$$C^v_{A\pi} = +\sqrt{\frac{f(\mathbf{k})}{2w(\mathbf{k})(1+sw(\mathbf{k}))}} \qquad C^v_{B\pi} = +\sqrt{\frac{f^*(\mathbf{k})}{2w(\mathbf{k})(1+sw(\mathbf{k}))}}, \tag{3.18}$$

$$C^c_{A\pi} = +\sqrt{\frac{f(\mathbf{k})}{2w(\mathbf{k})(1-sw(\mathbf{k}))}}, \qquad C^c_{B\pi} = -\sqrt{\frac{f^*(\mathbf{k})}{2w(\mathbf{k})(1-sw(\mathbf{k}))}}.$$

As shown in the final sections of this chapter, these Bloch wavefunction amplitudes play an important role for the calculation of the optical spectra of SWNTs, because they enter directly into the calculation of the graphene and SWNT transition dipole matrix elements. At the Γ point, where $\mathbf{k} = 0$, the amplitudes for the valence band become $C^v_{A\pi} = C^v_{B\pi}$, while for the conduction band we have $C^c_{A\pi} = -C^c_{B\pi}$. Thus the valence band wavefunction is $\Psi^v \propto \Phi_{A\pi} + \Phi_{B\pi}$ and the corresponding π molecular orbital has bonding character, while the conduction band wavefunction is $\Psi^c \propto \Phi_{A\pi} - \Phi_{B\pi}$ and the corresponding π^* molecular orbital has antibonding character. Obviously, for any $\mathbf{k} \neq \Gamma$, the Bloch wavefunctions of Eq. (3.3) have, in general, different phase factors for both A and B sublattices.

3.1.3 Graphene electronic band structure for π-electrons

As shown in Fig. 3.3, the valence and conduction bands touch each other at the corners $\mathbf{K}$ and $\mathbf{K}'$ of the 2D hexagonal Brillouin zone, also called Dirac points. The touching points are called Fermi points and denoted as $\mathbf{k_F}$ and $\mathbf{k'_F}$. They are defined by the setting the phase factor $f(\mathbf{k}) = 0$. Also the Fermi level passes through the Fermi points, because in the orthogonal TB model the on-site energy is set as $\varepsilon = 0$ eV. This property arises because in the unit cell there are two carbon atoms and the on-site energy parameter is the same for both A and B sites. If there were two different atomic species, such as in the case of hexagonal BN, which has the same crystal structure of graphite, a gap would occur since the secular equation at the BZ corners $\mathbf{K}$ and $\mathbf{K}'$ would be

$$\det \begin{pmatrix} \varepsilon_{A\pi A\pi} - E(\mathbf{K}) & 0 \\ 0 & \varepsilon_{B\pi B\pi} - E(\mathbf{K}) \end{pmatrix} = 0 \tag{3.19}$$

with the corresponding eigenvalues $E(\mathbf{K}) = \varepsilon_{A\pi A\pi}$ and $E(\mathbf{K}) = \varepsilon_{B\pi B\pi}$.
By inspection of Fig. 3.3, the density of the electronic states (DOS) goes to zero at the Fermi level, thus graphene is a zero-gap semiconductor. Another interesting characteristic of graphene is its linear dispersion relation around the Dirac points $\mathbf{K}$ and $\mathbf{K}'$. By making an expansion around these points in power series of $\Delta k_x a$ and $\Delta k_y a$ up to the

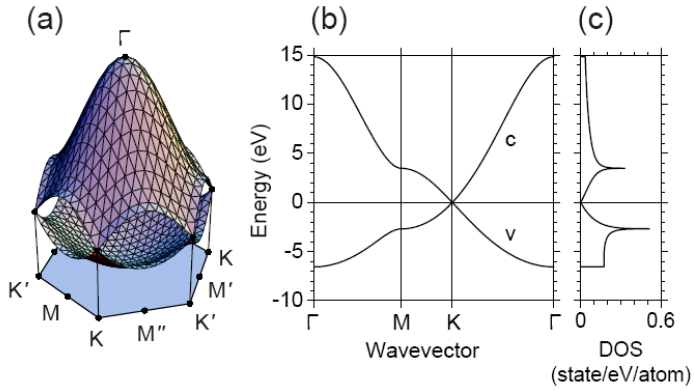

Fig. 3.3: Electronic dispersion relations of a graphene sheet given by Eq. (3.17) with STB parameters $t = 3.033\,\mathrm{eV}$, $s = 0.129$, and $\varepsilon = 0$ eV (a) throughout the entire first Brillouin zone and (b) along the high-symmetry directions in the first Brillouin zone. The valence and conduction bands are labeled by *v* and *c*, respectively. (c) The density of electronic states (DOS). The Fermi level is shown by the horizontal line at zero energy. Taken from Ref.[122]

second order, we have $w = \frac{\sqrt{3}}{2}\Delta k a$, where $\Delta k = \sqrt{\Delta k_x^2 + \Delta k_y^2}$ is the distance from the K (K') point of the electron wavevector at $\mathbf{k} = K + (\Delta k_x, \Delta k_y)$. Substituting $w\,(\mathbf{k})$ into Eq. (3.15), yields the following electronic dispersion relations linear in Δk for the graphene valence *v* and conduction *c* bands

$$E^b\,(\Delta k) = \varepsilon \mp \frac{\sqrt{3}}{2}\,(\varepsilon s - t)\,a\Delta k \qquad \text{with} \quad (-) \Rightarrow v, (+) \Rightarrow c \tag{3.20}$$

This fact, in addition to the increased electronic mobility, differentiates graphene from conventional semiconductors, which have indeed parabolic energy bands. Actually the effective mass approximation of the non-relativistic Schrödinger equation, used for these materials with parabolic bands, is not applicable to graphene. Instead, conduction π-electrons in graphene behave like massless fermions, whose behaviour is described by the relativistic Dirac equation. As a matter of fact, since its discovery in 2004, graphene has built the bridge between high-energy physics and condensed matter physics, namely relativistic condensed matter physics [5].

3.2 Electronic structure of SWNTs

In order to calculate the π-electronic band structure for SWNTs, a good approximation is represented by the zone-folding the 2D Brillouin zone of graphene, i. e. by sectioning the graphene dispersion relation $E^{2Dg}\,(k_x, k_y)$ along the cutting lines found with the aid

of Eq. (2.13). This concept is sketched in Fig. 3.4 below, where the cutting-lines are superimposed on the 3D graphene electronic dispersion for π electrons. Therefore, the general form for any (n, m) SWNT is given by

$$E(\mu, k_z) = E^{2Dg}\left(\mu\mathbf{K_1} + k_z\frac{\mathbf{K_2}}{|\mathbf{K_2}|}\right) \tag{3.21}$$

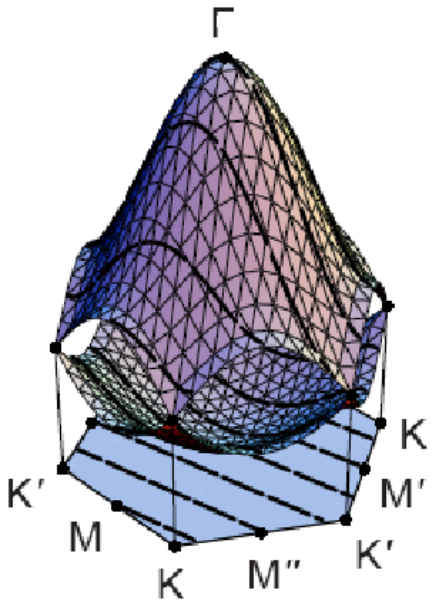

Fig. 3.4: Graphical representation of the zone-folding method applied to a chiral (4,2) SWNT: the cutting-lines are superimposed on the 3D dispersion relations and can be seen also on the 2D BZ. Taken from Ref. [122]

For a given SWNT, there are 2*N* π-electronic bands, originating from the wavevector quantization along the nanotube circumference. The three typical electronic structures of an armchair, zigzag and chiral SWNTs thus obtained are shown in Fig. 3.5 below.
The electronic density of states (DOS) profiles in Fig. 3.6 for the metallic (5,5) and semiconducting (5,0) SWNTs show the peaks of van Hove singularities (vHs), where the dispersion is flat and hence the DOS diverges. Moreover, one can see that for metallic tubes the DOS is constant at Fermi level, whereas it is zero for semiconducting SWNTs. The vHs are a signature of the one-dimensionality character of these systems and are relevant for understanding the nanotube electronic interband transitions. However, details about DOS and related quantities, such as the joint density of states (JDOS) will be discussed

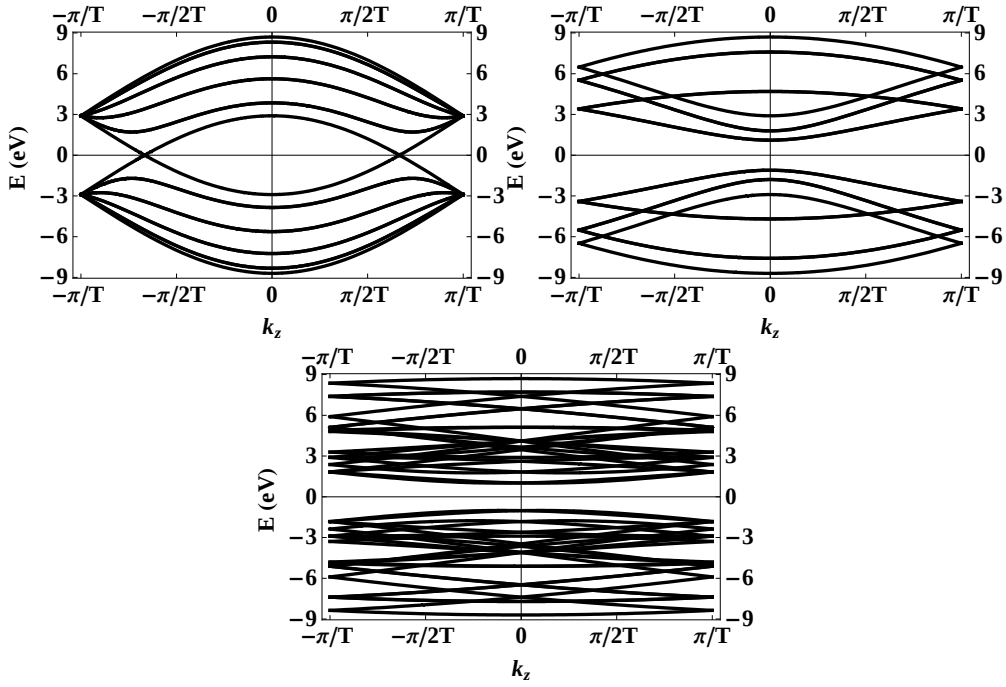

Fig. 3.5: Electronic band structures of SWNTs for the three representatives geometries obtained by zone-folding method: armchair (5,5) (left upper), zigzag (5,0) (upper right) and chiral (4,2) (bottom). Calculations reproduced from Ref. [89] with TB parameters $t_\pi = 2.9\,\mathrm{eV}$, $s = 0$, and $\varepsilon_\pi = 0\,\mathrm{eV}$.

in the third subsection, while in the next two subsections, we will consider in detail the metallicity condition for SWNTs and the important k-points belonging to the cutting lines near the Fermi energy, where the vHs in the DOS, important for the optical spectra, are found. Moreover, it will be shown that a particular nanotube classification arises from this cutting line analysis which relates the SWNT geometrical structure to these special BZ points [125, 122, 121].

3.2.1 Metallicity condition for SWNTs

By inspection of Fig. 3.7 (left), clearly a SWNT is metallic if a cutting line passes through a Dirac point **K** or $\mathbf{K}'$. In other words, the SWNT is metallic if its circumference is commensurate with the metallic wavefunction of graphene. Mathematically, for any SWNT chiral pair indices (n, m), this is expressed again by the condition of periodicity around the tube circumference of Eq. (2.14)

$$\mathbf{K} \cdot \mathbf{C}_h = 2\pi\mu, \quad (\mu \quad \text{integer}) \tag{3.22}$$

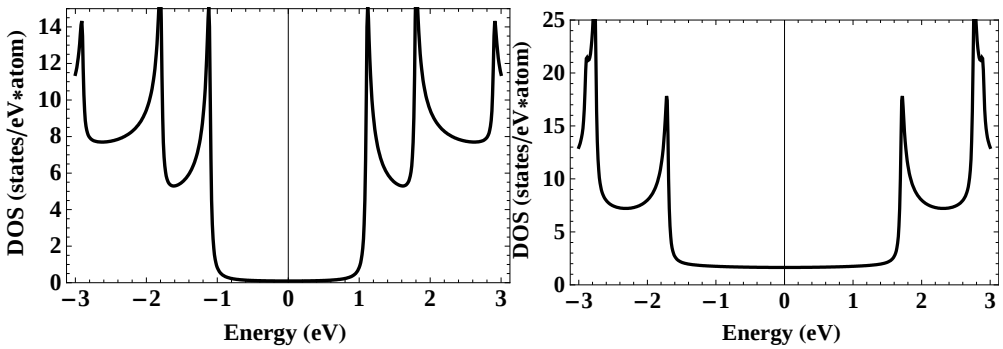

Fig. 3.6: Density of electronic states for a semiconducting (5,0) (left) and metallic (5,5) SWNT (right) calculated by zone-folding method.

where now the coordinates of the Dirac point have been substituted as

$$\mathbf{K} = \frac{2\mathbf{b_1} + \mathbf{b_2}}{3}. \tag{3.23}$$

Using the geometrical definitions for the real an reciprocal lattice vectors of Chapter 2, one obtains the important result

$$2n + m = 3\mu, \tag{3.24}$$

which can also be expressed in the form

$$n - m = 3\mu, \tag{3.25}$$

if we consider that $(2n + m) - (2m + n) = n - m$. Moreover, calculation of the normal distance from the $\mu = 0$ cutting line (i. e. the one which crosses the Γ point) to the $\mathbf{K}$ point in units of $\mathbf{K_1}$ gives

$$\frac{\mathbf{K} \cdot \mathbf{K_1}}{\mathbf{K_1} \cdot \mathbf{K_1}} = \frac{2n + m}{3} \tag{3.26}$$

which confirms Eq. (3.24). Thus, if $n - m$ is multiple of 3 the SWNT is metallic, otherwise it's semiconducting. In the latter case, Eq. (3.26), the normal distances from cutting line $\mu = 0$ to the cutting lines closest to $\mathbf{K}$ are found, as follows

$$\frac{\mathbf{K} \cdot \mathbf{K_1}}{\mathbf{K_1} \cdot \mathbf{K_1}} = \mathrm{mod}\,(2n + m, 3) = 1 \quad (S1) \quad \text{or} \quad \mathrm{mod}\,(2n + m, 3) = 2 \quad (S2) \tag{3.27}$$

from which the classification of semiconducting SWNTs into type 1 or type 2 is derived. Note that if the convention $\mathrm{mod}\,(2m + n, 3)$ or $\mathrm{mod}\,(n - m, 3)$ is used, the above $\mathrm{S1}$ and $\mathrm{S2}$ definitions are swapped, i. e. a former S1 SWNT would be an S2 tube and so on. In the following, we will always stick with the defintion of S1 and S2 types according to the values of $\mathrm{mod}\,(2n + m, 3)$.

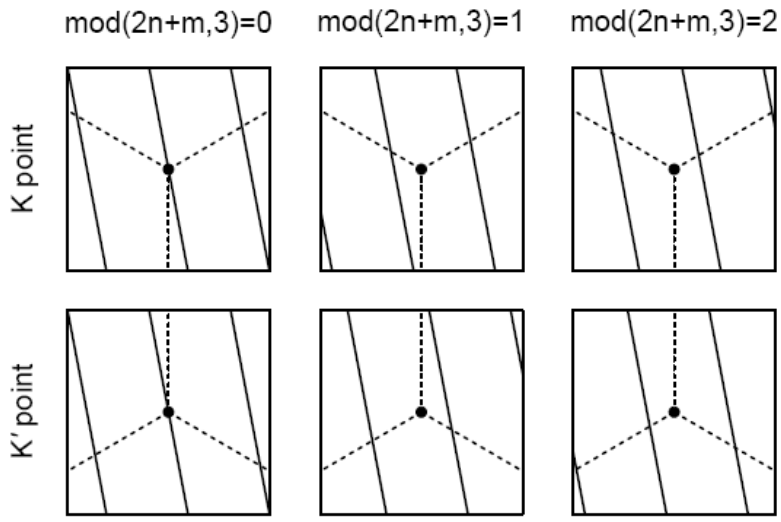

Fig. 3.7: Three possible configurations of the cutting lines in the vicinity of the Dirac points depending on the value of $\mathrm{mod}\,(2n+m,3)$. The dashed lines indicate the KM directions which are the boundaries of the first Brillouin zone. Taken from Ref. [122].

The values of constant $2n+m$ are also used in optical experiments to identify families of SWNTs of approximately the same diameter, which share a similar behavior in photoluminescence spectra. By plotting the SWNT chiral indices onto the graphene lattice, we could actually identify each family with a straight line joining chiral indices of the same $2n+m = const$. The above condition also implies that the number of semiconducting SWNTs is twice as the amount of metalllic tubes, which is as well useful in photoluminescence experiments. To summarize, a SWNT is metallic if $\mathrm{mod}\,(2n+m,3) = 0$ and semiconducting if $\mathrm{mod}\,(2n+m,3) = 1 \quad \mathrm{or} \quad 2$. In the nowadays accepted nanotube classification, these three types are referred to as M0, S1 and S2, respectively. In Fig. 3.7, the three different configurations of the cutting lines near the Dirac points **K** and $\mathbf{K}'$ are shown, together with the corresponding value of $\mathrm{mod}\,(2n+m,3)$. On the basis of other geometrical relations, this classification was further developed into several subtypes, namely M1+, M1-, M2+, M2-, S1+, S1-, S2+, S2-, as explained in the next subsection. However, only SWNTs of type M0, S1 and S2 have shown distinct optical properties in various spectroscopic measurements, while there was no experimental evidence of any difference among the above mentioned subtypes. So for practical purposes, it's sufficient to keep in mind only types M0, S1 and S2.

3.2.2 Critical k-points giving van Hove singularities

The purpose of this subsection is to make clear which k-points belonging to the cutting lines near the Fermi energy of SWNTs give van Hove singularities in the density of states, according to the specific geometry of a nanotube. This is extremely important for understanding which k-points dominates the optical spectra of these systems and it will be the subject of the next chapters of this thesis. We recall that in Chapter 2, SWNTs were classified into two categories: $d_R = 3d$ if $\mathrm{mod}\,(n-m, 3d) = 0$ and $d_R = d$ in all other cases. For M0 SWNTs, either $d_R = 3d$ or $d_R = d$ (metallic zigzag SWNTs) can always be satisfied, because the condition $\mathrm{mod}\,(n-m, 3d) = 0$ implies also $\mathrm{mod}\,(n-m, 3) = 0$. Instead, for S1 and S2 SWNTs the condition $d_R = d$ is always mantained. Thus, M0 SWNTs divide into subtypes M1 and M2, for which $d_R = d$ and $d_R = 3d$, respectively. Metallic zigzag SWNTs are always of subtype M1, while armchair belong to M2 subtype. Furthermore, M1 SWNTs can be classified as M1+ or M1- depending upon $\mathrm{mod}\,((2n+m)/d, 3) = 1$ or 2 and M2 SWNTs can be either M2+ or M2- according to whether $\mathrm{mod}\,(3m/d_R, 3) = 1$ or 2. Finally, SWNTs of type S1 (S2) divide into S1+ and S1- (S2+ and S2-) subtypes for which $\mathrm{mod}\,(N, 3) = 1$ or 2. As stated in the previous subsection, these further classification did not show experimental relevance. However, there exists a significative difference between zigzag SWNTs of types M1, S1, S2 and armchair M2 tubes, concerning the critical wavevectors giving vHs in the DOS, and this will be discussed in the following. For zigzag nanotubes, the critical wavevectors k_i^b at which the vHs at energy E_i^b are found always at the center of the 1D Brillouin zone of the $(n, 0)$ SWNT. For metallic zigzag tubes $(3n, 0)$ also the Fermi point k_F appears at the zone center, hence $k_F = 0$. Formally, this can be obtained by evaluating the projection of ΓK onto $\mathbf{K}_2$, which gives $(\Gamma K \cdot \mathbf{K_2}) / (\mathbf{K_2} \cdot \mathbf{K_2}) = m/d_R$. Since for M1, S1 and S2 $d_R = d$, the ratio m/d_R is an integer and the Fermi points appear at the center of the 1D BZ. Moreover, the critical wavevectors for these SWNTs, as well as the Fermi points, are doubly degenerate, that is $k_i^b = k_i^{b'} = 0$ and $k_F = k'_F = 0$, since the electronic dispersion relations around the Dirac points $\mathbf{K}$ and $\mathbf{K}'$ are isotropic. For M2 SWNTs, which include armchair nanotubes, we have $d_R = 3d$, which implies $\mathrm{mod}\,(m, d_R) = 1$ or 2. The Fermi wavevectors k_F thus appear at two-third of the distance from the center to the edge of the 1D Brillouin zone, $\pm K_2/3$, which stems from the shortening in real space of the length of the translational vector T by a factor of 3. It follows that $k_F = +K_2/3$ and $k'_F = -K_2/3$ for M2+ SWNTs, while $k_F = -K_2/3$ and $k'_F = +K_2/3$ for M2- SWNTs. In general, for a given (n, m) nanotube the condition for the critical Fermi wavevectors $k_F = 0$ or $k_F = \pm K_2/3$ are not mantained. Moreover, note that the degeneracy of the critical wavevectors, k_i^b and $k_i^{b'}$, holds only for achiral single-walled nanotubes due to the presence of a horizontal mirror plane [118]. For chiral SWNTs, the anisotropy of the electronic dispersion relation around the Dirac points $\mathbf{K}$ and $\mathbf{K}'$, which is neglected by the linear approximation showed in Eq. (3.20), lifts the degeneracy $k_i^b = -k_i^{b'} \neq 0$. Moreover, the critical points for M2 SWNTs are shifted $k_i^b = -k_i^{b'} \neq \pm K_2/3$. This

anisotropy is also called *trigonal warping effect* and is intrinsic to the complete TB orthogonal model [135]. To understand the trigonal warping effect, it's sufficient to look at the equi-energy contours around the **K** point, which are actually not circular but show a triangular distortion. Let's consider also the two cutting lines closest to the **K** point in a (chiral) metallic nanotube, as shown in Fig. 3.8. Though the cutting lines occur at the same distance from **K**, however the two points contributing to the lowest vHs, $\mathbf{k_1}$ and $\mathbf{k'_1}$, lie on different equi-energy contour. As a consequence, the trigonal warping effect induces a small splitting in the vHs peaks. The splitting is largest for zigzag nanotubes and equal to zero for armchair nanotubes, where the cutting lines are parallel to the vertical $K-M$ line and the energies at $\mathbf{k_1}$ and $\mathbf{k'_1}$ are actually equal. The origin of the triangular distortion beyond the linear approximation of Eq. (3.20) can be understood by expanding $w\left(\mathbf{k}\right)$ of Eq. (3.16) up to the second order around the **K** point

$$w = \frac{\sqrt{3}}{2}a\Delta k + \frac{1}{8}a^2\frac{\Delta k_y^3 - 3\Delta k_x \Delta k_y^2}{\Delta k} = \frac{\sqrt{3}}{2}a\Delta k + \frac{1}{8}\cos 3\varphi a^2 \Delta k^2. \tag{3.28}$$

where φ is the angle between $(\Delta k_x, \Delta k_y)$ and the direction ΓK, $\Delta k_x = \Delta k \sin\varphi$ and $\Delta k_y = \Delta k \cos\varphi$. Thus, the triangular symmetry of the equi-energy contours around the **K** point is explained with the factor $\cos 3\varphi$ in the expansion above.

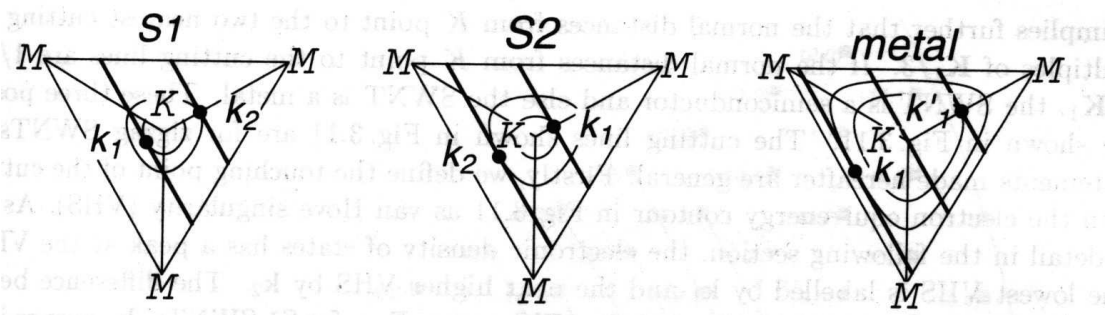

Fig. 3.8: Difference of the position of the touching points $\mathbf{k}_1$ and $\mathbf{k}_2$ of the cutting lines with the equienergy contour lines in semiconducting type I and II and metallic SWNTs. In semiconducting type S1 (S2) the E_{22}^S occurs outside (inside) the first 2D BZ. In metallic SWNTs, E_{11}^M is split due to the trigonal warping effect, since touching points belonging to cutting lines equidistant lie on different equienergy contours. Taken from Ref. [121].

3.2.3 Density of electronic states

As introduced in the beginning of this section, the flat regions of the electronic bands give rise to spikes in the electronic density of states, which are known as van Hove singu-

larities (vHs). The vHs dominate the density of electronic states (DOS) of 1D-systems. Moreover, in the next section we will see that, if a given interband transition is allowed by dipole selection rules, the profile of the optical absorption spectra of SWNTs is also dominated by the joint density of states (JDOS) between valence and conduction bands, which is a DOS-related quantity. In general, in order to obtain the DOS of a solid as a function of the energy $g(E)$, one needs to scan the whole energy range into small intervals of finite amplitude $\mathrm{d}E$, counting all over the states within each interval $[E, E+\mathrm{d}E]$. Thus the general profile of the DOS as a function of energy for a 1D crystal with volume *V* is obtained as

$$g(E) = 1/V \sum_{\sigma} \sum_{b,\mathbf{k}} 2\delta\left(E - E^{b}_{\mathbf{k}}\right), \tag{3.29}$$

where *b* is the usual band index, **k** the wavevector index in the BZ and the sum over σ accounts for the spin degeneracy, that is at most two electrons with opposite spin can be accomodated in each k-state. Then, the full DOS profile for the SWNT is obtained from integrating the zone-folding band structure of Eq. (3.21) over each 1D BZ and summing over the bands, as follows

$$g(E) = 1/(2\pi) \sum_{\sigma} \sum_{b=v,c} \sum_{\mu=0}^{N-1} \int_{-\pi/T}^{\pi/T} \mathrm{d}k_z \delta\left(E - E^{b}(\mu, k_z)\right) \tag{3.30}$$

Similarly, for the JDOS between valence and conduction states

$$g_J(E) = 1/V \sum_{\sigma} \sum_{\mathbf{k},\mathbf{k}'} \delta\left(E - (E^{c}_{\mathbf{k}'} - E^{v}_{\mathbf{k}})\right), \tag{3.31}$$

which can be expressed for SWNTs as

$$g_J(E) = 1/(2\pi) \sum_{\sigma} \sum_{\mu,\mu'=0}^{N-1} \int_{-\pi/T}^{\pi/T} \mathrm{d}k_z \delta\left(E - (E^{c}(\mu', k_z) - E^{v}(\mu, k_z))\right). \tag{3.32}$$

For numerical evaluations, the delta functions in Eqq. (3.30) and (3.32) can be more conveniently expressed in the form of a Lorentzian function (see for example Appendix G.5.1 in Ref. [94]) with broadening parameter β

$$\delta(E - E') = \lim_{\beta \to 0} \left(\frac{1}{\pi} \frac{\beta}{(E - E')^2 + \beta^2} \right) \tag{3.33}$$

In the next section, it will be shown that, according to the calculations of Refs. [139, 141], for light polarization parallel to the tube axis optical transitions occur between vHs of valence and conduction bands having $\mu = \mu'$, whereas for perpendicular polarization the selection rule is $\mu' = \mu \pm 1$. If the energy of an incoming photon matches the energy difference between two vHs, in the conduction and in the valence band, respectively, the

optical absorption is largely enhanced due to the high number of electronic states. Thus it is possible to observe from an isolated SWNT and even picking up resonant signal from only a few specific SWNTs in a sample with many different (n, m) chiralities. By changing the laser energy different SWNTs chiralities can be selectively probed. For electronic states near the Dirac points **K** and **K**′, Mintmire and White [65, 137] have derived very simple scaling relations for the lowest transition energies $\pi \rightarrow \pi^*$ at the vHs with index *i*, both for metallic and semiconducting nanotubes:

$$E_{ii}^{S} = \frac{2at_\pi i}{\sqrt{3}d_t} \quad \text{and} \quad E_{ii}^{M} = \frac{2\sqrt{3}at_\pi i}{d_t}, \quad (i = 1, 2, 3)\,. \tag{3.34}$$

It is clear that the energy gap at the vHs with index *i* is inversely proportional to the SWNT diameter d_t and that the first metallic transition occurs at three times the energy of a semiconducting SWNT. More accurate predictions for these transitions have been derived by Reich *et al.* taking into account the trigonal warping effect into the k-expansion of the energy dispersion around the **K** point [138]. We conclude this panoramic discussion about DOS and related quantities by pointing out that that there are other techniques (e.g. the *recursion method* [76, 80]) which allow to obtain the density of states even without the need of having at disposal the complete bandstructure. This can be the case for instance of non-periodic systems or with open boundary conditions. In literature about transport properties of carbon nanotubes, these techniques take advantage of the calculation of the local density of states (LDOS) for each atom from the Green's function for the hamiltonian, which is often found formulated in real space representation. In this case, the fundamental relation between LDOS and Green's function is [95, 149, 150]

$$g_{LDOS}\left(E\right) = -\frac{1}{\pi}\mathrm{Im}\left[\mathcal{G}\left(E\right)_{ii}\right] \tag{3.35}$$

from which several interesting quantities for transport properties, such as transmission, can be derived.

3.3 Optical properties of graphene and SWNTs

In this section the matrix elements for the electron-photon interaction for graphene and single-walled carbon nanotubes are derived from first order perturbation theory [96]. As anticipated, these elements together with the joint density of states are used for the calculation of the absorption spectra for the optically allowed transitions in the visible range which occur between the π bonding and the π^* antibonding molecular orbitals.

3.3.1 Electron-photon interaction and dipole approximation

The general form for the hamiltonian of a particle with charge *e* and mass *m* in an electromagnetic field with time-dependent vector potential $\mathbf{A}\left(t\right)$ and an external potential **V**,

such as the periodic crystal potential $V(\mathbf{r})$ is given by [121, 96]

$$H = \frac{1}{2m}\left[-\imath\hbar\nabla - e\mathbf{A}(t)\right]^2 + V(\mathbf{r}). \tag{3.36}$$

In the above expression the vector potential associated with the electomagnetic field acts as a time-dependent perturbation upon the eigenfunctions $\Psi^i(\mathbf{k})$ of the unperturbed crystal Hamiltonian $H_0 = -\frac{\hbar^2}{2m}\triangle + V(\mathbf{r})$. Neglecting the quadratic terms in $\mathbf{A}(t)^2$ and using the gauge $\nabla \cdot \mathbf{A}(t) = 0$ in the expansion of Eq. (3.36), the perturbative term acting on the electron and causing its transition from valence to conduction band is

$$H^{\lambda}_{pert} = \frac{\imath e\hbar}{m}\mathbf{A}^{\lambda}(t)\cdot\nabla \quad . \tag{3.37}$$

The vector potential associated with the quantized electromagnetic field can be expressed in second quantization formalism as [122]

$$\mathbf{A}^{\lambda}(\boldsymbol{\kappa},\mathbf{r},t) = \sqrt{\frac{\hbar}{2\kappa\kappa_0 V\omega(\boldsymbol{\kappa})}}\Big(\sqrt{n^{\lambda}(\boldsymbol{\kappa})}\exp(+\imath\boldsymbol{\kappa}\mathbf{r} - \imath\omega(\boldsymbol{\kappa})t)\mathbf{P}^{\lambda} + \sqrt{n^{\lambda}(\boldsymbol{\kappa})+1}\exp(-\imath\boldsymbol{\kappa}\mathbf{r} + \imath\omega(\boldsymbol{\kappa})t)\mathbf{P}^{\lambda *}\Big), \tag{3.38}$$

where κ is the dielectric constant of the material, κ_0 is the vacuum dielectric permittivity, *V* is the quantization volume for the electromagnetic field, $n^{\lambda}(\boldsymbol{\kappa})$ and $\omega(\boldsymbol{\kappa})$ are the photon occupation number and the photon frequency for wavevector $\boldsymbol{\kappa}$, respectively, and $\mathbf{P}^{\lambda}$ is the photon polarization vector. The "$+(-)$" sign in the frequency phase factors in Eq. (3.38) corresponds to the emission (absorption) of a photon with frequency ω. Within first-order perturbation theory, the general form for the matrix element for an optical transition from an initial state *i* at $\mathbf{k}_i$ to a final state *f* at $\mathbf{k}_f$ is obtained as

$$\begin{aligned} M^{f\lambda i}_{pert}(\mathbf{k}_f,\boldsymbol{\kappa},\mathbf{k}_i) &= \langle\Psi^f(\mathbf{k}_f,\mathbf{r},t)\,|H^{\lambda}_{pert}|\Psi^i(\mathbf{k}_i,\mathbf{r},t)\rangle \\ &= \langle\Psi^f(\mathbf{k}_f,\mathbf{r},t)\,|\frac{\imath e\hbar}{m}\mathbf{A}^{\lambda}(\boldsymbol{\kappa},\mathbf{r},t)\cdot\nabla|\Psi^i(\mathbf{k}_i,\mathbf{r},t)\rangle \end{aligned} \tag{3.39}$$

The spatial part of the above integral is expressed by the dipole vector

$$\mathbf{D}^{f\lambda i}(\mathbf{k}_f,\pm\boldsymbol{\kappa},\mathbf{k}_i) = \langle\Psi^f(\mathbf{k}_f,\mathbf{r})\,|\frac{\imath e\hbar}{m}\exp(\pm\imath\boldsymbol{\kappa}\mathbf{r})\nabla|\Psi^i(\mathbf{k}_i,\mathbf{r})\rangle. \tag{3.40}$$

In the dipole approximation, $\boldsymbol{\kappa}$ is neglected and is set $\boldsymbol{\kappa} = 0$, and the optical dipole transitions are vertical, $\mathbf{k}_i \equiv \mathbf{k}_f \equiv \mathbf{k}$. Therefore, the optical dipole transition matrix elements for the light absorption (A) and spontaneous emission (E) processes can be expressed as

$$M^{f\lambda i}(\mathbf{k}_f,\mathbf{k}_i) = \imath\frac{e\hbar}{m\omega}\sqrt{\frac{I}{2\sqrt{\kappa}\kappa_0 c}}\mathbf{P}^{\lambda}\cdot\mathbf{D}^{f\lambda i}(\mathbf{k}_f,\mathbf{k}_i), \tag{3.41}$$

where I is the radiant flux density of the light beam. Fermi's Golden Rule gives the transition probability between the initial state *i* and the final state *f* for the electron-photon interaction time τ of the perturbation

$$W^{f\lambda i}\left(\mathbf{k}_f,\mathbf{k}_i\right)=\frac{1}{\hbar^2\tau}|\int_0^\tau dt\, M^{f\lambda i}\left(\mathbf{k}_f,\mathbf{k}_i\right)|^2\propto \tag{3.42}$$
$$\propto |\mathbf{P}\cdot\mathbf{D}^{f\lambda i}\left(\mathbf{k}_f,\mathbf{k}_i\right)|^2\frac{\sin^2\left[\left(E^f\left(\mathbf{k}_f\right)-E^i\left(\mathbf{k}_i\right)\pm E^\lambda\right)\frac{\tau}{2\hbar}\right]}{\left(E^f\left(\mathbf{k}_f\right)-E^i\left(\mathbf{k}_i\right)\pm E^\lambda\right)^2}.$$

For long interaction time $\tau\rightarrow\infty$ the *sinc* function $\frac{\sin^2(\alpha t)}{\pi\alpha^2 t}\rightarrow\delta(\alpha)$. Therefore Eq. (3.42) expresses the energy conservation $E^f\left(\mathbf{k}_f\right)-E^i\left(\mathbf{k}_i\right)\pm E^\lambda=0$. In the following two sections we will show the expressions obtained in Refs. [122, 141, 121, 142, 144, 145] for the dipole vector of a graphene sheet and SWNTs, respectively. Also, we discuss the k-points in the BZ which are relevant for the optical absorption of these systems.

3.3.2 Dipole vector in graphene

As stated in the first part of this chapter, the features of the optoelectronic spectra of graphitic systems around the Fermi level are dominated by electrons with π character. Accordingly, the optical dipole transitions in the visible range occur between the π bonding and the π^* antibonding molecular orbitals. The dipole selection rules prohibit an optical transition within a $2p_z$ orbital at the same carbon atom, because of the odd symmetry of the transition dipole $\mathbf{D}^{fi}$ in *x*, *y* and *z*, whereas it is allowed between $2p_z$ orbitals on adjacent carbon atoms in graphene and SWNTs. Furthermore, even in the case of transition between nearest neighbor atoms, the *z*-component of $\mathbf{D}^{fi}$ is zero for all atomic matrix elements, since the *z*-component of $\mathbf{D}^{fi}$ has odd symmetry. Substituting the π-wavefunctions of Eq. (3.2) for valence and conduction bands, we get

$$\mathbf{D}_\pi^{cv}\left(\mathbf{k}_f,\mathbf{k}_i\right)=\langle\Psi^c\left(\mathbf{k}_f\right)|\nabla|\Psi^i\left(\mathbf{k}_i\right)\rangle= \tag{3.43}$$
$$=c_B^{c*}\left(\mathbf{k}_f\right)c_A^v\left(\mathbf{k}_i\right)\langle\Phi_B\left(\mathbf{k}_f,\mathbf{r}\right)|\nabla|\Phi_A\left(\mathbf{k}_i,\mathbf{r}\right)\rangle+c_A^{c*}\left(\mathbf{k}_f\right)c_B^v\left(\mathbf{k}_i\right)\langle\Phi_A\left(\mathbf{k}_f,\mathbf{r}\right)|\nabla|\Phi_B\left(\mathbf{k}_i,\mathbf{r}\right)\rangle.$$

Expressing the Bloch sums for the $2p_z$ orbitals centered at A and B sites as in Eq. (3.3) and splitting the coordinates of all atoms over the A and B sublattices, we obtain

$$\mathbf{D}_\pi^{cv}\left(\mathbf{k}_c,\mathbf{k}_v\right)=\frac{1}{U}\sum_{i=0}^{U-1}\sum_{l=1}^{3}\left[c_B^{c*}\left(\mathbf{k}_f\right)c_A^v\left(\mathbf{k}_i\right)\exp\left[\imath\left(\mathbf{k}_i-\mathbf{k}_f\right)\cdot\mathbf{R}_A^i\right]\times\right. \tag{3.44}$$
$$\times\exp\left(-\imath\mathbf{k}_f\cdot\mathbf{r}_A^l\right)\langle\varphi\left(\mathbf{r}-\mathbf{r}_A^l\right)|\nabla|\varphi\left(\mathbf{r}\right)\rangle+$$
$$\left.+c_A^{c*}\left(\mathbf{k}_f\right)c_B^v\left(\mathbf{k}_i\right)\exp\left[\imath\left(\mathbf{k}_i-\mathbf{k}_f\right)\cdot\mathbf{R}_B^i\right]\exp\left(-\imath\mathbf{k}_f\cdot\mathbf{r}_B^l\right)\langle\varphi\left(\mathbf{r}-\mathbf{r}_B^l\right)|\nabla|\varphi\left(\mathbf{r}\right)\rangle\right]$$

where we have introduced the vector $\mathbf{r}_A^l\left(\mathbf{r}_B^l\right)$, which connects nearest neighbour atoms starting from an A (B) atom and defined as

$$\mathbf{R}_A^i=\mathbf{R}_B^i+\mathbf{r}_B^l,\qquad\mathbf{R}_B^i=\mathbf{R}_A^i+\mathbf{r}_A^l,\qquad(l=1,2,3). \tag{3.45}$$

For vertical transitions the selection rule $\mathbf{k}_i \equiv \mathbf{k}_f \equiv \mathbf{k}$, so the exponential phase factors $\exp\left[\imath\left(\mathbf{k}_i - \mathbf{k}_f\right)\cdot\mathbf{R}_B^i\right]$ are equal to one and Eq. (3.44) is simply given by

$$\mathbf{D}^{cv}\left(k\right) = \langle\Psi^c\left(\mathbf{k}\right)|\nabla|\Psi^v\left(\mathbf{k}\right)\rangle. \tag{3.46}$$

The atomic dipole vectors for the $s = A, B$ sublattices are defined as [141, 121, 122]

$$\mathbf{d}_{\mathbf{r}_s^l} = \int \varphi^*\left(\mathbf{r} - \mathbf{r}_s^l\right)\nabla\varphi\left(\mathbf{r}\right)\, d\mathbf{r} = -\frac{m_{\mathrm{opt}}\mathbf{r}_s^l}{|\mathbf{r}_s^l|}. \tag{3.47}$$

For dipole transitions involving only first nearest neighbor interactions $|\mathbf{r}_s^l| = a/\sqrt{3}$. An important consequence of the assumption introduced with Eq. (3.47) is that the contribution to the susceptibility coming from two orbitals placed on the same atom can be neglected [101]. This is a reasonable approximation because the polarisability of a free atom is much smaller than that of the corresponding material. Since Eq. (3.47) involves the product between localized atomic wavefunctions and its derivative, which decreases quickly with increasing distance between atoms, it's sufficient considering only nearest neighbour coupling, as already assumed for the electronic dispersion relation. m_{opt} is the atomic matrix element for nearest neighbour carbon pairs and is defined as

$$m_{\mathrm{opt}} = \langle\varphi\left(\mathbf{r} - \mathbf{r}_s^l\right)|\frac{\partial}{\partial x}|\varphi\left(\mathbf{r}\right)\rangle. \tag{3.48}$$

Usually, the value of m_{opt} is obtained analytically from Gaussian functions fitted to the $2p_z$ wavefunctions previously obtained by a LDA calculation [121, 140]. The estimate obtained in Ref. [121] gives $m_{\mathrm{opt}} = 0.21\,[\mathrm{a.u.}]^{-1}$ (1 atomic unit is $0.529\,\text{Å}$). Other estimates obtained in Refs. [122, 152] give similar values. However, it's not particularly relevant to know the exact value of this parameter, as it can be considered simply a constant to normalize the resulting values of the dipole matrix elements [151]. Thus the graphene dipole vector of Eq. (3.44) for vertical transitions and nearest neighbour coupling can be written in extended form as

$$\begin{aligned}\mathbf{D}^{cv}\left(\mathbf{k}\right) &= -\frac{\sqrt{3}m_{\mathrm{opt}}}{a}\left[c_B^{c*}c_A^v\sum_l^3\exp\left(\imath\mathbf{k}\cdot\mathbf{r}_A^l\right)\mathbf{r}_A^l + c_A^{c*}c_B^v\sum_l^3\exp\left(\imath\mathbf{k}\cdot\mathbf{r}_B^l\right)\mathbf{r}_B^l\right] \\ &= c_B^{c*}c_A^v\mathbf{d}_A\left(\mathbf{k}\right) + c_A^{c*}c_B^v\mathbf{d}_B\left(\mathbf{k}\right)\end{aligned}. \tag{3.49}$$

By simmetry considerations upon the sign of the wavefunctions coefficients, it follows that $c_A^{c*}c_B^v = -\left(c_B^{c*}c_A^v\right)^*$. Moreover, the following relation for the atomic dipole vectors holds: $\mathbf{d}_A\left(\mathbf{k}\right)^* = -\mathbf{d}_B\left(\mathbf{k}\right)$. Therefore, Eq. (3.49) can be cast in the following shortened form:

$$\mathbf{D}^{cv}\left(\mathbf{k}\right) = -\frac{2\sqrt{3}m_{\mathrm{opt}}}{a}\mathrm{Re}\left[c_B^{c*}\left(\mathbf{k}\right)c_A^v\left(\mathbf{k}\right)\sum_l^3\exp\left(\imath\mathbf{k}\cdot\mathbf{r}_A^l\right)\mathbf{r}_A^l\right] \tag{3.50}$$

Eq. (3.50) asserts that $\mathbf{D}^{cv}(\mathbf{k})$ is a real vector, whose direction depends on $\mathbf{k}$. Therefore, one can always find a polarization vector $\mathbf{P}$, which is perpendicular to $\mathbf{D}^{cv}$ and which prevents some special k points from contributing to the optical absorption $W(\mathbf{k})$. Refs.[142, 143] shows that nodes in the optical absorption around the $\mathbf{K}$ and $\mathbf{K}'$ points arise in graphene as a consequence of the linear electronic dispersion relation around the Fermi and the mutual orthogonality relation between the light polarization vector $\mathbf{P}$ and the real-valued dipole vector $\mathbf{D}^{cv}(\mathbf{k})$. This characteristic is unique to graphene and can be observed in optical experiments on graphite nanoribbons. In conventional semiconductors the leading term in the energy dispersion relations are quadratic in k_x and k_y, therefore nodes in $W(\mathbf{k})$ cannot be observed in these materials. In Fig. 3.9 the plot of the vectorial field of $\mathbf{D}^{cv}$ on the 2D BZ is shown together with the contour plot of the oscillator strength $O(\mathbf{k}) = \sqrt{\mathbf{D}^{cv*}(\mathbf{k}) \cdot \mathbf{D}^{cv}(\mathbf{k})}$ in units of m_{opt}. Around the Dirac points, $\mathbf{D}^{cv}$ runs parallel to the equi-energy contour: around the $\mathbf{K}$ point the rotational direction is clockwise, around $\mathbf{K}'$ is counterclockwise. The oscillator strength has a minimum at $\mathbf{\Gamma}$ point and reaches its maximum value at $\mathbf{M}$ points, although it's considerable large also around the $\mathbf{K}$ and $\mathbf{K}'$ points, which are relevant for the electronic properties. This point will be extremely important for the discussion of the dependence of $\mathbf{D}^{cv}$ on $\mathbf{k}$ for single-walled nanotubes in the following section and its relation to the critical wavevectors for the electronic DOS.

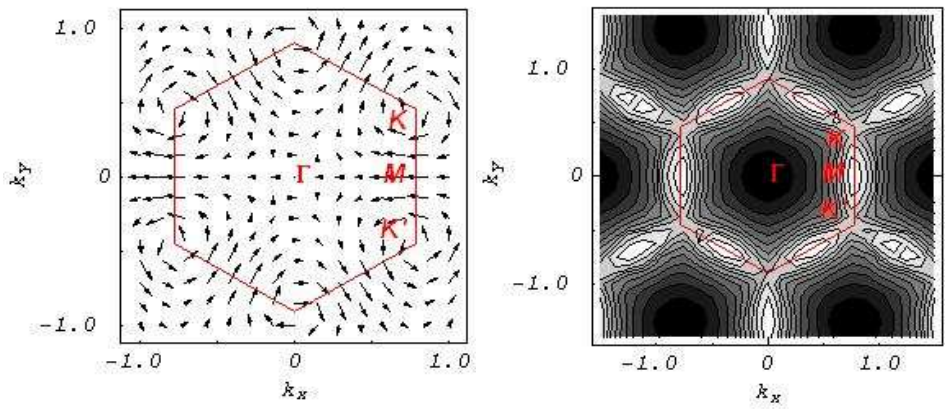

Fig. 3.9: Vectorial field of transition dipole vector (left) and contour plot of oscillator strength (right) in graphene. Calculations reproduced from Ref. [121] with Mathematica® 5.2.

3.3.3 Dipole vector in SWNTs

In order to obtain the optical dipole matrix element for SWNTs one can follow a treatment similar to that delined for graphene, as explained in Refs. [141, 143]. In this case, one needs to place the atomic dipole vectors $\mathbf{d}_s(\mathbf{k})$ on the cylindrical surface of the nanotube sidewall. This task can be accomplished by applying to the nearest-neighbor interatomic vectors $\mathbf{r}_s^l$ of $\mathbf{d}_s$ the rotation operators Ω of Eq. (2.20), introduced in Chapter 2.4.1. Actually, the operator Ω cannot be applied to the nearest-neighbor vectors $\mathbf{r}_s^l$ of the exponential phase factors of Eq. (3.49), since they are multiplied by the wavevectors $\mathbf{k}_f$ and $\mathbf{k}_i$ of the 2D reciprocal space of the unrolled graphene layer, according to the zone folding scheme. Moreover, curvature effects on the atomic dipole matrix element due to the cylindrical sidewall of the nanotube are neglected and the factor m_{opt} is the same used for graphene. Therefore, we have

$$\mathbf{D}^{cv}(\mathbf{k}) = \frac{\sqrt{3}m_{\text{opt}}}{aNU}\left[c_B^{c*}c_A^v\sum_{u=1}^{U}\sum_{h=1}^{N}e^{\imath\left(\mathbf{k}_i-\mathbf{k}_f\right)\cdot\mathbf{R}_{h,A}^u}\mathbf{d}_{hA} + c_A^{c*}c_B^v\sum_{u=1}^{U}\sum_{h=1}^{N}e^{\imath\left(\mathbf{k}_i-\mathbf{k}_f\right)\cdot\mathbf{R}_{h,B}^u}\mathbf{d}_{hB}\right] \tag{3.51}$$

where $\mathbf{d}_{hA}$ and $\mathbf{d}_{hB}$ are the rotated atomic dipole vectors for optical transitions from the *A* atom in the *h*th hexagon to its neighboring *B* atoms, and from the *B* atom in the *h*th hexagon to its neighboring *A* atoms, respectively. The general expressions for the rotatetd atomic dipole vectors $\mathbf{d}_{h,s}$ $(h = 1,\ldots,N \text{ and } s = A,B)$ are

$$\mathbf{d}_{hs} = \Omega_z\left(\Theta\varphi_{h,s}\right)\mathbf{d}_s, \tag{3.52}$$

$$\mathbf{d}_s = \sum_{l=1}^{3}\exp\left(-\imath\mathbf{k}_f\cdot\mathbf{r}_s^l\right)\Omega_y\left(\frac{\pi}{6}-\theta\right)\Omega_x\left(\frac{\pi}{2}\right)\mathbf{r}_s^l,$$

where for $\varphi_{h,s}$ we have used the expression given in Eq. (2.21). $\mathbf{d}_s$ $(s = A,B)$ are the atomic dipole vectors in the unrolled graphene layer and can be written explicitly as

$$\mathbf{d}_A = (d_x, 0, d_z) \qquad \text{and} \qquad \mathbf{d}_B = \qquad (-d_x^*, 0, -d_z^*)\,. \tag{3.53}$$

According to Eq. (3.52), the explicit expressions for $\mathbf{d}_{hA}$ and $\mathbf{d}_{hB}$ then become

$$\begin{aligned}\mathbf{d}_{hA} &= \left(\cos\left(\varphi_{hA}\right)d_x, \Theta\sin\left(\varphi_{hA}\right)d_x, d_z\right)\\ \mathbf{d}_{hB} &= \left(-\cos\left(\varphi_{hB}\right)d_x^*, -\Theta\sin\left(\varphi_{hB}\right)d_x^*, -d_z^*\right)\end{aligned} \tag{3.54}$$

3.3.4 Dipole selection rules in SWNTs

Now we discuss the selection rules for general transitions involving valence and conduction bands within the zone-folding scheme applied to SWNTs. Even including curvature effects, these selection rules aren't affected in any way. First we define the change in azimuthal index (cutting-line) $\Delta\mu = \mu_f - \mu_i$ and axial wavevector $\Delta k_z = k_{zf} - k_{zi}$. The

change in total wavevector is thus $\mathbf{k}_i - \mathbf{k}_f = -\Delta\mu\mathbf{K}_1 - \Delta k_z\mathbf{K}_2/U$. Then $\mathbf{k}_i - \mathbf{k}_f$ and $\mathbf{R}_{hs}^u$ as given in Eq. (2.19) are substituted into Eq. (3.51). The summation over the SWNT unit cells *u* can be factored out in the form $\sum_{u=1}^{U} \exp\left[-\imath\left(\Delta\mu\mathbf{K}_1 + \Delta k_z\mathbf{K}_2/U\right)\cdot u\mathbf{T}\right]$. By using the relations between nanotube real and reciprocal lattice vectors as given in Eq. (2.10), the previous sum over *u* becomes $\sum_{u=1}^{U} \exp\left[-\imath\left(2\pi u/U\right)\Delta k_z\right]$, which is equal to zero except for $\Delta k_z = 0$, where in such case the sum gives *U*. Thus the first selection rule for the electronic wavevector along the SWNT axis is obtained as $\Delta k_z = 0$. In order to obtain the selection rule for the cutting line index μ, a more involved procedure is necessary. First we have to perform the summation over the graphene unit cells inside the SWNT unit cell, labelled by the index *h*. The phase factors of Eq. (3.51) can be simplified to the form $\exp\left[-\imath\Delta\mu\mathbf{K}_1\cdot\left(h\mathbf{R} - \mathbf{r}_s^1/2\right)\right]$. Substituting the symmetry vector $N\mathbf{R} = \mathbf{C}_h + M\mathbf{T}$ and using again the relations of Eq. (2.10), we obtain $\exp\left[-\imath\Delta\mu 2\pi h/N + \imath\Delta\mu\mathbf{K}_1\cdot\mathbf{r}_s^1/2\right]$, where $\mathbf{K}_1\cdot\mathbf{r}_s^1 = \varphi_s^1$. By writing the $\cos\left(\varphi_{hs}\right)$ and $\sin\left(\varphi_{hs}\right)$ terms of Eq. (3.54) into sums and differences of complex exponentials, the general expressions for the *x, y, z* components of the nanotube dipole vector **D** can be obtained as

$$\begin{aligned} D_x &= \frac{1}{2}\left(C_{+1}S_{+1} + C_{-1}S_{-1}\right), \\ D_y &= \Theta\frac{1}{2\imath}\left(C_{+1}S_{+1} - C_{-1}S_{-1}\right), \\ D_z &= C_0 S_0\ , \end{aligned} \tag{3.55}$$

where the terms $S_l, C_0, C_{\pm1}$ are defined as in the following:

$$\begin{aligned} S_l &= \frac{1}{N}\sum_{h=1}^{N} \exp -\imath\left(\Delta\mu - l\right)2\pi h/N \\ C_0 &= \frac{\sqrt{3}m_{\text{opt}}}{a}\left[c_B^{f*}c_A^i d_z\xi_0 - c_A^{f*}c_B^i d_z^*\xi_0^*\right] \\ C_{\pm1} &= \frac{\sqrt{3}m_{\text{opt}}}{a}\left[c_B^{f*}c_A^i d_x\xi_{\pm1} - c_A^{f*}c_B^i d_x^*\xi_{\pm1}^*\right] \\ \xi_l &= \exp\imath\left(\Delta\mu - l\right)\varphi_A^1/2 \end{aligned} \tag{3.56}$$

We recall that the optical matrix element, as defined in Eq. (3.41), is proportional to the scalar product of the light polarization vector $\mathbf{P}_\rho$ $(\rho = A, E)$ and the dipole vector given by Eq. (3.55). From this equation one can see that the light polarized parallel to the SWNT axis $(\mathbf{P}_\rho = \hat{\mathbf{z}})$ selects the term S_0 in the matrix element, while the light polarized perpendicular to the SWNT axis $(\mathbf{P}_\rho = \hat{\mathbf{x}}$ or $\hat{\mathbf{y}})$ selects the terms S_{+1} and S_{-1}. The presence of the term S_l $(l = 0, \pm1)$ implies the azimuthal optical selection rule $\Delta\mu = l$, which can also be expressed explicitly as $\mu \rightarrow \mu + l$. Thus the dipole selection rules for

interband optical transitions in SWNTs and linearly polarized light are:

$$\begin{aligned} \Delta\mu = 0 \quad &\text{for parallel polarization} \quad \mathbf{P}\|\hat{\mathbf{z}} \\ \Delta\mu = \pm 1 \quad &\text{for perpendicular polarization} \quad \mathbf{P}\|\hat{\mathbf{x}} \text{ or } \hat{\mathbf{y}}. \end{aligned} \tag{3.57}$$

These rules were formerly derived by Ajiki and Ando [139], who additionally discussed the role of depolarization effects in suppressing almost completely the perpendicular polarized component in real optical absorption experiments due to self-consistent screening effects. Therefore, in order to analize the optical absorption spectra of SWNTs one is usually interested into the selection rules for light polarized parallel to the SWNT axis and optical dipole vector between initial state *i* and final state *f* is found expressed with the *z*-component highlighted as

$$\mathbf{D}^{fi}\left(\mathbf{k}_f, \mathbf{k}_i\right) = \left\langle \Psi_f\left(\mathbf{k}_f\right) \left| \nabla_z \right| \Psi_i\left(\mathbf{k}_f\right) \right\rangle \tag{3.58}$$

Actually for our purposes in the following chapter, we will take into account only this component. However, in spite of the depolarization effects, the predicted selection rules could be confirmed experimentally by Resonance Raman Spectroscopy studies on isolated SWNTs when changing the light polarization vector [153]. Selection rules for circularly polarized were also obtained [141], which are important for understanding other effects such as circular dichroism and birefringence in chiral SWNTs, but they will not be considered in this thesis.

3.3.5 SWNT optical matrix elements and critical wavevectors

In order to study the profile of the optical dipole matrix elements over the SWNT Brillouin zone and extract information about general trends for different chiralities and special k wavevectors, analytical expression for these matrix elements have also been derived by several authors, which are actually easier to evaluate and plot than Eq. (3.51). Here, for consistency with the previous notation, we consider the analytical expression obtained in the work of J. Jiang, A. Grüneis *et al.* [144] for the *z*-component of the optical matrix element for a single-walled nanotube of any (m, n) chirality. Similar results and conclusions follow also from other authors [145, 148]. In order to obtain this expression within the zone-folding scheme from the expression for graphene dipole vector of Eq. (3.49), one has to consider that:

- all A (B) atoms have the same *z* component of the atomic dipole vectors $\mathbf{d}_{gA}$ $(\mathbf{d}_{gB})$,
- each of the three nearest-neighbor atoms has the same relative coordinate from the original atoms,
- the directions of these nearest-neighbor atoms are determined only by the chiral angle θ by which the graphene sheet is wrapped into a SWNT (see Fig. 3.10).

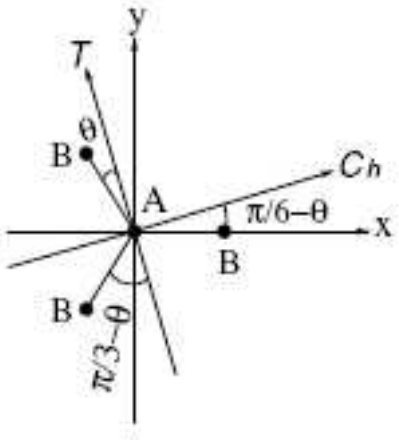

Fig. 3.10: The positions for an A atom at the origin and its three nearest neighbor B atoms. The angles between these bonds and the chiral vector $\mathbf{C}_h$ and translation $\mathbf{T}$ vectors are also shown. Picture taken from Ref. [144].

As a consequence, the functions $d_{g,z}^{A}$ and $d_{g,z}^{B}$ are dependent only on the projection angle $\vartheta_l\left(\theta\right)$,

$$d_{g,z}^{A}\left(\theta\right)=\sum_{l=1}^{3}\exp\left(\imath\mathbf{k}\cdot\mathbf{r}_{A}^{l}\right)\mathbf{r}^{l}\vartheta^{l}=\frac{a}{\sqrt{3}}\left[-\exp\left(\frac{\imath k_{x}a}{\sqrt{3}}\right)\sin\left(\frac{\pi}{6}-\theta\right)\right. \tag{3.59}$$
$$\left.+\exp\left(-\frac{\imath k_{x}a}{2\sqrt{3}}+\frac{\imath k_{y}a}{2}\right)\cos\theta-\exp\left(-\frac{\imath k_{x}a}{2\sqrt{3}}-\frac{\imath k_{y}a}{2}\right)\cos\left(\frac{\pi}{3}-\theta\right)\right],$$
$$d_{g,z}^{B}\left(\theta\right)=-d_{g,z}^{A*}\left(\theta\right).$$

Substituting the expressions given in Eq. (3.59) together with the eigenvectors of Eq. (3.18) into Eq. (3.50), the *z* component of the dipole vector for the unrolled nanotube unit cell on the 2D BZ of graphene is given in analytical form by

$$D_{z}\left(\mathbf{k}\right)=\frac{m_{\mathrm{opt}}\delta_{k_{z},k_{z}'}\delta_{\mu,\mu'}}{2w\left(\mathbf{k}\right)}\left[\sin\left(\frac{\pi}{6}-\theta\right)\times\left\{\cos k_{y}a-\cos\frac{k_{y}a}{2}\cos\frac{\sqrt{3}k_{x}a}{2}\right\}\right. \tag{3.60}$$
$$\left.+\sqrt{3}\cos\left(\frac{\pi}{6}-\theta\right)\sin\frac{\sqrt{3}k_{x}a}{2}\sin\frac{k_{y}a}{2}\right]$$

One can see that this expression includes the dependence of the dipole vector on both $\mathbf{k}$ wavevector and chiral angle θ in addition to the selection rules for parallel polarization of the light. One can see immediately from Eq. (3.60) that $D_z=0$ at the $\mathbf{\Gamma}$ point and at the Dirac points $\mathbf{K}$ and $\mathbf{K}'$. In Fig. 3.11 contour plots of $D_z\left(\mathbf{k}\right)$, over the 2D hexagonal BZ

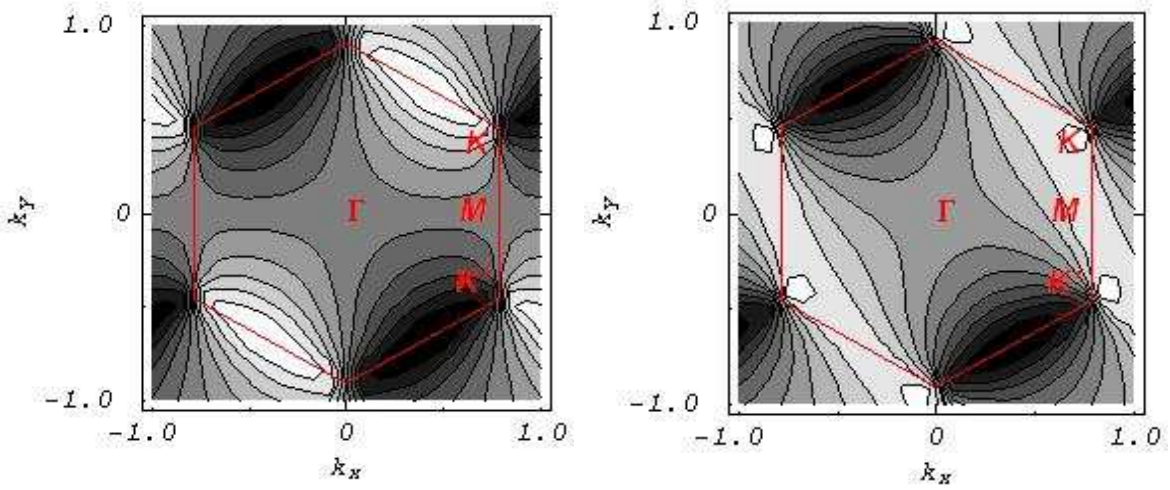

Fig. 3.11: Contour plot over the 2D BZ of the value of the dipole vector parallel to the SWNT axis for an armchair (left) and zigzag (right) SWNT. D_z is zero at the corners of the BZ. White and black colours mean (strongly) positive and negative values of D_z, respectively, while an intermediate gray level means that a sign change in D_z occurs. Calculations reproduced from Ref. [144] with Mathematica® 5.2.

are shown for zigzag and armchair nanotubes, respectively.
By superimposing the cutting lines on these contour plots, with the aid of Eq. (2.13), one obtains the dependence of D_z over the 1D nanotube BZ for a given band or cutting line μ, as shown in Fig. 3.12. For armchair SWNTs, Eq. (3.60) gives $D_z = 0$ for $k_x = 0$ or $k_y = 0$. Moreover, for all interband transitions $D_z = 0$ at $k_z = 0$. Also, $D_z = 0$ for all k_z values for the two optical transition connecting non-degenerate A-symmetry bands $(0 \rightarrow 0)$ and $(5 \rightarrow 5)$. Note that in (n, n) SWNTs, the cutting lines (which are also parallel to k_y and $\mathbf{K}_2$) with index $\mu = n$ always cross the $\mathbf{K}$ or $\mathbf{K}'$ point. Actually, these cutting-lines are parallel to the $\mathbf{K} - \mathbf{M} - \mathbf{K}'$ edge of the hexagonal 2D BZ. Thus, we can draw the conclusion that at the Fermi level $D_z = 0$ for armchair nanotubes. For zigzag metallic nanotubes, the situation is similar, with $D_z = 0$ at the Fermi level and close to zero in the proximity, whereas for semiconducting zigzag nanotubes $D_z \neq 0$. The reasons why D_z is vanishing near the Fermi level for metallic nanotubes are as follows. We recall that for graphite, around the Dirac points $\mathbf{K}$ and $\mathbf{K}'$ of the 2D BZ, there are nodes in the optical absorption, which lie one a line crossing the Dirac point and parallel to the light polarization direction. When the graphene layer is rolled up into a nanotube, the nanotube axis is parallel to the cutting lines. Thus, for light polarization parallel to the nanotube axis, if there is a cutting line crossing the $\mathbf{K}$ point, as it happens with

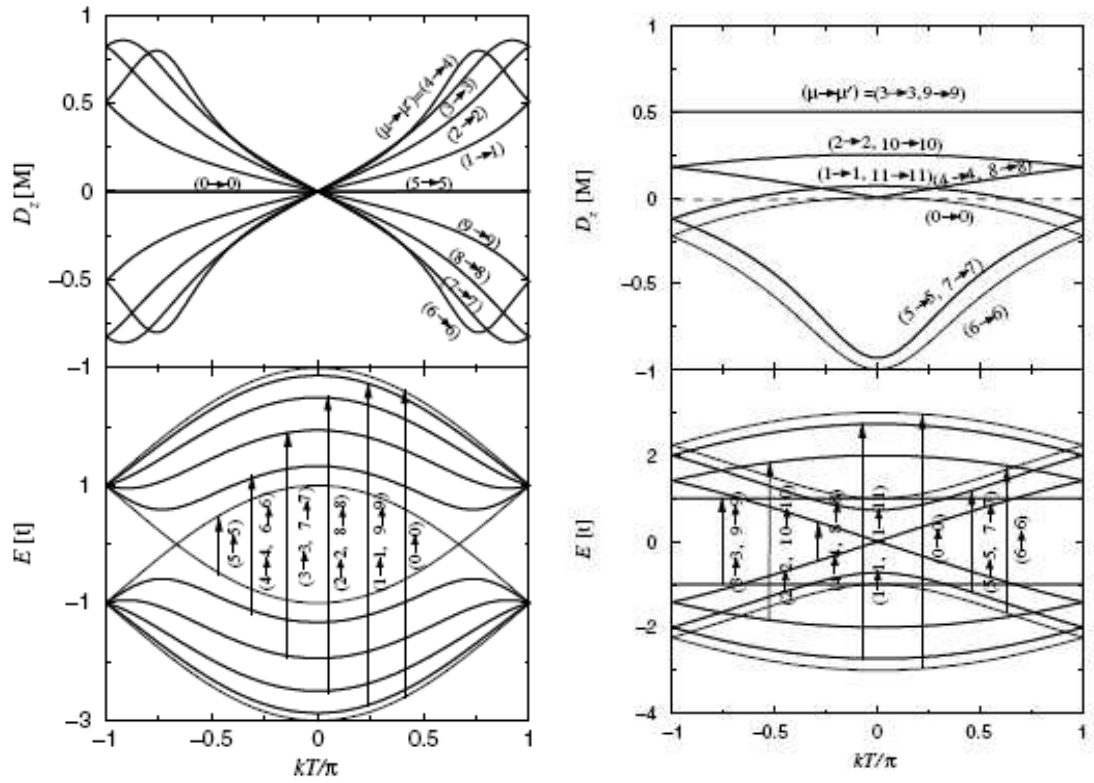

Fig. 3.12: Dependence of the dipole vector component D_z and energy E on the 1D wave vector k_z for an armchair (5,5) (left) and a zigzag (6, 0) nanotube (right) for various interband optical transitions for parallel polarization of the light. Taken from Ref. [144].

metallic nanotubes, then there is no optical absorption for the involved k-point. For the purposes of this thesis, however, it is important to notice that in zigzag nanotubes D_z has maximum absolute values at k_z values of the 1D wavevector of each μ-th band where van Hove singularities occur, that is the critical wavevector $(\mu, k_z = 0)$. Thus, one draws the conclusion that the strong optical absorption in zigzag SWNTs is due not only to a singularity in the joint density of states but also to the maximum matrix element value at the same vHs. The 2D contour plots of D_z of Fig. 3.11 show also other interesting features. For all nanotube geometries except the armchair one, it is seen that, for vHs away from the **K** point, $|D_z|$ values at the vHs decrease inside the BZ and increase outside (Fig. 3.11 right). For armchair nanotubes, Fig. 3.11 (left) shows that $|D_z|$ has a mirror simmetry with respect to the $\mathbf{K} - \mathbf{M} - \mathbf{K}'$ line. Thus, $|D_z|$ values near a vHs away from the **K** point will increase as we move away from the vHs on both sides of the singularity. In Fig. 3.13 values of $|D_z|$ calculated at the first, second, third vHs (the so called E_{11}, E_{22}, E_{33}) are shown for semiconducting nanotubes as a function of the chiral

angle θ of the corresponding SWNTs. The main result is that we have distinct optical properties for semiconducting tubes of type S1 (or I) (Fig. 3.13 b) and S2 (or II) (Fig. 3.13 a), as anticipated in Sect.3.2.2. For type S1 semiconducting nanotubes, the second and third vHs points are inside and outside the BZ, respectively. Consequently, the D_z values at the second vHs will decrease inside the BZ and the third vHs will increase outside the BZ. E_{22} transitions will have smaller $|D_z|$ values than E_{33} transitions. For type S2 semiconducting nanotubes the situation is specular. Moreover, it can be noticed that $|D_z|$ for the E_{11} transitions has a weaker chiral index dependence compared with that of the E_{22} and E_{33} transitions. Finally, we observe that, in the region of lower chiral angle, the D_z values have larger differences among the E_{11}, E_{22} and E_{33} transitions, while the differences become very small when the chiral angle approaches $\pi/6$ (armchair tubes).

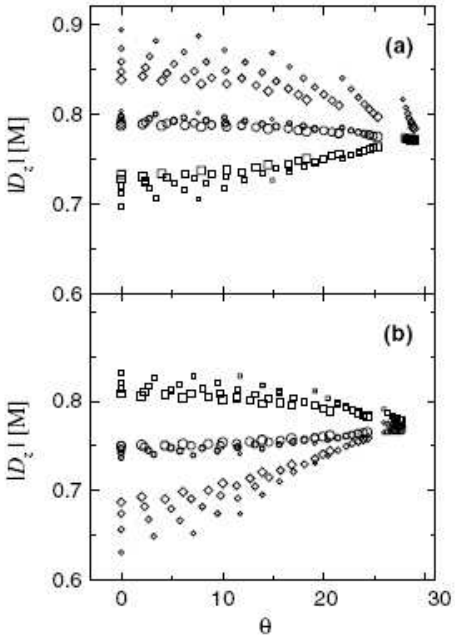

Fig. 3.13: $|D_z|$ dependence on chiral index for (b) type S1 (or I) and (a) type S2 (or II) semiconducting nanotubes. The nanotube diameter is in the region of $1\,\mathrm{nm} < d_t < 2\,\mathrm{nm}$. Circle, square and diamond points denote, respectively, data for E_{11}, E_{22}, and E_{33} transitions. The size of the symbols represents the magnitude of the nanotube diameter. Figure taken from Ref. [144]. Be aware that the convention used throughout this paper for semiconducting SWNTs of type S1 and S2 is $\mathrm{mod}\,(n-m,3)$, which is different from that adopted in this thesis (see Sect. 3.2.1).

In conclusion, it can be stated that in order to calculate correctly and understand the optical absorption features of a SWNT, one has to consider carefully both the van Hove

singularities in the joint density of states and the behaviour of the optical absorption matrix elements at the critical wavevectors which give vHs. If the optical dipole matrix element at the critical k point is zero, the transition will be forbidden and therefore the contribution of the vHs to the absorption spectrum will be suppressed; otherwise, the transition will be dipole-allowed and the intensity of the optical absorption peak will be proportional to the absolute square of the respective optical matrix element.

3.4 Summary

In this section a general review of the zone-folding method applied to the tight-binding calculation of the electronic and optical properties of single-walled nanotubes was given, according to the most relevant scientific results published in nanotube literature. Particular attention was dedicated to the analysis of the Brillouin zone for understanding the relevant k-points which determines the basic features of the SWNT optoelectronic spectra, according to the different SWNT chiralities. The result recalled in this analysis will be of fundamental importance for understanding the choices made in the following chapters, which present the original work developed in this thesis.

Chapter 4

Small crystal approach

In the previous chapter the general principles behind the tight-binding framework and the zone-folding technique were introduced for calculating the electronic and optical properties of graphene and single-walled carbon nanotubes from a reciprocal space point of view. In this section we re-obtain those properties from a real space point of view by applying the so called small crystal approach to SWNTs. Then we show how several issues of actual interest both in experimental and theoretical nanotube science can be easily treated by this method. Note that the validity of the theoretical treatment presented in this chapter is quite general and can be applied to nanotubes of any chiralities. The examples and calculations presented in the present chapter and in the chapter about DWNTs are referred to zigzag nanotubes just for convenience reasons, but can be as well extended to other nanotube geometries. The importance of the choice of zigzag geometry is essential for the developments shown in the chapter about many-body effects, where the choice is crucial both for the computational feasibility of the problem with our computer resources.

4.1 Basic facts behind the Small Crystal Approch

Many calculations in solid state physics, either by perturbative techniques or variational approach, involve the averaging over the Brillouin zone of a periodic function. Such calculations are often very complicated and computationally demanding, as they require in principle the knowledge of the value of the function at each k-point in the Brillouin zone. In practice the functional values are known or determined over a set of points in the zone and the values at the other points are found by using various type of approximations and interpolation methods. To obtain sufficient accuracy in these calculations, it is necessary in general to know the functional values over a large set of points. Thus the choice of the sampling grid of the first Brillouin zone of a periodic system is extremely important for the accurate prediction of the electronic and vibrational properties of the system. On the other hand, the computational effort in memory and time increases as the spacing of the sampling grid is reduced. However, it has to be pointed out that not all the k-points chosen

for the sampling contribute significatively to the computed property. For example, in the previous chapter, we saw that the van Hove singularities dominate the optical spectra of SWNTs and that the main contribution to the vHs spikes is given by those k-points which lie exactly on or close to the extrema of the dispersion curves, where the inverse derivative and, hence, the DOS diverges. Techniques for sampling systematically the BZ have been developed; they determine special sets of wavevector points in the BZ, which are most *efficient* in calculating the averages of the periodic functions. By *efficient* in this case one means determining the average of a function to an arbitrary degree of accuracy with the least number of sampled wavevector points [94, 99, 100]. Thus, in general, one would like to find out a method to get those few special k-points which allow the most accurate description of the investigated property of the extended system. As Falicov pointed out, however, regardless of the technique, sampling in a set of N points in reciprocal space is always essentially equivalent to solving the problem in real space in a minicrystal of N sites with periodic boundary conditions [91]. The real space method adopted in this work takes advantage of this finite sampling - finite cluster duality. By a finite sampling of N points in reciprocal space, the problem can be reduced to the study in real space of a cluster with N sites and periodic boundary conditions. Hence the nomenclature *small crystal* (SC) approach. Periodic boundary conditions employed in the SC approach guarantee that the discrete spectrum obtained for the periodic solid system gives the correct band-structure energies at the selected symmetry points. There are no boundaries or surfaces in this formalism, and the correct Bloch states are obtained. Moreover, by exploiting the presence of symmetry in the system, the problem is reduced to situations in which it can be solved sometimes even exactly, with symbolic solutions [103]. It should be noticed that the present formalism is not equivalent to usual cluster-type calculations typical of quantum-chemical approaches. There, a large molecule or free-standing cluster yields a discrete electronic spectrum that bears little resemblance to solid (see for instance in the case of zigzag carbon nanotubes Ref. [134]). SC models have already been successfully used to solve a variety of problems, ranging from tight-binding calculations to many-body problems, including the Hubbard model applied to several different model [105, 106] and real systems, including 1D systems (charge transfer salts, polyacetilene) [108, 109, 110, 111, 112, 113, 114], semiconductor compounds [107], metallic alloys and heavy fermion systems [104].

In the next paragraph we show how this real space approach works for simpler toy models in the tight-binding approximation (TBA), namely the (infinite) 1D periodic chain and the 2D square lattice. Then the case of a single-walled nanotube will be examined in detail and the comparison with the zone-folding method will be established. Finally, an expression for the optical matrix elements relevant for SWNTs will be obtained on the basis of this approach, which will be used for calculating the optical spectra of these systems.

4.2 SC approach applied to simple 1D and 2D models

In Chapter 3 we introduced for SWNTs the general theory of the so called Tight-Binding Approximation (TBA). We recall here that the basic assumption in TBA is the use of atomic-like orbitals as basis for expanding the crystal wavefunctions. Now, to understand how to apply the SC approach to carbon nanotubes in TBA approximation, we consider first the simplest possible case, a linear periodic chain of atoms. First we will derive the the electronic energy band dispersion for this system from a reciprocal-space diagonalization of the TB hamiltonian. Then, the generalization to a two-dimensional square lattice will be performed. We follow the usual treatment reported in most theoretical solid-state textbooks, such as Ref. [94]. Finally, the real-space diagonalization of the hamiltonian, put in real-space form, will be performed for these systems and the connection between both approaches will be established.

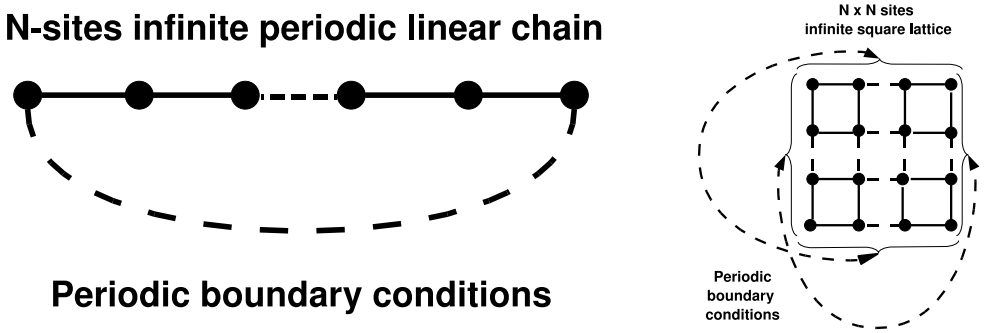

Fig. 4.1: Periodic linear chain (left) and square lattice (right).

4.2.1 Reciprocal space diagonalization

In the simplest approximation, we assume that the linear chain has only one type of atom and only one orbital associated with each atom. The first step is the construction of the crystal wavefunctions as done for the general case of Chapter 3. Because of the simplicity of the model, there are no summations over the orbital type indices *l* (i.e. there is only one type of orbital for each atom indexed as *l*) and over atoms per unit cell indices *i* (i.e. there is only one atom per unit cell). The basis for the crystal wavefunctions in this case will be

$$\chi_{k,l}(x) = \sum_{n=-\infty}^{\infty} e^{ikx}\phi_l(x - na) \tag{4.1}$$

where the notation has been further simplified since we are dealing with a 1D example: the position vector **r** has been set equal to the position *x* on the 1D axis, the reciprocal-space vector **k** has been set equal to *k*, while the lattice vectors **R** are given by *na*, with *a*

lattice constant and *n* integer number [94]. The atomic wavefunctions $\phi_l(x)$ have either *s*-like or *p*-like character. With these states the matrix elements can be calculated as well as the band structure for this model. The TBA with an orthogonal basis and nearest neighbor interactions implies that the overlap matrix elements are non-zero only for orbitals ϕ_l on the same atom, that is

$$\langle \phi_l(x) | \phi_l(x - na) \rangle = \delta_{n0}. \tag{4.2}$$

Similarly, nearest neighbor interactions require that the hamiltonian matrix elements are non-zero only for orbitals that are on the same or neighboring atoms. If the orbitals are on the same atom, the hamiltonian matrix element is defined as

$$\langle \phi_l(x) | H^{sp} | \phi_l(x - na) \rangle = \varepsilon_l \delta_{n0}, \tag{4.3}$$

if they are on neighboring atoms, that is $n = \pm 1$, we have

$$\langle \phi_l(x) | H^{sp} | \phi_l(x - na) \rangle = t_l \delta_{n\pm 1}, \tag{4.4}$$

where ε and t_l are the on-site hamiltonian matrix element and the hopping matrix element, respectively. The crystal wavefunctions are obtained from the general expression for the wavefunctions, already found in Chapter 3, that is

$$\psi_k(x) = c_k \chi_{kl}(x). \tag{4.5}$$

where only the index *k* has survived due to the simplicity of the model. Inserting the wavefunctions into the secular equations of Eq. (3.9), we find that we have to solve a 1×1 matrix, because we have only one atom per unit cell and one orbital per atom. With the above definitions for the matrix elements between atomic orbitals ϕ_l, we obtain

$$\begin{aligned} [\langle \phi_l(x) | H^{sp} | \phi_l(x) \rangle - \varepsilon_k \langle \chi_{kl}(x) | \chi_{kl}(x) c_k] = 0 \qquad (4.6) \\ \Rightarrow \sum_n e^{ikna} \langle \phi_l(x) | H^{sp} | \phi_l(x - na) \rangle = \varepsilon_k \sum_n e^{ikna} \langle \phi_l(x) | \phi_l(x - na) \rangle \\ \Rightarrow \sum_n e^{ikna} \varepsilon_l \delta_{n0} + t_l \delta_{n\pm 1} = \varepsilon_k \sum_n e^{ikna} \delta_{n0} \end{aligned}$$

The solution to the last equation is straightforward, giving the electronic energy band for the monoatomic periodic linear chain

$$\varepsilon_k = \varepsilon_l + 2t_l \cos ka. \tag{4.7}$$

The energy eigenvalues for the two-dimensional square lattice with either one *s*-like or one *p*-like orbital per atom and one atom per unit cell are given in similar fashion by

$$\varepsilon_k = \varepsilon_l + 2t_l \cos(k_x a + k_y a) \tag{4.8}$$

where now we are dealing with a two-dimensional wavevector $\mathbf{k} = k_x \hat{\mathbf{x}} + k_y \hat{\mathbf{y}}$. We make

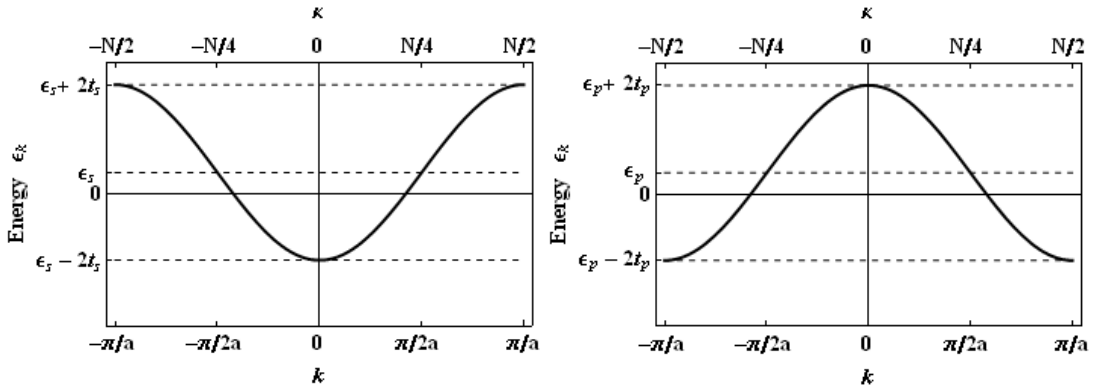

Fig. 4.2: Electronic dispersion relation for a periodic chain and effect of the sign of the hopping matrix elements for *s* orbitals (left) and *p* orbitals (right).

now briefly some considerations on the sign of the hopping matrix elements and the dispersion of the bands. The *s* orbitals are spherically symmetric and have everywhere the same sign, so the overlap between nearest neighboring orbitals is positive. In order to produce an attractive interaction between these orbitals, which contributes to the cohesive energy of the solid, the hopping matrix element must be negative:

$$t_s \equiv \int \phi_s^*(x)\, H^{sp} \phi_s\,(x-a)dx < 0. \tag{4.9}$$

The negative sign in Eq. (4.9) is due to the hamiltonian, since the product of the wavefunctions is positive. The band structure for the 1D model with one *s*-like orbital per unit cell is shown in Fig. 4.2 (left). On the other hand, the *p* orbitals have a positive and a negative lobe, as shown in Fig. 4.2 (right); consequently, the overlap between *p* orbitals situated at nearest neighbor sites and oriented in the same sense as required by translational periodicity is negative, because the positive lobe of one is closest to the negative lobe of the next. Therefore, in order to produce an attractive interaction between these orbitals, the hopping matrix element must be positive, giving

$$t_p \equiv \int \phi_p^*(x)\, H^{sp} \phi_p\,(x-a)dx > 0. \tag{4.10}$$

Thus, the band structure for a 1D model in the first BZ, for $-\pi/a \leq k \leq \pi/a$, with one *s*-like orbital per unit cell will have a maximum at $k = \pm\pi/a$ and a minimum at $k = 0$, while that of the *p*-like orbital will have the positions of the extrema reversed.

4.2.2 Real space diagonalization

In order to deal with a real space representation of the TB hamiltonian for the 1D system, it's more convenient to turn it into second-quantized form

$$H_{band} = \varepsilon_l \sum_{i,\sigma=\uparrow,\downarrow} c^{\dagger}_{i,\sigma} c_{i,\sigma} + 2t_l \sum_{i,\sigma=\uparrow,\downarrow} \left(c^{\dagger}_{i,\sigma} c_{i\pm1,\sigma} + c^{\dagger}_{i\pm1,\sigma} c_{i,\sigma} \right) \tag{4.11}$$

where the index *i* labels the unit cells or the sites in the linear crystal, σ is the index for spin up and spin down electrons, $c^{\dagger}$ and c are the fermionic creation and annihilation operators, respectively, which act on the many-particle states of this half-filled system (remember that each site is occupied by one electron on average). Let's make some further elaboration on the dispersion relation of the previous paragraph. This will be helpful for establishing the link between the real- and the reciprocal-space approach. Let's assume that the 1D crystal is composed of a finite number of equivalent translational unit cells, that is, we are dealing with a periodic linear chain of *N* atoms. We shall also assume for convenience that *N* is even. The translation operations are given in terms of the translation vectors

$$\boldsymbol{t}_m = m\boldsymbol{a} \qquad \text{with} \qquad m = 1, 2, \ldots, N \tag{4.12}$$

while the k-vectors *k* can be expressed in terms of the reciprocal-space lattice unit vector a^* and the translational quantum number κ

$$k = \kappa a^*/N \qquad \text{with} \qquad \kappa = 1, 2, \ldots, N \tag{4.13}$$

Because of the periodicity in *N* of κ, we can use different equivalent choices of intervals for it. For instance, in addition to the one in the previous equation, we can choose a symmetric interval

$$\kappa = -\frac{N}{2} + 1, -\frac{N}{2} + 2, \ldots, \frac{N}{2} \tag{4.14}$$

or another non-symmetric one

$$\kappa = 0, 1, 2, \ldots, N - 1. \tag{4.15}$$

Remembering that $a \cdot a^* = 2\pi$ and substituting Eq. (4.13) into Eq. (4.7), the dispersion relation for the periodic chain of *N* atoms becomes

$$\varepsilon_k = \varepsilon_l + 2t_l \cos\left(2\pi\kappa/N\right). \tag{4.16}$$

Now we come back to Eq. (4.11) and write the hamiltonian, defined in the single-particle orbital basis, in form of a sparse symmetric hermitian $N \times N$ matrix:

$$H^{sp} = \begin{pmatrix} \varepsilon_l & t_l & 0 & \dots & \dots & t_l \\ t_l & \varepsilon_l & t_l & 0 & \dots & \dots \\ 0 & \ddots & \ddots & \ddots & 0 & \dots \\ 0 & \dots & t_l & \varepsilon_l & t_l & 0 \\ 0 & \dots & 0 & t_l & \varepsilon_l & t_l \\ t_l & 0 & \dots & 0 & t_l & \varepsilon_l \end{pmatrix} \tag{4.17}$$

Eq. (4.17) shows that the on-site hamiltonian matrix elements are located on the main diagonal, the inter-site hopping matrix elements appear on the upper and lower diagonals, while the hopping matrix elements due to periodic boundary conditions are on the upper-right and lower-left corners. Solving the secular equation for this matrix, either by a symbolic or numeric diagonalization, one obtains *N* eigenvalues and *N* corresponding eigenvectors for the small *N*-sites 1D periodic crystal, which in turn give information about the sampled energy values and the related k-vectors belonging to the first BZ of the finite system, respectively. In Fig. 4.3 the sampled points of the energy dispersion relation for a four-site periodic chain and the corresponding k-vectors and k-quantum numbers in the first BZ are shown, superimposed on the dispersion curve obtained by reciprocal-space exact diagonalization.

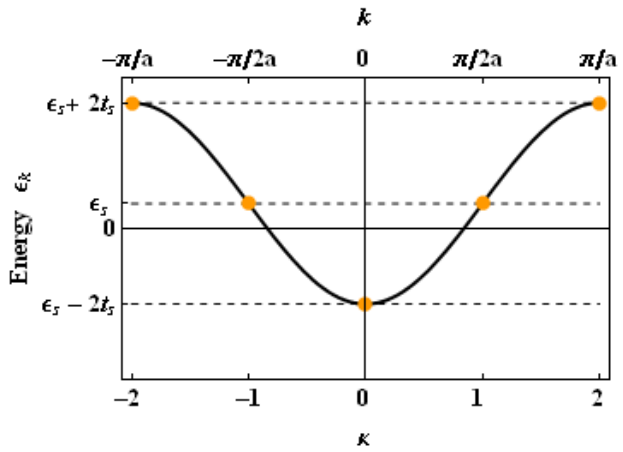

Fig. 4.3: k-points of the 1D BZ of a four-site periodic chain sampled by SC approach superimposed on the electronic dispersion relation obtained by reciprocal space diagonalization.

Actually, it can be shown that the knowledge of the k-quantum numbers and, hence, the sampled k-vectors, can be achieved systematically through a 1D discrete Fourier transform of the eigenvectors obtained by diagonalizing the $N \times N$ hamiltonian matrix. This

technique gives also direct information about the degeneracies of the sampled states. Fig. 4.4 shows the intensity patterns of the Fourier transformed eigenvectors of a periodic chain with $N = 4$ sites, together with the κ-quantum numbers assigned to the non-zero Fourier components (red colour). The states at the center ($k = 0$ or $\kappa = 0$) and at the edge of the Brillouin zone ($k = \pi/a$ or $\kappa = N/2 = 2$) are always non degenerate, the remaning ones ($k = \pm\pi/2a$ or $\kappa = \pm 1$) inside the BZ are doubly degenerate. Similarly, the electronic problem in TBA approximation for the periodic *N*-sites 2D square lattice can be approached with the aid of a two dimensional Fourier transform for assigning to each eigenstate its own wavevectors ($\kappa_{x,y}$ or $k_{x,y}$) .
We recall that the experimental optical spectra of dimerized half-filled organic 1D charge transfer compounds could be accounted for by a SC model with a two-site periodic chain, which allows to sample points at the center and at the edge of the 1D BZ, respectively [109, 110]. Later, more refined models based on tetramers and octamers were also successfully employed for an improved comparison with linear and non-linear spectroscopic measurements for π-conjugated compounds, such as trans-polyacetylene [111, 113]. Interestingly, one can verify that the BZ points sampled with a tetramer can be alternatively obtained by a periodic two-site chain with *periodic* (PBC) or *antiperiodic* (APBC) boundary conditions. By *antiperiodic* we mean that the hopping matrix element involving the opposite ends of the chain has a negative sign or, equivalently, an exponential complex phase equal to π. This property can be extended in a general way to chains with $2n$ sites, which can be investigated by applying (A)PBCs to reduced chain systems with *n*-sites. The use of (A)PBCs will be shown also in Sect. 4.5 and in the chapter about correlation effects investigated with the Hubbard model for 2D small clusters (Sect. 6.2.3). This is extremely useful when computing the optical properties of extended correlated systems involving a huge number of states.

4.3 SC approach for one unit cell SWNT clusters

In the previous chapter we showed that according to the band picture the optical spectra of SWNTs are dominated by the van Hove singularities in the JDOS. The vHs can be related to vertical transitions between valence and conduction bands characterized by the same azimuthal quantum number or cutting line μ. Moreover the main contribution to electronic spectra of the DOS is obtained in those regions of the 1D BZ (k_z quantum number) where the band dispersion is flat (minimum or a maximum in the energy dispersion), that is, where the density of states diverges. If we look at the plot of the energy dispersion of zigzag carbon nanotubes obtained by zone folding method, we can verify very easily that these states giving vHs in the DOS are found at the centre of the 1D BZ, i.e. $k_z = 0$. Moreover the optical matrix elements calculated at these k-points for this kind of tubes are always nonzero, except for the cutting line with azimuthal quantum number $\mu = 0$, which crosses the graphene $\mathbf{\Gamma}$ point, where the velocity matrix element

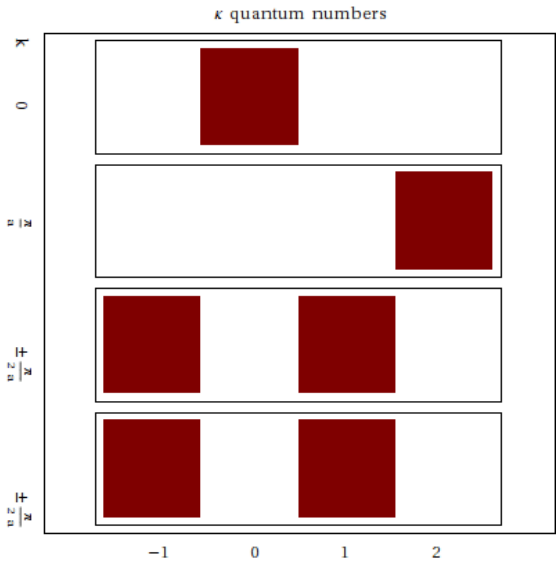

Fig. 4.4: Periodicity analysis of the eigenvectors of a 4-site period chain by Discrete Fourier Transform. The non-zero Fourier components of the transformed hamiltonian eigenvectors are coloured in red and assigned to the respective κ quantum numbers, from which the k wavevectors in the 1D BZ can be derived.

is zero. So in principle, in the tight-binding approximation we could compute the optical and electronic properties for a zigzag nanotube by taking exclusively into account the $k_z = 0$ states: we expect that the resulting spectra would be fairly similar to those obtained by fully integrating the bands along the cutting lines and summing over them, as usually done within zone-folding method. In Fig. 4.5 two optical spectra for the same zigzag nanotube $(5, 0)$ calculated by zone folding method are shown for comparison: spectrum a) is obtained by using Eq. (3.17), spectrum b) by including only $k_z = 0$ states in Eq. (3.17). Apart from the broadening of the peaks and the ground of the spectra, the two profiles are identical, as far as the energy position of the peaks is concerned. By applying the SC approach to this type of system one actually picks up in a very efficient way the smallest piece of graphene lattice and the appropriate set of periodic boundary conditions for sampling exactly those (μ, k_z) states which dominate the tight-binding optoeletronic spectrum of a zigzag nanotube. In principle, this will allow to address several issues of interest in nanotube science, such as:

- the inclusion of the Coulombian interaction into the non interacting model and the treatment of the electronic correlation effects, such as excitons;

- the handling of the intertube hopping interaction in more complicated structures such as doublewalled carbon nanotubes (DWNTs) and the calculation of the elec-

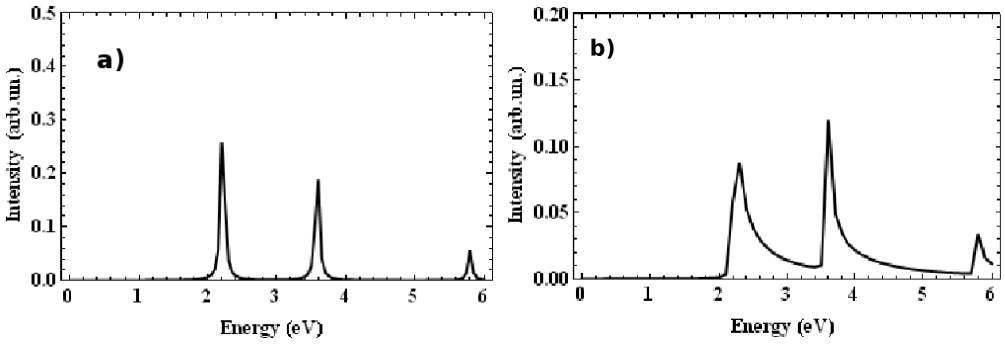

Fig. 4.5: Optical absorption intensity of (5, 0) tube calculated by a) zone-folding method including only $k_z = 0$ points and by b) full BZ integration of the dispersion relation.

tronic spectra for these systems;

- the treatment of doping and of the local breaking of the translational periodicity in disordered SWNTs.

4.3.1 Choice of the cluster and hamiltonian diagonalization

After determining the k-wavevectors related to the nanotube geometry we are interested in, the further step is to select the appropriate subset of graphene lattice points or *cluster* from the infinite ideal graphene sheet. As stated previously, a convenient choice to start with is the zigzag unit cell, shown in Fig. 4.6 for the tube $(5, 0)$. Here we recall that a zigzag $(n, 0)$ cluster contains $4n$ sites and $2n$ biatomic graphene cells. The graphene ribbon is rolled up along the circumferential direction and periodic boundary conditions are applied along the axial direction to account for the translational periodicity. Thus the $(4n \times 4n)$ real space tight-binding hamiltonian matrix in single particle orbital basis can be obtained in a straightforward manner similar to that of the periodic 1D chain or the 2D square lattice. As done in Chapter 3, we choose one p_z orbital per carbon atom and consider only nearest-neighbor interactions. The chosen tight-binding parameters are $\varepsilon_\pi = 0$ eV for the on-site energy integral and $t_\pi = -2.9$ eV for the nearest neighbor hopping integral, respectively [89, 90]. By diagonalization of the real symmetric hamiltonian matrix, we see that the obtained set of $4n$ eigenvalues correspond exactly to the zone-folding energies evaluated at $k_z = 0$, for each of the $2n$ bands labelled by μ, as shown in Fig. 4.6 (right).

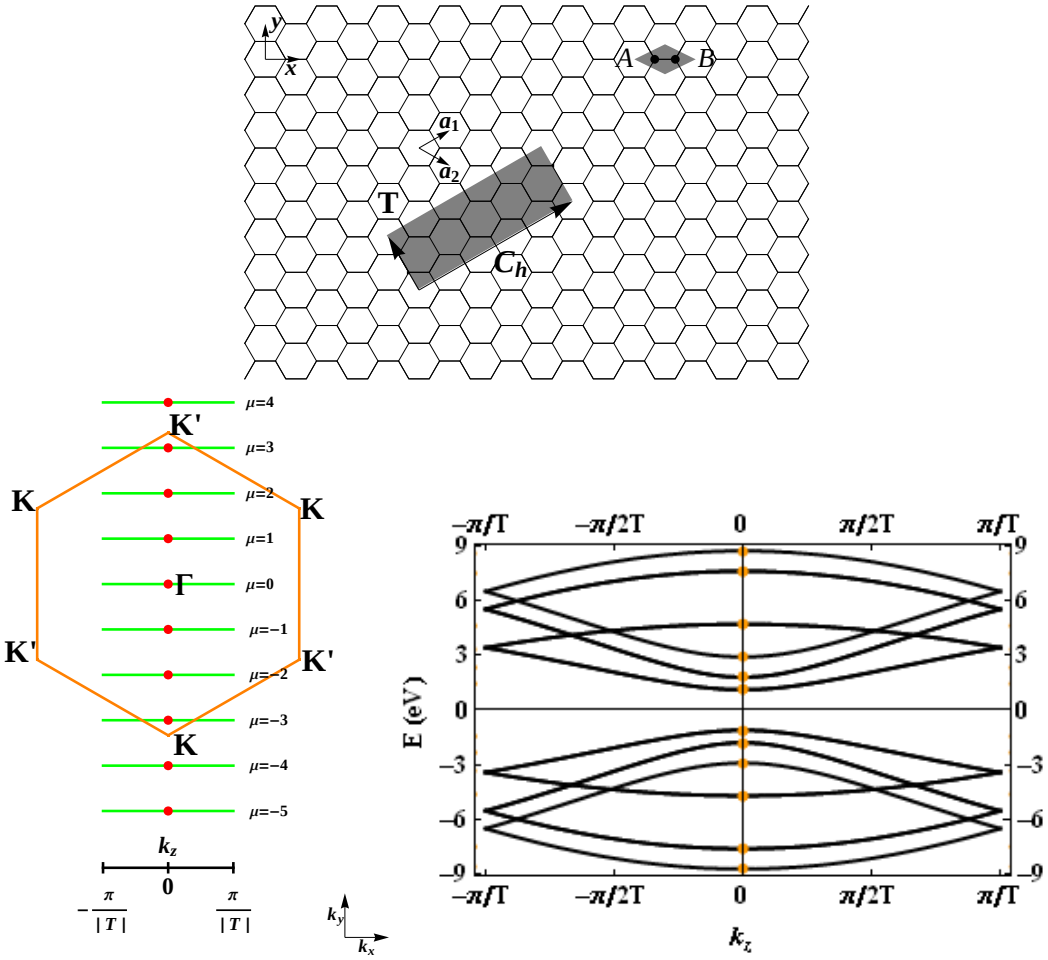

Fig. 4.6: Nanotube Brillouin zone for tube (5, 0) (left) and k-points sampled with a one unit cell cluster (right). The one unit cell cluster (5,0) on the graphene lattice is shown above.

4.3.2 Symmetry analysis of the sampled eigenstates

In order to verify if the sampled eigenstates of the zizgag small-crystal hamiltonian correspond effectively to the $k_z = 0$ states of the zone-folding electronic bandstructure, a careful symmetry analysis of the numerical eigenvectors has been conducted in this work. As a matter of fact, when working with real space methods, we haven't at our disposal an analytical expression similar to that of graphene electronic dispersion energy of Eq. (3.17), which puts in a biunivocal relation a given reciprocal space (k_x, k_y)-wavevector and the corresponding points of the 2D energy dispersion. That's the reason why a symmetry analysis of the eigenstates becomes necessary in a real space method to allow for a com-

plete identification and classification of the quantum numbers (μ, k_z) associated with the energy eigenstates of the nanotube SC hamiltonian. Two ways have been individuated: the first is based on the form of the Bloch wavefunction of Eq. (3.3) for carbon nanotubes, the second relies upon the application of the two-dimensional Discrete Fourier Transform (DiFT) to the numerical eigenvectors. In the following both methods will be described in detail. By using the tight-binding expression for the nanotube wavefunction of Eq. (3.3) for carbon nanotubes, we insert into this the quantum numbers $(\mu, k_z = 0)$, (guessed by comparison of the sampled energy eigenvalues with those at $k_z = 0$ of the zone folding method), and combine the traveling waves in form of sin- and cos-like stationary waves. At this point one can already verify that the obtained Bloch coefficients have the same Fourier transform intensity pattern and the same azimuthal periodicity as the eigenvectors of the $4n \times 4n$ real space hamiltonian. Alternatively, the azimuthal quantum number μ of the obtained eigenstates can be derived by fitting the Bloch coefficients of these cluster eigenvectors as a function of the azimuthal coordinate ϕ_i of the corresponding sites labelled by *i* (Fig. 4.7). The functional form used for the fitting is a sinusoide with amplitude *A* equal to the inverse square root of $4n$ (i.e. number of sites), azimuthal period μ and a generic phase Δ (this one is just an adjustable fitting parameter):

$$c_i = \frac{1}{\sqrt{4n}} \left[\sin\left(\mu\phi_i + \Delta\right) + \cos\left(\mu\phi_i + \Delta\right)\right] \qquad \text{for} \qquad i = 1, 2, \ldots, 2n \tag{4.18}$$

The resulting periodicity of the fitted stationary wave gives the integer number of wavelengths by which a period of 2π around the nanotube is covered (up to multiple integers of 2π). Note that the actual number of Bloch coefficients to be fitted is $2n$ and not $4n$ because of the higher symmetry implied by $k_z = 0$ states, that is, eigenvector coefficients referring to the same cylindrical coordinate but different axial coordinates, have the same value. Moreover, Fig. 4.7 shows how the azimuthal Fourier components $\mu = 0, 1, \ldots, 2n-1$ are in relation with the *2n*-graphene unit cells inside the cluster unit cell. By applying the DiFT procedure, after appropriately indexing the obtained non-zero Fourier coefficients, the eigenvectors can be straightforwardly assigned to the μ azimuthal quantum numbers. From the above analysis, one can conclude that the eigenstates individuated by the periodic SC approach describe correctly the symmetry of the $k_z = 0$ states giving van Hove singularities in the density of states for a zigzag nanotube.

4.4 SC approach using supercells

In this section we will see how it's possible to explore more other points inside the 1D BZ with clusters, in addiction to the previously found $k_z = 0$ states. Finally, in the second part of this section we will show the complete two-dimensional Fourier analysis developed for a full classification of the $(\mu, k_z = 0)$ quantum numbers associated with the cluster eigenstates.

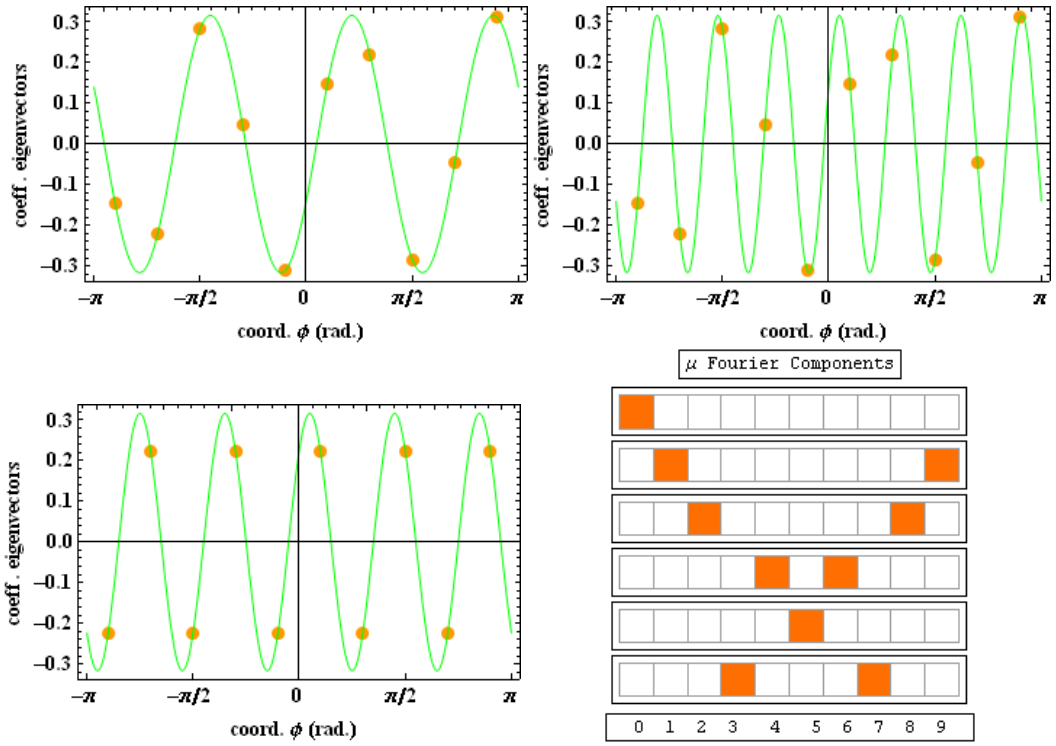

Fig. 4.7: Fitting and Discrete Fourier Transform analysis of the cluster eigenvectors

4.4.1 Choice of the cluster

To start with, we consider a super-cluster with the unit cell doubled along the **T** vector. We then construct the double-sized hamiltonian matrix as done before, but now translational periodic boundary conditions are applied for sites which have a distance equal to $2T$. From the diagonalization of the $(8n \times 8n)$ hamiltonian matrix we expect to sample $8n$ points in the nanotube Brillouin zone, but now for each of the $2n$ bands, indexed by μ, more k_z points are sampled in addition to the zone center. To be more specific, these new points are located at the edges of the 1D BZ, at $k_z = \pm\pi/T$ (see Fig. 4.8).
If the size of the cluster is doubled again along **T**, we obtain a $16n$-site cluster with translational period equal to $4T$ and with a $(16n \times 16n)$ matrix to be diagonalized. Therefore, in addiction to the states at $(\mu, k_z = 0, \pm\pi/T)$, states at $kz = \pm\pi/2T$ are sampled. In general, for a super-cluster of kind $(n, 0)$ made of *N* unit cells and translational period equal to NT, the k_z wavevectors sampled in the 1D BZ for each of the $2n$ bands are given by a relation similar to the Eq. (4.16) for the periodic infinite chain, adapted in this case to describe the quasi-1D nature of the nanotube system:

$$\mathbf{k} = (\mu, k_z) \qquad \text{with} \qquad k_z = \frac{2\pi\kappa}{NT} \qquad \kappa = 0, 1, 2, \ldots, N-1 \tag{4.19}$$

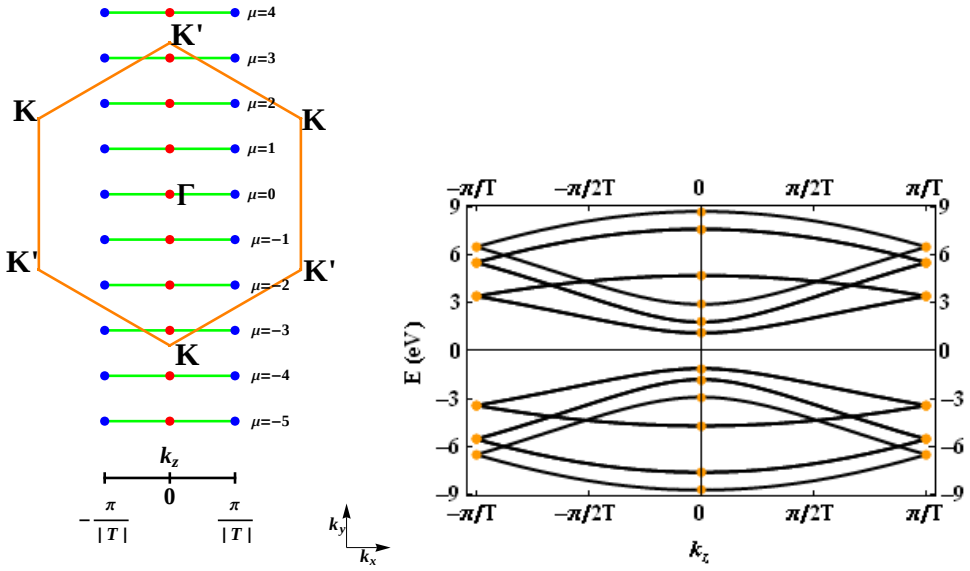

Fig. 4.8: Nanotube Brillouin zone for tube (5, 0) and k-points sampled with a two unit cell cluster (left), superimposed on the zone-folding electronic band structure (right).

4.4.2 Symmetry analysis of the eigenstates

At this point, we are able to identify explicitly the (μ, k_z)-wavevectors inside the nanotube Brillouin zone by performing a discrete Fourier transform of the hamiltonian $4nN$-sized eigenvectors along the azimuthal and axial directions (Fig. 4.9). Here we summarize briefly the procedure used for a super-cluster zigzag with an arbitrary number of unit cells. For determining the azimuthal quantum numbers μ , each set of $4nN$ coefficients forming any eigenvector is partitioned into N subsets of $4n$ coefficients, as indicated in the upper panel of Fig. 4.9. Then 1D DiFT is performed for any zigzag chain along the circumferential direction and the band index μ is obtained from the non-zero Fourier components (see example of Fig. 4.9 lower panel). For determining k_z, each set of the $4nN$ coefficients which form any eigenvector is partitioned into $4n$ subsets of N coefficients (see Fig. 4.9 upper panel). Then 1D discrete Fourier transform is performed along the axial direction and the non-zero Fourier components give the quantum number κ, (see example of Fig. 4.9 b lower panel). Finally the axial wavevector k_z is obtained with the aid of Eq. (4.19). Thus, by a two-dimensional DiFT of the eigenvectors mapped onto the real graphene lattice we could obtain a complete classification of the BZ-points associated with the sampled eigenstates of the cluster.

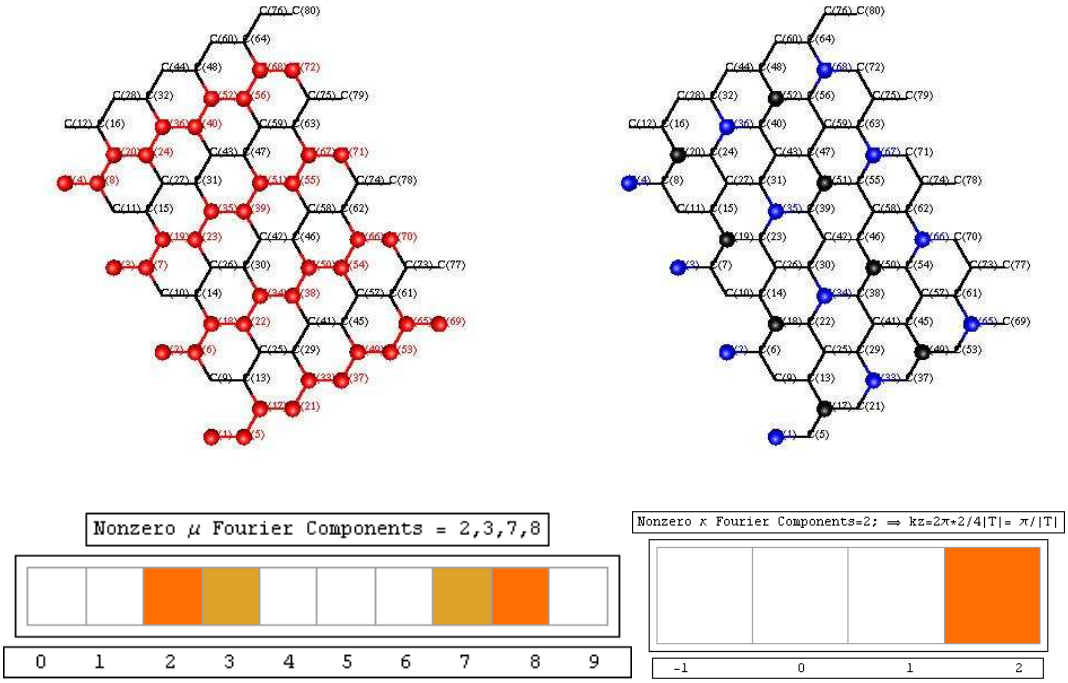

Fig. 4.9: Application of two-dimensional Discrete Fourier Transform analysis on eigenvector coefficients (coloured sites) for zigzag supercells in order to obtain the azimuthal quantum number μ (left) and the axial quantum number k_z (right).

4.5 SC approach with a Bloch phase factor

In principle, one would like to solve the electronic problem for a cluster of limited size, without having to build up and diagonalize very large hamiltonian matrices to sample any k-point inside the 1D BZ. However, Bloch's theorem for periodic lattices states that, under a crystal translation which carries a point $\mathbf{r}$ to $\mathbf{r}+\mathbf{T}$, the following relation for the wavefunction of a periodic system holds:

$$\psi_{\mathbf{k}}(\mathbf{r}+\mathbf{T}) = e^{i\mathbf{k}\cdot\mathbf{T}} e^{i\mathbf{k}\cdot\mathbf{r}} u_{\mathbf{k}}(\mathbf{r}+\mathbf{T}) = e^{i\mathbf{k}\cdot\mathbf{T}} \psi_{\mathbf{k}}(\mathbf{r}) \tag{4.20}$$

because $u_{\mathbf{k}}(\mathbf{r}+\mathbf{T}) = u_{\mathbf{k}}(\mathbf{r})$ is a function with the period of the crystal lattice. Therefore $\exp(i\mathbf{k}\cdot\mathbf{T})$ is the phase factor by which a Bloch function is multiplied when a crystal lattice translation is performed. This general fact can be applied to the case of the zigzag cluster with a single unit cell i.e. with $4n$ sites. We consider the hamiltonian matrix elements related to translational periodic boundary conditions and multiply each of them by a complex exponential phase factor of period 2π. Also the hamiltonian matrix is required to be both symmetric and hermitian. Therefore for these matrix elements the

following relation holds:

$$h_{i,j} = \widetilde{h_{j,i}}^{*} \text{ with } h_{i,j} = t_\pi \exp(i\phi) \text{ for } -\pi \leq \phi \leq \pi \text{ and } |r_i - r_j + (0,0,T)| < 1.1\, a_{CC}$$

We can recover the points $k_z = \pm\pi/T$ using a phase $\phi = \pm\pi$; this kind of condition is also called *antiperiodic* (APBC), while *periodic* boundary conditions (PBC), employed in the two previous sections, imply $\phi = 0$. For points at $k_z = \pm\pi/2T$ we need to apply a phase $\phi = \pm\pi/2$. In general, for any other point at $k_z = \pm\pi/nT$ the phase to be applied is $\phi = \pm\pi/n$. At this stage, the complete electronic dispersion can be promptly obtained by swapping the phase ϕ over the 2π range and verify that the SC band structure corresponds exactly to the band structure of the corresponding one known from the zone-folding approach, as shown in Fig. 4.10.

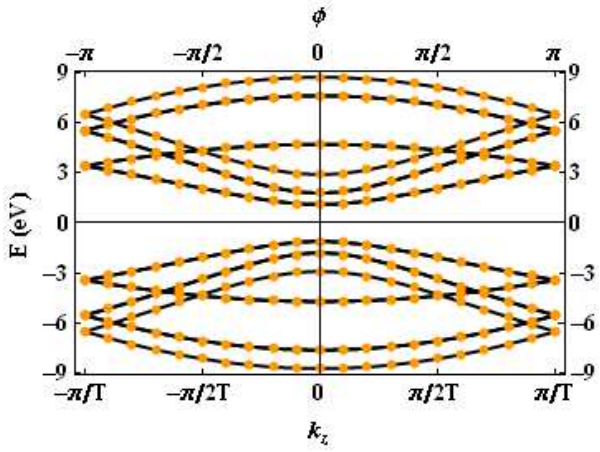

Fig. 4.10: Nanotube band structure for tube (5, 0) obtained by SC approach superimposed on that obtained by zone-folding method. Full correspondence between the two methods is obtained.

4.6 SC optical absorption matrix elements and spectra

In Chapter 3 a general literature overview of zone-folding based numerical and analytical expressions for the optical absorption matrix elements parallel to the tube axis was presented. It has been highlighted that a pure JDOS calculation (with constant dipole matrix elements) isn't enough to describe correctly the tight-binding optical spectra of carbon nanotubes and that the dipole selection rules and the k-space dependence of the value of the dipole matrix elements must be taken into account instead. Here we want to obtain the same quantity relevant for zigzag nanotubes using the properties of the clusters found in the previous paragraph. Moreover we will show how the interband optical selection

rules follow straightforwardly from the use of the appropriate cluster and periodic boundary conditions, which allow the sampling of correct k-states. We recall here that, in order to obtain the optical matrix element of Eq. (3.58) within the SC approach, we need to calculate the transition dipole vector **D**, defined by [122, 141, 121, 142, 144, 145]

$$\mathbf{D}^{fi} = \langle \Psi_f | \nabla_z | \Psi_i \rangle \tag{4.21}$$

which in turns requires the knowledge of the electronic wavefunctions Ψ^j, where *j* labels a generic valence *v* or conduction state *c*. In the SC approach these wavefunctions are the eigenfunctions of the hamiltonian which, according to our previous choice for zigzag nanotubes, selects all the $k_z = 0$ points, which are those relevant both for the JDOS and the z-component of the dipole matrix elements of these systems. In the TB approximation (LCAO) the nanotube wavefunctions are actually linear combination of the p_z orbitals weighted by the real space eigenvector coefficients obtained from the SC hamiltonian diagonalization; clearly these can be related to the atomic sites in the cluster unit cell, as shown in the Fourier analysis of the wavefunctions of Sects. 4.3 and 4.4. In what follows, we will label the real space eigenvector coefficients c_i referring to the coordinates of the atomic sites of the one unit cell cluster $(n, 0)$, according to the convention of Sect. 2.4.1. Therefore, $u = 0, \ldots U-1$ denotes the nanotube unit cells inside the clusters, $h = 0, ...N-1$ the biatomic graphene unit cells within a nanotube unit cell, and $s = A, B$ the atomic sites within each graphene unit cell. Inside the cluster lattice, each site of type A (B) is surrounded by three nearest neighbour sites of type B (A), as usual. In the LCAO Ansatz the cluster eigenfunctions for valence or conduction band states are written as

$$\Psi^{v,c} = \sum_{u=0}^{U-1} \sum_{h=0}^{N-1} \sum_{s=A,B} c^u_{h,s} \phi_z(r - \mathbf{R}^u_{h,s}), \tag{4.22}$$

where the correct k-point dependence is included thanks to the SC sampling, unlikely in Eq. (3.2) and Eq. (3.3), where we needed the Bloch phase factor to express the k-space dependence. We assume as done in Chapter 3 that the interband optical transition is vertical, that is $\Delta k_z = 0$. Substituting Eq. (4.22) into Eq. (4.21), we get in principle

$$\mathbf{D}^{cv} = \sum_{u'=0}^{U-1} \sum_{h'=0}^{N-1} \sum_{s'=A,B} c^{*u'}_{h',s'} \sum_{u=0}^{U-1} \sum_{h=0}^{N-1} \sum_{s=A,B} c^u_{h,s} \langle \phi |_z (r - \mathbf{R}^{u'}_{h,'s'}) \nabla_z | \phi \rangle_z (r - \mathbf{R}^u_{h,s}), \tag{4.23}$$

which can be simplified by first dropping the summations over the indices u, u', if we work with a one unit cell cluster. We also assume that only nearest neighbour interactions are relevant for these matrix elements; thus we can get rid of the sum over h' and maintain only the sum over *h* by introducing the index $l = 1, 2, 3$, which labels the interatomic vectors $r^l_{h,s} = \mathbf{R}_{l,s'} - \mathbf{R}_{h,s}$ pointing from one site A (B) in the h-th graphene cell to each of the three nearest neighbors B (A). Then we get

$$\langle \Psi^c | \nabla_z | \Psi^v \rangle = \sum_{h=0}^{N-1} \sum_{l=1,3} \sum_{s'=A,B} c^*_{l,s'} \sum_{s=A,B} c_{h,s} \langle \phi_z(r - \mathbf{R}^u_{l,s'}) | \nabla_z | \phi_z(r - \mathbf{R}^u_{h,s}) \rangle.$$

Table 4.1: Implementation of the calculation of Eq. (4.25) for zigzag cluster (5,0) with periodic boundary conditions along the *z* axis included.

h	site numb. *s*	$s = A, B$	$n.n\ s'$	*z*-component
1	1	*A*	2, 18, 20	$-1/2, -1/2, +1$
1	2	*B*	1, 3, 5	$+1/2, -1, +1/2$
2	3	*A*	2, 4, 20	$+1, -1/2, -1/2$
2	4	*B*	3, 5, 7	$+1/2, -1, +1/2$
3	5	*A*	2, 4, 6	$-1/2, +1, -1/2$
3	6	*B*	5, 7, 9	$+1/2, -1, +1/2$
4	7	*A*	4, 6, 8	$-1/2, +1, -1/2$
4	8	*B*	7, 9, 11	$+1/2, -1, +1/2$
5	9	*A*	6, 8, 10	$-1/2, +1, -1/2$
5	10	*B*	9, 11, 13	$+1/2, -1, +1/2$
6	11	*A*	8, 10, 12	$-1/2, +1, -1/2$
6	12	*B*	11, 13, 15	$+1/2, -1, +1/2$
7	13	*A*	10, 12, 14	$-1/2, +1, -1/2$
7	14	*B*	13, 15, 17	$+1/2, -1, +1/2$
8	15	*A*	12, 14, 16	$-1/2, +1, -1/2$
8	16	*B*	15, 17, 19	$+1/2, -1, +1/2$
9	17	*A*	14, 16, 18	$-1/2, +1, -1/2$
9	18	*B*	1, 17, 19	$+1/2, +1/2, -1$
10	19	*A*	16, 18, 20	$-1/2, +1, -1/2$
10	20	*B*	1, 3, 19	$-1, +1/2, +1/2$

The matrix element between p_z-like atomic orbitals $\phi_z(r - \mathbf{R}^u_{h,s})$ is written as [141, 115, 101, 121, 122]

$$\langle \phi_z(r - \mathbf{R}^u_{l,s'}) | \nabla_z | \phi_z(r - \mathbf{R}^u_{h,s}) \rangle = m_{opt} \frac{a}{\sqrt{3}} r^l_{h,s} \tag{4.24}$$

where m_{opt} is the atomic dipole transition matrix element, parallel to the interatomic vector $r^l_{h,s} = \mathbf{R}_{l,s'} - \mathbf{R}_{h,s}$ and evaluated at the first nearest-neighbor distance $a_{CC} = 0.142\,\mathrm{nm}$. For simplicity, it can be considered a constant to normalize the resulting values of the dipole matrix elements [121, 122, 151, 152]. Developing the summation over s and s' in terms of the contribution to the dipole matrix element from A-sites to B-sites

and viceversa, we obtain

$$\mathbf{D}^{cv} = \langle \phi_z(r - \mathbf{R}^u_{l,s'}) | \nabla_z | \phi_z(r - \mathbf{R}^u_{h,s}) \rangle = \tag{4.25}$$
$$m_{opt} \frac{a}{2\sqrt{3}} \left[\sum_{h=0}^{N-1} \sum_{l=1,3} c^*_{l,B} c_{h,A} \left(r^l_{h,A} \right)_z + \sum_{h=0}^{N-1} \sum_{l=1,3} c^*_{l,A} c_{h,B} \left(r^l_{h,B} \right)_z \right]$$

where the projection along the tube axis *z* has been considered. Again, periodic boundary conditions along the nanotube axis must be included when performing the summation in Eq. (4.25), as indicated in Table 4.6, which shows an example implementation. The selection rules for vertical transitions involving a given $(\mu, k_z = 0)$ valence band state and another $(\mu', k_z = 0)$ conduction band state are automatically obtained through Eq. (4.25), in full accord with the zone-folding selection rules [121, 122, 141, 142] :

$$\delta_{\mu,\mu'} = 0 \Longrightarrow D_z = 0 \tag{4.26}$$
$$\delta_{\mu,\mu'} = 1 \wedge (\mu, \mu' \neq 0) \Longrightarrow D_z \neq 0.$$

The exception case in the second selection rule involves vertical transitions between non-degenerate states lying exactly at graphene $\mathbf{\Gamma}$ point, (i. e. $(\mu = 0, k_z = 0)$ in the frame of nanotube BZ), where one can verify that the dipole matrix element is exactly zero, as seen in Chapter 3. We will see in the following chapters, that the symmetry-breaking effect due to the intertube hopping interactions in double-walled nanotubes (DWNTs) or the presence of defects will affect these rules, so that they will no longer hold, as a direct consequence of the mixing of the states related to the inner and outer shells in DWNTs and the lifting of the band degeneracies both in DWNTs and defected SWNTs. The following symmetry relation between the two terms contributing to Eq. (4.25) holds:

$$\sum_{h=0}^{N-1} \sum_{l=1,3} c^*_{l,B} c_{h,A} \left(r^l_{h,A} \right)_z = \sum_{h=0}^{N-1} \sum_{l=1,3} c^*_{l,A} c_{h,B} \left(r^l_{h,B} \right)_z . \tag{4.27}$$

This follows from the fact that 1) conduction band states are actually antisymmetric linear combinations of atomic orbitals, unlikely valence band states which are fully symmetric, and that 2) the following relation between nearest neighbor vectors joining A sites to B sites and viceversa holds:

$$\left(r^l_{h,A} \right)_z = - \left(r^l_{h,B} \right)_z . \tag{4.28}$$

Before comparing the numerical values for the dipole matrix elements obtained from Eq. (4.25) with those from zone-folding method, it has to be pointed out that an equivalent result could be obtained using the axial component of the velocity operator written in second-quantization formalism [92, 102, 110], instead of Eq. (4.25), which still involves the position of the atomic orbitals. In this case, the expression for the *z*-component of the dipole matrix element is:

$$\langle \Psi^c | \nabla_z | \Psi^v \rangle = \langle \Psi^c | v_z | \Psi^v \rangle \tag{4.29}$$

where the velocity operator is written as:

$$v_z = -\frac{\imath t_\pi}{\hbar} \sum_{\langle i,j\rangle,\sigma} \left[c^\dagger_{i,\sigma} c_{j,\sigma} - c^\dagger_{j,\sigma} c_{i,\sigma} \right]_z . \tag{4.30}$$

This form will also be used in the last chapter about the calculation of the optical spectra of the periodic cluster with the inclusion of the Columbian correlation effects in a Hubbard-like fashion. The quantum-mechanical derivation of the form of Eq. (4.30) from the commutator $[H, \mathbf{r}]_z$ of the hamiltonian and the position operator is shown in Appendix. Within this formalism, this operator is no longer dependent on the choice of the origin of the system reference frame and, therefore, it's more appropriate for the description of the optical properties of a periodic cluster [110]. For this reason the numerical values of the dipole matrix element involving either the position as in Eq. (4.25) or the velocity operator as in Eq. (4.30) cannot be expected to be the same. However, the optical selection rules reported previously, can still be verified for both approaches. For the case of $k_z = 0$ states of a zigzag cluster, one can recover the same numerical values of the *z*-component of the dipole matrix elements from both approaches, as explained in the following. The eigenfunctions we are dealing with at $(\mu, k_z = 0)$ have pure rotational symmetry. In other words, the eigenvector coefficients along the tube axis are all constant, thus their 1D Fourier transform gives zero. Therefore, Eq. (4.25) has to be put in a condition independent of the choice of origin of the system reference frame, taking into account the rotational symmetry of the zigzag system. The summation of Eq. (4.25) must be evaluated for every rotationally equivalent assignment of the conduction band eigenvector coefficients to the cluster sites, while keeping fixed the assignment of the valence band coefficients to the underlying lattice. Practically, for a zigzag cluster of one unit cell, this is simply obtained by a ciclic permutation within every $2\pi/N$ radians of the sequence of coefficients which form each eigenvector. For every ciclic permutation, Eq. (4.25) is evaluated and a value for the dipole matrix element is obtained, which always involves a vertical transition between $\mu, k_z = 0$ states. Finally, the *N* collected values of the dipole matrix element are fitted by a sinusoidal function of the azimuthal shift of $2\pi/N$:

$$d_i = A\left[\sin\left(\mu\phi_i + \Delta\right) + \cos\left(\mu\phi_i + \Delta\right)\right] \qquad \text{with} \qquad i = 1, 2, \ldots, N. \tag{4.31}$$

where the amplitude *A* gives the value of the dipole matrix element we wished to obtain (the same as that obtained by the velocity operator), μ is the azimuthal period of the stationary wave and thus the band quantum number, Δ is as always an adjustable fitting parameter. In Table 4.6 we compare the absolute values of the dipole matrix elements calculated by Eq. (4.25) with the above described procedure with those obtained by the zone-folding scheme of Refs. [142, 144, 141, 145]. The values show a very good correspondence beyond the numerical accuracy due to the direct diagonalization and the fitting procedure routine employed in the SC approach. Moreover all the symmetry properties, such as degeneracies and values at special k-points (graphene Γ point), are verified.

Table 4.2: Comparison of the absolute value of the z-component of dipole matrix elements for electron-photon interaction evaluated at $k_z = 0$ for (5, 0) tube by SC approach with Eq. (4.25) and ZF method.

$(\mu, k_z = 0)$	$\lvert D_z/M_{opt}\rvert$ [Å] (SC)	$\lvert D_z/M_{opt}\rvert$ [Å] (ZF)
$\mu = 0$	0.	0.
$\mu = 1, 9$	0.191765	0.190983
$\mu = 2, 8$	0.693811	0.690983
$\mu = 5$	2.00818	2.0
$\mu = 4, 6$	1.81642	1.80902
$\mu = 3, 7$	1.31437	1.30902

Moreover, we verified that the values obtained by zone-folding and those obtained by SC approach with the velocity operator are exactly the same (not shown). The calculation of the optical absorption spectrum can be obtained by the sum over states (SOS) method [154]. All possible transitions and optical matrix elements between valence and conduction states are included in the calculation. Using a Lorentzian function the optical absorption intensity for light polarization **P** parallel to the tube axis can be expressed as

$$I(E) \propto \sum_{i=1}^{2N}\sum_{j=1}^{2N} |\langle\Psi_j^c|\mathbf{P}\cdot\nabla_z|\Psi_i^v\rangle|^2 \delta\left(E - \left[E_j^c - E_i^v\right]\right) \tag{4.32}$$

$$\approx \sum_{i=1}^{2N}\sum_{j=1}^{2N} |\langle\Psi_j^c|\mathbf{P}\cdot\nabla_z|\Psi_i^v\rangle|^2 \frac{\Gamma/\pi}{\left(E - \left[E_j^c - E_i^v\right]\right)^2 + \Gamma^2}$$

Now the indices *i* and *j* identify a generic valence band state and conduction band state respectively within the set of the *2N* available eigenstates obtained by diagonalizing the $(2N \times 2N)$ hamiltonian. In Fig. 4.11 we compare the optical absorption spectrum of the periodic zigzag cluster (5, 0) based on a SC calculation (with either dipole matrix element from position operator or velocity operator) to that obtained with the ZF approach. The results show that the same fundamental features (transition energies and relative intensities of the transitions) are obtained. One can conclude that SC approach properly samples the first Brillouin zone of SWNT and that, therefore, the right choice of the cluster allows to obtain the full results of the zone folding approach using a real space approach.

4.7 Summary

In this chapter the basics of small crystal approach have been presented, which consists in a finite sampling of the Brillouin zone of a periodic system with a cluster of finite size

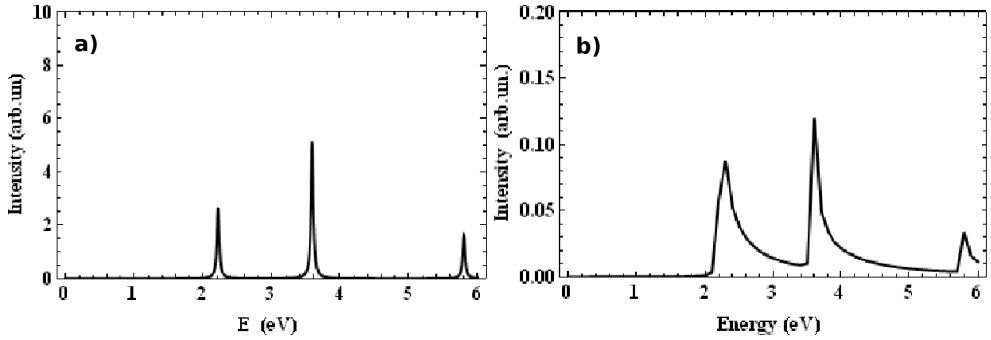

Fig. 4.11: Optical absorption intensity of (5, 0) tube calculated by a) SC approach including only $k_z = 0$ points and by b) full BZ integration of ZF dispersion relation.

and suitable periodic boundary conditions. First the method has been applied to a *n*-site periodic chain, then to a single-walled nanotube. The special case of zigzag clusters has been considered for which it's simpler to sample the critical k-points which give the van Hove singularities in the density of states and nonzero optical matrix elements. By a minimal calculation based on few k-points, we have shown that all the important features of the optical spectra, known by reciprocal space based method such as zone folding, could be completely recovered by this method.

Chapter 5

Double-wall carbon nanotubes

In this section the small-crystal approach is applied to double-walled nanotubes for the tight-binding calculation of their electronic dispersion relation and optical spectra. We will also show that the SC provides the flexibility of changing the orientation of the constituent walls, unlikely other reciprocal space-based methods, which cannot include in a general way the local symmetry breaking due to a non-negligible intertube interaction. As a consequence, the dependence of the optical properties on the geometric correlation between the walls can be investigated in a simpler way. The calculations show how the resulting optical spectra are visibly affected by these effects with the appearing of new transitions and suggest a revision of the Kataura plots used for the interpretation of the Raman spectra of DWNTs.

5.1 Introductory remarks

Double-wall carbon nanotubes (DWNTs) can be considered the simplest form of multi-wall nanotubes (MWNTs), as they consist of two coaxial graphene cylinders with very weak van der Waals type interaction between the two walls, yet with strong covalent bonds between atoms within each constituent tube. According to the commonly adopted geometrical convention, the geometrical structure of a DWNT is specified by the notation $(n, m) \circledcirc (n', m')$, which means that the constituent inner tube with chiral indices (n, m) is inserted into the outer wall with indices (n', m'). Recently, much theoretical and experimental interest has been generated for DWNTs, since they would play an essential role in future nanoelectronic device applications and biological applications [44, 157, 160]. From a physicist's standpoint, they can be considered molecular analogues to coaxial cables. Actually, a metallic@semiconducting (M@S) or a semiconducting@metallic (S@M) DWNT can be, respectively, a molecular conductive wire covered by an insulator or a molecular capacitor in a device [155]. It is believed that these structures would exhibit enhanced field emission, mechanical and thermal properties when compared to SWNTs [156]. Some examples of DWNT-based nanometer-scale electromechanical mo-

tors (NEMS) have recently been proposed in two theoretical papers, namely a molecular motor driven by temperature variation [158] and carbon nanotube *electron windmills*, which exploit the torque generated by applying a potential difference to the outer tube, causing the inner tube to rotate if the generated torque is enough to overcome the frictional forces existing between the walls of the DWNT [159]. From a chemist's point of view, the structure of a DWNT can be considered that of a SWNT protected by the external SWNT on which functionalization can be operated without affecting the properties of the internal tube [160]. This opens the route to novel preparation techniques which allow the solubilization of the outer SWNT system in different environments (e.g. cell membranes) without affecting the properties of the inner shell. Therefore, in recent years the production and characterization of DWNTs have drawn the attention of numerous scientists. As explained in the introductory chapter of this thesis, DWNTs can be produced by several techniques: the arc discharge method, the catalytic chemical vapour deposition method and the fusion of fullerenes enclosed in peapods by TEM irradiation or temperature. The last method [37] provides a DWNT yield greater than 95% and high-quality samples. The two constituent tubes of the DWNT can be characterized by Raman spectroscopy [161, 162] and high-resolution transmission electron microscopy (HRTEM) [163], since the atomic positions in a DWNT cannot be measured by STM/STS directly, as only the outermost nanotube contributes to the tunneling conductance. As usual, in Raman measurements the indices of the two coaxial layers of a DWNT can be assigned based on the respective radial breathing mode frequencies [165, 166] of the non-interacting constituent SWNTs. It was shown experimentally by optical absorption and PL measurements that the interaction between the constituent layers influences the optical transitions of the inner and outer tubules [164]. As we will see in the following, understanding the role and magnitude of the interlayer interaction and its relation with the geometry of the constituent walls is one of the most relevant issues concerning in particular the modeling of DWNT electronic properties.

5.2 Structure and symmetry properties

DWNTs can be commensurate (C) or incommensurate (I) if the ratio of the translational periods of the constituent SWNTs is a rational or irrational number, respectively. According to this definition, DWNTs with both armchair or zigzag nanotubes are always commensurate, while a DWNT with a zigzag tube inserted into an armchair one is incommensurate $\left(T_Z/T_A = \sqrt{3}\right)$. Experimentally, it has been found, that DWCNTs produced by arc discharge show no correlation in the chiralities of the walls [163], so both commensurate and incommensurate combinations are equally possible. In DWNTs the experimental interlayer spacing has been found ranging from 3.4 Å (the interlayer spacing of graphite) to 4.1 Å [167]. A complete treatment of the symmetries in DWNTs and MWNTs was presented by Damnjanović *et al.* [124], based on the line group classifi-

cation scheme already applied to SWNTs (see Sect. 2.5). However, a specific study of the symmetry in commensurate DWNTs (CDWNT) can be found in another paper by the same authors [177], which also considered the geometry-dependent symmetry breaking effect due to the interaction between the walls. Here we just summarize the main results of these papers, which will be useful for understanding the choices operated in the SC calculations presented in the following. In this work they consider a sample of 1280 carbon SWNTs with diameter range $2.8\,\text{Å} \leqslant d_t \leqslant 50\,\text{Å}$ and right-handed chirality. For each tube taken as innermost wall, all possible outer tubes are searched such that the intertube spacing $\left(d_t^{OUT} - d_t^{IN}\right)/2$ differs from the graphite interlayer spacing $\Delta = 3.44\,\text{Å}$ by at most $0.2\,\text{Å}$. It turns out that among the selected 1280 tubes which give rise to 42236 possible pairs, there are only 318 pairs with commensurate walls, which can give CDWNTs (less than 1%). In general, the symmetry group of a double-wall (and even multi-wall) nanotube (W@W′) can be found as intersection of the symmetry groups of the constituent SWNTs: $L_{WW'} = L_W \cap L_{W'}$. Therefore, any geometrical transformation common to both walls leaves the DWNT system invariant. The specific form of a DWNT group depends on the relative position of the walls: even when the constituent tubes are coaxial, there are special high symmetry positions, determined by the relative cylindrical coordinates (Φ, Z), which specify the azimuthal and translational shift of the outer wall with respect to the inner shell. However, this case refers only to some special symmetry elements, called *parities*, which are determined by the coincidence of horizontal axes (*U*,*U*′) and (in achiral pairs) mirror, glide or roto-reflection planes. Instead, the roto-translational symmetries symmetries are the same for all coaxial positions. For the specific formulas defining the roto-translational group of CDWNTs the reader is advised to consult Ref. [177], since for the purposes of this thesis it's actually more relevant considering the high-symmetry positions (Φ, Z) at which these parities occur. In their works, Damnjanović *et al.* pointed out that, according to the topological analysis of the symmetry breaking developed by Abud and Sartori [179], the most stable configurations (corresponding to the minima of the invariant interatomic pairwise Lennard-Jones potential) occur at the positions with maximal symmetry. This topological argument is extremely powerful, since it allows to determine the stable position of the walls by a symmetry analysis without the need to specify the pairwise interaction potential between the walls and finding its minima. In order to find these special high symmetry positions, the so called *symmetry breaking group* has to be found out which actually contains the symmetry of the interaction potential. The breaking group describes the maximal symmetry of the interaction potential. This can be understood by the following considerations. The interaction potential between the walls is

$$V\left(\mathbf{R}, \mathbf{R}'\right) = V\left(\Phi, Z\right) = \sum_{tsu} \sum_{t',s',u'} v\left(\mathbf{r}_{tsu}, \mathbf{r'}_{t's'u'}\right) \tag{5.1}$$

Table 5.1: Stable configurations for incommensurate and commensurate DWNTs found by symmetry analysis by Damnjanović *et al*. A is the translational period of the DWNT. [178]

type of DWNT	Φ_0	Z_0
IDWNT	$\Phi_0 = 0$	Z_0 arbitrary
CDWNT with chiral walls	$\Phi_0 = 0$	$Z_0 = 0$
$(9,0)$ @ $(18,0)$ and $(5,5)$ @ $(10,10)$	$\Phi_0 = \pi/4N$	$Z_0 = A/4$
$(n \neq 9,0)$ @ $(n+9,0)$,$(n \neq 5,n)$ @ $(n+5,n+5)$	$\Phi_0 = 0$	$Z_0 = A/4$

where the atomic positions in the inner wall coordinate system for the inner tube are expressed by Eq. (2.32) and for the outer tube by

$$\mathbf{r}_{tsu} = \left[\rho, (-1)^u \Phi_0 + 2\pi\left(\frac{wt}{N} + \frac{s}{d}\right) + \Phi, (-1)^u Z_0 + \frac{td}{N}T + Z\right], \tag{5.2}$$

according to Damnjanović's convention. This potential is invariant under the transformations generated by all the symmetry of both walls: $ll'V(\mathbf{R},\mathbf{R}') = V(ll'\mathbf{R}, ll'\mathbf{R}')$ for each $l \in \mathbf{L}_W$ and $l' \in \mathbf{L}_{W'}$. Only the transformation from the intersection $\mathbf{L}_W \cap \mathbf{L}_{W'}$ leave both walls invariant, while all other transformations change the relative position of the walls, despite the invariance of the potential. Therefore, the symmetry of the potential is the group $\mathbf{L}_\times$ generated by both $\mathbf{L}_W$ and $\mathbf{L}_{W'}$. Since the symmetry groups of the walls are much larger than the symmetry group of the CDWNT, the breaking group is very large, also for its roto-translational part. In other words, while the roto-translational symmetry of the DWNT is greatly reduced in comparison to those of the walls, the breaking group is much greater. In fact, the following relation holds for the orders of the symmetry groups:

$$|\mathbf{L}^{RT}_{W'W}||\mathbf{L}^{RT}_{B}| = |\mathbf{L}^{RT}_{W}||\mathbf{L}^{RT}_{W'}| \tag{5.3}$$

where $\mathbf{L}^{RT}_{W'W}$ refers to the roto-translational part (RT) of the DWNT symmetry group, $\mathbf{L}^{RT}_{B}$ to the breaking group and $\mathbf{L}^{RT}_{W(W')}$ to the symmetry group of each wall. This relation shows that the greater symmetry remaining in the DWNT, the less the order of the breaking group. This means that the periods of the interaction potential along *Z* and Φ, decrease with the translational *A* and rotational $\frac{2\pi}{N}$ (where $N = GCD\left(n^{IN}, n^{OUT}\right)$) periods of the DWNT. An incommensurate tube, which is actually an aperiodic structure, represents the limiting case in which the potential $V(\Phi, Z)$ is Z independent and thus remains unaffected by translations parallel to the *z* axis (superslippery along the DWNT axis). In Table 5.1 we report the stable configurations found for the studied DWNTs by the symmetry analysis of Damnjanović *et al.* [177, 178]. As already stated above, these positions are all special and the resulting symmetry groups are enlarged by a factor of 2, since in these cases (especially for achiral walls) one can have the coincidence of the *U*

axes which implies the coincidence of vertical or horizontal mirror planes with other mirror or glide planes. These predictions, although based on pure symmetry arguments and not on total energy calculations, can be helpful when considering total electronic energy profiles before computing optical spectra for some selected mutual configurations of the constituent walls.

5.3 Small crystal approach for the electronic structure of DWNTs

In Chapt. 3 we saw how the TB zone-folding method can provide a simple but powerful insight into the electronic structure of ideal single-wall carbon nanotubes. By taking into account the σ orbitals in the hamiltonian, this method can also be extended to include curvature effects, which play a significant role in the electronic structure of small diameter nanotubes ($d_t < 0.7\,\text{Å}$), since Eq. (3.21) overestimates the respective band gaps [83, 84]. A reciprocal space approach like this, however, finds difficulties for problems in which a local symmetry is broken like in the case of functionalization, doping and other disorder effects, such as orientation-dependent interactions among nanotubes and with the surrounding environment. This is the case with some attempts present in literature to solve the TB hamiltonian in reciprocal space for DWNTs, which could be obtained however only for a very restricted number of nanotube geometries with higher symmetry [155, 169, 168]. Formulating the single-particle electronic hamiltonian in real space representation can be an appropriate way to allow for the treatment of symmetry breaking effects due to the geometry-dependent interwall interaction. In some cases, a real space approach was tried [170], which had also been previously adopted for single-wall nanotubes as well [149], but poor attention was paid to the infinite translational periodicity of the nanotube: instead, a sufficiently long portion of the graphene cylinder is selected, such that boundary effects could be disregarded within reasonable approximations. This is usually done for investigating the transport properties of finite-length single and double-wall nanotubes [175]. Moreover, a detailed analysis of variations on the electronic structure and optical absorption features due to any change in the relative positions of the constituent walls is lacking in DWNT literature, except for some limited configurations presented in two papers by Lambin *et al.* [169] and Ho *et al.* [172, 174]. However, in these papers, the choice of the selected configurations was not supported by total electronic energy calculations or topological symmetry-based arguments, like those formulated by Damnjanović. In this section we show how the SC approach can be applied to double-wall nanotube with the possibility of addressing all the previously mentioned issues, with the flexibility of changing the mutual orientations of the constituent walls in any (Φ, Z) position.

5.3.1 Electronic band structure and stable configurations

We consider CDWNTs obtained with zig-zag nanotubes for which the cluster and the boundary conditions to study the relevant electronic states are simpler, as recalled in Chapt. 4, but the calculations can be done for all other type of nanotubes as well. Furthermore, among all possible ways to combine SWNTs into DWNTs, we consider those with an interlayer distance between $0.334\,\mathrm{nm}$ (graphite interlayer spacing) and $0.360\,\mathrm{nm}$, as it was experimentally found recently [163]. For zigzag DWNTs, we find in this interval all combinations of type $(n,0)@(n',0)$ such that $n - n' = 9$ which have an interlayer of $0.352\,\mathrm{nm}$, for CC bond-length of $0.142\,\mathrm{nm}$. We consider in our examples a semiconductor-semiconductor (S-S) DWNT, such as (5, 0)@(14, 0) and a metallic-metallic (M-M) one, such as (9, 0)@(18, 0). The TB hamiltonian for a DWNT can be written as a sum of the TB hamiltonians corresponding to the inner and outer nanotubes plus a perturbative term H_{inter} for the electronic hopping from a site l on the inner tube to another site m on the outer tube.

$$H_{DWNT} = H_{in} + H_{out} + H_{inter} \quad \text{with} \tag{5.4}$$

$$H_{in(out)} = \sum_{t=IN,OUT} \sum_{\sigma=\uparrow,\downarrow} \varepsilon_\pi \sum_{i=1}^{2Nt} c_{i,\sigma}^\dagger c_{i,\sigma} + t_\pi \sum_{i=1}^{2Nt} \sum_{j\in n.n} \left(c_{i,\sigma}^\dagger c_{j,\sigma} + c_{i,\sigma} c_{j,\sigma}^\dagger \right) \tag{5.5}$$

The intertube interaction is considered to decay exponentially with the distance $d_{l,m}$ between the sites according to:

$$H_{INTER} = \beta_\pi \sum_{\langle l,m\rangle,\sigma}^{out,in} \cos\theta_{l,m} \exp\left[\left(d_{l,m} - \Delta \right) / \delta_\pi \right] \left(c_{l,\sigma}^\dagger c_{m,\sigma} + c_{l,\sigma} c_{m,\sigma}^\dagger \right) \tag{5.6}$$

In the above expression for H_{INTER}, Δ is the interlayer spacing (semidifference between diameters), δ_π is the decay constant for π orbitals, $\theta_{l,m}$ is the angle between π orbitals pointing perpendicularly to the tubes' surface, $\beta_\pi$is the intertube hopping amplitude integral. According to literature, values for β_π can range from $t_\pi/8$ to $1.0\,\mathrm{eV}$ and $\delta_\pi = 0.045\,\mathrm{nm}$ [171, 180, 181]. We recall that the intertube hopping interaction depends on the mutual orientation of the constituent coaxial SWNTs, namely on the azimuthal angle $\Delta\Phi$ and the translation ΔZ parallel to the tube axis. Therefore, we can write:

$$\theta_{l,m} \equiv \theta_{l,m}\left(\Delta\Phi\right) \qquad d_{l,m} \equiv d_{l,m}\left(\Delta\Phi, \Delta Z\right) \tag{5.7}$$

When setting up the periodic SC hamiltonian, one has to be careful that no intertube matrix elements are dropped by restricting the length cutoff of interwall coupling only to first or second nearest neighbouring atoms. In this case, we imposed no restrictions on the interatomic distance between atoms on different tubes, instead a cutoff limit was set on the energy value of intertube matrix elements to be stored in memory for the diagonalization: $H_{INTER}\left(l,m\right) > 10^{-3}\,\mathrm{eV}$. No significative difference was found between the

eigenvalues computed by storing the full intertube off-diagonal block matrix and the one with the cutoff.

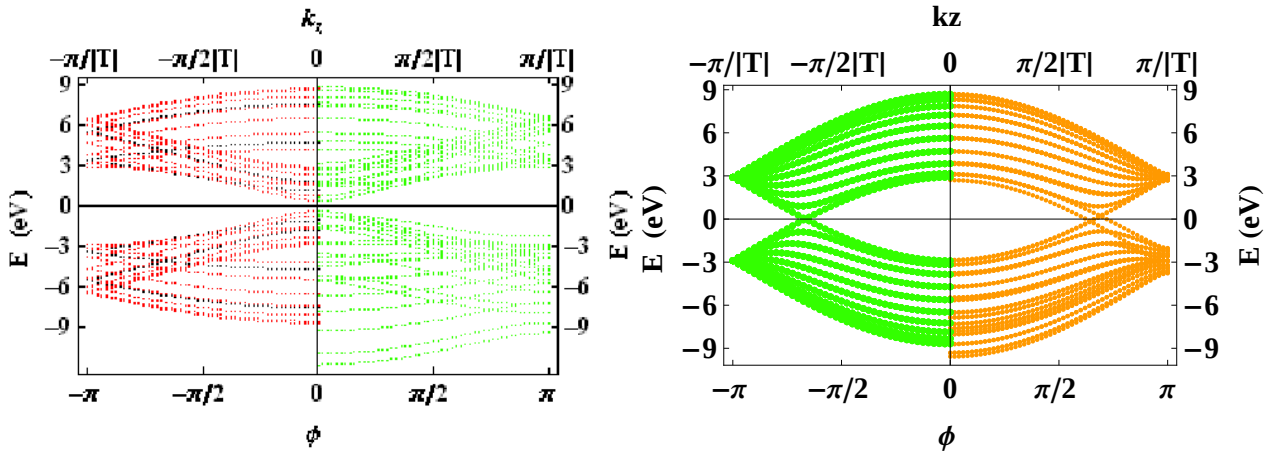

Fig. 5.1: Electronic band structure of (5, 0)@(14, 0) (left) and (5, 5)@(10, 10) (right) DWNT at default configuration $(\phi = 0, \Delta Z = 0)$ with non interacting costituent SWNTs (left panel) and with intertube hopping (right panel, $\beta_\pi = 1.0\,\mathrm{eV}$). Color legend for (5,0)@(14,0): black (inner SWNT), red (outer SWNT), green (DWNT with interaction on). Color legend for (5,5)@(10,10): green (outer SWNT), inner SWNT not shown for clarity (coincidence with some bands of outer SWNT), orange (DWNT with interaction on)

In Fig. 5.1 (left) the electronic dispersion relation obtained from diagonalization of the hamiltonian block matrix for DWNT (5,0)@(14,0) is shown for the default configuration $(\Delta\Phi = 0, \Delta Z = 0)$ using $\beta_\pi = 1.0\,\mathrm{eV}$. The main effect of H_{INTER} is the lifting of the doubly degenerate bands and the breaking of the symmetry of valence and conduction bands with respect to the Fermi level. This is more evident far from Fermi level and stronger for valence bands, rather than conduction bands. This effect is also called electron-hole asymmetry. A tiny gap of the order of the meV is also opened in metallic (9,0)@(18,0) DWNT, due to the degeneracy splitting of the bands, as predicted in Ref. [68], but it has not been reported here since it is difficult to notice in the picture. However it can be more easily seen in the DOS profile (Fig. 5.3), which will be discussed in the following. Early tight-binding investigations of commensurate DWNTs overlooked this asymmetry due to an over-simplified modeling of the interwall coupling [155], while for more recent models and parametrizations which adopt the form of Eq. (5.6) this feature is already included [171, 175]. Unlikely in armchair DWNTs (see Fig. 5.1 right), the band structure of the zigzag systems remains almost unperturbed near the Fermi energy. The explanation can be found by considering that the discrete angular momentum asso-

ciated with these states depends on the tube circumference and the rotational symmetry of each of the constituent shells. Thus, in principle, bands related to different walls have different rotational symmetry and in general the combined DWNT system does not share the rotational symmetry of the individual shells (see for instance the case in which the orders of the principal rotational axes of the walls have no common divisor except unity). As long as the interwall coupling is sufficiently weak and smooth, one can reasonably expect that the original symmetry will be preserved and the hybridization between states belonging to inner and outer wall will be minimal. We can now consider how the total π electronic energy varies as a function of the orientational parameters, namely the azimuthal shift $\Delta\Phi$ and the translational shift ΔZ. As noted in the previous section, Damnjanović *et al.* [177] found, by symmetry arguments, a minimum in total energy at $\Delta\Phi = \pi/36$ and $\Delta Z = A/4$ for $(9,0)@(18,0)$, and at $\Delta\Phi = 0$ and $\Delta Z = A/4$ for $(5,0)@(14,0)$ (in zigzag nanotubes $A = |T| = 0.426\,\mathrm{nm}$).

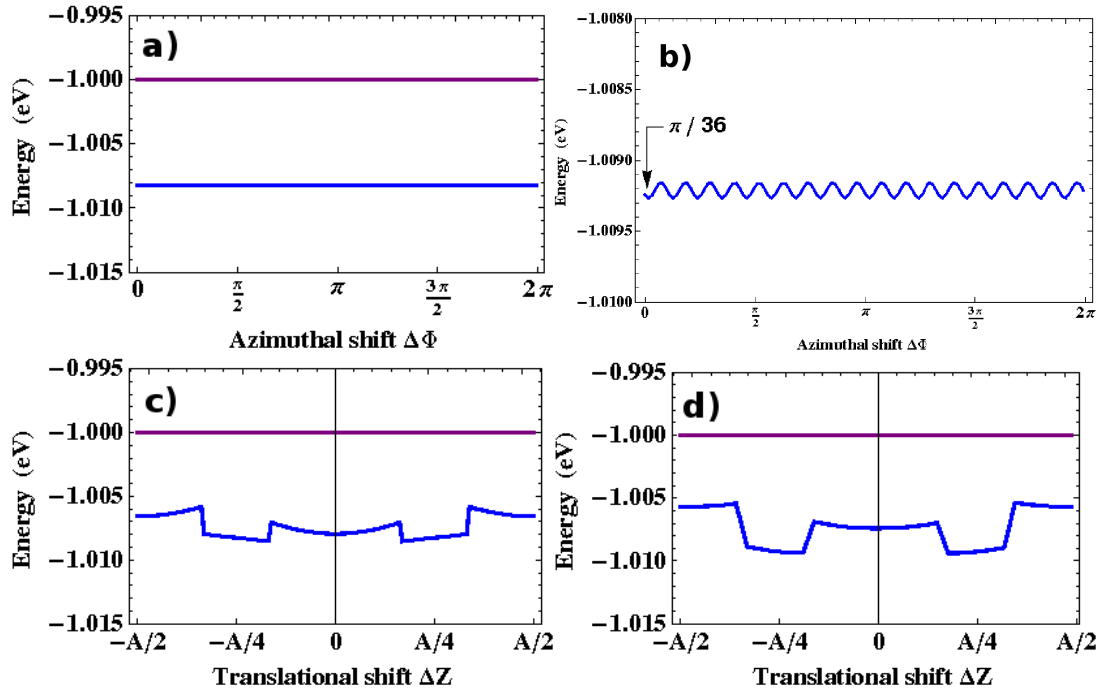

Fig. 5.2: (Color online) Dependence of total π electronic energy at $k_z = 0$ on a, b) azimuthal $\Delta\Phi$ and c, d) translational ΔZ for DWNTs $(5,0)\,@\,(14,0)$ (left) and $(9,0)\,@\,(18,0)$ (right) with $\beta_\pi = 1.0\,\mathrm{eV}$ (blue color). Energy data are normalized to absolute values of the total π electronic energy of the respective non-interacting constituent SWNTs (purple color).

Figg. 5.2 (a-d) shows some of our results summing to convergence the π electronic energy eigenvalues of the valence states obtained by changing the phase of the boundary

condition. According to Damnjanović *et al.* one observes in Figg. 5.2 c) and d) that the dependence on ΔZ has two minima around $\pm A/4$ using $\Delta\Phi = 0$ for $(5,0)@(14,0)$ and $\Delta\Phi = \pi/36$ for $(9,0)@(18,0)$. On the other hand, the dependence on $\Delta\Phi$, at $\Delta Z = A/4$ (Figg. 5.2 a) and b), shows a periodic oscillatory behaviour, with an energy minimum located at $\Delta\Phi = \pi/36$, only for $(9,0)@(18,0)$. Similar plots for the dependence of the total π electronic energy on $(\Delta\Phi, \Delta Z)$ have been obtained by considering only the $k_z = 0$ states in the 1D BZ, which therefore represent the leading contribution to the total energy profile. In the following calculations of DOS and optical absorption spectra we will use $\Delta Z = A/4$ for both DWNTs and $\Delta\Phi = 0$ and $\pi/36$ for $(5,0)@(14,0)$ and $(9,0)@(18,0)$, respectively. Interestingly, in this case the electronically most stable configurations are found to coincide with the most stable configurations from a crystallographic point of view, reported in Table 5.1.

5.3.2 Optical properties

By inspection of the electronic band structure of Fig. 5.1, one can see that the lowest energy vHs for zigzag DWNTs are still determined by the $k_z = 0$ states in the 1D BZ. This fact allows us to compute the optical spectra with minimal effort by including only this k-points into the JDOS and the optical matrix elements with the sum over states method, as done in Sect. 4.6. Instead, in armchair DWNTs, the extrema of valence and conduction band giving vHs do not occur at the same k-point, because of the stronger distorsion at Fermi level introduced by the interlayer coupling. This would require to include more k-points from the 1D BZ, in particular a more refined sampling around $\phi = 2\pi/3$, where k_F occurs for the unperturbed armchair SWNTs. However, this issue will be addressed in future work, since we have chosen to focus mainly on zigzag species, in order to introduce electronic correlation effects (see next chapter) into the tight-binding hamiltonian. By comparing DOS profiles for the chosen (Φ, Z) configurations for both DWNT geometries, one can observe that the azimuthal shift doesn't affect the DOS structure (not shown), while the translational shift alters considerably the spectra for both geometries with respect to the default configuration at $\Delta Z = 0$. Fig. 5.3 reports the DOS by changing ΔZ from 0 to $A/4$ together with the DOS spectra of the constituent non-interacting SWNTs. One can see important variations, also at low energies, for both type of DWNTs suggesting that also the optical spectra will have new features with respect to that of the constituent SWNTs. In particular one observes that also the DOS at the Fermi level $E = 0$, which is constant in the case of the metallic tubes and is calculated as a peak in our calculation for (9,0)@(18,0) due to the finite sampling of the Brillouin zone, suffers important changes.

Now, we consider the inclusion of the optical matrix element into the JDOS spectrum for the zigzag DWNTs for determining the SC absorption spectrum for these systems. Starting from the DWNT eigenvectors, in which the inner and outer tube wavefunction electron characters are mixed due to H_{INTER}, the dipole matrix elements for z-polarized

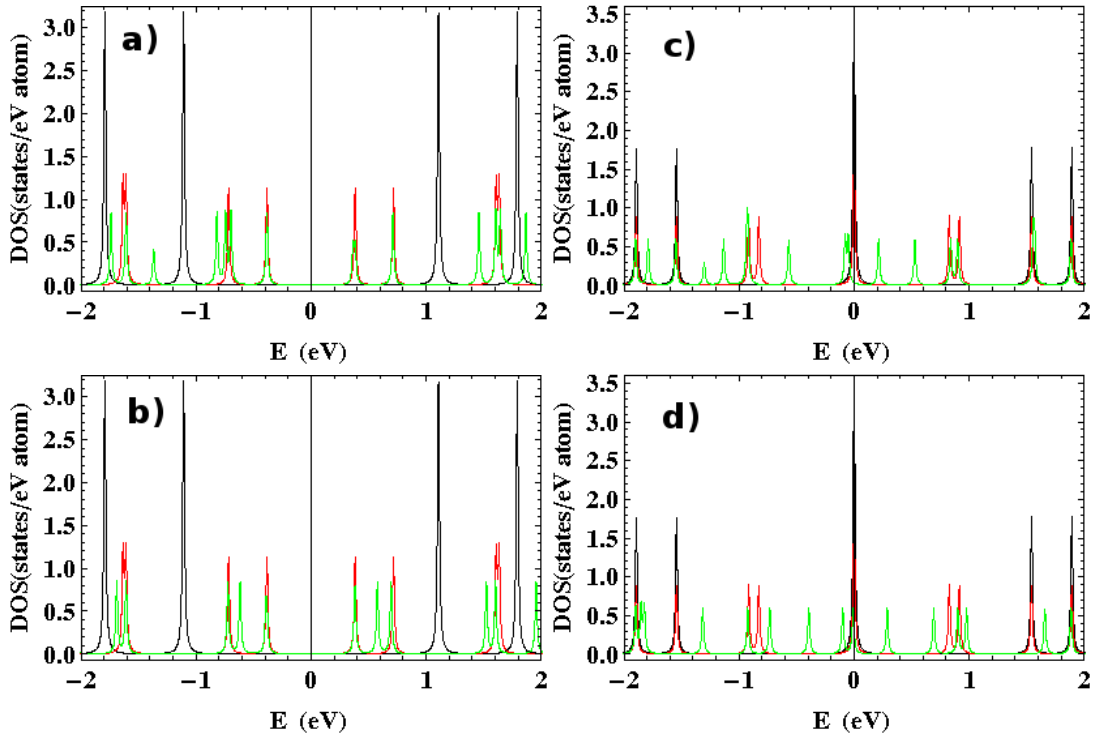

Fig. 5.3: (Color online) Electronic density of states ($\beta_\pi = 1.0\,\mathrm{eV}$) for (5, 0)@(14, 0) (left) with $(\Delta\Phi = 0, \Delta Z = 0)$ (upper) and $(\Delta\Phi = 0, \Delta Z = A/4)$ (bottom). DOS spectra for (9, 0)@(18, 0) (right) with $(\Delta\Phi = \pi/36, \Delta Z = 0)$ (upper) and $(\Delta\Phi = \pi/36, \Delta Z = A/4)$ (bottom). Color legend: inner SWNT (black), outer SWNT (red), DWNT with intertube interaction (green).

light are calculated with the aid of Eq. (4.25) for each constituent SWNT, that is

$$\mathbf{D}^{DW} \approxeq \sum_{t=in,out} \langle \widetilde{\Psi}_t^c | \nabla_z | \widetilde{\Psi}_t^v \rangle = \tag{5.8}$$

$$\sum_{t=in,out} \sum_{h=0}^{Nt-1} \sum_{l=1,3} \sum_{s'=A,B} \widetilde{c}^*_{l,s'} \sum_{s=A,B} \widetilde{c}_{h,s} \langle \phi_z^t(r - \mathbf{R}_{l,s'}) | \nabla_z | \phi_z^t(r - \mathbf{R}_{h,s}) \rangle .$$

where the perturbed nature of the DWNT eigenfunctions has been emphasized by the use of the tilde. Contributions of mixed type between p_z orbitals belonging to different nanotube shells can be safely ignored due to the fast decay rate of the π orbitals: as a matter of fact, the absolute value of m_{opt} is already very small at a distance of $2a_{CC}$ and is practically zero at the typical graphitic interlayer distance of $0.344\,\mathrm{nm}$ for all kinds of molecular orbital configurations [122]. Thus the resulting optical matrix elements are

obtained according to the following approximation

$$M^{opt}_{z\,DW} = |\langle\widetilde{\Psi}^{c}_{DW}|\mathbf{P}\cdot\nabla_z|\widetilde{\Psi}^{v}_{DW}\rangle|^2 \approxeq |\langle\widetilde{\Psi}^{c}_{in}|\mathbf{P}\cdot\nabla_z|\widetilde{\Psi}^{v}_{in}\rangle|^2 + |\langle\widetilde{\Psi}^{c}_{out}|\mathbf{P}\cdot\nabla_z|\widetilde{\Psi}^{v}_{out}\rangle|^2 \quad (5.9)$$

As the degree of wavefunction mixing due to the intertube electronic coupling is quite weak because of the different azimuthal symmetries involved for the two shells, one can reasonably expect that for a given $v \rightarrow c$ vertical transition one of the two addends will be dominating over the other. Ratios of $|\langle\widetilde{\Psi}^{c}_{in}|\mathbf{P}\cdot\nabla_z|\widetilde{\Psi}^{v}_{in}\rangle|/|\langle\widetilde{\Psi}^{c}_{out}|\mathbf{P}\cdot\nabla_z|\widetilde{\Psi}^{v}_{out}\rangle| \sim 1 \div 10^{-4}$ or inverse could be verified for a $(5,0)@(14,0)$ DWNT. Eventually the optical absorption intensity can be again calculated for DWNTs employing the SOS method, as shown in Eq. (4.32) for SWNTs. As previously noticed for the DOS of both DWNT species, the effect of geometrical parameters on the optical absorption spectra are more pronounced when a translational shift ΔZ is considered with respect to the default configuration at $(\Delta\Phi = 0, \Delta Z = 0)$, rather than an azimuthal shift $\Delta\Phi$ (Fig. 5.4). In general, additional absorption peaks can be found originating from the lifting of the band degeneracies due to the symmetry breaking effect of H_{INTER}. In $(5,0)@(14,0)$ with ($\Delta\Phi = 0$, $\Delta Z = 0$) however the peak corresponding to the E^S_{11} transition of SWNT (14,0) is poorly affected by the intertube coupling, while the new features are more visible around the E^S_{22} transition region, where two peaks are now found.
The lowest E^S_{22} peak, originating from the E^S_{22} peak of (14,0), is also slightly downshifted in energy if compared with the one of the non-interacting system. The estimated magnitude of the downshift is of $25\,\mathrm{meV}$, while the new highest E^S_{22} peaks are upshifted of $100\,\mathrm{meV}$. Instead, for the configuration ($\Delta\Phi = 0$, $\Delta Z = A/4$) the new E^S_{22} peak is downshifted of $200\,\mathrm{meV}$. As a matter of fact, RRS measurements on DWNTs samples have confirmed that the most important changes on the spectral features of the constituent SWNTs are found in the E^S_{22} transition energy region of the Kataura plot [166]. Moreover, by inspecting the transition energy interval around the E^S_{11} of the (5,0) tube, which is also close to the E^S_{22} range of the outer tube, it can be stated that the change brought by the intertube hopping interaction alters more consistently the inner tube electronic structure rather than the outer tube one (Fig. 5.4), as discussed in Ref. [166]. For metallic DWNT (9,0)@(18,0) the spectral features are richer both in proximity of E^M_{11} and E^M_{22} of the (18,0) tube, but there are also new low energy peaks originating from the gap opening at the Fermi level, as observed in the DOS spectra. Finally, we also compare the (5, 0)@(14, 0) DWNT optical spectra for three different values of the intertube hopping amplitude (see Fig. 5.5), namely $\beta = t_\pi/8$ [171], $\beta = t_\pi/4$ and $\beta = 1.0\,\mathrm{eV}$ [180, 181]. All the observations made above are still valid for the intermediate value $\beta = t_\pi/4$, while for $\beta = t_\pi/8$ only the spectral region above $2.0\,\mathrm{eV}$, is visibly affected by the intertube coupling, as shown in Fig. 5.6, where a shifted peak related to the inner tube is found.

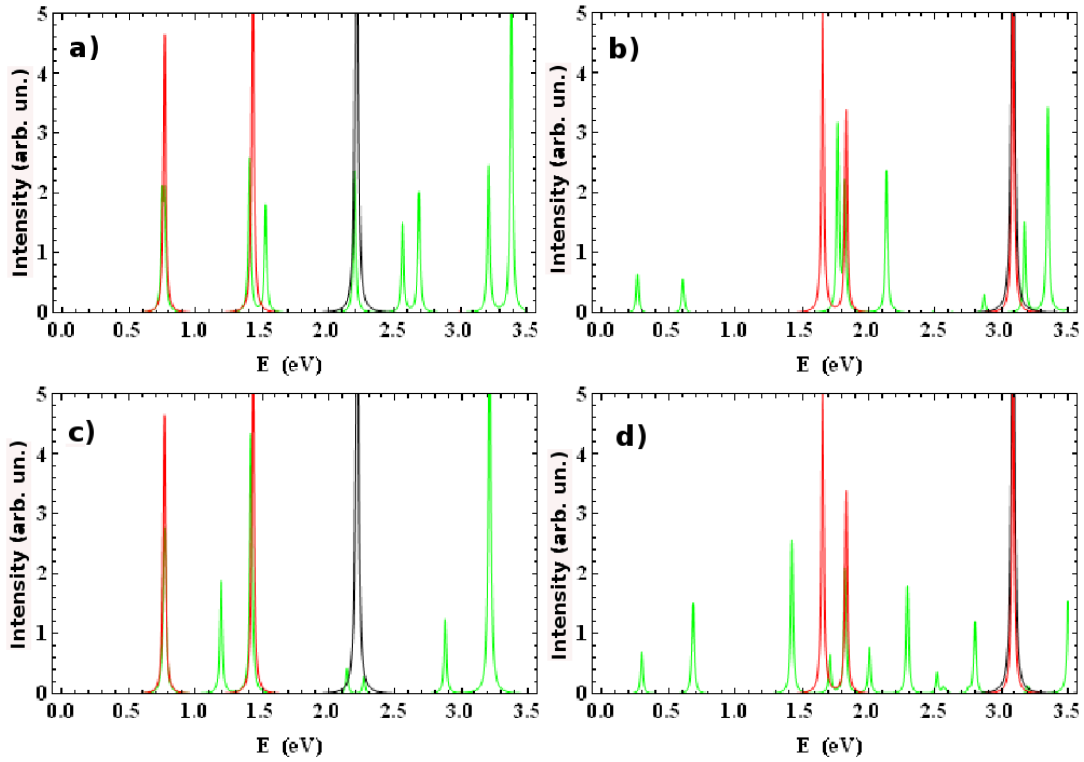

Fig. 5.4: (Color online) Absorption spectra ($\beta_\pi = 1.0\,\mathrm{eV}$) for (5, 0)@(14, 0) (left) with $(\Delta\Phi = 0, \Delta Z = 0)$ (upper) and $(\Delta\Phi = 0, \Delta Z = A/4)$ (bottom). Absorption spectra for (9, 0)@(18, 0) (right) with $(\Delta\Phi = \pi/36, \Delta Z = 0)$ (upper) and $(\Delta\Phi = \pi/36, \Delta Z = A/4)$ (bottom). Intensity is given in arbitrary units. Color legend: inner SWNT (black), outer SWNT (red), DWNT with intertube interaction (green).

5.3.3 Conclusions, summary and future perspectives

As recalled in the introduction, besides Photoluminescence, Resonance Raman spectroscopy allows to characterize the nanotubes present in a sample by assigning their radial breathing modes (RBM). The assignment is based on calculated Kataura plots [127] which correlate SWNT electronic excitations with their diameters. A similar route was also attempted, with less success, for DWNTs [166], with the basic assumption that these systems can be modelled as two almost non-interacting SWNTs. Based on this assumption, the electronic structure of a DWNT is simply the sum of the electronic structures of the constituent tubes. Perturbative effects due to weak intertube electronic coupling are considered negligible or at least responsible for a slight shift on the single-particle transition energies around Fermi level. By applying the SC approach to DWNTs, we have shown that this picture is only partially correct and that new transitions can be ex-

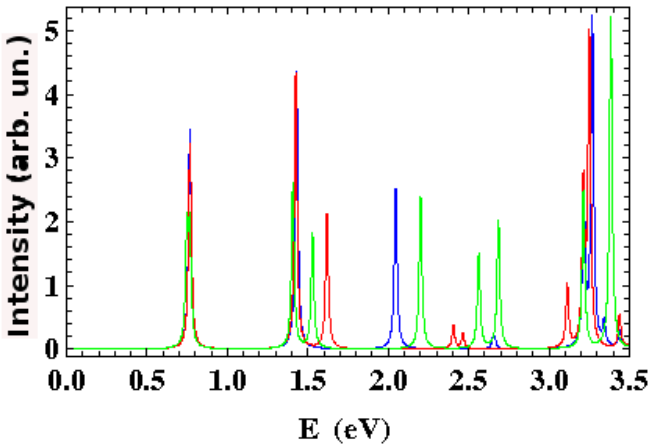

Fig. 5.5: (Color online) Absorption spectra for (5, 0)@(14, 0) (left) with $(\Delta\Phi = 0, \Delta Z = 0)$ calculated for different values of the intertube hopping parameter β_π. Color legend: $\beta = t_\pi/8$ (blue), $\beta_\pi = t_\pi/4$ (red), $\beta_\pi = t_\pi/8 \times 2.75 = 1.0\,\mathrm{eV}$ (green).

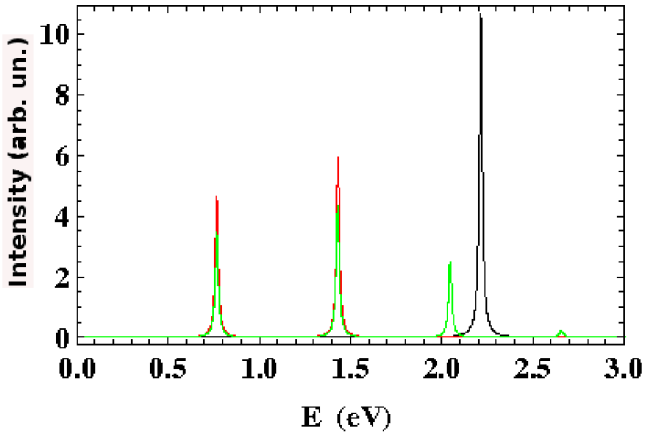

Fig. 5.6: (Color online) Absorption spectra for (5, 0)@(14, 0) (left) with $(\Delta\Phi = 0, \Delta Z = 0)$ calculated for non interacting SWNT constituents $(\beta_\pi = 0.\,\mathrm{eV})$ and $\beta_\pi = t_\pi/8$. Color legend: $\beta = t_\pi/8$ (green), inner SWNT (black), outer SWNT (red).

pected originating from the symmetry breaking of the band degeneracies in particular in the visible range. The optical spectral features have been shown to be strongly affected by the orientational configuration of the constituent tubes, particularly by the translational shift parallel to the DWNT axis. The results allow to understand the usual difficulties in assigning the Resonance Raman spectra of double wall nanotubes since important variations of the electronic spectra of these carbon nanotubes are found with respect to those of the constituent single wall nanotubes. Moreover, although variations of the spectra can be found for all the values of the intertube hopping parameters found in literature (Fig. 5.5), a careful evaluation of this parameter must be obtained for an appropriate electronic structure calculation for DWNTs. As a matter of fact, the widely used value of the intertube hopping parameter $\beta = t_\pi/8$ adopted since the work by Roche *et al.* [171], was introduced ten years earlier by Lambin *et al.* [169], who in turn obtained it from fitting *ab initio* calculations for turbostratic graphite [79, 80], which well reproduced experimental results for this system. In other cases, such as $\beta = 1.0\,\mathrm{eV}$ by M. Grifoni and S. Wang [180, 181], the reasons behind the choice have not been made clear at all. Several full *ab initio* calculations of the electronic properties of double-wall nanotubes have also been done [182, 183, 176, 184], although they're notoriously difficult because of the large unit cells involved in the computation, but still a well- documented tight-binding parametrization from fitting DFT calculations for the interlayer coupling in DWNTs could not be found. Finally, we point out that the experimental Raman measurements on DWNTs actually provide averaged electronic spectra of these systems, since each wall can assume in principle any orientation with respect to the other shell. This holds in particular for incommensurate DWNT pairs, for which geometric correlation is poor and frictionless dynamics has been predicted [185] and experimentally verified [186]. On the other hand, for deep minima in total energy, which occur prevalently in commensurate DWNTs, one can reasonably expect that the corresponding geometric configurations will play a dominant role in determining the resulting spectral profile, since the constituent walls will hardly change their mutual positions, because of the higher optential energy barrier. Therefore more accurate molecular dynamics calculations which take into account also this aspect need to be performed in the future in order to obtain reliable Kataura plots for these systems.

Chapter 6

Electronic correlation effects

In this chapter, starting from experimental evidence, we will introduce the issue of the electronic correlation effects in single-walled nanotubes, which are reflected in the excitonic nature of their optical spectral features. The treatment of many-body effects in these systems requires the necessity of going beyond the single-particle approximation of tight-binding methods. The first section presents a brief overview of the main theoretical approaches developed in order to treat excitonic effects in SWNTs, together with a discussion of their most relevant results and drawbacks of the respective methods. In the second section we will present the method developed in this thesis, which combines the simple but powerful description of the Hubbard model for correlated fermionic systems with the features of the small crystal approach for the treatment of extended periodic systems. A whole section has also been devoted to the description of the computational implementation and issues behind the method. In the final part the results of the calculations for small-size systems are presented and discussed in relation to the most relevant literature works. Then, future work directions are suggested for further research developments.

6.1 Many-body effects and electronic correlations in SWNTs

6.1.1 Experimental evidence for the limits of tight-binding

In Chapt. 3 the tight-binding method was introduced in order to provide a simple but realistic description of the optical properties of SWNTs. In the introductory chapter we highlighted the importance of tight-binding methods in supporting the interpretation of experimental Kataura plots obtained by Raman and photoluminescence spectroscopy. We recall that these tools are widely used in nanotube science for assigning the spectral features (i.e. the measured transition energies) to the respective SWNT diameters and chiralities. Early Raman studies on SWNTs were interpreted in terms of the simple tight-binding (STB) scheme for π-electrons according to the zone-folding method applied to the graphene sheet, as presented in Chapt. 3. This scheme however doesn't

take into account long-range interactions, curvature effects and σ-π rehybridization effects, which cannot be neglected in small diameter nanotubes. As a consequence, more refined tight-binding based methods have been developed, in order to provide accurate and reliable interpretations of the experimental Kataura plots also in the small diameter range. In particular, we mention the symmetry-adapted non-orthogonal TB method by V. N. Popov [84], which takes into account nanotube curvature and structural optimization effects in the electronic hamiltonian. Soon afterwards, a similar approach was followed by Saito's group [122, 132], with the so-called *extended tight-binding* method (ETB). Within this framework, they use the tight-binding parametrization for carbon determined from density-functional theory with local density approximation and a local orbital basis set [70, 71]. Then they include curvature-induced rehybridization by alignment of the atomic orbitals along directions normal and tangential to the SWNT sidewall. Subsequently, geometrical structure optimization is performed by minimization of the total energy of the system with respect to the atomic degrees of freedom. In general, the constructed ETB Kataura plot showed a good agreement both with first principles calculations (long-range interactions are taken into account) and with experimental PL and RRS Kataura plots, in particular for the spreads of the SWNT families of constant $2n+m$ (Fig. 6.1). This experimental family spread is attributed to the relaxation of the geometrical structures of the SWNTs [122, 132].

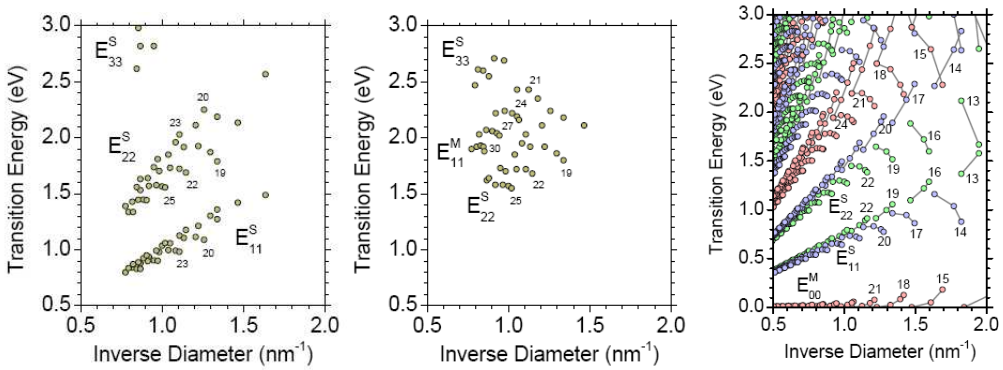

Fig. 6.1: Experimental Kataura plots derived from PL (upper left) and RRS (upper right) measurements on HiPCO SWNTs suspended by SDS surfactant in acqueous solution. The numbers show the families of constant $2n+m$. ETB Kataura plot (bottom) as a function the inverse diameter $1/d_t$: long-range atomic interactions, curvature effects and geometrical optimizations are taken into account in the calculation. Taken from Ref. [122].

However, in spite of a good agreement in the family spread, both PL and RRS experimental Kataura plots exhibit an overall blueshift of the transition energies by about $200 - 300\,\mathrm{meV}$ from the ETB Kataura plot. Moreover, the E_{22}^S to E_{11}^S ratio in the experimental Kataura plots tends to 1.8 in the large diameter d_t limit (where the family

spread is small), while in the ETB predicted Kataura plot the E_{22}^S/E_{11}^S ratio for large d_t tends to 2. These can be considered the two main effects of the many-body Coulomb interactions on the single-particle transition energies E_{ii}, which cannot be accounted by ETB method.

6.1.2 Theoretical investigations of exciton photophysics in SWNTs

Although many-body were already investigated in 1997 in a theoretical work by T. Ando based on the effective-mass approximation [194], only in 2004 it became definitely clear that electron interactions play an important role in determining the optical transition energies in these systems [197]. As previously explained, this happened because the experiments were always interpreted in the framework of simple non-interacting models, such as tight-binding calculations. Because of the spatial confinement of electrons in the quasi-one dimensional structure of the SWNTs and, consequently, the poor dielectric screening, the Coulomb interactions between photoexcited electrons and electrons in the ground state are strongly enhanced if compared to bulk semiconductors [187]. As pointed out in the pionieristic work by Ando, the electron-electron (*e-e*) interactions lead to two competing opposite effects: a) the increase of the single-particle transition energy by the quasi-particle self-energy and b) the binding of photoexcited electrons and photogenerated holes (*e-h*) into excitons whose binding energies are comparable but slightly smaller than the quasi-particle self-energies. The resulting effect is thus a moderate blueshift of the single-particle transition energies due to the Coulomb *e-e* interactions and the exciton *e-h* attraction, together referred to as the many-body interactions. A more detailed analysis of the many-body effects was conducted in a seminal paper by Kane and Mele [196], starting from an effective-mass theory for statically screened interacting electrons in graphene. In this work they examine the many-body interactions separately: a) on scales larger than the tube circumference πd_t, where both *e-e* and *e-h* Coulomb interactions have 1D long-range character; b) on length scale smaller than πd_t, where the many-body interactions have 2D short-range character. Therefore, in principle one can write for the transition energy E_{ii} including many-body effects:

$$E_{ii} = E_{ii}^{e} + E_{ii}^{2Dee} + E_{ii}^{1Dee} - E_{ii}^{2Deh} - E_{ii}^{1Deh}, \tag{6.1}$$

where E_{ii}^{e} is the single-particle transition energy, E_{ii}^{ee} is the quasiparticle self-energy and E_{ii}^{eh} is the binding energy of the lowest bright exciton. As explained above, both E_{ii}^{ee} and E_{ii}^{eh} in Eq. (6.1) are split into two terms competing to short-range (2D) and long-range (1D) interactions, respectively. The E_{ii}^{2Dee} self-energy is given by the logarithmic correction term [196, 122]

$$E_{ii}^{2Dee} = \frac{\sqrt{3}}{2}\left(\varepsilon s - t\right)\Delta k_i a \frac{g}{4} \ln \frac{\Lambda}{\Delta k_i}, \tag{6.2}$$

where ($\varepsilon = 5.372$ eV, $s = 0.151$, $t = 3.370$ eV) are the values for the ETB parameters used in Saito's papers [122], g is the Coulomb interaction parameter, and Λ is an ultraviolet interaction cutoff, all of which depend on the dielectric constant κ of the SWNT environment, and Δk_i is the critical wavevector measured from the K point in the 2D Brillouin zone. The latter is given by $\Delta k_1^S = 2/(3d_t)$, $\Delta k_2^S = 4/(3d_t)$, and $\Delta k_1^M = 6/(3d_t)$ for the E_{11}^S, E_{22}^S, and E_{11}^M transition energies, respectively. The E_{ii}^{2Deh} binding energy in Eq. (6.1) vanishes due to the absence of excitons in the graphene sheet. The E_{ii}^{1Dee} and E_{ii}^{1Deh} terms scale with the SWNT diameter d_t, the reduced mass of the exciton μ_{ii} (which is diameter and chirality dependent), and the dielectric constant κ of the SWNT environment. Thus, the E_{ii}^{1Dee} and E_{ii}^{1Deh} energies develop family patterns. In small diameter SWNTs, the E_{ii}^{1Dee} and E_{ii}^{1Deh} terms significantly exceed the E_{ii}^{2Dee} self-energy of Eq. (6.1) due to a strong spatial confinement of the Coulomb interaction. Neverthless, as shown by Kane and Mele, E_{ii}^{1Dee} and E_{ii}^{1Deh} nearly perfectly cancel each other. If we assume that that these energy terms completely cancel out, which is actually a good approximation, then Eq. (6.1) becomes $E_{ii} = E_{ii}^e + E_{ii}^{2Dee}$ and the resulting values for the transition energies are moderately blueshifted from the ETB single-particle values, as found experimentally. The difference between the experimental E_{ii} and the ETB E_{ii}^e transition energies as a function of the wavevector Δk_i with the to the functional form of Eq. (6.2). This yields the following values for the fitting parameters, which are reported in Saito's papers: $g = 1.7$ and $\Lambda = 3.5$ nm^{-1} [122], in good agreement with Kane and Mele's values [196]. Since E_{ii}^{2Dee} only depends on d_t and is independent of θ, Saito and Dresselhaus in their work again interpret the experimental Kataura plots of SWNTs (and DWNTs as well) on the basis of ETB calculations: the single-particle transition energies are simply shifted by $200 - 300$ meV to account for the logarithmic κ-dependent (according to the environment) correction of the E_{ii}^{2Dee} term [132, 204, 205, 166].
However, besides Ando's effective-mass approximation method [194, 86, 211], in these years several other theoretical studies were carried out in order to explore the photophysics of excitons in SWNTs. Among first-principles methods, two different classes of calculation scheme for excitons can be found in nanotube literature: density-functional calculations with Dyson's equation for self-energy and Bethe-Salpeter equation (BSE) for the electron-hole correlation, performed by the groups headed by S.G. Louie [199] and E. Molinari [200, 203], respectively; Hartree-Fock Configuration Interaction with single-excited basis set, performed by the group headed by S. Mazumdar [208, 210]. Additionally, other schemes were adopted first by Pedersen [201] (a variational approach, in which a Gaussian trial wavefunction is used to estimate excitonic binding energies) and later by Perebeinos *et al.* [202] (a semi-empirical excitonic calculation based on a tight-binding modeling of quasi-particle energies and an Ohno potential for electron-hole interaction) for determining exciton scaling relations in these systems. Later, ETB calculations with BSE were also performed by the group of Saito and Dresselhaus [204, 205]. In the following we will overview only first-principles calculations, since at the moment only these methods are capable of providing a reasonably accurate description of the rich

excitonic structure in SWNTs.

BSE-based schemes In the ab-initio calculations performed by Louie [199] the optical absorption spectra with electron-hole excitations are calculated in three steps: (i) the electronic ground state is obtained via pseudopotential density-functional theory within local density approaximation (LDA) and with a plane-wave basis set; (ii) the quasiparticle energies $E_{n\mathbf{k}}$ are obtained within the *GW* approximation for the electron self-energy Σ by solving the Dyson equation

$$\left[-\frac{\nabla^2}{2} + V_{ion} + V_{Hartree} + \Sigma\left(E_{n\mathbf{k}}\right)\right]\Psi_{n\mathbf{k}} = E_{n\mathbf{k}}\Psi_{n\mathbf{k}} \tag{6.3}$$

and finally (iii) the coupled electron-hole excitation energies Ω^S and relative spectrum are calculated by solving the Bethe-Salpeter equation of the two-particle Green's function

$$\left(E_{c\mathbf{k}} - E_{v\mathbf{k}}\right)A^S_{vc\mathbf{k}} + \sum_{\mathbf{k}'v'c'}\langle vc\mathbf{k}|K^{\mathrm{eh}}|v'c'\mathbf{k}'\rangle A^S_{v'c'\mathbf{k}'} = \Omega^S A^S_{vc\mathbf{k}}, \tag{6.4}$$

where $A^S_{vc\mathbf{k}}$ is the exciton amplitude, K^{eh} is the electron-hole interaction kernel, and $|c\mathbf{k}\rangle$ and $|v\mathbf{k}\rangle$ are the quasi-electron and quasi-hole states, respectively. This method can account for the ratio problem, the large self-energy corrections ($\sim 20\%$ of the single-particle gap) and exciton binding energies ($0.1 - 1.0\,\mathrm{eV}$) found in photophysics experiments on SWNTs [197, 198]. Although very accurate, BSE-based methods are computationally very intensive, since they scale as the number of atoms to the 4th power. As a matter of fact, Louie *et al.* reported that the calculation for the (8,0) tube (with 32 atoms in the unit cell) was very challenging, as well as (4,2) tube (with 56 atoms), which was far more difficult.

Soon later, a more efficient BSE-based scheme was proposed by the group headed by E. Molinari [200, 203] to handle the computation of (4,2) and (6,4) tubes. They used a symmetrized basis set taking advantage of the screw symmetry of nanotube systems. This approach also allows for a better physical understanding of the problem, since it allows to characterize the symmetry of excitonic wavefunctions and which transitions are allowed or forbidden by certain selection rules [198].

Neverthless, the calculations reported until now by these research groups have been performed just for very few tubes: this points out that the solution of the Bethe-Salpeter equation for larger diameter SWNTs by *ab initio* techniques is still a formidable task, even by exploiting helical symmetries in SWNTs. Additionally, although Bethe-Salpeter methods attempt to go beyond mean-field approximation, they are limited to consider only single-excitation (*1e-1h*) bounded excitons, making a full many-body calculation for all excitations still impracticable for these systems. Moreover, from these calculations it's notoriously difficult to extract an effective estimate of the strength of the electron-electron

Coulomb interaction, which is a fundamental key parameter for formulating general predictions and establishing a comparison with experimental data or other theoretical methods, such as in Ando's and Mazumdar's works, where the correlation strength instead is an independent input parameter.

Hartree-Fock Configuration Interaction method In the first-principles calculations by Mazumdar's group [208, 210], electronic correlations in SWNTs are investigated by a Hartree-Fock method with single-configuration interaction (SCI) approximation and a semi-empirical Pariser-Parr-Pople (PPP) π-electron Hamiltonian, that was also used for excitonic properties of π-conjugated polymers. The PPP model Hamiltonian is given by

$$\begin{aligned} H &= H_{1e} + H_{e-e} \\ H_{1e} &= -t \sum_{\langle i,j\rangle,\sigma} c^{\dagger}_{i,\sigma} c^{\dagger}_{j,\sigma} + h.c., \\ H_{e-e} &= U \sum_{i} n_{i,\uparrow} n_{j,\downarrow} + \frac{1}{2} \sum_{i,j} V_{ij} \left(n_i - 1\right) \left(n_j - 1\right) \end{aligned} \tag{6.5}$$

where H_{1e} is the one-electron tight-binding Hamiltonian and H_{e-e} is the *e-e* interaction term. $c^{\dagger}_{i,\sigma}$ creates a π electron of spin σ on carbon atom *i*, $\langle \ldots \rangle$ denotes nearest neighbors, $n_i = \sum_{\sigma} c^{\dagger}_{i,\sigma} c_{i,\sigma}$ is the total number of π electrons on site *i*. The parameters *t*, *U*, and V_{ij} are the nearest-neighbor hopping integral, and the on-site and intersite Coulomb interactions, respectively. V_{ij} value is chosen according to the standard Ohno parametrization

$$V_{ij} = \frac{U}{\kappa \sqrt{1 + 0.6117 R_{ij}^2}} \tag{6.6}$$

where R_{ij} is the distance between C atoms *i* and *j* in Å and κ is a screening parameter. Calculations have been performed for $U/t = 1.9, 2.5, 3.33, 4.0$ and $\kappa = 1$ and 2, with similar qualitative conclusions in all cases [208]. When only first nearest-neighbor interactions are considered in the PPP hamiltonian, the exciton-binding energy is determined almost entirely by the difference in Coulomb parameters $U - V$. In this case ($R_{ij} = a_{CC}$), the calculated value is of the order of 5.5 eV for $t = 2.4$ eV, $U = 8$ eV and $\kappa = 2$ [209]. Several chiralities have been considered for semiconducting nanotubes: seven zigzag $(n, 0)$ nanotubes with *n* ranging from 7 to 17, and three chiral SWNTs, namely (6,2), (6,4) and (7,6). Although both longitudinal and transversal excitons have been investigated with this method, we report here the main results for the electronic structure for dipole-allowed excitons polarized along the tube axis. The energy spectra of SWNTs consist of a series of energy manifolds, whose energy increase with their index *n* (see Fig. 6.2). Clearly, in the non-interacting limit the different manifolds are independent from one another. This picture still continues to be meaningful even with

non-zero H_{e-e}, because of the relatively weak mixing between the different *n* excitation manifolds. Within each energy manifold, the single optically-allowed (bright) exciton and several dark excitons occur, as well as a continuum band separated from the optical exciton by a characteristic exciton binding energy, as shown in Fig. 6.2. Interestingly, according to these calculations, the highest state in the first excited manifold is strongly-dipole allowed, while all the remaining states underneath are dark (dipole-forbidden). Due to the non-zero value of H_{e-e} the four-degenerate optically-allowed single-particle excitations between the highest occupied and lowest unoccupied one-electron levels are split into a series of levels, with the highest one collecting almost all the oscillator strength [208], as sketched in Fig. 6.9. The calculated exciton binding-energies for large diameter SWNTs compare well with the experimental spectrofluorimetric measurements by Wang and Dukovic [197], whereas a large disagreement is found for $d_t < 0.75\,\mathrm{nm}$, due to the breakdown of the π-electron approximation. Also, disagreements between calculated and experimental E_{22} are larger, since it should be necessary to include higher order CI in order to achieve greater precision. Actually, SCI approximation works best for lower energy regions; as the energy increases higher order excitations contribute more to the wavefunctions. This requires at least double excited CI, hence more computationally intensive calculations which are beyond todays capabilities for such extended systems. The splitting between bright and dark excitons in $n = 1$ manifold has also been considered, in virtue of several recents experimental measurements which claimed values between few millielectronvolts and $0.14\ \mathrm{eV}$ (see [210] and references therein). Anyway, a theoretical estimation was difficult to be obtained within HF-SCI because of convergence problems due to the small-size of the bright-dark exciton gap.
In conclusion, unlikely BSE-based *ab initio* calculations, the HF-SCI method adopted by Mazumdar allows the understanding of some important features of the excitonic electronic structure for a larger set of SWNTs. Moreover, this method can account for the large exciton binding energies in these systems on the basis of a simple parametrization for π-electrons and a semi-empirical hamiltonian (appropriate for large diameter tubes), already applied successfully to π-conjugated polymers. By including higher orders configuration interaction terms more reliable results could certainly be obtained, although this implies prohibitively increasing the computational complexity of the problem.
Clearly, for a proper treatment of many-body effects other theoretical models are needed, which allow both to go beyond mean-field approximation and for a full inclusion of all possible correlation excitations in the single-particle hamiltonian.

6.2 Hubbard model and SC approach

In the previous section, we saw that in SWNTs the many-body corrections to the measured single-particle transition energies are actually determined by the short-range electron-electron interactions, since the electron-hole Coulomb interaction and the long-range con-

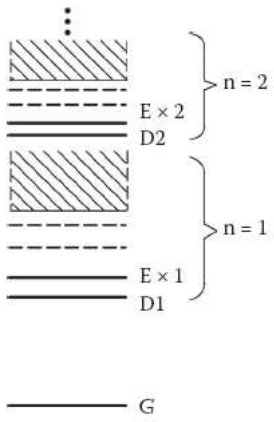

Fig. 6.2: Schematic of the excitonic electronic structure of a semiconductor SWNT for $n = 1$ and $n = 2$ manifolds. Ex*n* and D*n* are dipole-allowed and -forbidden excitons, respectively. Shaded areas indicate continuum band for each manifold. Note that all levels of the $n = 2$ manifold should be buried in the $n = 1$ continuum band; however for clarity the $n = 1$ continuum band end is represented below D2. Taken from Ref. [209, 210].

tribution to the self-energy cancel perfectly. In this section we will show that the Hubbard model [188], although in somewhat oversimplified manner, includes all the necessary features for describing electronic correlation effects in a quantum lattice system and going beyond mean-field approximation. Moreover, given the real-space formulation of the Hubbard model, the small crystal approch can be appropriately used to investigate the problem of the many-body electronic correlation effects on the optical spectra of periodic systems such as SWNTs.

6.2.1 The physics of the Hubbard model

The model introduced by J. Hubbard [188] in 1963 is perhaps one of the simplest yet physically powerful descriptions of the many-body effects in quantum mechanical systems. For this reason since its formulation it has been one of the most extensively studied microscopic models for correlated electron systems, such as for instance high-T_C superconductors [189], transition metal oxides displaying Mott insulator transition [190], organic one-dimensional conductors [210] and recently also low dimensional systems including quantum dots [191, 192]. Unfortunately the exact solution is not known aside from the ground state in the one dimensional model [193], hence we depend on approximations and/or computer simulations for investigating more complex systems. The rich physics of the Hubbard model is determined by the interplay between the kinetic and

potential energy of the electrons in the system lattice, which is captured by the following Hamiltonian:

$$H = -t \sum_{\langle i,j\rangle,\sigma} \left(c^{\dagger}_{i,\sigma} c_{j,\sigma} + h.c \right) + U \sum_{i} n_{i,\uparrow} n_{i,\downarrow}, \tag{6.7}$$

where *i* and *j* are site indices, $\langle i, j\rangle$ are all pairs of nearest neighbor sites, $n_{i,\sigma} = c^{\dagger}_{i,\sigma} c_{i,\sigma}$ is the number of electrons on site *i* with spin σ, $c^{\dagger}_{i,\sigma}$ and $c_{i,\sigma}$ are electron creation and annihilation operators, and *t* and *U* are positive interaction constants. The *t*-term describes the hopping process of electrons localized on atomic-like orbitals between nearest neighbor sites and models the kinetic energy of the system. This part is derived from the tight-binding approximation, which was extensively treated in the previous chapters: since it is an independent particle theory, it contains no many-body features. The *U*-term models the Coulomb repulsion between two electrons with opposite spin in the same orbital, hence it gives a potential energy contribution to the hamiltonian. Whereas other methods based on mean-field approximations (such as density functional theory) replace this interaction with an average one, retaining an effective single-particle picture, the Hubbard model incorporates the Coulomb potential as a pair interaction, which effectively allows to include all the relevant many-body features in the hamiltonian. The potential energy term is diagonal in real space and tends to immobilize the electrons at certain positions of minimum energy, whereas the kinetic energy term is diagonal in momentum space and tries to move around the electrons. The basic formulation of the Hubbard hamiltonian in Eq. (6.7) can be extended in several ways, which have been widely discussed in literature. The most natural are the introduction of an off-site Coulomb interaction between nearest-neighbor orbitals

$$H_V = V \sum_{\langle i,j\rangle} n_i n_j \tag{6.8}$$

and/or the addition of hopping terms beyond first nearest neighbor sites, such as second nearest neighbor hopping

$$H_{t'} = -t' \sum_{\langle\langle i,j\rangle\rangle,\sigma} \left(c^{\dagger}_{i,\sigma} c_{j,\sigma} + h.c \right) \tag{6.9}$$

where $\langle\langle i, j\rangle\rangle$ are all pairs of second nearest neighbor sites. However we will not discuss these terms.

Since the Hubbard model describes the interplay of potential and kinetic energy, depending on the ratio of U/t either the Coulomb interaction or the kinetic energy dominates. In case of $U/t \ll 1$ and systems of dimension $n > 1$ we retain the results of the TBA for independent particles with small corrections and thus the well-known cosine band presented in Chapt. 4. The system therefore is metallic unless the band is completely filled. Electrons are delocalized all over the system and their wave functions can to good approximation be written as Slater determinants. If $U/t \gtrapprox 1$ the movement of one electron

is influenced by the locations of all other electrons in the system since double occupation of a site is energetically expensive and thus they try to avoid each other. Hence the independent-electron approximation cannot be used and analytical solution of the problem cannot be easily found out. Usually wave functions for those systems generally have to be computed numerically. This regime is said to be *correlated*. If the ratio $U/t \gg 1$ it is even called *strongly correlated*. Electrons try to distribute themselves as uniformly as possible on the sites in order to minimize the Coulomb energy. At *half-filling*, i.e. at a mean electron density of one electron per site, the competition between kinetic and potential energy has particularly interesting considerations: because of the strong on-site Coulomb repulsion, the simultaneous occupation of a site by two electrons is strongly disfavored, thus each site will be occupied exactly by one electron. In other words, every hopping process of a single electron implies a large energy cost *U* for the system; therefore, all the electrons are localized and the system is in an insulating state, generated by pure electron-electron interactions, namely it is a *Mott-Hubbard insulator*.
In summary, the Hubbard model and its other numerous derivatives and counterparts (e.g. Heisenberg model for ferromagnetic systems), although with a rather simple formulation, provide all the necessary features to treat the electronic correlations of quantum-mechanical many-body systems, such as an electron gas in a crystal lattice; hence the nomenclature *quantum lattice model*, often used referring to these methods.
In principle, in order to treat the quantum mechanics of interacting electrons, which are actually indistinguishable particles, one has to construct the multiparticle states by superpositions of products of single-particle states, taking into account the Pauli exclusion principle (Slater determinants). In the Hubbard model the single-particle states are electron wavefunctions localized at lattice sites. However, the second quantization formalism, which has already been implicitly introduced in Eq. (6.7), provides us with a suitable basis for dealing with the problem without the explicit specification of the wavefunction determinant. This basis in the Hilbert space is orthonormal and is called *occupation number basis* (or Fock space). This set includes states describing all possible distributions of *N* electrons over *M* lattice sites. There are 4 possible electron occupancies at each site (unoccupied, singly occupied either for spin up or down, doubly occupied with one spin up and one spin down). Since the possible configurations of upspins are independent of the configurations of the down spin, the $\mathcal{H}_{Hubbard}$ space of all possible configurations is just the direct product of the Hilbert space of down spins $\mathcal{H}_{\uparrow}$ and that of up-spins $\mathcal{H}_{\downarrow}$:

$$\mathcal{H}_{Hubbard} = \mathcal{H}_{\uparrow} \otimes \mathcal{H}_{\downarrow}. \tag{6.10}$$

A convenient way to represent and generate these multiparticle states is to keep the spin up and spin down configurations separately by assigning each lattice site a 1 if the site is occupied or zero if it is not (*bit-string coding*). In this way, every multiparticle state is described by the occupancy numbers of the single-particle states for a given spin. For example, a generic state in this basis having 5 electrons on an 8 site lattice with 3 up and

2 down spin is coded as

$$|00101010\rangle|00100100\rangle, \tag{6.11}$$

where the spin up electrons are found at sites 3, 5, 7, the down spin electrons are found at sites 3 and 6 and the remaining sites are unoccupied. Formally, these states can be generated by applying second quantization creation and annihilation operators to the vacuum $|0\rangle$

$$c^\dagger_{k_1} c_{k_2} \ldots c^\dagger_{k_N} |0\rangle \quad \text{etc.}, \tag{6.12}$$

where $(k_1, k_2 \ldots k_N)$ is an ordered *N*-tuple of indices and k_i is the index of the corresponding single-particle state. The antisymmetry of the fermionic states is taken into account via the operator algebra expressed by the following anticommutation rules

$$\begin{aligned} \left[c_l, c^\dagger_m\right] &= \delta_{l,m}, \\ \left[c^\dagger_l, c^\dagger_m\right] &= 0, \\ \left[c_l, c_m\right] &= 0. \end{aligned} \tag{6.13}$$

The operator $c^\dagger_k$ generates a single-particle wavefunction $\varphi_k(r)$ within the multiparticle state if that wavefunction is not present yet; otherwise, the result is 0. The adjoint operator c_k annihilates the single-particle wavefunction if present; otherwise it returns 0. The Pauli exclusion principle follows from $c^\dagger_k c^\dagger_k = 0$. Since the Hubbard Hamiltonian is represented by non-commutative products of creation and destruction fermionic operators as well, one can reasonably expect that the corresponding Hamiltonian matrix can be constructed algebraically. In the following section we will show how to build up the Hamiltonian matrix for the one-dimensional Hubbard model applied to a working example, namely a chain with *M* sites and periodic boundary conditions. This will help in understanding the construction of the working code developed in this thesis for small periodic clusters, presented in Sect. 6.3.

6.2.2 The Hubbard model for a periodic M-site chain

The Hubbard Hamiltonian for a chain with *M* sites and periodic boundary conditions is

$$H = -t \sum_{i=1}^{M} \sum_{\sigma} \left(c^\dagger_{i,\sigma} c_{i+1,\sigma} + c^\dagger_{i+1,\sigma} c_{i,\sigma} \right) + U \sum_{i=1}^{M} n_{i,\uparrow} n_{i,\downarrow} \tag{6.14}$$

with the periodic boundary conditions expressed by $c^\dagger_{M+1,\sigma} = c^\dagger_{1,\sigma}$ and $c_{M+1,\sigma} = c_{1,\sigma}$. Here, $n_{i,\sigma} \equiv c^\dagger_{i,\sigma} c_{i,\sigma}$ yields the value 1, if an electron with spin σ is located at the site *i*, otherwise $n_{i,\sigma}$ yields the value 0. Now the basis set in the occupation number formalism has to be constructed. First, however, one has to label the single-particle states upon

which constructing the multi-particle states and define their order. For the order of the single-particle states, we choose the following convention [219]

$$\{1\uparrow, 2\uparrow, \ldots, M\uparrow\}, \{1\downarrow, 2\downarrow, \ldots, M\downarrow\}. \tag{6.15}$$

Thus, the generic multiparticle state in the example of Eq. (6.11) in second quantization is written as

$$|\{00101010\}, \{00100100\}\rangle = c^\dagger_{3,\uparrow} c^\dagger_{5,\uparrow} c^\dagger_{7,\uparrow} c^\dagger_{3,\downarrow} c^\dagger_{6,\downarrow} |0\rangle. \tag{6.16}$$

If the operator $c^\dagger_{l,\sigma}$ is applied to a multiparticle state, then one has to swap this operator with the operators $c^\dagger_{m,\sigma\prime}$ using the algebra of Eq. (6.13), until the sequence is recovered in the correct order as in Eq. (6.15). By this procedure one also obtains the sign of the state. For example, we get

$$\begin{aligned} c_{M,\downarrow}|\{1,0,\ldots,0\}, \{0,\ldots,0,1\}\rangle &= c_{M\downarrow} c^\dagger_{1\uparrow} c^\dagger_{M\downarrow}|0\rangle \\ &= -c^\dagger_{1\uparrow} c_{M\downarrow} c^\dagger_{M\downarrow}|0\rangle \\ &= -c^\dagger_{1\uparrow}|0\rangle + c^\dagger_{1\uparrow} c^\dagger_{M\downarrow} c_{M\downarrow}|0\rangle \\ &= -c^\dagger_{1\uparrow}|0\rangle \\ &= -|\{1,0,\ldots,0\}, \{0,\ldots,0\}\rangle \end{aligned} \tag{6.17}$$

Generally, when applying $c^\dagger_{l,\sigma}$ or $c_{l,\sigma}$ to a state $|\mathbf{n}\rangle = |\{n_{1\uparrow},\ldots,n_{M\uparrow}\}, \{n_{1\downarrow},\ldots,n_{M\downarrow}\}\rangle$, the number of particles to the left of $l\sigma$ determines the sign. Therefore, one can define the sign function in the following way:

$$\text{sign}\,(l\sigma, \mathbf{n}) = (-1)^{\delta_{\sigma\downarrow}\sum_{i=1}^{M} n_{i\uparrow}} (-1)^{\sum_{j=1}^{l-1} n_{j\sigma}} \tag{6.18}$$

This function produces as many factors -1 as there are non-zero entries in $\mathbf{n}$ in front of the position l, σ. This fact allows us to write the effect of the creation operator as

$$c^\dagger_{l\sigma}|\mathbf{n}\rangle = (1 - n_{l\sigma})\,\text{sign}\,(l\sigma, \mathbf{n})\,|\{n_{1,\uparrow},\ldots,1,\ldots,n_{M\downarrow}\}\rangle, \tag{6.19}$$

where the number 1 is at the position $l\sigma$ and the factor $(1 - n_{l\sigma})$ ensures that there is no double occupancy of the same state. On the other hand, for the destruction operator we get

$$c_{l\sigma}|\mathbf{n}\rangle = n_{l\sigma}\text{sign}\,(l\sigma, \mathbf{n})\,|\{n_{1\uparrow},\ldots,0,\ldots,n_{M\downarrow}\}\rangle, \tag{6.20}$$

which annihilates the state $l\sigma$. In order to obtain the Hamiltonian matrix, one needs to obtain the scalar product between any multiparticle state of the Fock space $\langle\mathbf{n}_i|$ with $H|\mathbf{n}_j\rangle$. In general, the Hubbard matrix is mostly filled with zeros and the on-diagonal elements can be obtained in a very straightforward manner by inspecting the number of doubly-occupied sites in each multiparticle state and multiplying this double-occupancy number by *U*, the Coulomb repulsion energy. If two states $|\mathbf{n}_i\rangle$ and $\langle\mathbf{n}_j|$ differ by the

hopping of one electron from a given site to its nearest neighbour, then the corresponding off-diagonal matrix element is *t*, with the sign determined by the chosen convention for the hopping. In the computer program presented in Ref. [219], the following rule was adopted for the sign of the off-diagonal *t* matrix elements: if the hopping involves just nearest neighbor sites which are not related by periodic boundary conditions (unlikely those at the opposite ends of the chain), then the matrix element is set equal to $-t$, otherwise it is set equal to $+t$. However, other conventions can be adopted as well, without affecting the resulting eigenvalues obtained from the matrix diagonalization. Similarly, one can construct the matrix for the velocity operator v_{1D} (or correspondingly the current operator), needed for the calculation of the optical matrix element between the ground state $|\psi_0\rangle$ and any other eigenstate $\langle\psi_m|$ of the Hubbard matrix. For a chain with *M* sites and periodic boundary conditions this operator is defined as [92, 215, 216]

$$v_{1D} = -\frac{\imath t}{\hbar}\sum_{i=1}^{M}\sum_{\sigma}\left(c^{\dagger}_{i,\sigma}c_{i+1,\sigma} - c^{\dagger}_{i+1,\sigma}c_{i,\sigma}\right) \tag{6.21}$$

This allows us to compute the intensity of the optical absorption spectrum for the Hubbard chain with the SOS method as a spectral function

$$I(E) = \sum_{m}|\langle\psi_m|v_{1D}|\psi_0\rangle|^2\delta\left(E + E_0 - E_m\right) = \tag{6.22}$$

$$= \lim_{\Gamma\to 0^+}\sum_{m}|\langle\psi_m|v_{1D}|\psi_0\rangle|^2\frac{\Gamma}{\Gamma^2 + \left(E + E_0 - E_m\right)^2},$$

where E_0 is the ground-state energy of the system and E_m the energy of any other eigenstate $|\psi_m\rangle$ obtained from exact diagonalization (ED) of the hamiltonian. This general procedure can be extended as well to higher-dimensional systems, although it is rather unpracticable from a computational point of view, since the number of states in the basis to be stored grows exponentially with the number of sites in the systems, as discussed in the following section.

6.2.3 Reduction of the basis size and application to small clusters

As stated previously, every site of the Hubbard *M*-site chain has four possible states: empty, singly occupied by either one spin up or spin down electron, or doubly occupied with electrons having opposite spins. Thus there are altogether 4^M multiparticle states in the occupation number basis and the Hamiltonian is therefore a $4^M \times 4^M$ matrix. For instance, for $M = 16$ there are $4\,294\,967\,296$ states in this basis and the Hamiltonian matrix has over 1.8×10^{19} elements. Although Hubbard matrices are generally very sparse, clearly the number of nonzero elements is still very large and their storage in a computer memory is well beyond what is possible, even with today's capabilities. In order to make

the problem more tractable, one can use symmetries to block-diagonalize the Hamiltonian in smaller submatrices along the diagonal. If we need to find the ground state energy, we can simply find the smallest eigenvalue from each of these smaller submatrices. In general, for quantum many-body lattice models in condensed matter physics, such as the Hubbard model, the following symmetries are considered: the conservation of the total number of electrons *N*, the conservation of the number of electrons with a particular spin N_σ, the quantum number of total spin and eventually spatial symmetries. In this way the size of the Hilbert space for the occupation number basis is greatly reduced, hence the matrices to diagonalize turn out to be smaller. In the following we will always consider *half-filled* systems, for which the number of electrons *N* is fixed and equal to the number of sites *M*in the system, i.e. averagely one electron per site. Moreover, the conservation of N_σ is also required, such that $N_\uparrow = N_\downarrow = N/2$. Thus the size of the obtained Hamiltonian block is given by

$$\prod_\sigma \frac{N!}{N_\sigma!\,(N-N_\sigma)!} = \left(\frac{N!}{N_\uparrow! N_\downarrow!}\right)^2 \quad \text{with} \quad N_\uparrow = N_\downarrow = \frac{N}{2}. \tag{6.23}$$

Again, for a half-filled system with $M = 16$ sites, the size of the Hamiltonian block to diagonalize is $165\,636\,900$, which is still a very large number to be handled by today's ordinary personal computer. Remember that 16 is the number of atoms inside the unit-cell of the (4,0) nanotube, which still remains experimentally unidentified up to date, because of the very small diameter and high curvature which are highly unfavourable for the energetic stability of the system.

At this point the use of spatial symmetries plays a fundamental role for further reducing the number of sites and, consequently, the basis size. Clearly, however, the huge number of states restricts our choice to small lattice clusters, i. e. with $M \leq 12$ sites. In order to avoid problems due to finite size effects, a good choice is to take advantage of the lattice periodicity and other symmetries, so that the properties of the infinite system can be extrapolated from that of the finite system with reasonably good approximations. Usually in exact diagonalization studies, in order to simulate the infinite number of sites in the crystal *periodic*(PBC) or *antiperiodic boundary conditions* (APBC) are introduced, by connecting the left boundary of the finite lattice to its right-boundary (as in a chain) and/or its lower edge to its upper edge, as already explained in Chapt. 4.

In the case of zigzag clusters the number of sites needed to sample correctly the $(\mu, k_z = 0)$ BZ points (which are relevant for the optical properties) can be reduced from $4n$ to $2n$, as depicted in Fig. 6.3, thus allowing us to perform exact diagonalization studies for half-filled systems with 8 sites for a (4,0) SWNT and with 10 sites for a (5,0) SWNT on an ordinary PC. This fact can be explained with the presence of an order-two rotation axis (U and U' axis according to Damnjanović symmetry classification of Sect. 2.5), perpendicular to the tube axis and centered on a C-C bond or a graphene hexagon for (4,0) and (5,0) SWNTs, respectively.

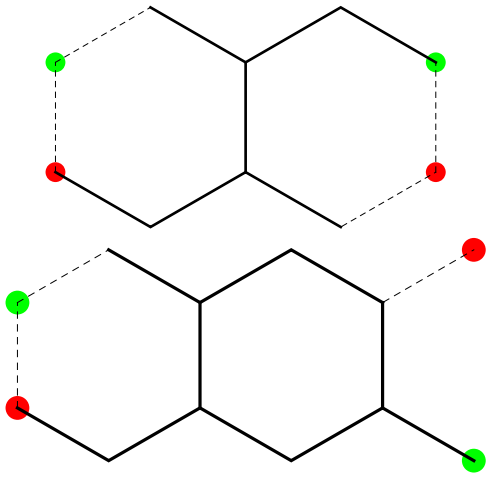

Fig. 6.3: Zigzag (4,0) (upper) e (5,0) (bottom) clusters with $2n$ sites and azimuthal periodic boundary conditions to sample $(\mu, k_z = 0)$ points in the nanotube BZ. Points with the same color mean same index site.

On the basis of these developments and the definitions given in Chapt. 4, one can verify that by applying PBCs (i.e. with phase $\phi = 0$) along the azimuthal direction, $k_z = 0$ points with μ even are sampled, while by applying APBCs (i.e. with phase $\phi = \pi$) $k_z = 0$ points with μ odd are sampled (see Fig. 6.4). This fact can be applied for the construction of both the Hubbard hamiltonian matrix and the velocity matrix (for polarization along the tube axis), according to the chosen phase. We recall that for the optical properties of nanotubes it is relevant considering only light polarization parallel to the tube axis, for which the selection rule $\Delta\mu = 0$ holds. Computing the spectral function separately for (A)PBCs with the aid of Eq. (6.22), adapted to 2D graphene clusters, implies again the automatic fulfilment of the selection rule $\Delta\mu = 0$, since each of the two velocity operators always acts on states with the same parity. On the contrary, the optical spectrum for perpendicular polarization of the light, for which the selection rule $\mu \rightarrow \mu \pm 1$ holds, cannot be obtained this way, since the velocity operators need to act between states of different parities, therefore always returning zero. It is likely that this case can be treated by computing the full matrices for the true zigzag cell with $4n$ sites, i.e. considering a larger set of states, with both parities implicitly included. However, this requires more sophisticated computational techniques and facilities and will be addressed in the future. Thus one can expect that in the tight-binding limit $U = 0$, the optical spectrum of a $(n, 0)$ zigzag nanotube with light polarization parallel to the tube axis can be obtained exactly by the superposition of the spectral functions calculated from $2n$-site clusters with periodic and antiperiodic boundary conditions, respectively. This is shown in the final section of this chapter where the calculated results for (4,0) and (5,0) SWNTs are reported.

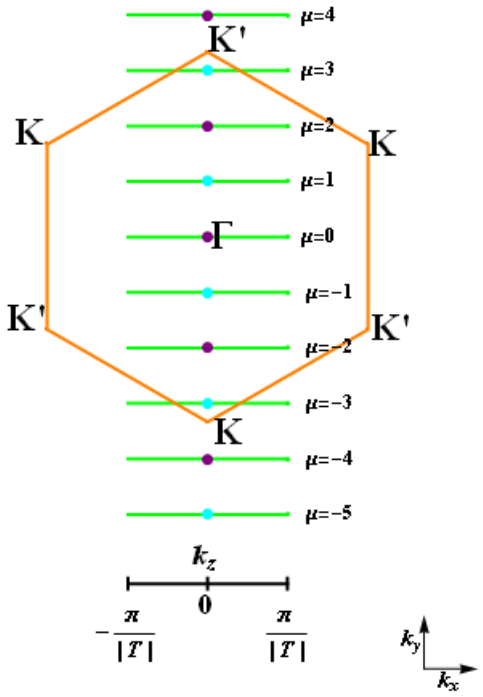

Fig. 6.4: BZ sampling with a $2n$-site zigzag $(n, 0)$ cluster: by applying azimuthal PBCs, $(\mu \text{ even}, k_z = 0)$ points (purple color) are sampled, by applying azimuthal APBCs $(\mu \text{ odd}, k_z = 0)$ points (blue color) are sampled.

6.3 Computational details

In this section we show the computer algebra implementation of the exact diagonalization technique for the Hubbard model applied to small clusters with periodic boundary condition. The algorithm was developed for the computer algebra system *Mathematica*® [218] and is taken from Ref. [219]. Another more complete and versatile package based on similar principles is the SNEG library [220], a Mathematica package developed in the Ljubljana University, which provides a framework for performing calculations using the operators of the second quantization with an emphasis on the anti-commuting fermionic operators in the context of solid-state and atomic physics. *Mathematica*® is particularly suitable for formulating the representation of the operator algebra of Eq. (6.13) according to Eqq. (6.19-6.20). As a working example we consider again the Hubbard chain with M sites and periodic boundary conditions. In *Mathematica* the multiparticle states can be defined by using the header `s`, instead of the ket symbol $|\ldots\rangle$, as in the following:

$$\mathtt{s}\,[\mathtt{arg}], \quad \text{where} \quad \mathtt{arg} = \{\{n_{1\uparrow}, \ldots, n_{M\uparrow}\}, \{n_{1\downarrow}, \ldots, n_{M\downarrow}\}\} \text{ and } n_{l\sigma} \in \{0, 1\}\,.$$

We need the header s because we have to perform the addition and multiplication of the states by scalars by manipulating the argument of s. If we were to perform these operations on the list arg itself, we would get incorrect results. For example, according to *Mathematica* conventions for lists, one obtains $n_{l\sigma}$ from arg [[sigma, l]] with l $= l$, sigma $= 1$ and sigma $= 2$ respectively, for $\sigma =\uparrow$ and $\sigma =\downarrow$.
After specifying the numbers of sites *M*, spin-up $N_\uparrow$ and spin-down $N_\downarrow$ electrons, we can use the functions Permutations [...] and Table [...] to generate the list index, which contains all possible multiparticle states, coded in binary form. This procedure can be implemented as in the following code lines, for spin-up and spin-down particles.

```
(* Left (spin up particles) *)
left = Permutations[ Table[ If[ j <= spinup, 1, 0], { j, 1, sites}]];

(* Right (spin down particles) *)
right = Permutations[ Table[ If[ j <= spindown, 1, 0], { j, 1, sites}]];

(* Left and Right (spin up and down particles) *)
index = Flatten[ Table[ {left[[i]],right[[j]]}, { i, 1, Length[left]},
{ j, 1, Length[right]}], 1];
```

The operator $c^\dagger_{l\sigma}$ has to generate a 1 in the right location specified by l and sigma in the argument of s. This is done by the function plus. Correspondingly, the function minus generates a 0.

```
plus[k_,sigma_][arg_]:= ReplacePart[arg, 1, {sigma, k}]
minus[k_,sigma_][arg_]:= ReplacePart[arg, 0, {sigma, k}]
```

Using the sign function introduced in Eq. (6.18), we can now define in a functional form the second quantization operators $c^\dagger_{l\sigma}$ and $c_{l\sigma}$, which are going to act on the states as in Eq. (6.19) and Eq. (6.20).

```
sign[l_,sigma_,arg_] := (-1) ^ (spinup* (sigma-1)) *
(-1)^(Sum[ arg [[sigma,j]],{ j, 1, l-1}])

cdagger[l_, sigma_][factor_.* s[arg_]]:= factor*(1 - arg[[sigma,l]])*
sign[l, sigma, arg]*s[plus[l, sigma][arg]]

c[l_, sigma_][factor_.* s[arg_]]:= factor*arg[[sigma,l]]*
sign[l, sigma, arg]*s[minus[l,sigma][arg ]]
```

The parameter factor_. is set by default to the value 1 in *Mathematica*, if the state

does not have an additional factor. Since these operators can always generate the value 0 (e.g. $c^{\dagger}_{1\uparrow}|\{1,\ldots\},\{\ldots\}\rangle = 0$), `cdagger` and `c` have to be defined for the number 0 as well:

```
cdagger[l_, sigma_][0]:= 0
c[l_, sigma_][0]:= 0
```

Additionally, we still need the operator $n_{l\sigma}$:

```
n[l_,sigma_][0]:= 0
n[l_,sigma_][factor_.*s[arg_]]:= factor*arg[[sigma,l]]*s[arg]
```

Periodic boundary conditions for the chain can be expressed as :

```
cdagger[sites+1,sigma_][any_]:=cdagger[1,sigma_][any_]
c[sites+1,sigma_][any_]:=c[1,sigma_][any_]
```

Eventually, the Hamiltonian (Eq. 6.14) of the Hubbard chain can simply be written as:

```
H[vector_]=Expand[
-t*Sum[cdagger[l,sigma][c[l+1,sigma][vector]] +
cdagger[l+1,sigma][c[l,sigma][vector]],
{l,1,sites},{sigma,1,2}] +
u*Sum[n[l,1][n[l,2][vector]],{l,1,sites}]
]
```

More complicated Hamiltonians, such as those considered in this work for the zigzag clusters with $2n$ sites can be expressed in a similar way, by writing explicitly the site index needed for the nearest neighbor hopping terms with the correct translational and azimuthal periodic boundary conditions included. In order to obtain the Hamiltonian matrix, we need to compute the scalar products $\langle \mathbf{n}_i|H|\mathbf{n}_j\rangle$ of each state $|\mathbf{n}_i\rangle$ with $H|\mathbf{n}_j\rangle$. Since the multiparticle states are already orthonormal, we only need to define the linearity of the scalar product:

```
scalarproduct[a_ , 0]:= 0
scalarproduct[a_ , b_ + c_ ]:=scalarproduct[a,b] +
scalarproduct[a,c]
scalarproduct[s[arg1_],factor_.s[arg2_]]:=
factor*If[arg1==arg2,1,0]
```

where the comparison of two states, which is expressed by the comparison of two nested

lists, is written in a very compact manner by using `arg1==arg2`.
The desired Hamiltonian matrix $\langle \mathbf{n}_i|H|\mathbf{n}_j\rangle$ can be computed by first defining the following table:

```
hlist=Table[H[s[index[[j]]]], {j, 1, end}];
```

and then setting up in the sparse matrix as with the help of `SparseArray` as in the following lines:

```
h=SparseArray[{i_,j_} ↦ scalarproduct[s[index[[j]]],hlist[[j]]],
{end,end}]
```

The upper limit for the loop indices, which also provides the size of the basis or the number of multiparticle states can be determined via `end = Length[index]`, soon after the construction of the basis set list `index`. The computed matrices are Hermitian and symmetric, thus their eigenvalues are real and only the upper-diagonal part needs to be computed and stored. One can choose among several file formats suitable for sparse matrix storage on the hard-disk, such as the NIST MatrixMarket format (*.mtx) [221], which allows to specify the non-zero entries for the matrix elements and its transposition rules (Hermitian, symmetric, skew-symmetric or general). When the *.mtx file is imported and the diagonalization method (see the commands `Eigensystem` for obtaining the eigenvalue-eigenvector pair) is called by the system, *Mathematica* detects automatically the (hermitian symmetric) structure of the matrix and switches to the most efficient routine for the numerical diagonalization. In order to perform the sparse matrix numerical diagonalization within the *Mathematica* system [218], one can choose between either LAPACK [222] or Arnoldi (also known as ARPACK or Lanczos [223]) algorithms. The Lapack is the default method for accurately computing the entire set of eigenvalues and eigenvectors and works well when the order of the matrix size is at maximum between 10^4 and 10^5. In this work it was used for the diagonalization of 4900×4900 matrices for a periodic 8-sites half-filled zigzag (4,0) cluster, since the memory requirements for storing on disk the full eigenvector set (needed by the velocity operator) were not prohibitive at all (500 MBs). The Arnoldi method is an iterative method, usually suitable for sparse matrices, used for finding a few eigenvalues of a large matrix. Since in our case we need to find only the lowest eigenpairs of the Hubbard matrix (their number should usually be less than 20% of the matrix size) for calculating the low energy optical spectrum, this method can be applied to the periodic 10-sites half-filled zigzag (5,0) cluster, whose matrix dimensions are 63504×63504. In *Mathematica* this task can be accomplished in the following way:[1]

[1]Unfortunately, the *Mathematica* documentation on this subject is very sparse and not very detailed, so these lines are intended as a short tutorial on the matter for helping in reproducing calculations

```
{eigenvalues,eigenvectors}=-Eigensystem[-hubmatrix,200,
Method↦{Arnoldi, MaxIterations↦10^5,Criteria↦RealPart}]
```

As shown in the code lines above, *Mathematica* has the ARPACK library built in and all the options for that library apply, which are passed by the command `Method`. Since we know that our matrix is Hermitian and that the eigenvalues are all real, one can use the real part as a criterion for computing the smallest eigenvalue. Moreover, with the above instructions, one can see that the (200) largest eigenvalues of `-hubmatrix` (by real part) correspond to the (200) smallest eigenvalues of `hubmatrix`. This allows to avoid *Mathematica* default setting, which always computes the smallest eigenvalues in absolute value, consequently with a large waste of computational resources.
To summarize, in this section we have shown how to implement the exact diagonalization method for the Hubbard model on ordinary personal computers for periodic clusters with 8 and 10 sites with the aid of *Mathematica*, a system which is suitable mainly for computer algebra but also for numerical computing. The most intensive and time-consuming part of the computational procedure is represented by the construction of the Hubbard and velocity matrices: for a 10 sites periodic cluster it took five days to write the upper-diagonal part of the 63504×63504 matrix on an ordinary personal computer. This is partly due to the fact that *Mathematica* is based on an interpreted language, which is 100-200 slower than compiled languages like Fortran or C++. However, the main advantages of choosing an interpreted system like *Mathematica* for treating small clusters are represented by a gain in user productivity, i.e. a large amount of time spared in coding the algorithms and a minimized risk of programming errors, if compared with low-level languages usually adopted in scientific computation (Fortran and C/C++). Clearly, in order to cope with systems with larger size we have to depart from interpreted languages and look for other implementation techniques. Expression templates for quantum mechanical operators have already been implemented in specialized C++ libraries to allow even non-expert users to define and use easily Hamiltonians and other operators in second quantization formalism, so that matrix elements can be computed more efficiently with less programming effort by the user [224]. Additionally, one has to face the problem of storing on disk huge matrices, from which the diagonalization routines read the needed elements. Sometimes, even if the matrix can be stored on computers with fast and capable hard disks, the difficulty is that the I/O speed is still too slow compared to the computational speed. To avoid these problems with the storage, the matrix elements have to be calculated efficiently *on the fly* at each Lanczos iteration. These algorithms are also suitable for parallelization techniques and have already been implemented efficiently for exact diagonalization on strongly correlated quantum systems with up to 36 sites (see PALM++). Recently, the international open-source project ALPS (Algorithms and Libraries for Physics Simulations, http://alps.comp-phys.org [225, 226]) was established with the purpose of developing and merging also several existing different algorithms (such as PALM++) and libraries for simulating the properties of strongly correlated

systems within a wide range of theoretical approaches, exact diagonalization included. Certainly, the ALPS libraries will be a very interesting and useful tool for applying the ideas presented in this thesis to larger zigzag clusters (e.g. a (7,0) cluster with 14 sites) and it is likely that exact diagonalization calculations could be carried out on full zigzag unit cells with parallel and/or supercomputing facilities.

6.4 Results

In this section we present the results of the application of the Hubbard model combined with the small crystal approach for the investigation of the optical spectra of zigzag SWNTs, according to the choices for the clusters formulated in the previous sections: a (4,0) zigzag cluster with 8 sites and a (5,0) cluster with 10 sites, with translational periodic boundary conditions and (anti)periodic azimuthal boundary conditions to sample nanotube BZ points at $k_z = 0$ and μ even (odd), respectively.
SC calculations were all performed based on the simplest formulation of the Hubbard model hamiltonian of Eq. (6.7), that is, with only first nearest-neighbor hopping interactions *t* and on-site Coulomb repulsion *U*.
In order to test the correctness of the developed computer programs, we first performed exact diagonalization (ED) calculations for both clusters in the noninteracting limit $U = 0$ and compare the resulting transition energies in the optical spectra (for light polarization parallel to the tube axis) to those obtained according to the classical tight-binding (LCAO) formulation, by either the zone-folding (Chapt. 3) or the real space SC approach (Chapt. 4). In Fig. 6.5 we report the (4,0) and (5,0) optical spectra computed with the SOS method (Eq. (6.22)) after ED of the Hubbard matrices obtained by switching alternatively between periodic and antiperiodic boundary conditions to sample even or odd azimuthal band quantum numbers. Additionally, the full absorption spectra calculated as explained in Chapt. 4 (LCAO scheme) are shown for comparison. One can see that the absorption profiles of the full LCAO calculation are completely recovered by the ED spectra with APBCs and PBCs considered together. In Table 6.1, we compare the numerical values of the interband transition energies for both zigzag systems calculated from ED with $U = 0$ and classical TB method (ZF or SC) with the same value of hopping parameter $t_\pi = 2.9\,\mathrm{eV}$ and verify the perfect matching of the energy values for the different $\mu, k_z = 0$ BZ points involved in the interband transitions.
Having tested the validity of our ED method in the non-interacting limit, we can include the electronic correlations by setting $U \neq 0$ for the on-site screened Coulomb repulsion term in the Hubbard Hamiltonian. In Fig. 6.6 the optical spectra for both cluster geometries are reported, where the Hubbard parameters obtained in the work by Cini *et al* [212] have been used. These parameters were deduced from fitting calculations on the experimental Auger spectra of graphite and carbon nanotubes. For carbon nanotubes the obtained parameter values are $t_\pi = 2.6\,\mathrm{eV}$ and $U = 4.6\,\mathrm{eV}$. It has to be stressed

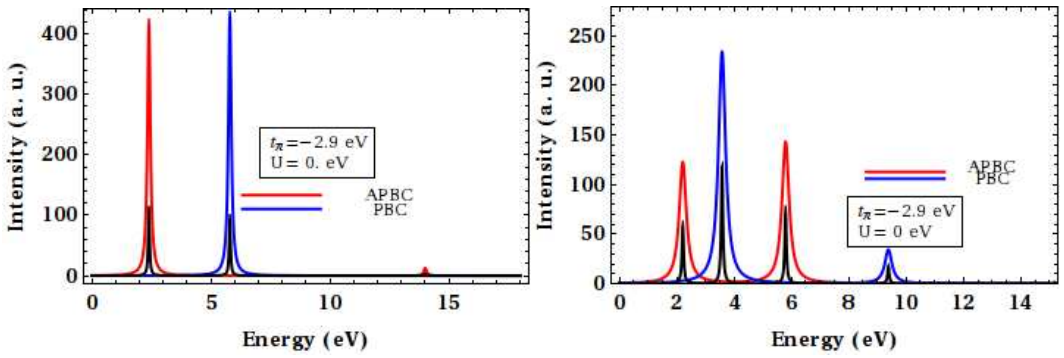

Fig. 6.5: Optical absorption spectra for (4,0) and (5,0) zigzag cluster with $2n$ sites calculated by ED method and azimuthal periodic (blue) and antiperiodic (red) boundary conditions in the non-interacting limit $U = 0$. The chosen values for the parameters are: $t_\pi = 2.9\,\mathrm{eV}$ and $U = 0\,\mathrm{eV}$. The full absorption spectra (black) calculated as in Chapt. 4 are also shown and scaled for better comparison.

Table 6.1: Comparison of the calculated transition energies (in eV) of (4,0) and (5,0) zigzag clusters obtained from ED method ($t_\pi = 2.9\,\mathrm{eV}$ and $U = 0\,\mathrm{eV}$) with those from classical tight-binding method (ZF and SC, $t_\pi = 2.9\,\mathrm{eV}$).

E_{ii}, D_z $(0$ or $\neq 0)$ SWNT (4,0)	$(\mu, k_z = 0)$	E_{ii} from TB (ZF, SC) [eV]	E_{ii} from ED with $U = 0$ [eV]
$E_{11}, D_z \neq 0$	3, 5	2.40244	2.40244
$E_{22}, D_z \neq 0$	2, 6	5.8	5.8
$E_{22}, D_z \neq 0$	4	5.8	5.8
$E_{33}, D_z \neq 0$	1, 7	14.00244	14.00244
$E_{44}, D_z \neq 0$	0	17.4	17.4

E_{ii}, D_z $(0$ or $\neq 0)$ SWNT (5,0)	$(\mu, k_z = 0)$	E_{ii} from TB (ZF, SC) [eV]	E_{ii} from ED with $U = 0$ [eV]
$E_{11}, D_z \neq 0$	3, 7	2.2154	2.2154
$E_{22}, D_z \neq 0$	4, 6	3.5846	3.5846
$E_{33}, D_z \neq 0$	5	5.8	5.8
$E_{44}, D_z \neq 0$	2,8	9.3846	9.3846
$E_{55}, D_z \neq 0$	1,9	15.1846	15.1846
$E_{66}, D_z \neq 0$	0	17.4	17.4

out that Cini has verified a very small dependence of the correlation parameter *U* on nanotube diameter: no substantial changes were found in the theoretical Auger spectra of (10,10) and (20,20) SWNTs, and by comparing the experimental Auger spectra of SWNTs with average diameter of $2\,\mathrm{nm}$ with the theoretical ones for tubes with average diameter of $1.3\,\mathrm{nm}$. We note that the value for the screened Coulomb interaction strength is well above the perturbative ones used in the effective-mass approximation calculations by Ando ($0.1 - 0.2\,\mathrm{eV}$) [211]. Moreover, the values of the bare (unscreened) Coulomb interaction *U* used by Cini ($U^b_{\pi\pi\pi\pi} = 14.6\,\mathrm{eV}$) [213] have magnitude comparable to those used by Sørensen [214] for the Hubbard ED studies on C_{20} isomers, in particular carbon rings ($t_\pi = 2.36\,\mathrm{eV}$, $U = 10.1\,\mathrm{eV}$) and nanobowls ($t_\pi = 3.16\,\mathrm{eV}$, $U = 10.3\,\mathrm{eV}$), which have degree of curvature similar to nanotube walls. From our calculated optical spectra of Fig. 6.6, we can see that the inclusion of the on-site electron-electron Coulomb interactions produces an evident blueshift of all the optical transition peaks with respect to those obtained in the tight-binding limit. This is consistent with both experimental [195, 196] and theoretical findings [194]. One can also notice that the blueshift affects more considerably the E_{11} transition energy rather than the E_{22} transition energy: this fact is particularly evident in the spectral profile of (4,0) cluster.

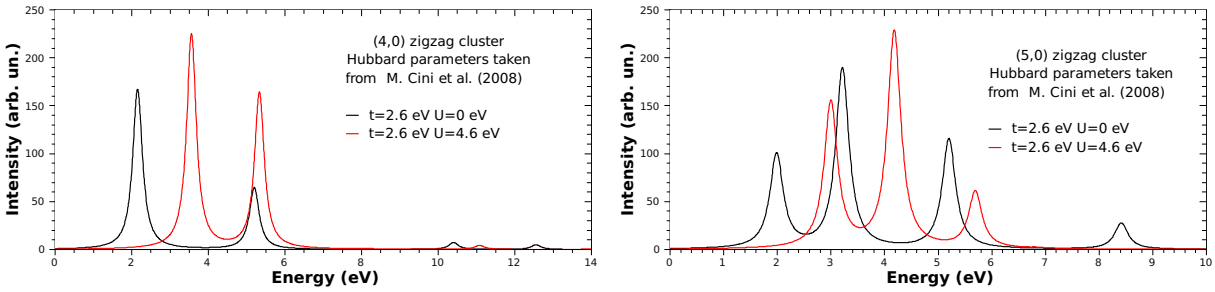

Fig. 6.6: Optical absorption spectra for cluster (4,0) (left) and (5,0) (right) from ED with (anti)periodic BCs in the non-interacting limit $U = 0$ (black) and for the value $U = 4.6\,\mathrm{eV}$ for the Hubbard correlation parameter obtained by M. Cini *et al.*(red) [212].

In order to study the dependence of the allowed E^S_{11} and E^S_{22} on the electron correlation strength U/t, we performed several ED calculations for different *U* values of the on-site Coulomb interaction, whose results are presented in Fig. 6.7. In the case of (4,0) geometry, one can actually see that in intermediate-low coupling regime ($U/t < 2$) the E_{11} transition energies increase faster than E_{22}s, which have almost a constant trend. On the other hand, for cluster (5,0) in the same coupling regime, the slopes of both E_{11} and E_{22} curves are similar. This can be explained by considering the inverse proportionality relation between energy gap and diameter in SWNTs, as discussed in TB approximation: (5,0) cluster describes a SWNT having a larger diameter than (4,0), hence more values

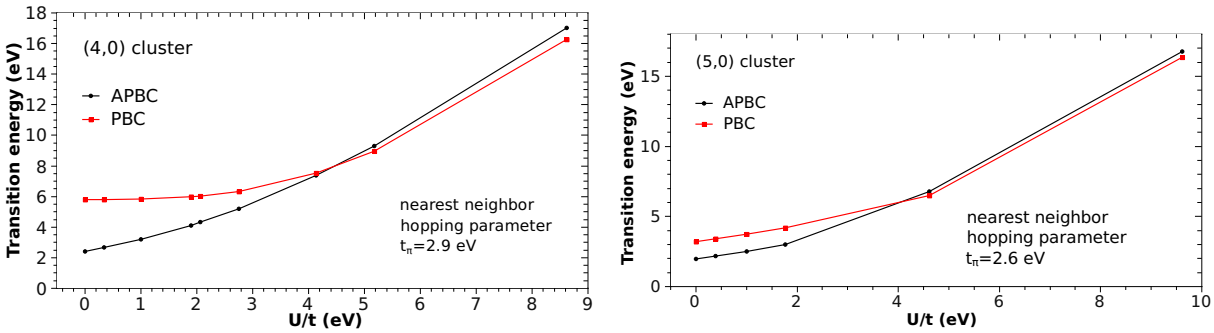

Fig. 6.7: Dependence on the correlation strength U/t of E_{11}^S and E_{22}^S transition energies for (4,0) (left) and (5,0) (right) zigzag $2n$-site clusters obtained from ED method with azimuthal APBCs (red) and PBCs (black).

for the azimuthal quantum number are allowed and the absolute energy difference between bands with different index μ are lower than in small diameter tubes. However, if we consider a wider range in coupling strength ($U/t < 5$), the same general behaviour of cluster (4,0) is found also for (5,0) geometry, i.e. the E_{22}^S trend increases at a slower rate than E_{11}^S. In this regime one can verify that the ratio E_{22}^S/E_{11}^S is actually lower than 2, therefore it's consistent with the previously summarized experimental and theoretical findings about the *ratio problem* in correlated SWNTs, although these actually refer to large diameter nanotubes.

In general, in the low-coupling regime the use of APBCs provides always lower values of the transition energies than PBCs do. This fact can be understood by considering that in the TB limit, the use of azimuthal APBCs allows to sample Brillouin points with $(\mu \,\mathrm{odd}, k_z = 0)$ and that the azimuthal quantum number of the energy gap bands (E_{11}^S) is actually always odd in semiconducting zigzag tubes (see Ref. [117]).

Looking at the plots of Fig. 6.7, one can also observe that an inversion occurs at $U/t \simeq 4$ for the transition energies of both geometries: the transition energies obtained from ED with APBC, which were formerly labelled by E_{11}^S, become larger in magnitude than the former E_{22}^S obtained from ED with PBCs. Thus, in strong coupling regime the roles played by APBCs and PBCs for E_{11}^S and E_{22}^S are exchanged.

In order to compare the structure of the lowest excited energy levels obtained from the SC-ED method developed in this thesis with the excitonic levels obtained by Mazumdar [210, 206], it's interesting to look at the energy scale plot of the calculated eigenvalues in the very low coupling regime $U/t < 0.4$ (with APBCs) for cluster (4,0), which is shown in Fig. 6.8. We set the ground state energy to zero on the plot ordinata, so all the reported energy data are relative to the ground state energy. The ground state is always non-degenerate for all values of the correlation coupling strength. In the noninteracting limit $U = 0$, the excited levels are grouped on the energy scale and multiply degener-

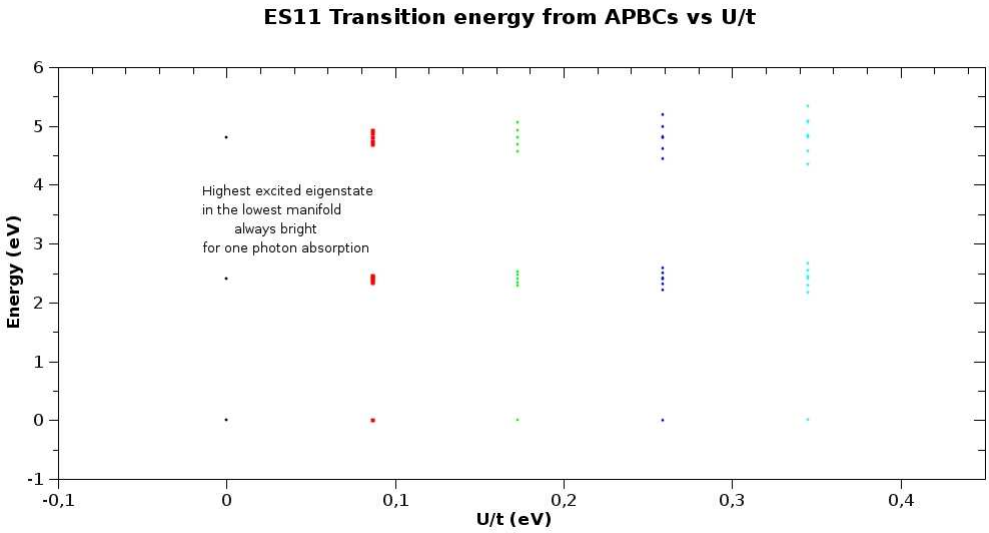

Fig. 6.8: Excited energy levels as a function of the correlation coupling U/t in the limit of very low coupling strength for cluster (4,0) and APBCs. Several manifolds are obtained whose bandwidth increase with coupling strength. The highest excited level of the lowest manifold starting from the ground state is always bright for one photon absorption, therefore providing the optical transition energy E_{11}^{S}.

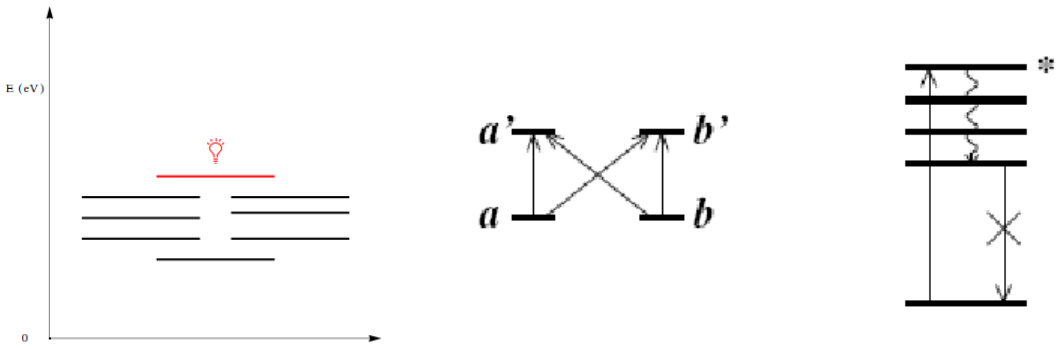

Fig. 6.9: Schematic structure of the lowest excited manifold in semiconducting zigzag nanotubes in very low coupling limit ($U/t = 0.04$) obtained in this work (left) and in Mazumdar's work (right)[208]: the manifold obtained from our ED comprises eight excited states. With increasing U/t the level spacings change and degeneracies of levels formerly at nearly the same energy are eventually lifted to give eight distinct states.

ate, in particular the lowest excited energy level includes eight degenerate states, which are all optically active (bright) for one photon absorption. This fact can be verified also for (5,0) cluster and can be explained as it follows. The gap states of semiconducting zigzag nanotubes are always doubly-degenerate. Thus interband single-excitation electronic transitions are allowed between each of the two valence band states and each of the two conduction band states. Since each band can be filled with at most two electrons with opposite spin, by taking into account spin degeneracy, we have $(2 \times 2) \times 2 = 4 \times 2 = 8$ states, as found in our calculations. This degeneracy is actually lifted off by switching on the Coulomb interaction with $U > 0$.

In general, one can observe for each $U/t > 0$ the appearence of several distinct energy level manifolds, whose energy bandwidth becomes larger with increasing coupling strength (Fig. 6.8). For $U/t > 1$ the higher energy manifolds are mixed with the lower energy ones and cannot be distinguished anylonger. Interestingly, one can verify that for each value of the correlation coupling strength U/t in the very low regime $U/t \ll 1$ the highest energy level belonging to the lowest excited energy manifold is always bright and non-degenerate. The same result could be verified for cluster (5,0) and $U/t = 0.4$. This result actually gives a similar picture of the lowest excitonic manifold given by Zhao and Mazumdar in Ref. [208] and reported in Fig. 6.9, together with a schematic representation of the energy level structure obtained in this work.

In order to get a deeper understanding of the correlated structure of these eigenstates, a charge distribution analysis over the cluster sites was performed for the ground state, the bright state and the dark states belonging to the manifold. We considered which occupation number basis states are related to the largest (in absolute value) eigenstate coefficients. Although this method could seem rather rough, it actually provides an essentially correct picture, which is also confirmed by a more formal method involving the calculation of the charge density correlation function for a given eigenstate, as we will see in the following. In general, we observed that the ground state and the remaining dark states in this manifold have uniform charge distribution for any U/t in low-intermediate coupling regime. On the other hand, the optically active state has a strongly non-uniform charge distribution over the cluster sites: the occupation number states giving the dominating contribution are actually represented by doubly-occupied sites regularly alternated with empty sites, as sketched schematically in Fig. 6.10 for cluster (4,0). This is actually the pattern of a charge-density wave (CDW).

As stated above, the peculiarity of this bright state is reflected in particular in the values of the charge-density correlation function and in the double-empty site correlation function calculated for a given eigenstate. The general expression for a correlation function is [217]

$$\langle \hat{O} \rangle = \frac{\langle \psi_i | \hat{O} | \psi_i \rangle}{\langle \psi_i | \psi_i \rangle} \tag{6.24}$$

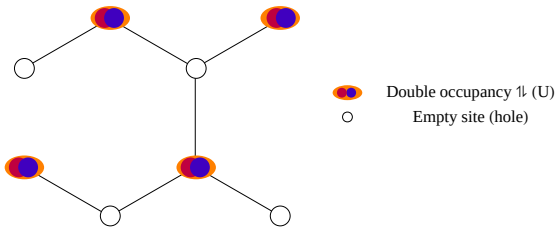

Fig. 6.10: Schematic representation of the charge distribution for the optically active state giving the E_{11}^S transition: doubly occupied sites alternate regularly with empty sites.

where ψ_i is any eigenstate wavefunction and $\hat{O}$ is a generic quantum mechanical operator. For charge density wave correlation functions between sites of separation *j*, $\hat{O}$ is expressed by

$$\hat{O_{CDW}} = \frac{1}{L}\sum_i \left(n_{i,\uparrow} + n_{i,\downarrow}\right)\left(n_{i+j,\uparrow} + n_{i+j,\downarrow}\right), \tag{6.25}$$

where *L* is the number of sites in the system. Similarly, we can define other useful correlation functions, such as the doubly occupied correlation function [2], the empty site correlation function [3], the spin S_z correlation function [4] and the above mentioned double-empty correlation function, which is expressed by

$$\hat{O_{ed}} = \frac{1}{L}\sum_i \left(1 - n_{i,\uparrow}\right)\left(1 - n_{i,\downarrow}\right) n_{i+j,\uparrow} n_{i+j,\downarrow}. \tag{6.26}$$

In Fig. 6.11 we report the values for the charge and the empty-double correlation functions calculated for $j = 1$ (i.e. considering only nearest neighbor sites) for each eigenstate of the lowest excited manifold of cluster (4,0) obtained from ED with APBCs. For the Hubbard parameters we used those computed by Cini *et al.*, hence we are in an intermediate coupling regime. However, we verified that the situation is similar also for other values of U/t in low-intermediate coupling (not shown). The light bulb symbol is used to highlight the bright state. One can see a strong deviation of the value related to the optically active state from the average of the other dark states for both correlation functions. The energy spacings between the bright state in this manifold and the immediately two underlying dark states have been also considered for both clusters with PBCs and APBCs and compared with some recently available experimental measurements by photoluminescence microscopy reported in Ref. [206]. The measured values found in this experimental paper are reported in Fig. 6.12, together with the results from our ED: the two

[2] $\hat{O_d} = \frac{1}{L}\sum_i n_{i,\uparrow} n_{i,\downarrow} n_{i+j,\uparrow} n_{i+j,\downarrow}$
[3] $\hat{O_e} = \frac{1}{L}\sum_i \left(1 - n_{i,\uparrow}\right)\left(1 - n_{i,\downarrow}\right)\left(1 - n_{i+j,\uparrow}\right)\left(1 - n_{i+j,\downarrow}\right)$
[4] $\hat{O_{SDW}} = \frac{1}{L}\sum_i \left(n_{i,\uparrow} - n_{i,\downarrow}\right)\left(n_{i+j,\uparrow} - n_{i+j,\downarrow}\right)$

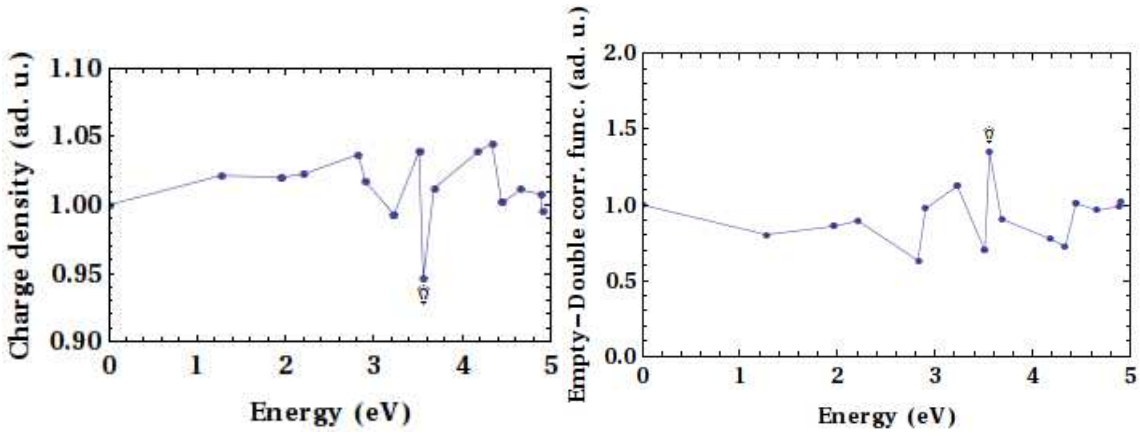

Fig. 6.11: Charge and empty-double correlation function with $j = 1$ for the eigenstates in the lowest excited manifold (APBCs) of cluster (4,0) calculated from ED with the Hubbard parameters by M. Cini *et al* [212]. The values calculated for each eigenstate are normalized to the ground state value. The optically active state is represented by the light bulb symbol.

dark states are 40 meV and 110 meV under the bright state, respectively. Our ED calculations with Cini's Hubbard parameters actually provide values which agree well with these estimates: for cluster (5,0) the dark states are between 70 meV and 90 meV under the optically active state, while for (4,0) they are located 40 meV and 330 meV under the bright state.

The situation is different for the bright state involved in E_{22} transition. In low-coupling limit (where PBCs have to be used) the optical absorption peak related to this transition is related to two degenerate states for cluster (4,0) and one non-degenerate state for cluster (5,0). This fact can be traced back to the different parity symmetries for the two systems. With increasing U/t the charge distribution associated with these states becomes uniform more quickly than observed in E_{11} states. Moreover, the dominating contribution to the charge distribution profile over the cluster sites is given by basis states with a low degree of double occupancy, with at most one or no doubly occupied sites at all. In particular, in the case of cluster (4,0) for U/t in intermediate-strong coupling limit one can verify that one of the two degenerate bright states has a non-uniform charge distribution (i.e similar to that of E_{11}), while the other state has a uniform one, with single occupancy almost everywhere. This suggests that in low-intermediate regime $U/t < 2$, where *U* is still comparable to the system bandwidth *w*, the low energy eigenstates are dominated by the kinetic energy term of the Hubbard hamiltonian. Thus, charge fluctuations with a high degree of double occupancy (3-4 doubly occupied sites in a 8-site cluster) dominate the optically active state E_{11}. On the other hand, the higher energy states, such as

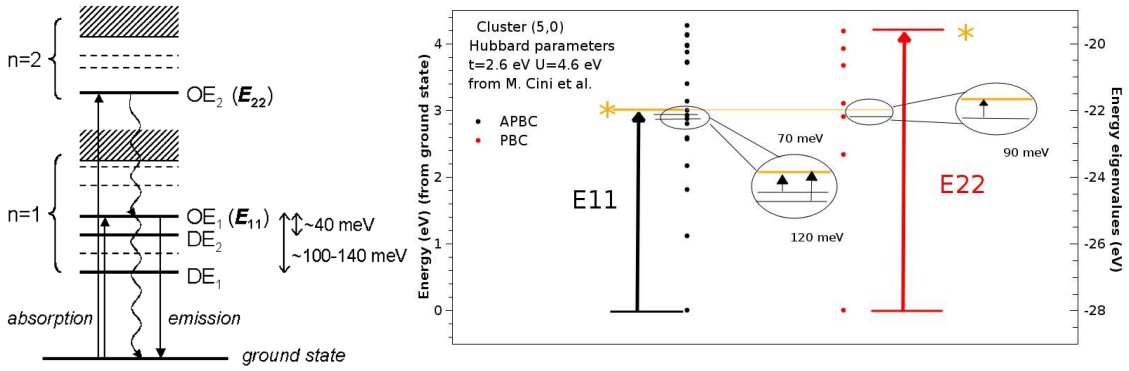

Fig. 6.12: Schematic diagram of manifolds ($n = 1, 2$) of excitonic states (horizontal lines) and electron-hole continuum bands (shaded areas) in semiconducting SWNTs (left) and the results obtained for cluster (5,0) with Cini's parameters in this thesis (right). One-photon optically active excitons are associated with transition energies E_{11} and E_{22}. Dark states lie 40 and 140 meV (left) and 70 and 90 meV(right) below the E_{11} state, respectively. Notice that in our analysis both states from ED with APBCs and PBCs were considered. The picture on the left is taken from Ref. [206].

those involved in E_{22}, are closer to the point-zero energy and thus are mostly governed by the Coulomb repulsion term *U*, which tends to minimize double occupancy as much as possible. Additional ED calculations were performed for $U \gg w$, where the system bandwidth is specified by $w = 2zt$, with *z* being the system coordination number ($z = 3$ for graphene and nanotubes). One can notice from Fig. 6.13 that in this limit the highest energy dark states below the E_{11} bright state are found very deep in energy at about 7 eV from this state. The excited electronic structure in this strong coupling limit is clearly different from the one found previously for low-intermediate coupling strength, since a large optical gap can be observed in this case.

This investigation actually confirms that in strong coupling limit, where *U* is significatively higher than the system bandwidth, a charge redistribution occurs such that double occupancy is avoided as much as possible. Charge fluctuations are frozen and at most only states with one double occupied site are allowed in order to minimize the total energy. In this case the system can be considered to be in the *Mott insulator* regime.

Thus, we can conclude that for intermediate correlation coupling the two competing terms in the Hubbard hamiltonian act differently on E_{11} and E_{22} bright states, allowing consistent charge fluctuations in the lowest part of the electronic spectrum and minimal charge repulsion at higher energy. Although our approach can be applied at the moment only to small systems with a limited number of sites, all these results point out for the validity of the method developed in this thesis and the necessity of further investigations in this di-

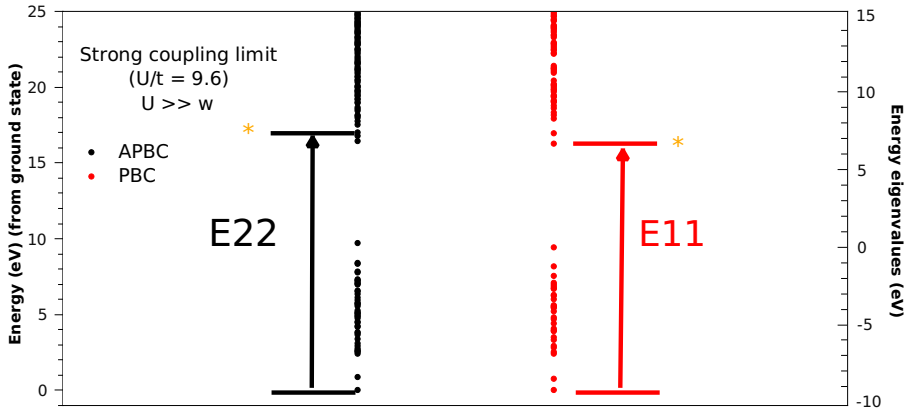

Fig. 6.13: Structure of the energy manifolds in strong coupling limit with $U \gg w$, calculated for cluster (4,0) and $U/t = 9.6$.

rection for larger size systems, since the important features of the excitonic description of the electronic structure in SWNTs, as provided by Mazumdar's SCI-HF calculations for large diameter tubes, could be recovered by a small crystal Hubbard model calculation.

6.5 Other applications: doping and defects

In this last section we report some basic facts and preliminary results of the application of TB-SC approach for treating the effects of electronic doping and point defects on the electronic structure of SWNTs. We recall that the issue of local symmetry breaking of the lattice due to impurities or doping is usually treated with difficulty by reciprocal space based methods.

First, we consider the case of electron doping, namely the addition or subtraction of electrons to the π-system. In real experiments, this happens with charge-transfer doping, which can be achieved by intercalation of the SWNT with alkali metals, and with electrochemical doping, by varying the potential at the SWNT contact interface with an electrolytic solution. We limit our considerations to semiconducting SWNTs, to which we apply the usual TB treatment for calculating the corresponding electronic and optical properties. We recall here that the states at E_{11}^S and E_{22}^S in semiconductor SWNTs are doubly degenerate and that every valence or conduction band level can be filled with at most two electrons, with opposite spin. Since one expects that transitions related to states which are involved in doping will be suppressed, four electrons have to be added or removed to find the complete suppression of a transition. Clearly, if we fill (deplete) the conduction (valence) band with two electrons with opposite spin, we expect an E_{11}^S peak

with lower absorption intensity, since one channel is still available for the electronic transition. In order to test this hypothesis, we performed a tight-binding calculation within small-crystal approach using the exact-diagonalization scheme used for the Hubbard calculations on (4,0) clusters. This allows us to have a direct control on the number of input electrons which are necessary for constructing the basis set of the multiparticle states and the hamiltonian matrix. As usual with ED, we apply PBCs or APBCs to sample $k_z = 0$ points with μ even or odd. By increasing the number of input electrons, the size of the basis set becomes smaller, because of the increased average occupancy of the sites. Hence the hamiltonian and velocity matrices are smaller. In Fig. 6.14 we report ED optical absorption spectra with 2 and 4 electrons added to the system, respectively. By comparison of these results with the TB spectra of Fig. 6.5 one can verify respectively the partial intensity reduction of the E_{11}^S absorption peak when two electrons (with opposite spin) added to the system and the total suppression when four electrons are added, as expected.

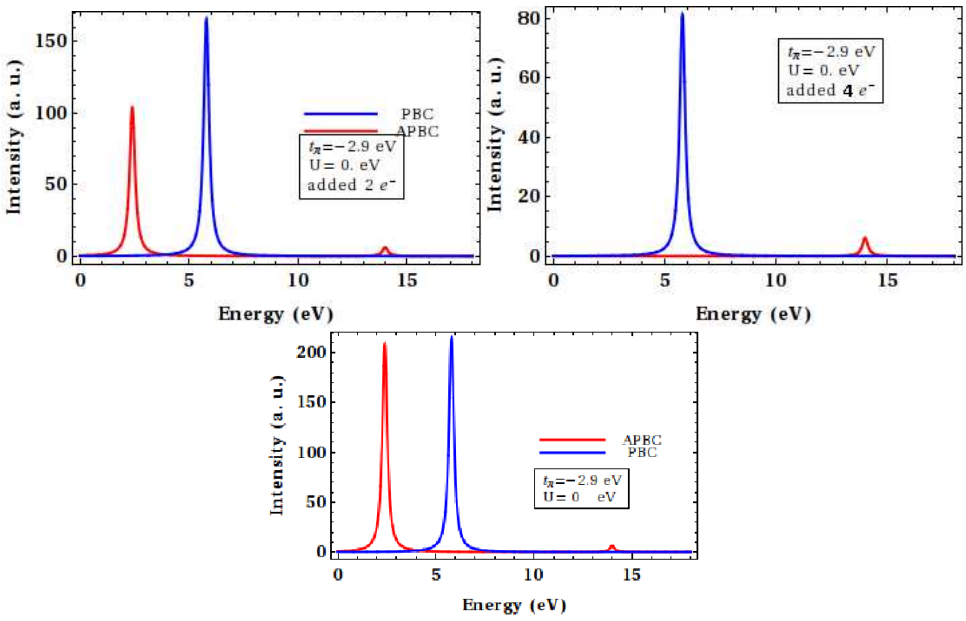

Fig. 6.14: Effect of electrochemical doping with two (upper left) and four (upper right) electrons on the tight-binding optical spectrum of cluster (4,0): the intensity of the lowest energy peak is clearly reduced and suppressed. The original spectrum unaffected by doping (bottom) is also shown for better comparison.

Besides pure electronic doping, the modeling of point defects and their effects on the nanotube electronic structure is another relevant issue in this research field. Since the electronic properties of SWNTs are deeply related with the delocalization of the π-electron system, one can actually tune the properties of the system by choosing the appropriate

type of modification affecting the π system delocalization. Several characterizations of nanotube point-defects have been performed experimentally and theoretical calculations have confirmed that vacancies, topological defects such as heptagon-pentagon pairs, substitutional impurities like B or N and lattice deformations due to sp^3 hybridized carbon atoms saturated with hydrogen or oxygen can substantially modify the electronic density of states of the system. For example, nitrogen-doped SWNTs are particularly interesting in nanotube chemistry, as they can be synthesized in large amount and because less drastic reaction conditions can be adopted for the sidewall functionalization [228]. Moreover since their first discovery they have been the subject of several theoretical investigation concerning nanotube transport properties both by *ab initio* and tight-binding methods (see [229] and references therein).
In TBA, a point defect can be modeled by assigning to a particular site a value of the on-site energy ε_{def} which differs significatively from the values of other sites, which are set by default to the same value (e.g. for SWNTs $\varepsilon_C = 0\,\mathrm{eV}$) [227]. In this work we applied the periodic SC approach both to N- and B-substituted zigzag clusters. When replacing a C atom, B or N not only act as hole or electron dopants, respectively, but also introduce lattice distortions due to deviations of their atomic radius and atomic number from those of the C atom. This fact has to be carefully considered when choosing the appropriate TB parametrization for the defect site. The effect of a different on-site energy has been studied in the past [229], but only recently the effect of a different hopping has been taken into account [230]. However, we considered in our π-TB calculations only the change in on-site energy ε_{def} related to the N (B) impurity. Assuming C on-site energy to be zero, the local energy of a N occupied site should be modeled as negative, because of the larger atomic number of N if compared with C. On the contrary, for a B-substitution, the on-site energy is positive. The following values have been used for the TB parametrization of the substitutional impurity: $\varepsilon^{\pi-\pi}_{N/B} = \mp 0.525 |t^{\pi-\pi}_C|$ [230], that is $\varepsilon^{\pi-\pi}_{N/B} = \mp 1.5225\,\mathrm{eV}$ for $|t^{\pi-\pi}_C| = 2.9\,\mathrm{eV}$. The SC approach can be applied either via the classical LCAO scheme, as explained in Chapt.4, or the more computationally expensive ED method, described in the previous sections of this chapter. Experimentally a normal atomic impurity concentration is estimated to be about 1%, very high concentrations are above 10%. For instance, in (5,0) SWNT with one unit cell cluster with one N (B) atom every 20 sites, we get an impurity concentration of 5%, a quite strong doping condition. The electronic band structures in Fig. 6.15 show clearly a weak overall lifting of the band degeneracies due to the symmetry breaking of the lattice. These plots show that even for this strongly doped system the electronic properties are dominated again by $k_z = 0$ states. Usually, one of the main effects of the substitution of a C atom by atomic species with a different number of valence electrons is the introduction in the DOS of additional states. This can be clearly seen for the nitrogen substitution in the DOS histogram superimposed on the plot for the perfect tube: the nitrogen state is located approximately 150 to $200\,\mathrm{meV}$ below the first van Hove singularity in the conduction band of the undoped tube. Thus N acts as a donor impurity and if ionization occurs such semiconducting tubes are defined

as *n*-type. For the B substitution, the situation is symmetrical, as the acceptor level is located one hundred meV above the first vHS in the valence band and if the empty B states are occupied holes are created at the edge of the valence band and the semiconducting tube is *p*-type (Fig. 6.16). This suggests that the SC optical spectra for the chosen cluster are virtually the same for both heteroatoms. The exact position of the nitrogen or boron states depends in general on the diameter, helicity and number of heteroatoms incorporated in the SWNT. The optical spectra for this system can be obtained by applying the SOS method within one of the two methods described previously (LCAO or ED scheme). The optical absorption spectrum reported for cluster (4,0) with a B impurity is reported in Fig. 6.17, where one can recognize the appearance of additional transition peaks around the transition energy peak of the perfect tube. Because of the use of periodic boundary conditions and the use of cluster of different size, the SC approach allow us to calculate the electronic density of states by properly tuning the defect concentration. In Fig. 6.18 the linear dependence on the impurity concentration of the energy position of the donor (acceptor) state with respect to the conduction (valence) is plotted for a (5,0) supercluster with a number of unit cells between 1 and 10. The intercept gives the conduction (valence) band energy for the tube without impurity. Although SC-TB calculations provide an oversimplified picture of the effects of defects on the electronic structure of SWNTs, they can be useful for a basic interpretation of electrochemical spectra of substitutionally doped or functionalized nanotubes. Clearly, *ab initio* calculations provide a more accurate and realistic treatment of electronic charge density distribution and structural deformation around the defected sites and are necessary for a more specific parametrization of the on-site energies for heteroatoms of different chemical species. Moreover, the inclusion of electronic correlation effects according to the Hubbard model, will allow to interpret the effects of the breaking of the lattice periodicity in the framework of the excitonic picture for SWNTs. This will be however the subject of future investigations with more refined theoretical and computational tools.

6.6 Conclusions, summary and future perspectives

In this chapter we presented the main experimental facts which point out for the presence of relevant excitonic correlation effects in the optical spectral features of single-walled nanotubes. First the basic features, results and limitations of the currently available theoretical methods for treating excitonic effects in these systems have been reviewed and discussed. Where possible, attention was also paid to the different parametrizations of the Coulomb correlation strength adopted in these methods, as this is a key parameter for the comparison between experimental data and the considered calculations. In order to overcome the limitations inherent to the currently available theoretical methods, we considered the Hubbard model, one of the simplest and yet most powerful methods for treating full many-body hamiltonians beyond mean field approximation. In the central

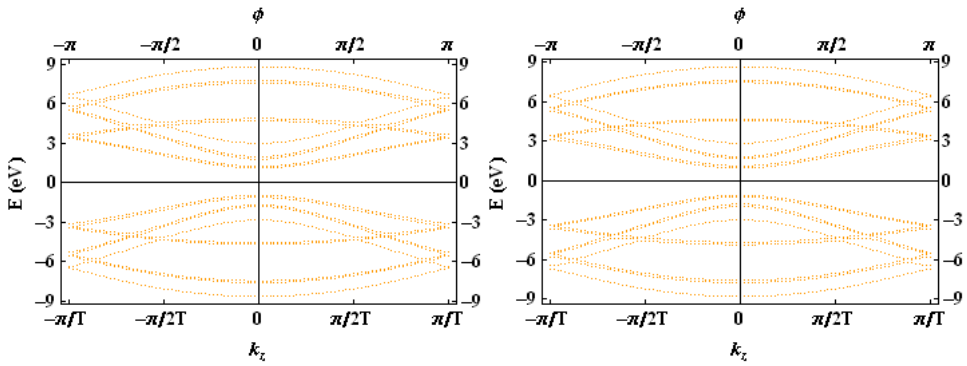

Fig. 6.15: Introduction of a point defect in zigzag cluster (5,0) with one unit cell (left: substitutional B atom with $\varepsilon_B = 1.52\,\mathrm{eV}$,right: substitutional N atom with $\varepsilon_N = -1.52\,\mathrm{eV}$) and its effects on the TB electronic band structure. The overall lifting of the doubly-degenerate effects can be observed.

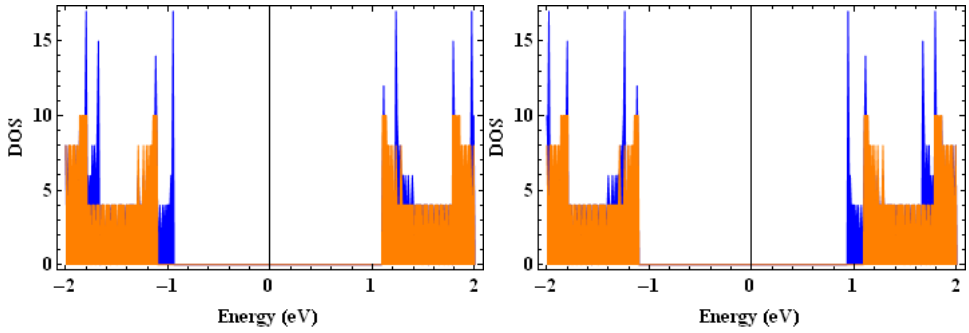

Fig. 6.16: Introduction of a point defect in zigzag cluster (5,0) with one unit cell (left: substitutional B atom with $\varepsilon_B = 1.52\,\mathrm{eV}$; right: substitutional N atom with $\varepsilon_N = -1.52\,\mathrm{eV}$) and its effects on the TB electronic density of states (blue histogram) compared to the DOS of the ideal tube (orange histogram).

part of this chapter we have showed how to apply the small crystal approach to zigzag clusters with a small number of sites (8 and 10 sites for (4,0) and (5,0) SWNTs) for the exact diagonalization of the Hubbard hamiltonian and the computation of the one-photon optical spectra for the relevant $(\mu, k_z = 0)$ points. Although our small crystal Hubbard model was applied to such small test systems, for which non-negligible curvature effects were not taken into account, we could verify that the outcoming description of the excited electronic energy levels is consistent with the SCI-HF results obtained by Mazumdar for large diameter tubes. In particular, we were able to verify two main effects of the introduction of the Coulomb correlations: the expected blueshift of the single-particle

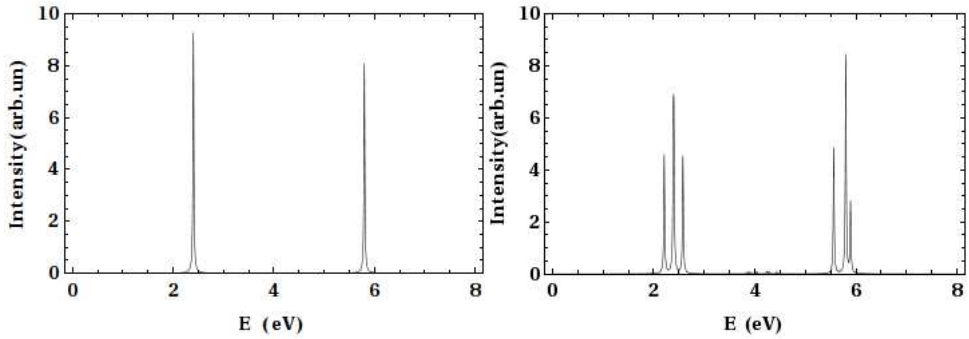

Fig. 6.17: Introduction of a point defect in zigzag cluster (4,0) with one unit cell (substitutional B, $\varepsilon_B = 1.52\,\mathrm{eV}$) and its effects on the TB optical spectra (right). The spectrum of the perfect tube (left) is also shown for better comparison.

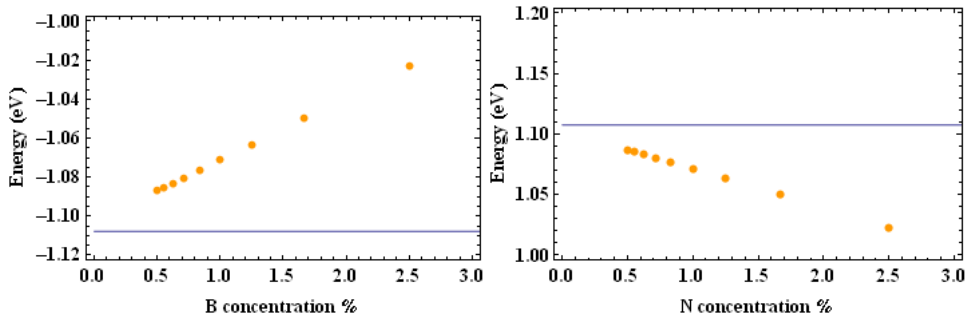

Fig. 6.18: Dependence of the energy of acceptor (donor) states on concentration, i.e. number of unit cell in the super-cluster (left: substitutional B atom, acceptor states; right: substitutional N atom, donor states.

transition energies and the presence of a strong dipole-allowed excited state, which is found at the highest energy level in the first excited manifold E_{11}. We showed that this state is characterized by strong charge fluctuations or charge density waves for low and intermediate correlation coupling strengths. Moreover, we could verify that the energy spacings between this *bright* state and each of the two underlying dipole-forbidden states are consistent with experimental measurements from photoluminescence microscopy on isolated SWNTs. In the final part we also showed a preliminary single-particle treatment of electronic doping and the inclusion of point defects which break the lattice periodicity. These aspects are of fundamental importance for understanding the electronic properties of functionalized systems.

All these results point out for the validity of the approach developed in this thesis and the necessity of performing calculations for larger size clusters, in order to establish deeper

and more accurate comparisons with experimental results for larger diameter tubes. This opens up the way for other interesting extensions and applications, such as the treatment of more complicated many body hamiltonians, including for instance an electron-phonon coupling term, triplet excitations, point defects and the computation of two-photon optical absorption spectra, for both parallel and transversal polarization of the light. Certainly, all these developments would allow for an overall deeper understanding of the excitonic properties of these systems.

Chapter 7

Summary and Conclusions

This thesis examined the theoretical aspects of the electronic properties of carbon nanotubes which are necessary for a detailed understanding of the experimental optical features of these systems and the relation with their geometrical structure. A real space based method, called *small crystal* (SC) *approach*, has been introduced for carrying on electronic structure calculations with a minimal sampling strategy of reciprocal space points. In this way, local symmetry breaking effects which are usually difficult to consider in reciprocal space can be handled more easily. Two main applications of this method were shown in this thesis: orientation dependent intertube interactions in double-walled nanotubes and Coulomb electron-electron correlations. Doping and point defects, which break the lattice periodicity of the nanotube, were also considered as additional applications. In the following we summarize the key points and the main conclusions of this thesis and suggest future directions for further developments.

In the first part of this work we introduced basic notions about carbon nanotubes and related graphitic nanostructures, including a general overview of the most used experimental characterization techniques and theoretical methods for electronic structure calculations and a whole chapter dedicated to nanotube geometry in real and reciprocal space (Chap. 1-2). From a theoretical point of view, nanotube electronic structure in its simplest approximation can be described on the basis of tight-binding calculation scheme carried in reciprocal space, also called zone-folding scheme, which was reviewed in detail in Chapt. 3. Matrix elements for electron-photon coupling can be obtained in this way, thus allowing to simulate the optical absorption spectra of single-walled nanotubes (SWNTs). By comparing experimental and theoretical Kataura plots, which show family patterns of measured/calculated transition energies with nanotube diameter, a structural assignment of nanotube chiralities to their optical signatures can be attempted. More refined tight-binding methods which include curvature effects and take into account optimized geometries can actually improve the agreement between theoretical and experimental Kataura plots of SWNTs of a wide diameter range.

However, in Chapt. 4 we pointed out that tight-binding calculations carried in recip-

rocal space usually find difficulties when considering local symmetry breaking in the electronic structure. This is the case with orientation dependent intertube interactions in double-walled nanotubes and, more generally, Coulomb electron-electron correlations (as treated in the Hubbard model) and point defects in real nanotube systems, for which a real space approach can accomplish these tasks more flexibly. The *small crystal approach* allows to sample a finite set of *n* relevant Brillouin zone points in reciprocal space starting from a finite lattice of *n* sites (cluster) with appropriate periodic boundary conditions, which ensure that the obtained energy eigenvalues and eigenstates of the corresponding Hamiltonian describe correctly the properties of an infinite system with translational periodicity. After describing the SC approach applied to periodic chains with *n* sites, we turned to finite-size graphene cluster in order to re-obtain the electronic band structure of SWNTs according to the tight-binding scheme. A full correspondence between small crystal approach and zone-folding method could be established in a general way. We stressed the special case of zigzag nanotubes, in which the critical wavectors in the 1D BZ giving both van Hove singularities and maximum absolute values of the optical matrix elements are always found at the centre of the 1D BZ ($k_z = 0$). This is a particularly convenient choice for performing hamiltonian diagonalizations with minimal computational effort, both in the case of double-walled nanotubes and Hubbard treatment of many-body effects, because of the relatively small number of sites in the unit cell, due to the high symmetry in geometrical structure. As a main result of Chapt. 4, the optical absorption profiles of a zigzag SWNT calculated from a full BZ sampling with zone-folding method and with only $k_z = 0$ points considered by SC approach are actually the same, as far as the energy position and relative intensity absorption of the transition peaks are concerned. In Chapt. 5 we showed the application of SC approach to the TB electronic structure calculation of zigzag double-walled nanotubes (DWNTs), with the possibility of changing the mutual orientation of the walls along the azimuthal and axial directions ($\Delta\Phi, \Delta Z$). The orientational effects on the DWNT electronic structure have never been fully taken into account in previous TB calculations for these systems. The pairs (5,0)@(14,0) and (9,0)@(18,0) were selected, for which the highest symmetry positions giving the most stable geometrical configurations were considered, according to both a symmetry-based analysis and a total π electronic energy calculation performed by SC approach. The electronic density of states and optical absorption profiles were calculated for these ($\Delta\Phi, \Delta Z$) positions and compared to those at default positions ($\Delta\Phi = 0, \Delta Z = 0$). Significative changes in the spectral profiles were found, in particular when a translational shift parallel to the tube axis was considered. Calculations were also performed for different values of the intertube hopping strength, which all affected the resulting sprectra, although in different manner. The changes affected mostly the energy range involving the E_S^{22} transition energy for the outer tube and the E_S^{11} transition energy for the inner tube. The appearance of additional spectral features besides those recognizable from the constituent SWNTs is explained with the lifiting of the band degeneracies due to the intertube hopping interaction, which mixes inner and outer tube wavefunctions. In light of these results the

DWNT optical spectra cannot be simply considered the sum of the optical spectra of the constituents, because of relevant effects related to the intertube hopping strength and geometric correlations between the constituent walls. Thus we point out the necessity of revising Kataura plots of DWNTs, which have been constructed until now on the basis of the hypothesis of negligible intertube interactions. However, this step will require a more accurate parametrization of the intertube hopping strength, which has not been obtained yet by density functional methods, and the averaging of the optical absorption intensity over all geometrical configurations, each with its own energy probability weight.
In Chapt. 6 the issue of the electronic correlation effects in SWNTs was introduced on the basis of the most relevant literature experimental findings: ratio problem and blueshift of the single-particle transition energies. We also summarized the current theoretical advances towards a deeper understanding of the excitonic picture for these systems and highlighted the limitations of *ab initio* methods in providing a full many-particle description of the problem. The Hubbard model was introduced with the purpose of performing a full many-body calculation on SWNTs, for which it was confirmed that short-range electron-electron repulsions play a dominant role in determining the optical features of these systems. By choosing appropriate zigzag lattice clusters with a sufficiently small number of sites (less than a dozen) and applying (anti)periodic azimuthal boundary conditions, we showed how the small crystal approach allows to set up the Hubbard hamiltonian matrix for the usual selected $k_z = 0$ critical points, including the Coulombian effects as an effective pair interaction in real space. The SC optical absorption spectra with the many-body Coulomb interaction could then be obtained by computing the optical matrix element from the velocity operator between the Hubbard groundstate and each of the lowest energy eigenstates. We showed that this simple model can account for the blueshift of the single-particle transition energies and more notably could reproduce the manifold structure of the excited electronic states, as found in the HF-SCI calculations by Mazumdar. Results for the E^{11} and E^{22} dipole-allowed states were shown for several values of the Coulomb interaction strength. In particular, our calculation confirmed that the lowest optically allowed state (bright) is found at the highest excited energy level in the first manifold starting from the ground state, as in Mazumdar's papers. Moreover, the calculated energy spacings of the two underlying dark states from the E^{11} bright state were found to be consistent with the measured PL values reported in a recent experimental paper by Kiowski. The different correlation regimes were finally discussed for supporting the charge density wave pattern of the E^{11} bright state and the all-singly occupied structure of the E^{22} bright state. We pointed out the severe limitations imposed to computer memory requirements needed for treating larger systems within the Hubbard model, due to the exponential increase of the multiparticle basis size with the number of sites in the system. This limited our computer algebra implementation of the exact diagonalization (ED) method to consider periodic clusters with 8 and 10 sites, for (4,0) and (5,0) tubes. Further advances towards a better and wider comparison with experimental and theoretical results will be certainly possible if also larger diameter tubes can be treated with more powerful

algorithms and computer architectures. Besides exact diagonalization for a larger set of tubes, calculations can also be performed for other relevant physical observables, such as two-photon absorption spectra, ED with triplet excited states and one-photon optical absorption spectra for transversal polarization of the light. In the last section of Chapt. 6, we also reported some preliminary results of the application of the TB-SC approach to the investigation of doping effects on the electronic structure of SWNTs, which will be helpful for the interpretation of electrochemical spectra of defected and/or functionalized nanotubes.

In conclusion, on the basis of the present work we prospect for the small crystal approach a wide range of promising developments in the field of theoretical nanotube science.

Appendix A

Here we show how to obtain the form of the velocity operator for expressing the optical matrix elements of a periodic Hubbard chain with *l* sites in second quantization formalism. Then the derivation will be extended to two-dimensional periodic clusters, as those considered in this work.

A.1 Velocity operator for a periodic Hubbard chain

Recall that the real part of the optical conductivity $\sigma(\omega)$ is directly proportional to the linear optical absorption coefficient $\tilde{\alpha}(\omega)$, hence it gives the optical absorption spectrum of the system. Standard time-dependent perturbation theory gives the Kubo formula for the optical conductivity which is related to the equilibrium current-current correlation function $\chi(\omega)$ by the fluctuation-dissipation theorem. Here we omit for brevity the derivation procedure, which is reported in standard many-body solid-state textbooks, such as [92, 97]. Here we just outline the fundamental steps in order to arrive at the definitions of the current and velocity operator, as in Ref. [215, 216]. The retarded current-current correlation function is defined by

$$\chi(\omega) \propto \imath \int_0^\infty dt e^{i\omega t} \langle \left[\hat{j}(t), \hat{j}(0) \right]_- \rangle \tag{A.1}$$

where $\hat{j}(t)$ is the Heisenberg current operator for the unperturbed system. The current-current correlation function can be spectrally decomposed in terms of exact eigenstates $|n\rangle$ and energy levels E_n of the Hubbard hamiltonian.

$$\chi(\omega) \propto \sum_n |\langle n|\hat{j}|0\rangle|^2 \left[\frac{1}{\omega + (E_n - E_0) + \imath\gamma} - \frac{1}{\omega - (E_n - E_0) + \imath\gamma} \right] \tag{A.2}$$

As usual $|0\rangle$ and E_0 denote the ground-state and the ground-state energy, respectively. γ is a phenomenological positive broadening parameter of the resonances at $\omega = \pm(E_n - E_0)$.

The real part of the conductivity is thus given by

$$\mathrm{Re}\left\{\sigma\left(\omega\right)\right\} = \frac{\mathrm{Im}\left\{\chi\left(\omega\right)\right\}}{\omega} \propto \sum_{n} \left|\langle n|\hat{j}|0\rangle\right|^2 \left[\delta\left(\omega - \left(E_n - E_0\right)\right) - \delta\left(\omega + \left(E_n - E_0\right)\right)\right] \tag{A.3}$$

which is positive for all ω.
With the aid of Heisenberg equation of motion, the current operator $\hat{j}$ can be expressed in terms of the following commutator [1]

$$\hat{j} = \frac{\partial \hat{P}}{\partial t} = \frac{\imath}{\hbar}\left[\hat{P}, H\right], \tag{A.4}$$

where we have introduced the polarization operator $\hat{P} = -e\sum_{l,\sigma} \mathbf{R}_l c^{\dagger}_{l,\sigma} c_{l,\sigma}$. In a periodic linear chain with *l* sites and lattice spacing we have $\mathbf{R}_{l+1} - \mathbf{R}_l = a$, thus we can write $\mathbf{R}_l = la$ and the polarization operator becomes $\hat{P} = -ea\sum_{l,\sigma} l c^{\dagger}_{l,\sigma} c_{l,\sigma}$.
The velocity operator is simply given by $\hat{j}/e$, thus by developing the commutator in Eq. A.4 for the Hubbard chain we obtain

$$\hat{v} = \frac{\imath}{\hbar}\left[\hat{P}/e, H\right] = \tag{A.5}$$

$$\imath\left[-a\sum_{l,\sigma} l c^{\dagger}_{l,\sigma} c_{l,\sigma}, -t\sum_{l,\sigma}\left(c^{\dagger}_{l+1,\sigma} c_{l,\sigma} + c^{\dagger}_{l,\sigma} c_{l+1,\sigma}\right) + U\sum_{l} n_{l,\uparrow} n_{l,\downarrow}\right] =$$

$$-\frac{\imath}{\hbar} at \sum_{l,\sigma}\left(c^{\dagger}_{l+1,\sigma} c_{l,\sigma} - c^{\dagger}_{l,\sigma} c_{l+1,\sigma}\right)$$

Clearly, only the first term of the Hubbard hamiltonian contributes to the velocity (current) operator, since it describes a hopping from one site to its nearest neighbor. The *U* term contains only the position operator $n_{i,\sigma}$, which clearly commutes with itself, so its contribution to the velocity operator is zero.

A.2 Velocity operator generalized to two-dimensional systems

Consider a general 2D infinite lattice specified by *a* and *b* directions where $\vec{i}, \vec{j}$ are the unit vectors and a_a and a_b be the lattice parameters along these directions, respectively. The position vector of any site in the 2D lattice is defined as $\mathbf{R}_{l_a,l_b} = \left(l_a a_a\right)\vec{i} + \left(l_b a_b\right)\vec{j}$. Thus the polarization vector can be written as

$$\hat{P} = -ea\sum_{l_a,l_b,\sigma} c^{\dagger}_{l_a,l_b,\sigma} c_{l_a,l_b,\sigma}\left[\vec{i}\left(l_a a_a\right) + \vec{j}\left(l_b a_b\right)\right]. \tag{A.6}$$

[1] We note that elsewhere the current operator can be found expressed in equivalent form with the commutator of the hamiltonian and the position operator $\hat{r} = n_{l,\sigma} = c^{\dagger}_{l,\sigma} c_{l,\sigma}$, as in Ref.[215]

In order to write the form for the 2D tight-binding hamiltonian, in principle we have to consider that there are two kinds of hopping parameters for the *a* and *b* directions, namely t_a for hopping occurring between nearest-neighbor sites along *a* direction ($l_b a_b$ position is fixed), and t_b for hopping occurring between nearest-neighbor sites along *b* direction ($l_a a_a$ position fixed). Thus the tight-binding hamiltonian is composed of two contributing terms, each decoupled from the other

$$H_t = \sum_{l_a,l_b,\sigma} -t_a \left(c^\dagger_{l_a,l_b,\sigma} c_{l_a+1,l_b,\sigma} + c^\dagger_{l_a+1,l_b,\sigma} c_{l_a,l_b,\sigma} \right) + \sum_{l_a,l_b,\sigma} -t_b \left(c^\dagger_{l_a,l_b,\sigma} c_{l_a,l_b+1,\sigma} + c^\dagger_{l_a,l_b+1,\sigma} c_{l_a,l_b,\sigma} \right) \tag{A.7}$$

From this point on, we assume for simplicity that the system is isotropic along both directions *a* and *b*, namely $a_a \equiv a_b \equiv a$ and $t_a \equiv t_b \equiv t$. This is actually the case considered in this thesis.
At this point we have to calculate $\left[\hat{P}/e, H\right]$ commutators of the general form

$$\left[c^\dagger_{l'_a,l'_b,\sigma} c_{l'_a,l'_b,\sigma}, \left(c^\dagger_{l_a,l_b,\sigma} c_{l_a+1,l_b,\sigma} + c^\dagger_{l_a+1,l_b,\sigma} c_{l_a,l_b,\sigma} \right) \right], \tag{A.8}$$

where the following cases have to be considered:

- $l'_a = l_a,\ l'_b = l_b \quad \Rightarrow \quad \delta_{l'_a l_a} = 1,\ \delta_{l'_b l_b} = 1.$

$$c^\dagger_{l_a,l_b,\sigma} c_{l_a+1,l_b,\sigma} - c^\dagger_{l_a+1,l_b,\sigma} c_{l_a,l_b,\sigma} \tag{A.9}$$

- $l'_a = l_a + 1,\ l'_b = l_b \quad \Rightarrow \quad \delta_{l'_a l_a+1} = 1,\ \delta_{l'_b l_b} = 1.$

$$-c^\dagger_{l_a,l_b,\sigma} c_{l_a+1,l_b,\sigma} + c^\dagger_{l_a+1,l_b,\sigma} c_{l_a,l_b,\sigma} \tag{A.10}$$

- $l'_a = l_a,\ l'_b = l_b + 1 \quad \Rightarrow \quad \delta_{l'_a l_a} = 1,\ \delta_{l'_b l_b+1} = 1.$

$$-c^\dagger_{l_a,l_b,\sigma} c_{l_a,l_b+1,\sigma} + c^\dagger_{l_a,l_b+1,\sigma} c_{l_a,l_b,\sigma}. \tag{A.11}$$

One can notice that the above intermediate results in Eqq. (A.9-A.10) of the commutation have all the same structure, so we can label them by I_a or I_b . Then the second quantization expressions for the velocity operators along *a* and *b* directions can be written in a

more compact form as:

$$v_a = \frac{\imath}{\hbar} ta \sum_{l_a,l_b,\sigma} l'_a I_a \left(\delta_{l'_a l_a}\delta_{l'_b l_b} - \delta_{l'_a l_a+1}\delta_{l'_b l_b}\right) = \frac{\imath}{\hbar} ta \sum_{l_a,l_b,\sigma} I_a \left(l_a - l_a - 1\right) = \tag{A.12}$$

$$= -\frac{\imath}{\hbar} ta \sum_{l_a,l_b,\sigma} c^\dagger_{l_a,l_b,\sigma} c_{l_a+1,l_b,\sigma} - c^\dagger_{l_a+1,l_b,\sigma} c_{l_a,l_b,\sigma}$$

$$v_b = \frac{\imath}{\hbar} ta \sum_{l_a,l_b,\sigma} l'_b I_b \left(\delta_{l'_a l_a}\delta_{l'_b l_b} - \delta_{l'_a l_a}\delta_{l'_b l_b+1}\right) = \frac{\imath}{\hbar} ta \sum_{l_a,l_b,\sigma} I_b \left(l_b - l_b - 1\right) = \tag{A.13}$$

$$= -\frac{\imath}{\hbar} ta \sum_{l_a,l_b,\sigma} \left(c^\dagger_{l_a,l_b,\sigma} c_{l_a,l_b+1,\sigma} - c^\dagger_{l_a,l_b+1,\sigma} c_{l_a,l_b,\sigma}\right)$$

Appendix B

In the following we report for practical use the extended expressions of the Hamiltonian and velocity v_z operators written in second quantization formalism for zigzag clusters (4,0) and (5,0) with $4n$ (full unit cell) and $2n$ sites with the proper boundary conditions.

B.1 Cluster (4,0) with *4 n* sites

Here translational periodic boundary conditions are used where the phase $-\pi \leq \phi \leq \pi$ for sweeping the whole 1D BZ.

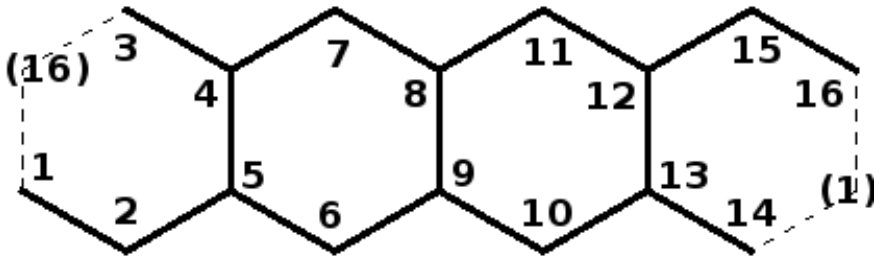

Fig. B.1: Cluster (4,0) with $4n$ sites.

$$
\begin{aligned}
H = \sum_{\sigma=\uparrow,\downarrow} \quad & c^{\dagger}_{1,\sigma}c_{2,\sigma} + \exp(\imath\phi)\, c^{\dagger}_{2,\sigma}c_{3,\sigma} + c^{\dagger}_{2,\sigma}c_{5,\sigma} + (\text{h.c.terms}) + \\
& c^{\dagger}_{3,\sigma}c_{4,\sigma} + c^{\dagger}_{3,\sigma}c_{16,\sigma} + c^{\dagger}_{4,\sigma}c_{5,\sigma} + c^{\dagger}_{5,\sigma}c_{6,\sigma} + (\text{h.c.terms}) + \\
& c^{\dagger}_{4,\sigma}c_{7,\sigma} + \exp(\imath\phi)\, c^{\dagger}_{6,\sigma}c_{7,\sigma} + c^{\dagger}_{7,\sigma}c_{8,\sigma} + (\text{h.c.terms}) + \\
& c^{\dagger}_{6,\sigma}c_{9,\sigma} + c^{\dagger}_{8,\sigma}c_{9,\sigma} + c^{\dagger}_{9,\sigma}c_{10,\sigma} + (\text{h.c.terms}) + \\
& c^{\dagger}_{8,\sigma}c_{11,\sigma} + c^{\dagger}_{11,\sigma}c_{12,\sigma} + \exp(\imath\phi)\, c^{\dagger}_{10,\sigma}c_{11,\sigma} + (\text{h.c.terms}) + \\
& c^{\dagger}_{10,\sigma}c_{13,\sigma} + c^{\dagger}_{12,\sigma}c_{13,\sigma} + c^{\dagger}_{13,\sigma}c_{14,\sigma} + c^{\dagger}_{1,\sigma}c_{14,\sigma} + (\text{h.c.terms}) + \\
& c^{\dagger}_{12,\sigma}c_{15,\sigma} + c^{\dagger}_{15,\sigma}c_{16,\sigma} + \exp(\imath\phi)\, c^{\dagger}_{14,\sigma}c_{15,\sigma} + c^{\dagger}_{1,\sigma}c_{16,\sigma} + (\text{h.c.terms})
\end{aligned}
\tag{B.1}
$$

$$v_z = -\frac{\imath t}{\hbar}\sum_{\sigma=\uparrow,\downarrow}\left(-\frac{1}{2}\right)c^{\dagger}_{1,\sigma}c_{2,\sigma} + \exp\left(\imath\phi\right)\left(-1\right)c^{\dagger}_{2,\sigma}c_{3,\sigma} + \frac{1}{2}c^{\dagger}_{2,\sigma}c_{5,\sigma} + \left(\text{h.c.terms}\right) \tag{B.2}$$
$$+\left(-\frac{1}{2}\right)c^{\dagger}_{3,\sigma}c_{4,\sigma} + \left(-\frac{1}{2}\right)c^{\dagger}_{3,\sigma}c_{16,\sigma} + \left(-1\right)c^{\dagger}_{4,\sigma}c_{5,\sigma} + \left(-\frac{1}{2}\right)c^{\dagger}_{5,\sigma}c_{6,\sigma} + \left(\text{h.c.terms}\right) +$$
$$\left(\frac{1}{2}\right)c^{\dagger}_{4,\sigma}c_{7,\sigma} + \exp\left(\imath\phi\right)\left(-1\right)c^{\dagger}_{6,\sigma}c_{7,\sigma} + \left(-\frac{1}{2}\right)c^{\dagger}_{7,\sigma}c_{8,\sigma} + \left(\text{h.c.terms}\right) +$$
$$\left(\frac{1}{2}\right)c^{\dagger}_{6,\sigma}c_{9,\sigma} + \left(-1\right)c^{\dagger}_{8,\sigma}c_{9,\sigma} + \left(-\frac{1}{2}\right)c^{\dagger}_{9,\sigma}c_{10,\sigma} + \left(\text{h.c.terms}\right) +$$
$$\left(\frac{1}{2}\right)c^{\dagger}_{8,\sigma}c_{11,\sigma} + \left(-\frac{1}{2}\right)c^{\dagger}_{11,\sigma}c_{12,\sigma} + \exp\left(\imath\phi\right)\left(-1\right)c^{\dagger}_{10,\sigma}c_{11,\sigma} + \left(\text{h.c.terms}\right) +$$
$$\left(\frac{1}{2}\right)c^{\dagger}_{10,\sigma}c_{13,\sigma} + \left(-1\right)c^{\dagger}_{12,\sigma}c_{13,\sigma} + \left(-\frac{1}{2}\right)c^{\dagger}_{13,\sigma}c_{14,\sigma} + \left(-\frac{1}{2}\right)c^{\dagger}_{1,\sigma}c_{14,\sigma} + \left(\text{h.c.terms}\right) +$$
$$\left(\frac{1}{2}\right)c^{\dagger}_{12,\sigma}c_{15,\sigma} + \left(-\frac{1}{2}\right)c^{\dagger}_{15,\sigma}c_{16,\sigma} + \exp\left(\imath\phi\right)\left(-1\right)c^{\dagger}_{14,\sigma}c_{15,\sigma} + \left(+1\right)c^{\dagger}_{1,\sigma}c_{16,\sigma} + \left(\text{h.c.terms}\right).$$

B.2 Cluster (5,0) with *4 n* sites

Here translational periodic boundary conditions are used where the phase $-\pi \leq \phi \leq \pi$ for sweeping the whole 1D BZ.

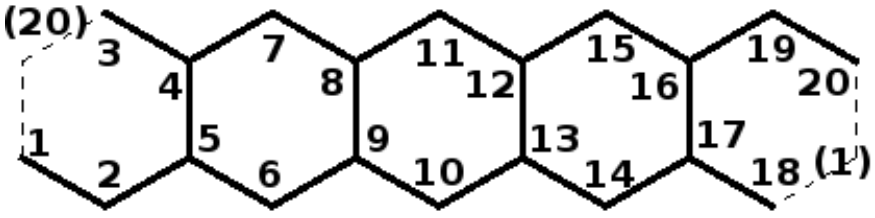

Fig. B.2: Cluster (5,0) with $4n$ sites.

$$
\begin{aligned}
H = \sum_{\sigma=\uparrow,\downarrow} & c^{\dagger}_{1,\sigma}c_{2,\sigma} + \exp(\imath\phi)\, c^{\dagger}_{2,\sigma}c_{3,\sigma} + c^{\dagger}_{2,\sigma}c_{5,\sigma} + (\text{h.c.terms}) + \\
& c^{\dagger}_{3,\sigma}c_{4,\sigma} + c^{\dagger}_{4,\sigma}c_{5,\sigma} + c^{\dagger}_{5,\sigma}c_{6,\sigma} + (\text{h.c.terms}) + \\
& c^{\dagger}_{4,\sigma}c_{7,\sigma} + \exp(\imath\phi)\, c^{\dagger}_{6,\sigma}c_{7,\sigma} + c^{\dagger}_{7,\sigma}c_{8,\sigma} + (\text{h.c.terms}) + \\
& c^{\dagger}_{6,\sigma}c_{9,\sigma} + c^{\dagger}_{8,\sigma}c_{9,\sigma} + c^{\dagger}_{9,\sigma}c_{10,\sigma} + (\text{h.c.terms}) + \\
& c^{\dagger}_{8,\sigma}c_{11,\sigma} + c^{\dagger}_{11,\sigma}c_{12,\sigma} + \exp(\imath\phi)\, c^{\dagger}_{10,\sigma}c_{11,\sigma} + (\text{h.c.terms}) + \\
& c^{\dagger}_{10,\sigma}c_{13,\sigma} + c^{\dagger}_{12,\sigma}c_{13,\sigma} + c^{\dagger}_{13,\sigma}c_{14,\sigma} + (\text{h.c.terms}) + \\
& c^{\dagger}_{12,\sigma}c_{15,\sigma} + c^{\dagger}_{15,\sigma}c_{16,\sigma} + \exp(\imath\phi)\, c^{\dagger}_{14,\sigma}c_{15,\sigma} + c^{\dagger}_{14,\sigma}c_{17,\sigma} + (\text{h.c.terms}) \\
& c^{\dagger}_{1,\sigma}c_{18,\sigma} + c^{\dagger}_{1,\sigma}c_{20,\sigma} + c^{\dagger}_{3,\sigma}c_{20,\sigma} + c^{\dagger}_{16,\sigma}c_{17,\sigma} + (\text{h.c.terms}) + \\
& c^{\dagger}_{16,\sigma}c_{19,\sigma} + c^{\dagger}_{17,\sigma}c_{18,\sigma} + \exp(\imath\phi)\, c^{\dagger}_{18,\sigma}c_{19,\sigma} + c^{\dagger}_{19,\sigma}c_{20,\sigma} + (\text{h.c.terms})\,.
\end{aligned}
\tag{B.3}
$$

$$
\begin{aligned}
v_z = -\frac{\imath t}{\hbar} \sum_{\sigma=\uparrow,\downarrow} & \left(-\frac{1}{2}\right) c^{\dagger}_{1,\sigma}c_{2,\sigma} + \exp(\imath\phi)\,(-1)\, c^{\dagger}_{2,\sigma}c_{3,\sigma} + \left(\frac{1}{2}\right) c^{\dagger}_{2,\sigma}c_{5,\sigma} + (\text{h.c.terms}) + \\
& \left(-\frac{1}{2}\right) c^{\dagger}_{3,\sigma}c_{4,\sigma} + (-1)\, c^{\dagger}_{4,\sigma}c_{5,\sigma} + \left(-\frac{1}{2}\right) c^{\dagger}_{5,\sigma}c_{6,\sigma} + (\text{h.c.terms}) + \\
& \frac{1}{2} c^{\dagger}_{4,\sigma}c_{7,\sigma} + \exp(\imath\phi)\,(-1)\, c^{\dagger}_{6,\sigma}c_{7,\sigma} + \left(-\frac{1}{2}\right) c^{\dagger}_{7,\sigma}c_{8,\sigma} + (\text{h.c.terms}) + \\
& \frac{1}{2} c^{\dagger}_{6,\sigma}c_{9,\sigma} + (-1)\, c^{\dagger}_{8,\sigma}c_{9,\sigma} + \left(-\frac{1}{2}\right) c^{\dagger}_{9,\sigma}c_{10,\sigma} + (\text{h.c.terms}) + \\
& \frac{1}{2} c^{\dagger}_{8,\sigma}c_{11,\sigma} + \left(-\frac{1}{2}\right) c^{\dagger}_{11,\sigma}c_{12,\sigma} + \exp(\imath\phi)\,(-1)\, c^{\dagger}_{10,\sigma}c_{11,\sigma} + (\text{h.c.terms}) + \\
& \left(\frac{1}{2}\right) c^{\dagger}_{10,\sigma}c_{13,\sigma} + (-1)\, c^{\dagger}_{12,\sigma}c_{13,\sigma} + \left(-\frac{1}{2}\right) c^{\dagger}_{13,\sigma}c_{14,\sigma} + (\text{h.c.terms}) + \\
& \frac{1}{2} c^{\dagger}_{12,\sigma}c_{15,\sigma} + \left(-\frac{1}{2}\right) c^{\dagger}_{15,\sigma}c_{16,\sigma} + \exp(\imath\phi)\,(-1)\, c^{\dagger}_{14,\sigma}c_{15,\sigma} + \frac{1}{2} c^{\dagger}_{14,\sigma}c_{17,\sigma} + (\text{h.c.terms}) \\
& \left(-\frac{1}{2}\right) c^{\dagger}_{1,\sigma}c_{18,\sigma} + (+1)\, c^{\dagger}_{1,\sigma}c_{20,\sigma} + \left(-\frac{1}{2}\right) c^{\dagger}_{3,\sigma}c_{20,\sigma} + (-1)\, c^{\dagger}_{16,\sigma}c_{17,\sigma} + (\text{h.c.terms}) + \\
& \frac{1}{2} c^{\dagger}_{16,\sigma}c_{19,\sigma} + \left(-\frac{1}{2}\right) c^{\dagger}_{17,\sigma}c_{18,\sigma} + \exp(\imath\phi)\,(-1)\, c^{\dagger}_{18,\sigma}c_{19,\sigma} + \left(-\frac{1}{2}\right) c^{\dagger}_{19,\sigma}c_{20,\sigma} + (\text{h.c.terms})\,.
\end{aligned}
\tag{B.4}
$$

B.3 Cluster (4,0) with *2n* sites

Here azimuthal (anti)periodic boundary conditions are used in order to sample $k_z = 0$ points on cutting lines with μ even (odd), where the phase $\phi = 0, \ldots, 2n\pi$ for PBCs and $\phi = \pm\pi, \ldots, \pm(2n+1)\pi$ for APBCs.

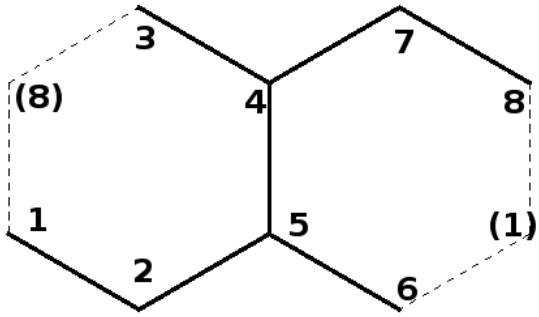

Fig. B.3: Cluster (4,0) with $2n$ sites.

$$
\begin{aligned}
H = -t \sum_{\sigma=\uparrow,\downarrow} & c^{\dagger}_{1,\sigma}c_{2,\sigma} + c^{\dagger}_{2,\sigma}c_{3,\sigma} + c^{\dagger}_{2,\sigma}c_{5,\sigma} + (\text{h.c.terms}) + \\
& c^{\dagger}_{3,\sigma}c_{4,\sigma} + c^{\dagger}_{4,\sigma}c_{5,\sigma} + c^{\dagger}_{5,\sigma}c_{6,\sigma} + (\text{h.c.terms}) + \\
& c^{\dagger}_{4,\sigma}c_{7,\sigma} + c^{\dagger}_{6,\sigma}c_{7,\sigma} + c^{\dagger}_{7,\sigma}c_{8,\sigma} + (\text{h.c.terms}) + \\
\exp(\imath\phi) & \left[c^{\dagger}_{1,\sigma}c_{8,\sigma} + c^{\dagger}_{3,\sigma}c_{8,\sigma} + c^{\dagger}_{1,\sigma}c_{6,\sigma}\right] + \exp(-\imath\phi)\,[\text{h.c.terms}]
\end{aligned}
\tag{B.5}
$$

$$
\begin{aligned}
v_z = -\frac{\imath t}{\hbar} \sum_{\sigma=\uparrow,\downarrow} & -\frac{1}{2}c^{\dagger}_{1,\sigma}c_{2,\sigma} + (-1)\,c^{\dagger}_{2,\sigma}c_{3,\sigma} + \frac{1}{2}c^{\dagger}_{2,\sigma}c_{5,\sigma} - (\text{ h.c.terms}) + \\
& \left(-\frac{1}{2}\right)c^{\dagger}_{3,\sigma}c_{4,\sigma} + (-1)\,c^{\dagger}_{4,\sigma}c_{5,\sigma} + \left(-\frac{1}{2}\right)c^{\dagger}_{5,\sigma}c_{6,\sigma} - (\text{h.c.terms}) + \\
& \frac{1}{2}c^{\dagger}_{4,\sigma}c_{7,\sigma} + (-1)\,c^{\dagger}_{6,\sigma}c_{7,\sigma} + \left(-\frac{1}{2}\right)c^{\dagger}_{7,\sigma}c_{8,\sigma} - (\text{h.c.terms}) + \\
\exp(\imath\phi) & \left[(+1)\,c^{\dagger}_{1,\sigma}c_{8,\sigma} + \left(-\frac{1}{2}\right)c^{\dagger}_{3,\sigma}c_{8,\sigma} + \left(-\frac{1}{2}\right)c^{\dagger}_{1,\sigma}c_{6,\sigma}\right] - \exp(-\imath\phi)\,[\text{h.c.terms}]\,.
\end{aligned}
\tag{B.6}
$$

B.4 Cluster (5,0) with *2n* sites

Here azimuthal (anti)periodic boundary conditions are used in order to sample $k_z = 0$ points on cutting lines with μ even (odd), where the phase $\phi = 0, \ldots, 2n\pi$ for PBCs and $\phi = \pm\pi, \ldots, \pm(2n+1)\pi$ for APBCs.

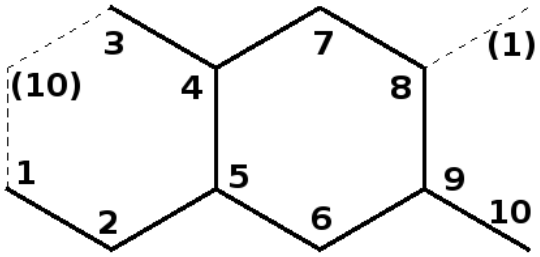

Fig. B.4: Cluster (5,0) with $2n$ sites.

$$
\begin{aligned}
H = -t \sum_{\sigma=\uparrow,\downarrow} & c^{\dagger}_{1,\sigma}c_{2,\sigma} + c^{\dagger}_{2,\sigma}c_{3,\sigma} + c^{\dagger}_{2,\sigma}c_{5,\sigma} + (\text{h.c.terms}) + \\
& c^{\dagger}_{3,\sigma}c_{4,\sigma} + c^{\dagger}_{4,\sigma}c_{5,\sigma} + c^{\dagger}_{5,\sigma}c_{6,\sigma} + (\text{h.c.terms}) + \\
& c^{\dagger}_{4,\sigma}c_{7,\sigma} + c^{\dagger}_{6,\sigma}c_{7,\sigma} + c^{\dagger}_{7,\sigma}c_{8,\sigma} + (\text{h.c.terms}) + \\
& c^{\dagger}_{6,\sigma}c_{9,\sigma} + c^{\dagger}_{8,\sigma}c_{9,\sigma} + c^{\dagger}_{9,\sigma}c_{10,\sigma} + (\text{h.c.terms}) + \\
\exp(\imath\phi) & \left[c^{\dagger}_{1,\sigma}c_{8,\sigma} + c^{\dagger}_{1,\sigma}c_{10,\sigma} + c^{\dagger}_{3,\sigma}c_{10,\sigma} \right] + \exp(-\imath\phi)\left[\text{h.c.terms}\right].
\end{aligned}
\tag{B.7}
$$

$$
\begin{aligned}
v_z = -\frac{\imath t}{\hbar} \sum_{\sigma=\uparrow,\downarrow} & -\frac{1}{2}c^{\dagger}_{1,\sigma}c_{2,\sigma} + (-1)\, c^{\dagger}_{2,\sigma}c_{3,\sigma} + \frac{1}{2}c^{\dagger}_{2,\sigma}c_{5,\sigma} - (\text{h.c.terms}) + \\
& \left(-\frac{1}{2}\right) c^{\dagger}_{3,\sigma}c_{4,\sigma} + (-1)\, c^{\dagger}_{4,\sigma}c_{5,\sigma} + \left(-\frac{1}{2}\right) c^{\dagger}_{5,\sigma}c_{6,\sigma} - (\text{h.c.terms}) + \\
& \frac{1}{2}c^{\dagger}_{4,\sigma}c_{7,\sigma} + (-1)\, c^{\dagger}_{6,\sigma}c_{7,\sigma} + \left(-\frac{1}{2}\right) c^{\dagger}_{7,\sigma}c_{8,\sigma} - (\text{h.c.terms}) + \\
& \frac{1}{2}c^{\dagger}_{6,\sigma}c_{9,\sigma} + (-1)\, c^{\dagger}_{8,\sigma}c_{9,\sigma} + \left(-\frac{1}{2}\right) c^{\dagger}_{9,\sigma}c_{10,\sigma} - (\text{h.c.terms}) + \\
\exp(\imath\phi) & \left[\left(-\frac{1}{2}\right) c^{\dagger}_{1,\sigma}c_{8,\sigma} + (-1)\, c^{\dagger}_{1,\sigma}c_{10,\sigma} + \left(-\frac{1}{2}\right) c^{\dagger}_{3,\sigma}c_{10,\sigma} \right] - \exp(-\imath\phi)\left[\text{h.c.terms}\right].
\end{aligned}
\tag{B.8}
$$

Bibliography

[1] H. W. Kroto, J. R. Heath, S. C. O' Brien, R. F. Curl, and R. E. Smalley. C_{60}*: Buckminsterfullerene*. Nature **318**, 162 (1985).

[2] K. S. Novoselov, A. K. Geim, S. V. Morozov, D. Jiang, Y. Zhang, S. V. Dubonos, I. V. Grigorieva, and A. A. Firsov. *Electric field effect in atomically thin carbon films*. Science **306**, 666 (2004).

[3] K. S. Novoselov, D. Jiang, F. Schedin, T. J. Booth, V. V. Khotkevich, S. V. Morozov, and A. K. Geim. *Two-dimensional atomic crystals*. Proc. Natl. Acad. Sci. **102**, 10451 (2005).

[4] J. C. Meyer, A. K. Geim, M. I. Katsnelson, K. S. Novoselov, T. J. Booth, and S. Roth. *The structure of suspended graphene sheets*. Nature **446**, 60 (2007).

[5] A. K. Geim and K. S. Novoselov. *The rise of graphene*. Nature Materials **6**, 183 (2007).

[6] S. Stankovich, R. D. Piner, X. Chen, N. Wu, S. T. Nguyen, and R. S. Ruoff. *Stable aqueous dispersions of graphitic nanoplatelets via the reduction of exfoliated graphite oxide in the presence of poly(sodium 4-styrenesulfonate)*. J. Mater. Chem. **16**, 155 (2006).

[7] A. E. Karu and M. Beer. *Pyrolytic formation of highly crystalline graphite films*. J. Appl. Phys. **37**, 2179 (1966).

[8] C. Oshima and A. Nagashima. *Ultra-thin epitaxial films of graphite and hexagonal boron nitride on solid surfaces*. J. Phys.: Cond. Matter **9**,1 (1997).

[9] L. C. Isett and J. M. Blakely. *Segregation isosteres for carbon at the (100) surface of nickel*. Surf. Sci. **58**, 397 (1976).

[10] J. C. Hamilton and J. M. Blakely. *Carbon segregation to single crystal surfaces of Pt, Pd and Co*. Surf. Sci. **91**, 199 (1980).

[11] S. Iijima. *Helical microtubules of graphitic carbon*. Nature **354**, 56 (1991).

[12] S. Iijima and T. Ichihashi. *Single-shell carbon nanotubes of 1-nm diameter*. Nature **363**, 603 (1993).

[13] M. Monthioux and V. L. Kuznetsov. *Who should be given the credit for the discovery of carbon nanotubes?* Carbon **44**, 1621 (2006).

[14] L. V. Radushkevich and V. M. Lukyanovich. *O strukture ugleroda, obrazujucegosja pri termiceskom razlozenii okisi ugleroda na zeleznom kontakte*. Zurn. Fisic. Chim. **26**, 88 (1952).

[15] A. Oberlin, M. Endo, and T. Koyama. *Filamentous growth of carbon through benzene decomposition*. J. Cryst. Growth **32**, 335 (1976).

[16] D. Bethune, C. Klang, M. de Vries, G. Gorman, R. Savoy, J. Vazquez, and R. Beyers. *Cobalt-catalysed growth of carbon nanotubes with single-atomic-layer walls*. Nature **363**, 605 (1993).

[17] P. M. Ajayan and S. Iijima. *Smallest carbon nanotube*. Nature **358**, 23 (1992).

[18] L.-C. Qin, X. Zhao, K. Hirahara, Y. Miyamoto, Y. Ando, and S. Iijima. *The smallest carbon nanotube*. Nature **408**, 50 (2000).

[19] L. F. Sun, S. S. Xie, W. Liu, W. Y. Zhou, Z. Q. Liu, D. S. Tang, G. Wang, and L. X. Qian. *Creating the narrowest carbon nanotubes*. Nature **403**, 384 (2000).

[20] N. Wang, Z. K. Tang, G. D. Li, and J. S. Chen. Materials science: *Single-walled 4 Å carbon nanotube arrays*. Nature **408**, 50 (2000).

[21] C.-H. Kiang. *Growth of large-diameter single-walled carbon nanotubes*. J. Phys. Chem. A **104**, 2454 (2000).

[22] M. Reibold, P. Paufler, A. A. Levin, W. Kochmann, N. Ptzke, and D. C. Meyer. *Materials: Carbon nanotubes in an ancient Damascus sabre*. Nature **444**, 286 (2006).

[23] T. W. Ebbesen and P. M. Ajayan. *Large-scale synthesis of carbon nanotubes*. Nature **358**, 220 (1992).

[24] T. Guo, P. Nikolaev, A. Thess, D. T. Colbert, and R. E. Smalley. *Catalytic growth of single-walled manotubes by laser vaporization*. Chem. Phys. Lett. **243**, 49 (1995).

[25] Y. Li,W. Kim, Y. Zhang, M. Rolandi, D.Wang, and H. Dai. *Growth of single-walled carbon nanotubes from discrete catalytic nanoparticles of various sizes*. J. Phys. Chem. B **105**, 11424 (2001).

[26] L. Ci, Z. Zhou, X. Yan, D. Liu, H. Yuan, L. Song, J.Wang, Y. Gao, J. Zhou,W. Zhou, G.Wang, and S. Xie. *Raman characterization and tunable growth of double-wall carbon nanotubes*. J. Phys. Chem. B **107**, 8760 (2003).

[27] A. M. Cassell, N. R. Franklin, T. W. Tombler, E. M. Chan, J. Han, and H. Dai. *Directed growth of free-standing single-walled carbon nanotubes*. J. Am. Chem. Soc. **121**, 7975 (1999).

[28] W. A. de Heer, W. S. Bacsa, A. Chatelain, T. Gerfin, R. Humphrey-Baker, L. Forro, and D. Ugarte. *Aligned carbon nanotube films: production and optical and electronic properties*. Science **268**, 845 (1995).

[29] T. Tanaka, A. Tajima, R. Moriizumi, M. Hosoda, R. Ohno, E. Rokuta, C. Oshima, and S. Otani. *Carbon nano-ribbons and their edge phonons*. Solid State Comm. **123**, 33 (2002).

[30] K. Nakada, M. Fujita, G. Dresselhaus, and M. S. Dresselhaus. *Edge state in graphene ribbons: nanometer size effect and edge shape dependence*. Phys. Rev. B **54**, 17954 (1996).

[31] Y. Ouyang, Y. Yoon, J. K. Fodor, and J. Guo. *Comparison of performance limits for carbon nanoribbon and carbon nanotube transistors*. Appl. Phys. Lett. **89**, 203107 (2006).

[32] B. W. Smith, M. Monthioux, and D. E. Luzzi. *Encapsulated* C_{60} *in carbon nanotubes*. Nature **396**, 323 (1998).

[33] S. Okada, S. Saito, and A. Oshiyama. *Energetics and electronics structures of encapsulated* C_{60} *in a carbon nanotube*. Phys. Rev. Lett. **86**, 3835 (2001).

[34] S. Berber, Y.-K. Kwon, and David Tománek. *Microscopic Formation Mechanism of Nanotube Peapods*. Phys. Rev. Lett. **88**, 185502 (2002).

[35] D. Tománek. *Mesoscopic origami with graphite: scrolls, nanotube, peapods*. Physica B **323**, 86 (2002).

[36] B. W. Smith, M. Monthioux, and D. E. Luzzi. *Carbon nanotube encapsulated fullerenes: a unique class of hybrid materials*. Chemical Physics Letters **315**, 31 (1999).

[37] S. Bandow, K. Hirahara, T. Hiraoka, G. Chen, P. C. Eklund, and S. Iijima. *Turning peapods into double-walled carbon nanotubes*. MRS Bullettin/April 2004, 260 (2004).

[38] J. G. Lavin, S. Subramoney, R. S. Ruoff, S. Berber, and D. Tománek. *Scrolls and nested tubes in multiwall carbon nanotubes*. Carbon **40**, 1123 (2002).

[39] S. Berber and D. Tománek. *Stability differences and conversion mechanism between nanotube and scrolls*. Phys. Rev. B **69**, 233404 (2004).

[40] H. Shioyama and T. Akita. *A new route to carbon nanotubes*. Carbon **41**, 179 (2003).

[41] J. L. Li, Q. S. Peng, G. Z. Bai, and W. Jiang. *Carbon scrolls produced by high energy ball milling of graphite*. Carbon **43**, 2817 (2005).

[42] D. Tománek. *Carbon-based nanotechnology on a supercomputer*. J. Phys.: Condens. Matter **17**, R413-R459 (2005).

[43] H. Terrones and M. Terrones. *Curved nanostructured materials*. New Journ. Phys. **5**, 126 (2003).

[44] M. P. Anantram and F. Léonard. *Physics of carbon nanotube electronic devices*. Rep. Prog. Phys. **69**, 507 (2006).

[45] A. W. Hull. *A new method of X-Ray crystal analysis*. Phys. Rev. **10**, 661 (1917).

[46] J. D. Bernal. *The structure of graphite*. Proc. R. Soc. London, Ser. A **106**, 749 (1924).

[47] R. E. Peierls. *Bemerkungen über Umwandlungstemperaturen*. Helv. Phys. Acta **7**, 81 (1934).

[48] N. D. Mermin. *Crystalline order in two dimensions*. Phys. Rev. **176**, 250 (1968).

[49] J.-C. Charlier, X. Blase, and S. Roche. *Electronic and transport properties of nanotubes*. Rev. Mod. Phys. **79**, 677 (2007).

[50] A. A. Lucas, V. Bruyninckx, and P. Lambin. *Calculating the diffraction of electrons or X-rays by carbon nanotubes*. Europhys. Lett. **35**, 355 (1996).

[51] M. Kociak, K. Hirahara, K. Suenaga, and S. Iijima. *How accurate can the determination of chiral indices of carbon nanotubes be ?* Eur. Phys. J. B **32**, 457 (2003).

[52] Lu-Chang Qin. *Electron diffraction from carbon nanotubes*. Rep. Prog. Phys. **69**, 2761 (2006).

[53] S. G. Lemay, J. W. Janssen, M. van den Hout, M. Mooij, M. J. Bronikowski, P. A. Willis, R. E. Smalley, L. P. Kouwenhoven, and C. Dekker. *Two-dimensional imaging of electronic wavefunctions in carbon nanotubes*. Nature **412**, 617 (2001)

[54] P. Lambin, G. I. Márk, V. Meunier, and L. P. Biró. *Computation of STM images of carbon nanotubes*. Int. Journ. Qua. Chem. **95**, 493 (2003).

[55] T. W. Odom, J.-L. Huang, P. Kim, and C. M. Lieber. *Atomic structure and electronic properties of single-walled carbon nanotubes*. Nature **391**, 62 (1998).

[56] M. O'Connell, S. M. Bachilo, X. B. Huffman, V. C. Moore, M. S. Strano, E. H. Haroz, K. L. Rialon, P. J. Boul, W. H. Noon, C. Kittrell, J. Ma, R. H. Hauge, R. B. Weisman, and R. E. Smalley. *Band gap fluorescence from individual single-walled nanotubes,* Science **297**, 593 (2002).

[57] S. M. Bachilo, M. S. Strano, C. Kittrell, R. H. Hauge, R. E. Smalley, and R. B. Weisman. *Structure-assigned optical spectra of single-walled carbon nanotubes*, Science **298**, 2361 (2002).

[58] X. Liu, T. Pichler, M. Knupfer, M. S. Golden, J. Fink, H. Kataura, and Y. Achiba. *Detailed analysis of the mean diameter and diameter distribution of single-wall carbon nanotubes from their optical response*. Phys. Rev. B **66**, 45411 (2002).

[59] T. Belin and F. Epron. *Characterization methods of carbon nanotubes: a review*. Mat. Sci. Eng. B **119**, 105 (2005).

[60] S. Goedecker and G. E. Scuseria. *Linear scaling electronic structure methods in chemistry and physics*. Computing in Science and Engineering **5**, July/August 2003, 14 (2003).

[61] P. Hohenberg and W. Kohn. *Inhomogeneous electron gas*. Phys. Rev. **136**, B864 (1964).

[62] W. Kohn and L. J. Sham. *Self-consistent equations including exchange and correlation effects*. Phys. Rev. **140**, A1133 (1965).

[63] J. M. Soler, E. Artacho, J. D. Gale, A. García, J. Junquera, P. Ordejón, and D. Sánchez-Portal. *The SIESTA method for ab initio order-N materials simulation*. J. Phys.: Cond. Matter **14**, 2475 (2002).

[64] J. W. Mintmire, B. I. Dunlap, and C. T. White. *Are fullerene tubules metallic ?* Phys. Rev. Lett. **68**, 631 (1992).

[65] J. W. Mintmire and C. T. White. *First-principles band structures of armchair nanotubes*. Appl. Phys. A **67**, 65 (1998).

[66] X. Blase, L. X. Benedict, E. L. Shirley, and S. G. Louie. *Hybridization effects and metallicity in small radius carbon nanotubes*. Phys. Rev. Lett. **72**, 1878 (1994).

[67] D. Östling, D. Tománek, and A. Rosén. *Electronic structure of single-wall, multiwall, and filled carbon nanotubes*. Phys. Rev. B **55**, 13980 (1997).

[68] Y.-K. Kwon and D. Tománek. *Electronic and structural properties of multiwall carbon nanotubes*. Phys. Rev. B **58**, R16001 (1998).

[69] O. Dubay and G. Kresse. *Density functional calculations for C_{60} peapods*. Phys. Rev. B **70**, 165424 (2004).

[70] D. Porezag, Th. Frauenheim, Th. Köhler, G. Seifert, and R. Kaschner. *Construction of tight-binding-like potentials on the basis of density functional theory:application to carbon*. Phys. Rev. B **51**, 12947 (1995).

[71] T. Frauenheim, G. Seifert, M. Elstner, T. Niehaus, C. Köhler, M. Amkreutz, M. Sternberg, Z. Hajnal, A. Di Carlo, and S. Suhai. *Atomistic simulations of complex materials: ground-state and excited-state properties*. J. Phys.: Condens. Matter **14**, 3015 (2002).

[72] M. Born and K. Huang. *Dynamical Theory of Crystal Lattices* (Oxford University Press, Oxford, 1954).

[73] B. S. Kandemir and M. Keskin. *Analytical approach to phonons and electron-phonon interactions in single-walled zigzag carbon nanotubes*. J. Phys.: Condens. Matter **20**, 325222 (2008).

[74] J. C. Slater and G. F. Koster. *Simplified LCAO Method for the Periodic Potential Problem*. Phys. Rev. **94**, 1498 (1954).

[75] C. M. Goringe, D. R. Bowler, and E. Hernández. *Tight-binding modelling of materials*. Rep. Prog. Phys. **60**, 1447 (1997).

[76] R. Haydock, V. Heine, and M. J. Kelly. *Electronic structure based on the local atomic environment for tight-binding bands*. J. Phys. C: Solid State Phys. **5**, 2845 (1972).

[77] J. C. Slonczewski and P. R. Weiss. *Band structure of graphite*. Phys. Rev. **109**, 272 (1958).

[78] J. W. McClure. *Band structure of graphite and de Haas-van Alphen Effect*. Phys. Rev. **108**, 612 (1957).

[79] J.-C. Charlier, J. P. Michenaud, X. Gonze, and J.-P. Vigneron. *Tight-binding model for the electronic properties of simple hexagonal graphite*. Phys. Rev. B **44**, 13237 (1991).

[80] J.-C. Charlier, J. P. Michenaud, and Ph. Lambin. *Tight-binding density of electronic states of pregraphitic carbon*. Phys. Rev. B **46**, 4540 (1992).

[81] N. Hamada, S. Sawada, and A. Oshiyama. *New one-dimensional conductors: graphitic microtubules*. Phys. Rev. Lett. **68**, 1579 (1992).

[82] C. T. White, D. H. Robertson, and J. W. Mintmire. *Helical and rotational symmetries of nanoscale graphitic tubules*. Phys. Rev. B **47**, 5485 (1993).

[83] J. W. Mintmire and C. T. White. *Electronic and structural properties of carbon nanotubes*. Carbon **33**, 893 (1995).

[84] V. N. Popov. *Curvature effects on the structural, electronic and optical properties of isolated single-walled carbon nanotubes within a symmetry-adapted non-orthogonal tight-binding model*. New J. Phys. **6** 1 (2004).

[85] M. Damnjanović, T. Vuković, and I. Milosević. *Modified group projectors: tight-binding method*. J. Phys. A: Math. and Gen. **33** 6561 (2000).

[86] T. Ando. *Theory of electronic states and transport in carbon nanotubes*. J. Phys. Soc. Jpn. **74**, No.3 (2001).

[87] D. Tománek, W. Zhong, and E. Krastev. *Stability of multishell fullerene*. Phys. Rev. B 48, 15461 (1993).

[88] D. Kahn, K. W. Kim, and M. A. Stroscio. *Quantized vibrational modes of nanospheres and nanotubes in the elastic continuum model*. J. Appl. Phys. **89**, 5107 (2001).

[89] R. Saito, G. Dresselhaus and M. S. Dresselhaus. *Physical Properties of Carbon Nanotubes* (Imperial College Press, London, 1998).

[90] S. Reich, C. Thomsen and J. Maultzsch. *Carbon nanotubes: basic concepts and physical properties* (Wiley, 2004).

[91] L. M. Falicov. *Recent Progress in Many-Body Theories*,**1**, 275, (Plenum, New York, 1988) and references therein.

[92] G. D. Mahan. *Many-Particle Physics* (Plenum Press, New York, 1990).

[93] F. Jensen. *Introduction to Computational Chemistry* (John Wiley & Sons, 1999)

[94] E. Kaxiras. *Atomic and Electronic Structure of Solids* (Cambridge University Press, 2003).

[95] E. N. Economou. *Green's Functions in Quantum Physics* (Springer-Verlag Berlin Heidelberg New York 1979).

[96] L. I. Schiff. *Quantum Mechanics*, 3rd edition, (McGraw-Hill, New York, 1968).

[97] R. F. Wallis and M. Balkanski. *Many-Body Aspects of Solid State Spectroscopy* (North-Holland Amsterdam Oxford NewYork Tokyo, 1986).

[98] R. M. Martin and L. M. Falicov. *Resonant Raman Scattering*, in *Light Scattering in Solids I: edited by M. Cardona*, 70-145, (Springer-Verlag, Berlin, 1983), Vol. 8. Chapter 3, Topics in Applied Physics.

[99] D. J. Chadi and M. L. Cohen. *Special points in the Brillouin zone*. Phys. Rev. B **8**, 5747 (1973).

[100] S. L. Cunningham. *Special points in the two-dimensional Brillouin zone*. Phys. Rev. B **10**, 4988 (1974).

[101] L. Brey and C. Tejedor. *Raman tensor of covalent semiconductors*. Solid State Commun. **48**, 403 (1983).

[102] L. C. Lew Yan Voon and L. R. Ram-Mohan. *Tight-binding representation of the optical matrix elements: Theory and applications*. Phys. Rev. B **47**, 15500 (1993).

[103] J. Yepez. *A symbolic solution of the Hubbard model for small clusters*. Advanced Exam in Physics, PhD program, (Brandeis University, Massachussets, 1991). Available at: http://xyz.plh.af.mil/Papers/pdf/ae91.pdf

[104] J. Callaway, D. P. Chen, and R. Tang. *Ground state and thermodynamic properties of the Hubbard model applied to small custers*. Phys. Rev. B **35**, 3705 (1987).

[105] L. Milans del Bosch and L. M. Falicov. *Extended one-dimensional Hubbard model: A small-cluster approach*. Phys. Rev. B **37**, 6073 (1988).

[106] C. R. Proetto and L. M. Falicov. *Exact solution of a quantum electron-phonon system for a two-site periodic cluster*. Phys. Rev. B **39**, 7545 (1989).

[107] B. Koiller, M. A. M. Davidovich and L. M. Falicov. *Small-crystal approach to ordered semiconductor compounds*. Phys. Rev. B **41**, 3670 (1990).

[108] M. Meneghetti and C. Pecile. *Vibrational and electronic spectra of one-dimensional organic charge-transfer crystals: Model for a tetramerized cluster structure*. Phys. Rev. B **40**, 12187 (1989).

[109] M. Meneghetti and C. Pecile. *Periodic-dimer-cluster models for the study of the optical properties of dimerized half-filled organic charge-transfer crystals*. Phys. Rev. B **42**, 1605 (1990).

[110] M. Meneghetti. *Optical properties of organic conductor and semiconductor crystals: Model for a half-filled dimerized chain*. Phys. Rev. B **44**, 8554 (1991).

[111] M. Meneghetti. *Model for the linear and nonlinear optical properties of one-dimensional organic π-conjugated compounds*. Phys. Rev. B **47**, 13151 (1993).

[112] M. Meneghetti. *Optical properties of one-dimensional π-conjugated compounds: Study of the pressure-dependent linear properties of K-tetracyanoquinodimethane*. Phys. Rev. B **50**, 16899 (1994).

[113] M. Meneghetti and L. Feltre. *Electronic and vibronic excitations of quarter-filled periodic octamer*. Synthetic Metals **85**, 1629 (1997).

[114] M. Meneghetti. *Dynamic modulation of electron correlation by intramolecular modes in charge-transfer compounds*. Phys. Rev. B **60**, 15472 (1999).

[115] B. Koiller, R. Osó rio and L. M. Falicov. *Gap properties of* $\mathrm{Al}_n\mathrm{Ga}_{8-n}\mathrm{As}_8$. Phys. Rev. B **43**, 4170 (1991).

[116] G. G. Samsonidze, R. Saito, A. Jorio, M. A. Pimenta, A. G. Souza Filho, A. Grueneis, G. Dresselhaus, and M. S. Dresselhaus. *The concept of cutting lines in carbon nanotube science*. J. Nanosci. Nanotech. **3**, (2003).

[117] R.Saito, K. Sato, Y. Oyama, J. Jiang, Ge. G. Samsonidze, G. Dresselhaus, and M. S. Dresselhaus. *Cutting-lines near the Fermi energy of single-wall carbon nanotubes*, Phys. Rev. B **72**, 153413 (2005).

[118] E. B. Barros, A. Jorio, G. G. Samsonidze, R. B. Capaz, A. G. Souza Filho, J. Mendez Filho, G. Dresselhaus, and M. S. Dresselhaus. *Review on the symmetry-related properties of carbon nanotubes*. Phys. Reports, **431**, 261, (2006).

[119] M. S. Dresselhaus, G. Dresselhaus, R. Saito, and A. Jorio. *Raman spectroscopy of carbon nanotubes*. Phys. Reports, **409**, 47 (2005).

[120] M. S. Dresselhaus, G. Dresselhaus, and A. Jorio. *Raman spectroscopy of carbon nanotubes in 1997 and 2007*. J. Phys. Chem. C, **111**, 17887 (2007).

[121] A. Grueneis. *Resonance Raman spectroscopy of single wall carbon nanotubes*. Ph.D. Thesis, (University of Tokyo, 2004).

[122] Ge. G. Samsonidze. *Photophysics of carbon nanotubes*. Ph.D. Thesis (MIT, Boston, 2007).

[123] N. Nemec. *Quantum transport in carbon-based nanostructures*. Ph.D. Thesis (University of Regensburg, 2007).

[124] M. Damnjanović, I. Milošević, T. Vuković and R. Sredanović. *Full symmetry, optical activity, and potentials of single-wall and multiwall nanotubes*. Phys. Rev. B, **60**, 2728 (1999) and references therein.

[125] R. Saito, K. Sato, Y. Oyama, J. Jiang, G. G. Samsonidze, G. Dresselhaus, and M. S. Dresselhaus. *Cutting-lines near the Fermi-energy of single-wall carbon nanotubes*. Phys. Rev. B **72**, 153413, (2005).

[126] A. M. Rao, E. Richter, S. Bandow, B. Chase, P. C. Eklund, K. W. Williams, S. Fang, K. R. Subbaswamy, M. Menon, A. Thess, R. E. Smalley, G. Dresselhaus, and M. S. Dresselhaus. *Diameter-selective Raman scattering from vibrational modes in carbon nanotubes*. Science **275**, 187 (1997).

[127] H. Kataura, Y. Kumazawa, Y. Maniwa, I. Umezu, S. Suzuki, Y. Ohtsuka, and Y. Achiba. *Optical properties of single-wall carbon nanotubes*. Synth. Metals, **103**, 2555 (1999).

[128] A. Jorio, R. Saito, J. H. Hafner, C. M. Lieber, M. Hunter, T. McClure, G. Dresselhaus, and M. S. Dresselhaus. *Structural (n,m) determination of isolated single-wall carbon nanotubes by resonant Raman scattering*. Phys. Rev. Lett. **86**, 1181 (2001).

[129] R. B. Weisman and S. M. Bachilo. *Dependence of optical transition energies on structure for single-walled carbon nanotubes in acqueous suspension: an empirical Kataura plot*. Nanoletters **3**, 1235 (2003).

[130] A. Jorio, M. A. Pimenta, A.G. Souza Filho, R. Saito, G. Dresselhaus, and M. S. Dresselhaus. *Characterizing carbon nanotube samples with resonance Raman scattering*. New J. Phys. **5**, 1 (2003).

[131] C. Fantini, A. Jorio, M. Souza, M. S. Strano, M. S. Dresselhaus, and M. A. Pimenta. *Optical transition energies for carbon nanotubes from Resonant Raman Spectroscopy: Environment and Temperature Effects*. Phys. Rev. Lett. **93**, 147406 (2004).

[132] G. G. Samsonidze, R. Saito, N. Kobayashi, A. Grüneis, J. Jiang, A. Jorio, S. G. Chou, G. Dresselhaus, and M. S. Dresselhaus. *Family behaviour of the optical transition energies in single-wall carbon nanotubes of smaller diameters*. Appl. Phys. Lett. **85**, 5703 (2004).

[133] J. Maultzsch, H. Telg, S. Reich, and C. Thomsen. *Radial breathing mode of single-walled carbon nanotubes: optical transition energies and chiral-index assignment*. Phys. Rev. B **72**, 205438 (2005).

[134] L. G. Bulusheva, A. V. Okotrub, D. A. Romanov, and D. Tománek. *Electronic structure of (n,0) zigzag carbon nanotubes: cluster and crystal approach*. J. Phys. Chem. A **102**, 975 (1997).

[135] R. Saito, G. Dresselhaus, and M. S. Dresselhaus. *Trigonal warping effect of carbon nanotubes*. Phys. Rev. B **61**, 2981 (2000).

[136] J. W. Mintmire and C. T. White. *Universal density of states for carbon nanotubes*. Phys. Rev. Letter **81**, 2506 (1998).

[137] C. T. White and J. W. Mintmire. *Density of states reflects diameter in nanotubes*. Nature **394**, 29 (1998).

[138] S. Reich and C. Thomsen. *Chirality dependence of the density-of-states singularities in carbon nanotubes*. Phys. Rev. B **62**, 4273 (2000).

[139] H. Ajiki and T. Ando. *Aharonov-Bohm effect in carbon nanotubes*. Physica B Condensed Matter **201**, 349 (1994).

[140] S. Tasaki, K. Maekawa and T. Yamabe. *π-band contribution to the optical properties of carbon nanotubes: effects of chirality*. Phys. Rev. B **57**, 9301 (1998).

[141] Ge. G. Samsonidze, A. Grüneis, R. Saito, A. Jorio, A. G. Souza Filho, G. Dresselhaus, and M. S. Dresselhaus. *Interband optical transitions in left- and righthanded single-wall carbon nanotubes*. Phys. Rev. B **69**, 205402 (2004).

[142] A. Grüneis, R. Saito, G. G. Samsonidze, T. Kimura, M. A. Pimenta, A. Jorio, A. G. Souza Filho, G. Dresselhaus, and M. S. Dresselhaus. *Inhomogeneous optical absorption around the K point in graphite and carbon nanotubes*. Phys. Rev. B **67**, 165402 (2003).

[143] R. Saito, A. Grueneis, Ge. G. Samsonidze, G. Dresselhaus, M. S. Dresselhaus, A. Jorio, L. G. Cancado, M. A. Pimenta, and A. G. Souza. *Optical absorption of graphite and single-wall carbon nanotubes*. Appl. Phys. A **78**, 1099 (2004).

[144] J. Jiang, R. Saito, A. Grueneis, G. Dresselhaus, and M. S. Dresselhaus. *Optical absorption matrix elements in single-wall carbon nanotubes*. Carbon **42**, 3169 (2004).

[145] E. Malic, M. Hirtschulz, F. Milde, A. Knorr, and S. Reich. *Analytical approach to optical absorption in carbon nanotubes*. Phys. Rev. B **74**, 195431 (2006).

[146] J. Jiang, R. Saito, A. Grüneis, S. G. Chou, Ge. G. Samsonidze, A. Jorio, G. Dresselhaus, and M. S. Dresselhaus. *Intensity of the resonance Raman excitation spectra of single-wall carbon nanotubes*. Phys. Rev. B **71**, 205420 (2005).

[147] L. G. Johnson and G. Dresselhaus. *Optical properties of graphite*. Phys. Rev. B **7**, 2275 (1973).

[148] A. Zarifi and T. G. Pedersen. *Analytic approach to the linear susceptibility of zigzag carbon nanotubes*. Phys. Rev. B **74**, 155434 (2006).

[149] J. C. Charlier, T. W. Ebbesen, and Ph. Lambin. *Structural and electronic properties of pentagon-heptagon pair defects in carbon nanotubes*. Phys. Rev. B **53**, 11108, (1996).

[150] N. Nemec and G. Cuniberti. *Hofstadter butterflies of carbon nanotubes: pseudofractality of the magnetoelectronic spectrum*. Phys. Rev. B **74**, 165411 (2006).

[151] H. Hsu and L. E. Reichl. *Selection rule for the optical absorption of graphene nanoribbons*. Phys. Rev. B **76**, 045418 (2007).

[152] A. K. Gupta, O. Alon, and N. Moiseyev. *Generation and control of high-order harmonics by the interaction of an infrared laser with a thin graphite layer*. Phys. Rev. B **68**, 205101 (2003).

[153] A. Jorio, M. A. Pimenta, A. G. Souza Filho, Ge. G. Samsonidze, A. K. Swan, M. S. Ünlü, B. B. Goldberg, R. Saito, G. Dresselhaus, and M. S. Dresselhaus. *Resonance Raman spectra of carbon nanotubes by cross-polarized light*. Phys. Rev. Lett. **90**, 107403 (2003).

[154] X. P. Yang, J. W. Chen, H. Jiang, and J. M. Dong. *Chiral symmetry of double-walled carbon nanotubes detected in first-principles optical absorption spectra*. Phys. Rev. B **69**, 193401 (2004).

[155] R. Saito, G. Dresselhaus, and M. Dresselhaus. *Electronic structure of double-layer graphene tubules*. J. Appl. Phys. **73**, 494 (1993).

[156] Y. A. Kim, H. Muramatsu, T. Hayashi, M. Endo, M. Terrones, and M. S. Dresselhaus. *Thermal stability and structural changes of double-walled carbon nanotubes by heat treatment*. Chem. Phys. Lett. **398**, 87 (2004).

[157] Y. E. Lozovik and A. M. Popov. *Properties and nanotechnological applications of nanotubes*. Physics-Uspekhi **50**, 749 (2007)

[158] Z. C. Tu and Z. C. Ou-Yang. *A molecular motor constructed from a double-walled carbon nanotube driven by temperature variation*. J. Phys.:Condens. Matter **16**, 1287 (2004).

[159] S. W. D. Bailey, I. Amanatidis, and C. J. Lambert. *Carbon nanotube electron windmills: a novel design for nanomotors*. Phys. Rev. Lett. **100**, 256802 (2008).

[160] G. Marcolongo, G. Ruaro, M. Gobbo, and M. Meneghetti. *Amino acid functionalization of double-wall carbon nanotubes studied by Raman spectroscopy*. Chem. Comm. **46**, 4925 (2007).

[161] S. Bandow, G. Chen, G. U. Sumanasekera, R. Gupta, M. Yudasaka, S. Iijima, and P. C. Eklund. *Diameter-selective resonant Raman scattering in double-wall carbon nanotubes*. Phys. Rev. B **66**, 075416 (2002).

[162] W. Ren, F. Li, P. Tan, and H.-M. Cheng. *Raman evidence for atomic correlation between the constituent tubes in double-walled carbon nanotubes*. Phys. Rev. B **73**, 115430 (2006).

[163] A. Hashimoto, K. Suenaga, K. Urita, T. Shimada, T. Sugai, S. Bandow, H. Shinohara, and S. Iijima. *Atomic correlation between adjacent graphene layers in double-walled carbon nanotubes*. Phys. Rev. Lett. **94**, 045504 (2005).

[164] T. Hertel, A. Hagen, V. Talalaev, K. Arnold, F. Hennrich, M. Kappes, S. Rosenthal, and J. McBride. *Spectroscopy of single- and double-wall carbon nanotubes in different environments*. NanoLett. **5**, 511 (2005).

[165] R. Pfeiffer, F. Simon, H. Kuzmany, and V. N. Popov. *Fine structure of the radial breathing mode of double-wall carbon nanotubes*, Phys. Rev. B **72**, 161404(R) (2005).

[166] E. B. Barros, H. Son, Ge. G. Samsonidze, A. G. Souza Filho, R. Saito, Y. A. Kim, H. Muramatsu, T. Hayashi, M. Endo, J. Kong, and M.S. Dresselhaus. *Raman spectroscopy of double-walled carbon nanotubes treated with* H_2SO_4. Phys. Rev. B **76**, 045425 (2007).

[167] F. Li, S. G. Chou, W. Ren, J. A. Gardecki, A. K. Swan, B. B. Goldberg, and M. S. Dresselhaus. *Identification of the constituents of double-walled carbon nanotubes using Raman spectra taken with different laser-excitation energies*. J. Mater. Res. **18**, 1251 (2003).

[168] Shi-Dong Liang. *Intrinsic properties of electronic structure in commensurate double-wall carbon nanotubes*. Physica B **352**, 305 (2004).

[169] Ph. Lambin, L. Philippe, J. C. Charlier, and J. Michenaud. *Electronic band structure of multilayered carbon tubules*. Comput. Mat. Sci. **2**, 350 (1994).

[170] Ph. Lambin, V. Meunier, and A. Rubio. *Electronic structure of polychiral carbon nanotubes*. Phys. Rev. B **62**, 5129 (2000).

[171] S. Roche, F. Triozon, A. Rubio, and D. Mayou. *Conduction mechanisms and magnetotransport in multiwalled carbon nanotubes*. Phys. Rev. B **64**, 121401(R) (2001).

[172] Y. H. Ho, C. P. Chang, F. L. Shyu, R. B. Chen, S. C. Chen, and M. F. Lin. *Electronic and optical properties of double-walled armchair carbon nanotubes*. Carbon **42**, 3159 (2004).

[173] Y. H. Ho, G. W. Ho, S. J. Wu, and M. F. Lin. *Band structures of double-walled carbon nanotubes*. J. Vac. Sci. Technol. B **24**, 1098 (2006).

[174] Y. H. Ho, G. W. Ho, S. C. Chen, J. H. Ho, and M. F. Lin. *Low-frequency excitation spectra in double-walled armchair carbon nanotubes*. Phys. Rev. B **76**, 115422 (2007).

[175] S. Uryu and T. Ando. *Electronic intertube transfer in double-wall carbon nanotubes*. Phys. Rev. B **72**, 245403 (2005).

[176] V. Zólyomi, Á. Rusznyák, J. Kürti, Á. Gali, F. Simon, H. Kuzmany, Á. Szabados, and P. R. Surján. *Semiconductor-to-metal transition of double walled carbon nanotubes induced by intershell interaction*. Phys. Status Solidi B **243**, 3476 (2006).

[177] M. Damnjanović, I. Milošević, E. Dobardžić, T. Vuković, and B. Nikolić. *Symmetry of commensurate double-wall carbon nanotubes*. J. Phys. A: Math. Gen. **36**, 10349 (2003).

[178] M. Damnjanović, E. Dobardžić, I. Milošević, T. Vuković, and B. Nikolić. *Lattice dynamics and symmetry of double wall carbon nanotubes*. N. J. Phys. **5**, 148 (2003).

[179] H. Abud and G. Sartori. *The geometry of spontaneous symmetry breaking*. Annals of Physics (NY) **150**, 307 (1983).

[180] Shidong Wang and Milena Grifoni. *Helicity and electron-correlation effects on transport properties of double-walled carbon nanotubes*. Phys. Rev. Lett. **95**, 266802 (2005).

[181] Jie Lu and Shidong Wang. *Tight-binding investigation of the metallic proximity effect of semiconductor-metal double-wall carbon nanotubes*. Phys. Rev. B **76**, 233103 (2007).

[182] J.-C. Charlier and J.-P. Michenaud. *Energetics of multilayered carbon tubules*. Phys. Rev. Lett. **70**, 1858 (1993).

[183] S. Okada and A. Oshiyama. *Curvature-induced metallization of double-walled semiconducting zigzag carbon nanotubes*. Phys. Rev. Lett. **91**, 216801 (2003).

[184] P. N. D'yachkov and D. V. Makaev. *Linear augmented cylindrical wave for calculating the electronic structure of double-wall carbon nanotubes*. Phys. Rev. B **74**, 155442 (2006).

[185] M. Damnjanović. *Super-slippery carbon nanotubes: symmetry breaking breaks friction*. Eur. Phys. Journ. B **25**, 131 (2002).

[186] J. Cumings and A. Zettl. *Low-friction nanoscale linear bearing realized from multiwall carbon nanotubes*. Science **289**, 602 (2000).

[187] R. Loudon. *One-dimensional hydrogen atom*. Am. J. Phys. **27**, 649 (1959).

[188] J. Hubbard. *Electron correlations in narrow energy bands*. Proc. Roy. Soc. London A **276**, 238 (1963); ibid **277**, 237 (1964); ibid **281**, 401 (1965).

[189] E. Dagotto. *Correlated electrons in high-temperature superconductors*. Rev. Mod. Phys. **66**, 763 (1994).

[190] N. F. Mott and Z. Zinamon. *The metal-nonmetal transition*. Rep. Prog. Phys. **33**, 881 (1970).

[191] I. Bâldea and L. Cederbaum. *Unusual scarcity in the optical absorption of metallic quantum-dot nanorings described by the extended Hubbard model*. Phys. Rev. B **77**, 165339 (2008).

[192] J.-P. Nikkarila, M. Koskinen, and M. Manninen. *Magnetism of quantum dot clusters: a Hubbard model study*. Eur. Phys. J. B **64**, 95 (2008).

[193] E. H. Lieb and F. Y. Wu. *Absence of Mott transition in an exact solution of the short-range, one-band model in one dimension*. Phys. Rev. Lett.**20**,1445 (1968).

[194] Tsuneya Ando. *Excitons in carbon nanotubes*. Journ. Phys. Soc. Japan **66**, 1066 (1997).

[195] C. L. Kane and E. J. Mele. *Ratio problem in single carbon nanotube fluorescence spectroscopy*. Phys. Rev. Lett. **90**, 207401 (2003).

[196] C. L. Kane and E. J. Mele. *Electron Interactions and scaling relations for optical excitations in carbon nanotubes*. Phys. Rev. Lett. **93**, 197402 (2004).

[197] F. Wang, G.Dukovic, L.E. Brus, and T. F. Heinz. *The optical resonances in carbon nanotubes arise from excitons*. Science **308**, 5723 (2005).

[198] J. Maultzsch, R. Pomraenke, S. Reich, E. Chang, D. Prezzi, A. Ruini, E. Molinari, M. S. Strano, C. Thomsen, and C. Lienau. *Exciton binding energies in carbon nanotubes from two-photon photoluminescence*. Phys. Rev. B **72**, 241402 (2005).

[199] C. D. Spataru, S. Ismail-Beigi, L. X. Benedict, and S. G. Louie. *Excitonic effects and optical spectra of single-walled carbon nanotubes*. Phys. Rev. Lett. **92**, 077402 (2004).

[200] E. Chang, G. Bussi, A. Ruini, and E. Molinari. *Excitons in carbon nanotubes: an ab initio symmetry-based approach*. Phys. Rev. Lett. **92**, 196401 (2004).

[201] T. G. Pedersen. *Variational approach to excitons in carbon nanotubes*. Phys. Rev. B **67**, 073401 (2003).

[202] V. Perebeinos, J. Tersoff, and P. Avouris. *Scaling of excitons in carbon nanotubes*. Phys. Rev. Lett. **92**, 257402 (2004).

[203] E. Chang, G. Bussi, A. Ruini, and E. Molinari. *First-principles approach for the calculation of optical properties of one-dimensional systems with helical symmetry: the case of carbon nanotubes*. Phys. Rev. B **72**, 195423 (2005).

[204] J. Jiang, R. Saito, K. Sato, J. S. Park, Ge. G. Samsonidze, A. Jorio, G. Dresselhaus, and M. S. Dresselhaus. *Exciton-photon, exciton-phonon matrix elements, and resonant Raman intensity of single-wall carbon nanotubes*. Phys. Rev. B **75**, 035405 (2007).

[205] J. Jiang, R. Saito, Ge. G. Samsonidze, A. Jorio, G. Dresselhaus, and M. S. Dresselhaus. *Chirality dependence of exciton effects in single-wall carbon nanotubes: tight-binding model*. Phys. Rev. B **75**, 035407 (2007).

[206] O. Kiowski, K. Arnold, S. Lebedkin, F. Hennrich, and M. Kappes. *Direct observation of deep excitonic states in the photoluminescence spectra of single-walled carbon nanotubes*. Phys. Rev. Lett. **99**, 237402 (2007).

[207] R. Matsunaga, K. Matsuda, and Y. Kanemitsu. *Evidence for dark excitons in a single carbon nanotube due to the Aharonov-Bohm effect*. Phys. Rev. Lett. **101**, 147404 (2008).

[208] H. Zhao and S. Mazumdar. *Electron-electron interaction effects on the optical excitations of semiconducting single-walled carbon nanotubes*. Phys. Rev. Lett. **93**, 157402 (2004).

[209] Z. Wang, H. Zhao, and S. Mazumdar. *Quantitative calculations of the excitonic energy spectra of semiconductig single-walled carbon nanotubes within a π-electron model*. Phys. Rev. B **74**, 195406 (2006).

[210] S. Mazumdar, Z. Wang, and H. Zhao. *Universality in the photophysics of π-conjugated polymers and single-walled carbon nanotubes* in *Ultrafast dynamics and laser action of organic semiconductors* (2008) and references therein, arXiv.org: 0809.2119.

[211] S. Uryu, H. Ajiki, and T. Ando. *Excitonic two-photon absorption in semiconducting carbon nanotubes within an effective-mass approximation*. Phys. Rev. B **78**, 115414 (2008).

[212] E. Perfetto, M. Cini, S. Ugenti, P. Castrucci, M. Scarselli, M. De Crescenzi, F. Rosei, and M. A. El Khakani. *Experimental and theoretical study of electronic correlations in carbon nanotubes and graphite from Auger spectroscopy*. Journ. Phys.: Conference Series **100**, 052082 (2008).

[213] E. Perfetto, M. Cini, S. Ugenti, P. Castrucci, M. Scarselli, M. De Crescenzi, F. Rosei, and M. A. El Khakani. *Electronic correlations in carbon nanotubes and graphite from Auger spectroscopy*. arXiv:0710.3721 [cond-mat.str-el] (2008).

[214] F. Lin and E. S. Sørensen. *Estimates of effective Hubbard model parameters for* C_{20} *isomers*. Phys. Rev. B **78**, 085435 (2008).

[215] P. F. Maldague. *Optical spectrum of a Hubbard chain*. Phys. Rev. B **16**, 2437 (1977).

[216] F. Gebhard. *Optical absorption of non-interacting tight-binding electrons in a Peierls-distorted chain at half band-filling*. Phil. Mag. B 75, pp. 1-12 (1997), also available from arXiv:cond-mat/9609089v1 (1996).

[217] H. Q. Lin and J. E. Gubernatis. *Exact diagonalization method for quantum systems*. Computers in Physics **7**, 400 (1993).

[218] http://www.wolfram.com

[219] W. Kinzel and G. Reents. *Physics by Computer: Programming Physical Problems using Mathematica and C*. (Springer, 1998).

[220] Rok Zitko. The SNEG Ljubljana Library v. 1.161 (2008). Available from http://nrgljubljana.ijs.si/sneg/

[221] http://math.nist.gov/MatrixMarket/formats.html

[222] http://math-atlas.sourceforge.net/

[223] http://www.caam.rice.edu/software/ARPACK/

[224] M. Troyer. *Are generic parallel algorithms feasible for quantum lattice models ?* Proceedings of ISCOPE ' 99, Lecture Notes in Computer Science **1732**, 164, (1999), Springer-Verlag Berlin Heidelberg (1999).

[225] F. Alet, P. Dayal, A. Grzesik, A. Honecker, M. Körner, A. Läuchli, S. R. Manmana, I. P. McCulloch, F. Michel, R. M. Noack, G. Schmid, U. Schollwöck, F. Stöckli, S. Todo, S. Trebst, M. Troyer, P. Werner, and S. Wessel. *The ALPS project: open source software for strongly correlated systems*. J.Phys. Soc. Jpn **74**, Suppl. , 30 (2005).

[226] A. F. Albuquerque, F. Alet, P. Corboz, P. Dayal, A. Feiguin, S. Fuchs, L. Gamper, E. Gull, S. Gürtler, A. Honecker, R. Igarashi, M. Körner, A. Kozhevnikov, A. Läuchli, S. R. Manmana, M. Matsumoto, I. P. McCulloch, F. Michel, R. M. Noack, G. Pawłowski, L. Pollet, T. Pruschke, U. Schollwöck, S. Todo, S. Trebst, M. Troyer, P. Werner, and S. Wessel. *The ALPS project release 1.3: open-source software for strongly correlated systems*. J. Magn. Magn. Mater. **310**, 1187 (2007).

[227] L. Salem. *The Molecular Orbital Theory of Conjugated Systems*,W.A. Benjamin, Inc., New York, 1966, par.1-10, p. 43.

[228] M. Glerup, V. Krstic, C. Ewels, M. Holzinger, and G. Van Lier, *Doping of Carbon Nanotubes* in *Doped Nanomaterials and Nanodevices*, Ed. Wei Chen (2007) and references therein.

[229] S. Latil, S. Roche, D. Mayou, and J.-C. Charlier, *Mesoscopic transport in chemically doped carbon nanotubes*, Phys. Rev. Lett. **92**, 256805 (2004).

[230] N. M. Peres, F. D. Klironomos, S.-W. Tsai, J. R. Santos, J. M. B. Lopes dos Santos, and A. H. Castro Neto, *Electron waves in chemically substituted graphene*, arXiv:0705.3040v1 [cond-mat], (2007).